SUBDURAL HEMATOMA AND AGING: CRASH CHARACTERISTICS AND ASSOCIATED INJURIES

Ann Mallory
Rod Herriott
Transportation Research Center Inc.
Heather Rhule
National Highway Traffic Safety Administration

United States of America
Paper Number 11-0399

ABSTRACT

Among motor vehicle crash head injuries, subdural hematomas (SDH) are both frequent and life-threatening, especially for older occupants. Previous research on the mechanism of injury and on the increased vulnerability of older individuals to SDH has focused on the failure of bridging veins, which are one possible source of subdural bleeding. For all age groups, the injury mechanism and injury tolerance for SDH as a result of other bleeding sources has not been addressed. In the current study, two US crash databases were used to compare crash and injury characteristics for SDH cases in different age groups, with a focus on the original source of bleeding. Review of cases from the Crash Injury Research and Engineering Network (CIREN) database showed that both bridging veins *and* bleeding sources other than bridging veins are responsible for SDH among crash occupants in all age groups. Analysis of weighted data from the National Automotive Sampling System Crashworthiness Data System (NASS CDS) showed that the frequency of isolated SDH increases with age, potentially reflecting an increase in the frequency of SDH caused by bridging vein bleeding, particularly in frontal crashes and among women. SDH accompanied by brain contusions or other potential bleeding sources on the surface of the brain are also common, especially in side impacts and among occupants younger than 70. These cases potentially represent injuries where subdural bleeding came from sources other than bridging veins. Improved definition of SDH injury tolerance for all adult occupants will require a better understanding of the mechanism of injury from sources other than bridging veins, but determination of SDH injury tolerance for older occupants should focus on evaluation of the increasing risk of bridging vein failure with age.

INTRODUCTION

Subdural hematoma (SDH) is a frequent and life-threatening injury, especially for older adults. SDH has been reported in 26-36% of serious head injury cases [Gennarelli and Graham, 2005, Perel et al., 2009] and is reported to be among the most frequent injuries seen by neurosurgeons [Taussky et al., 2008]. Mortality rates are reported from 33 to 79% [Sawauchi and Abe, 2008, Servadei, 1997, Taussky et al., 2008]. For older occupants, SDH presents doubly-increased risks since it is not only more frequent among older individuals [Mallory, 2010, Seelig et al., 1981] but also presents an increasing rate of mortality and poor outcome with increasing age [Hanif et al., 2009, Hukkelhoven et al., 2003, Raju et al., 2004, Stitzel et al., 2008].

SDH are collections of blood that form in the dural border cell layer between the dura and arachnoid [Haines et al., 1993] or between the dura and the pial surface of the brain [Miller and Statham, 2000]. The original source for the bleeding that produces SDH can be from adjacent brain contusions, lacerations or intracerebral hematomas; from ruptured cortical vessels on the surface of the brain; or from the bridging veins that cross the meninges en route to the dural sinuses [Depreitere et al., 2006, Graham, 1996, Lee et al., 1987, Miller et al., 1996, Miller and Statham, 2000, Toyama et al., 2005]. Although ruptured bridging veins are generally believed to be a major source of SDH [Gennarelli and Thibault, 1982, Gennarelli and Graham, 2005, Lee and Haut, 1989], post-mortem studies of fatal traumatic subdural cases showed that as many as two thirds of SDH were the result of brain contusions [Maxeiner, 1997]. In the remaining third of cases, bleeding was attributed to bridging vein rupture and torn cortical arteries with

equal frequency [Maxeiner and Wolff, 2002]. Previously, in a study of surgically-treated SDH cases, bleeding from cerebral lacerations or intracranial hematoma was identified as the cause of SDH in 40.5% of cases [Jamieson and Yelland, 1972].

Subdural Hematoma Originating from Bridging Veins Experimental studies exploring injury mechanism and tolerance for SDH at any age have primarily focused on those that originate with the rupture of parasagittal bridging veins. Holbourn proposed that rotational motion of the brain relative to the skull stretched the bridging veins that cross the meningeal layers [Holbourn, 1943]. Ommaya et al. produced parasagittal SDH in rhesus monkeys by simulating a rear impact and attributed it to veins draining into the sagittal sinus [Ommaya et al., 1968]. Löwenhielm produced bridging vein rupture in frontal sled tests with post-mortem human subjects to estimate tolerance relative to anterior-posterior rotation [Löwenhielm, 1974]. Gennerelli and Thibault produced SDH in rhesus monkeys by applying anterior-posterior acceleration in a 60 degree arc, with demonstrable damage to bridging veins underlying the hematoma [Gennarelli and Thibault, 1982]. Depreitere documented parasagittal bridging vein failure in post-mortem human subjects by pressurizing the superior sagittal sinus with radiopaque fluid. Radiographs following anterior-posterior impacts were used to identify bridging vein rupture and predict tolerance to sagittal plane rotation/acceleration [Depreitere et al., 2005, Depreitere et al., 2006].

Age-related brain atrophy is thought to contribute to bridging vein failure in older individuals because it can lead to increased relative motion between the skull and brain, resulting in increased tension in the bridging veins [Hanif et al., 2009, Meaney, 1991, Yamashima and Friede, 1984]. Modeling studies have predicted a tripling of bridging vein strain in frontal impacts with modeled increase in the thickness of the subdural space to simulate age-related atrophy [Kleiven and von Holst, 2002]. Other explanations explored for decreased tolerance to SDH in older individuals associated with bridging vein rupture include age-related alterations in the mechanical properties of bridging veins [Meaney, 1991, Monson, 2001] and in the viscoelastic properties of the brain [Jane and Francel, 1996].

Subdural Hematoma Originating from Other Sources In contrast to the body of work on SDH resulting from bridging vein failure, there is limited documentation on the mechanism of SDH as a result of other bleeding sources, or on how tolerance to these types of SDH changes with age. Studies that have addressed SDH from sources other than bridging veins have focused on the conditions under which SDH from sources other than bridging veins occur rather than the mechanical loading required to produce both the original bleeding injury and the SDH.

Comparison Studies of Subdural Hematomas from Different Bleeding Sources A long-term study of surgically treated SDH cases found that in 40.5% of cases there was a laceration, intracerebral clot, or "exploded" temporal poles that was a cause of the SDH [Jamieson and Yelland, 1972]. These were categorized as "complicated" SDH and were more common among males but less common for adults over age 60. These complicated SDH were more common in motor vehicle crashes than "simple" SDH that were not associated with a surface contusion or laceration. In complicated SDH cases, the head impact was lateral 55% of the time. Among those lateral head impact cases, the impact and SDH were on the same side in 53% of cases and on contralateral sides in 47%.

In an autopsy study comparing 42 SDH cases with associated cerebral contusions to 30 cases of isolated SDH [Maxeiner, 1998], those with contusions were more common in falls (81%) or traffic events (17%), while isolated subdural cases occurred most often in falls (37%), from violence (26%), or from unclear sources [Maxeiner, 1998]. Isolated SDH were attributed to lateral impacts in only 12% of cases where direction was determined, while those with contusions were sustained in lateral impacts in 44% of cases.

While these two previous studies suggest that there are differences in the head impact conditions that produce SDH by bridging vein failure versus by other sources, they do not address the mechanical loading that results in SDH from sources other than bridging veins or address how tolerance might be affected by age.

Objective of Current Study To determine how tolerance to SDH changes for older occupants, the bleeding sources for SDH among different age groups need to be identified. With bleeding source information by age group, it can be determined if either bridging vein ruptures or other bleeding sources are primarily responsible for the increase in SDH for older occupants.

The current study uses available US crash data to explore how crash and injury characteristics for occupants who sustain SDH change with age. Specifically, the available US crash data was analyzed to look for any evidence that older occupants may be more susceptible to SDH as a result of bridging vein failure versus as a result of contusions or ruptured vessels on the surface of the brain.

METHODS

In order to understand how the risk of SDH changes for motor vehicle crash occupants as they age, US databases were used to compare crash and injury characteristics for adult SDH cases in different age groups, with a focus on evidence of the original bleeding source.

Medical information available in CIREN was used for detailed review of cases where the probable bleeding source in SDH cases could be identified. Cases were categorized by the bleeding source: *bridging veins*, *brain contusions*, or *other bleeding sources*.

Because NASS CDS does not contain the detailed medical information included in CIREN, a different approach was used to identify possible bleeding sources for SDH. Crash data from NASS CDS was compiled to determine the frequency of different serious bleeding head injuries that accompany SDH. SDH cases were sorted into three categories. Those sustained in the absence of other serious head injuries were identified as *isolated*. The remaining cases were categorized as SDH *with contusion* or SDH *with other serious head injury*. In the absence of specific information on bleeding sources in NASS CDS cases coded with SDH, it was assumed that isolated cases with no other serious head injury documented were more likely than other cases to be associated with bridging vein failure directly into the subdural border cell region since bridging veins are the only potential bleeding source that pass through the dural border cell layer. Similarly it was assumed that subdural cases that also had a documented brain contusion were the injury category most likely to include SDH sourced to contusions. Other potential subdural bleeding sources were combined in a third category with all other serious head injuries.

CIREN Case Review

All SDH cases in NHTSA's CIREN crash database up to August 2010 were selected. Those with recorded intracranial surgery for evacuation of SDH were reviewed individually. Operative reports were evaluated for documentation of bleeding source for each of these cases. SDH cases with operative reports were categorized into those associated with (1) bridging vein rupture, (2) brain contusions, or (3) other specified bleeding sources.

After categorizing the CIREN cases by associated bleeding source using the detailed medical descriptions available in the operative reports, the cases were also sorted by the accompanying injury categories used for the NASS CDS analysis using only the Abbreviated Injury Scale (AIS) coded injuries: *isolated, with contusion,* or *with other serious injury*. For example, a CIREN case that documented subdural bleeding from a bridging vein might have been coded as *isolated,* or *with other serious injury*, if it were sorted as in the NASS CDS analysis. A case-by-case comparison was made to determine if the NASS CDS accompanying injury categories, determined from AIS code only, were consistent with the CIREN categories based on the probable bleeding sources identified in the detailed records. This comparison was used to confirm the suitability of using the accompanying injuries in NASS CDS cases as surrogate variables for probable bleeding sources in the absence of explicitly coded information on bleeding source in NASS CDS.

NASS CDS Analysis

SDH cases in NASS CDS from 1993 to 2008 were selected based on seven-digit AIS codes. The AIS codes used in NASS CDS were based on the Association for the Advancement of Automotive Medicine's AIS-90 from 1993 to 1999, and on the

AIS-90/98 Update from 2000 to 2008. Serious injuries are those with an AIS score of 3 to 6.

All analyses compared three adult age groups: 20-49 years, 50-69 years, and age 70 and older. Occupants under age 20 were excluded. Occupants in all seat positions were included. Cases with unknown impact direction or velocity change were excluded only from analyses that included those variables. Weighted data was used for all NASS CDS analyses. Analysis was performed using survey analysis procedures in SAS, Version 9.2 (SAS Institute, Cary NC).

Accompanying Head Injuries The percentage of occupants in NASS CDS with SDH who also had other types of serious head injuries was estimated by age group. AIS 3+ head injuries were initially classified by their seven-digit AIS code into categories as follows:

- Skull fracture (*including crush, fracture)*
- Subarachnoid hemorrhage
- Contusions
- Intraventricular hemorrhage
- Epidural hematoma
- Other intracranial bleeding injury (*Including blood vessel injury, hematoma or hemorrhage not further specified, subpial hemorrhage, laceration or penetration, sinus bleeding, intracerebellar or intracerebral bleeding)*
- Closed head injury (*Including loss of consciousness or concussion, diffuse axonal injury, or closed head injury/blunt head injury/ traumatic brain injury not further specified)*
- Sequelae (*Including swelling, ischemia, pneumocephalus)*
- Brain stem injury (*Including any injury to the brain stem)*
- Other intracranial injury *(Any other injury to the AIS head region not included in the categories above, such as pituitary injury or serious scalp injury)*

SDH cases with no other serious injuries were classified as Isolated SDH.

Relative Frequency of Isolated Subdural Hematoma For the purpose of comparing the crash characteristics of SDH cases that were isolated to cases where the SDH was accompanied by a contusion, or by other serious head injury, SDH cases were grouped as follows:

Isolated
: No other documented AIS 3+ head injury

With contusion
: SDH combined with AIS 3+ coded brain contusion

With other serious injury
: SDH combined with serious head injuries (AIS 3+) other than contusion.

The frequency of isolated SDH was compared to the frequency of SDH accompanied by contusion or other serious injuries for different types of occupant and impact conditions. Frequency of each sub-type of SDH case was calculated as a percentage of all SDH cases among each occupant or crash type. Data is presented by sex, age group, vehicle impact direction, and head contact location.

Vehicle impact directions are defined by the direction of force (DOF1) variable in NASS CDS. Frontal impacts included those from 11 o'clock to 1 o'clock, as well as those at 10 or 2 o'clock only if the general area of damage (GAD1) was to the front of the vehicle. Side impacts were defined as all other cases with direction of force from 2 to 4 o'clock and 8 to 10 o'clock. Rear impacts included those from 5 to 7 o'clock and rollovers were any crash where the primary damage (variable TDD1) was overturn damage. Head contact locations were estimated based on the location of cutaneous and fracture injuries coded to the head and face. Injuries coded to the frontal aspect of the head were classified as frontal contacts and to the left or right aspects were classified as lateral contacts. Any face contact injury in combination with a frontal head contact, or without any other contact injuries to the head was classified as a frontal head contact. If face contact injuries were coded to the left or right aspect and were combined with a lateral head contact injury, the case was classified as a lateral head contact.

For vehicle side impact cases, the location of the SDH was compared to the vehicle impact direction. Cases where the vehicle impact and SDH were on the same side were categorized as ipsilateral, and those on opposite sides were contralateral. Side impact cases

with documented SDH on both sides of the brain were classified as bilateral.

Injury Rate Analysis For each of the three AIS-based accompanying injury categories (isolated, with contusion, and with other serious injury), injury rate was estimated by dividing the weighted number of injured occupants by the total weighted number of NASS CDS occupants in each age and impact direction category. The only cases excluded from the rate calculations were those where the occupant was listed as injured, but with details unknown (INJNO=97) since inclusion of these cases would increase the denominator of the rate calculations even though it was unknown whether they would be included in the numerator.

Injury rates were presented by age group for all occupants, then separately by impact direction for impact directions with sufficient numbers of cases to present rates by age group.

Odds Ratio Analysis Odds ratios were calculated to compare the odds of sustaining either isolated SDH or SDH with contusion for the oldest age group compared to the youngest age group. SDH cases with other serious head injuries were not included in the odds ratio analysis.

The SAS SURVEYLOGISTIC procedure was used to estimate odds ratios by age group separately for male and female occupants in frontal and side impacts. For each age and impact direction, a multinomial logistic regression model was developed, where the dependent injury variable could take on one of four values: no SDH, isolated SDH, SDH with contusion, or SDH with other serious injury. Categorical variables for age group were used to compare the 70 years and older group to a baseline 20 to 49 year-old group. To account for possible confounding differences in crashes for different age groups, independent variables reflecting potential differences in crash conditions and crash severity between young and old motor vehicle crash victims were included. The regression models for each sex and impact condition combination were built using a backward elimination stepwise procedure until the multinomial regression model contained only significant explanatory variables. Variables in the final models included a continuous variable for ΔV, dichotomous variables for the presence of a skull fracture and air bag deployment, and a categorical variable for seat position with possible values of driver, front seat passenger, or rear seat passenger.

Ninety-five percent confidence limits for the odds ratios were based on variance calculated by the Taylor series. In order to correct for simultaneous estimation of confidence intervals for each group (two-sided confidence interval for two injury types), Bonferroni correction was applied by dividing the significance level of 0.05 by 4 so that alpha was equal to 0.0125.

RESULTS

CIREN Search Results

A search of the CIREN database identified 277 cases with SDH. Case occupant age ranged from 4 days to 96 years, with a mean age of 37 years. Eighty-one cases were fatal, with the mean age of the fatal cases being 44 years. Operative reports were available for 37 individuals who underwent surgical evacuation of the SDH. These operative reports were reviewed for documentation of the source of subdural bleeding in each case.

In fourteen of the 37 cases with surgical records, a specific source of adjacent bleeding was identified. Two of these cases involved children and were excluded from the current analysis. The remaining 12 CIREN cases with documented bleeding sources adjacent to the evacuated SDH are summarized in Appendix A. Included are occupant age and sex, as well as CIREN-estimated impact direction and change in velocity (ΔV) or barrier equivalent velocity (BEV) for the primary impact. The location of the impact on the head and the head contact surface were drawn from CIREN investigation conclusions. Cases involving bridging vein bleeding sources are listed in Table A1, and cases involving only other bleeding sources are in Table A2.

In *four* of the twelve adult CIREN cases with documented bleeding source adjacent to the evacuated SDH, a bridging vein was the only identified bleeding source. In *two* of the twelve cases, bleeding was documented from a bridging vein as well as from cortical vessels: the vein of Labbé in the case

involving a 46 year-old woman and a posterior parietal superficial cortical vein in the case involving a 27 year-old woman (Table A1). In the remaining *six* adult CIREN cases with bleeding sources listed in the operative reports, bridging veins were not involved (Table A2). In three of those cases, documented bleeding adjacent to the evacuated SDH was attributed to contusions. Of the remaining three cases attributed to other bleeding sources, two documented intracerebral hematomas and the third documented an adjacent arterial bleeder on the brain surface.

The CIREN cases with information on subdural bleeding source were also reviewed to determine how they would have been categorized under the AIS-based accompanying injuries system used to sort cases in the NASS CDS analysis (Table 1). The objective was to determine whether the AIS-based categories to be used as surrogate variables for bleeding sources were consistent with the actual bleeding source identified in CIREN cases with additional medical information.

Table 1. Number of CIREN cases in each injury source category sorted by how they would have been categorized under AIS-based accompanying injury system used in NASS CDS analysis.

		Bleeding Source (from CIREN)		
		Bridging Vein	**Contusion**	**Other**
Based on AIS only	***Isolated***	**2 cases**		1 case
	With Contusion		**3 cases**	
	With Other Serious Injury	4 cases		2 cases

Of the CIREN cases, three would have been classified as isolated, three as with contusion, and six as with other serious injury by the AIS-based system. As shown in Table 1, two of the three cases that would have been categorized as isolated using the AIS-based system were associated with bridging vein failure in the CIREN operative report. All three cases that would have been categorized as with contusion using the AIS-based system were associated with contusion in CIREN records. This correspondence provides support for the use of isolated and with contusion injury categories as surrogate variables for SDH originating from bridging vein rupture and contusion, respectively. Of the CIREN cases that would have been categorized as with other serious injury by the AIS-based system, four were actually associated with bridging vein failure, and two were attributed to adjacent hematomas. Thus, the other serious injury category was not used as a surrogate variable for any specific bleeding source.

NASS CDS Search Results

In NASS CDS 1993-2008, there were 1,943 adult occupants coded with SDH, representing a weighted total of 105,980 cases. Among these, 46,907 cases were occupants age 20-49, 41,578 were age 50-69, and 17,494 were age 70 or older.

Accompanying Head Injuries The percentage of adult SDH cases where there were also other serious head injuries documented are shown in Figure 1. The percentages for each age group sum to greater than 100% since each SDH case may have multiple accompanying serious head injuries.

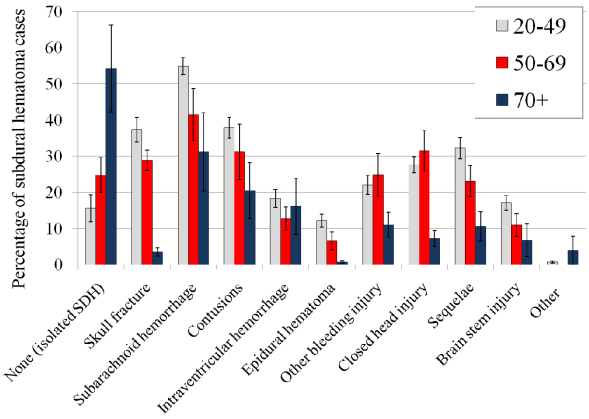

Figure 1. Percentage of SDH cases in each age group where other serious head injuries are also present (with standard error).

Among the youngest age group, 16% of those with SDH sustained no other serious head injuries. In the oldest age group, 54% of SDH cases were isolated. For adults in all age groups, subarachnoid hemorrhage and contusions were among the most common serious injuries to accompany SDH. For those younger than 70, skull fracture and closed head injury were recorded

in more than 25% of subdural cases. In contrast, among the oldest group of occupants with SDH, skull fractures were documented in fewer than 3% of cases and closed head injuries in fewer than 10% of cases. For the youngest age group, injuries in the sequelae category were also common.

Relative Frequency of Isolated Subdural Hematoma The frequency of isolated SDH versus SDH with contusion or with other serious injury was compared for occupants by age group and sex (Figure 2) as a percentage of all SDH cases. The percentage of subdural cases that are isolated among younger occupants is similar for men (15%) and women (17%). Among older occupants, however, the percentage of SDH that are isolated among men increases to only 33% while for women isolated SDH make up 65% of all subdural cases.

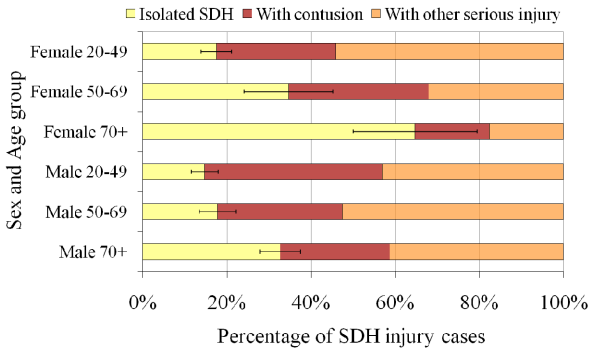

Figure 2. Percentage of SDH cases by sex and age group that are isolated versus with contusion or other serious head injury (standard error shown for percentage of isolated only).

The frequency of isolated SDH compared to SDH with contusion or SDH with other serious head injury is compared by crash impact direction in Figure 3. Of the vehicle impact directions, frontal impacts showed the highest percentage of isolated SDH, with over 30% of frontal SDH cases having no other serious head injuries.

Broken down by head impact location where cutaneous or bone injuries were present, Figure 4 shows that cases with isolated SDH were more likely to be associated with evidence of only frontal contact while cases with contusion were more likely to have evidence of a head impact on the side, either alone or with frontal contact.

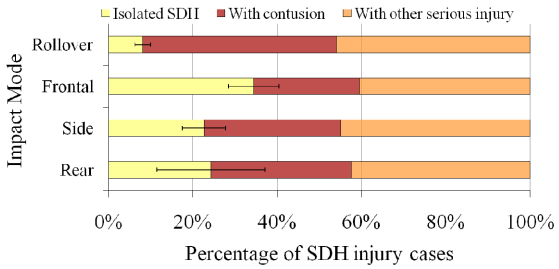

Figure 3. Percentage of SDH cases by impact direction that are isolated versus with contusion or other serious head injury (standard error shown for percentage of isolated only).

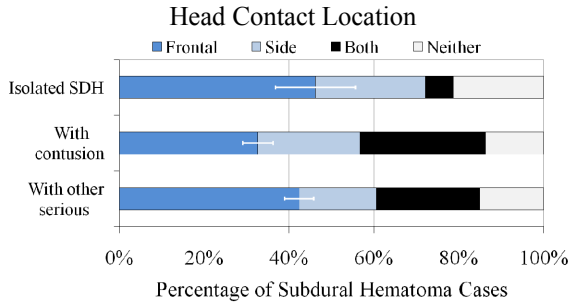

Figure 4. Percentage of SDH cases by accompanying injury category that have evidence of head contact location (with standard error shown for frontal cases only).

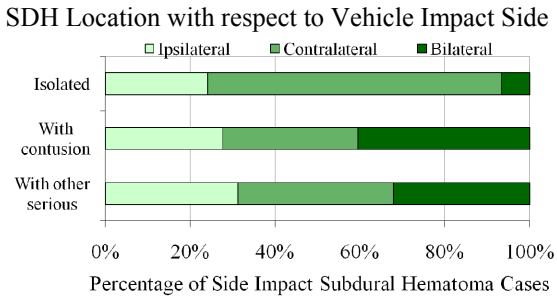

Figure 5. Percentage of side impact SDH cases by type (isolated versus accompanied by contusion or other serious head injuries) where SDH is ipsilateral or contralateral to vehicle impact side.

For side impact cases with SDH, the vehicle impact direction was compared to the side of the SDH (Figure 5). Cases where the vehicle impact and subdural were on the same side were categorized as ipsilateral, and those on opposite sides were contralateral. Cases with

isolated SDH were rarely bilateral (7%) compared to cases with subdural and contusion (41% bilateral) or subdural and other serious injury (32% bilateral). Isolated SDHs were predominantly contralateral (69%). In subdural cases with contusion or other serious head injury, ipsilateral or contralateral SDH occurred with similar frequency.

Injury Rate Analysis The rate of SDH injury goes up with age, regardless of whether the injury is isolated or in combination with contusion or other serious head injuries (Figure 6), but the increase in injury rate for occupants age 70 and older is especially dramatic for isolated SDH. The oldest group had a rate of isolated SDH that was 15 times higher than the rate of injury for younger occupants. For younger occupants, the rate of SDH in combination with contusion or other serious head injury is higher than the rate of isolated SDH. The opposite is true for older occupants, who are twice as likely to sustain an isolated SDH as one accompanied by contusion or other serious head injury.

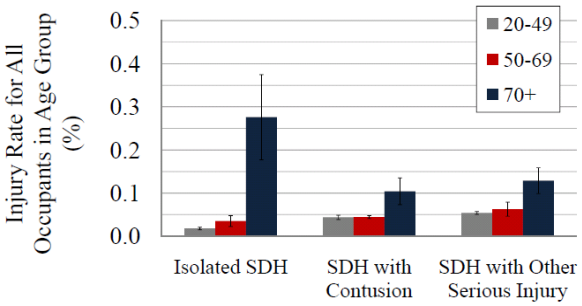

Figure 6. Injury rate for each type of SDH as percentage of all included occupants in all crash directions in each age group (with standard error).

When injury rates are calculated by impact direction (Figure 7), the age-related increase in rate of isolated SDH is especially notable in frontal impacts, while side impacts show a consistent increase in all types of SDH for the oldest occupants. The rate of SDH with contusions is higher in side impact than in frontal impact for all age groups.

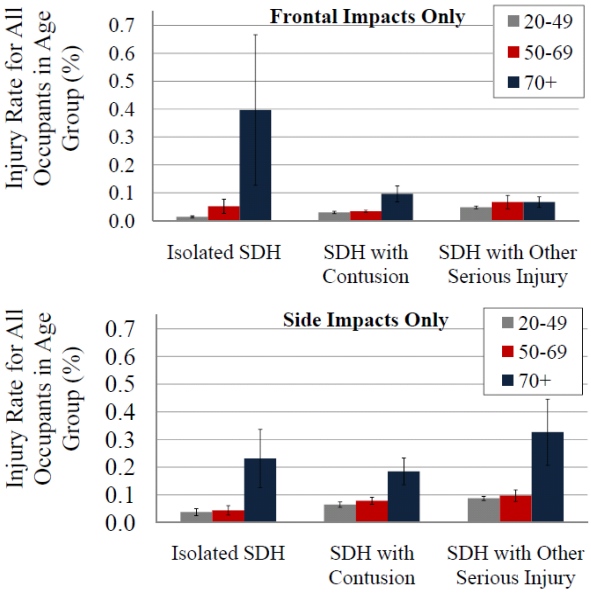

Figure 7. Injury rate for each type of SDH as percentage of all included occupants in frontal and side impact crashes (with standard error).

Odds Ratios Odds ratios were calculated to compare the odds of sustaining either isolated SDH or SDH accompanied by contusion for the oldest age group compared to the youngest age group. Regression models developed using backward elimination for males and females in frontal impacts included the potential confounding variables ΔV, skull fracture, and occupant seat location (driver, front passenger or rear passenger). Models for side impact for both males and females additionally included the potential confounder of air bag deployment.

Table 2 shows the point estimate for each odds ratio for males and females and for impact direction separately. To compare odds of each type of injury for older occupants versus younger adults, injuries that have a point estimate odds ratio greater than 1.0 and do not include 1.0 in the Bonferroni-corrected 95% confidence interval are annotated with an asterisk(*) to indicate significantly increased odds of injury for the older age groups. The resulting odds ratio for males in frontal crashes, for example, estimates that the odds of isolated SDH for an individual in the oldest age group were 11.4 times the odds of injury for a young adult *under the same conditions.* Since the entire confidence interval is greater than 1.0, this difference is significant at the 95% confidence level. As shown in Table 2, odds of injury for isolated SDH or for SDH

with contusion are especially elevated for older occupants in frontal crashes. The age-related increases in injury odds in frontals are particularly notable for isolated SDH and for women.

Table 2.
Odds ratios for types of SDH for 70+ age group compared to age 20 to 49 age group (Significant point estimates highlighted and marked with an asterisk*)

			Odds Ratio	95% CI
Frontal	Male	Isolated SDH	11.4*	2.0 - 64.9
		With Contusion	2.6*	1.03 - 6.7
	Female	Isolated SDH	118.4*	11.9 - >999
		With Contusion	11.5*	2.4 - 54.5
Side	Male	Isolated SDH	2.1	0.4 - 12.5
		With Contusion	2.4	0.7 - 7.8
	Female	Isolated SDH	4.5	0.7 - 30.4
		With Contusion	3.9*	1.6 - 9.4

DISCUSSION

Previously, the focus in SDH tolerance research has been on those originating from bridging vein failure. To begin to explore how tolerance to SDH changes with age, it needs to be determined whether bridging vein failure is the dominant injury mechanism for adults of all ages, or whether certain bleeding sources are particularly associated with the increase in SDH for older occupants.

Although autopsy and surgery studies have shown that SDH are commonly caused by bleeding from sources other than bridging veins [Jamieson and Yelland, 1972, Maxeiner, 1998], no large scale crash data set includes bleeding source information for SDH to evaluate the proportion of motor vehicle crash SDH cases that are caused by bleeding sources other than torn bridging veins for different age groups.

CIREN Results The current analysis of the CIREN database revealed a small number of cases where surgical reports documented adjacent bleeding that was assumed to be the most probable source of bleeding in each case. Review of these cases demonstrated that bridging veins are not the exclusive cause of SDH for any age group, and that other bleeding sources do need to be considered. SDH cases in CIREN were associated with surface contusions, intracerebral hematoma, and bleeding vessels on the surface of the brain as well as with bridging vein bleeding (Tables A1 and A2). The results of the CIREN search were consistent with previous studies that showed that SDH was not exclusively associated with bleeding from bridging veins and that SDH from non-bridging vein sources were relatively common in motor vehicle crashes [Jamieson and Yelland, 1972, Maxeiner, 1998].

Although review of the CIREN cases showed that bleeding sources other than bridging veins can contribute to SDH, there are too few cases with documentation on bleeding sources to analyze the distribution of age or crash conditions among cases originating either with bleeding from the bridging veins or from other bleeding sources.

Comparison of Probable Bleeding Source by Categories in CIREN and NASS CDS Analyses In contrast, NASS CDS has a large number of occupants coded with SDH, but no detailed medical information to specifically attribute those injuries to individual sources of bleeding. Therefore, the current study used available information on accompanying head injuries in NASS CDS to categorize the cases according to other serious head injuries present. In the absence of specific information on bleeding sources in cases coded with SDH, the accompanying injuries were used as surrogate variables for potential bleeding sources for the SDH in each case.

CIREN cases were used to evaluate the suitability of categorizing NASS CDS occupants into isolated SDH cases and SDH cases with contusion as surrogate variables for bridging-vein sourced subdural cases and contusion-sourced SDH cases, respectively. The CIREN cases with documented probable bleeding sources were reviewed and sorted by the same categories used in the NASS CDS search based on AIS codes (Table 1). The objective was to confirm whether the information drawn from AIS codes was consistent with the more detailed information available in operative reports. A good match would support use of the AIS-based categories as surrogate variables for probable bleeding source in NASS CDS which has no narrative injury detail.

Of the three CIREN cases that would have been classified as isolated from the categories used in the NASS analysis, two were indeed associated with bridging vein failure and one with a torn artery on the surface of the brain. Of the three cases that would have been classified as subdural with contusion, all three were associated with a contusion in the operative report. Among the six cases that would have been classified as subdural with other serious injury, operative reports indicated that two were associated with intracerebral hematoma, and four were associated with bridging vein failure or bridging vein failure as well as failure of other surface veins. This comparison suggests that cases categorized as isolated SDH are more likely to be associated with bridging vein rupture than with other sources and that cases in the SDH with contusion category are more likely to be from contusions than from bridging veins or other sources. The other serious head injury category may contain cases caused by bridging vein rupture or from bleeding sources on the surface of the brain. Therefore, although the injury categories used are only surrogates for variables describing the original source of bleeding, it is reasonable to use the trends in the isolated SDH and the SDH with contusion categories to approximate trends between cases where the SDH was produced by bridging vein bleeding versus by brain contusions, respectively. Since the true source of subdural bleeding is not available in NASS CDS or any other large-scale crash database, this data represents the best available estimate.

NASS CDS Results Based on the assumption that the injury categories used are reasonable surrogate variables for bleeding source for SDH, the increased tendency for older occupants to sustain isolated SDH (Figure 1) potentially reflects an increased frequency of SDH caused by bridging vein damage. Although the rate of SDH increases with age, regardless of accompanying injuries (Figure 6), cases with isolated SDH are 15 times more frequent among those aged 70 and older than among adults younger than 50. In comparison, SDH with contusion or other serious injury is only about 2.4 times as frequent among the oldest group compared to the youngest group.

The age-associated increase in isolated SDH is especially prominent for women and in frontal impacts (Table 2). Although isolated SDHs make up about the same proportion of SDH cases in women and men in the age 20 to 49 age group (15% and 17% respectively), SDH in the 70 and older age group are isolated in 65% of female cases but only 33% of male cases (Figure 2). SDH are isolated in 34% of cases sustained in frontals, compared to 23% of cases in side impacts (Figure 3). For the oldest age group, the injury rate for isolated SDH in frontals is almost twice that in side impacts (Figure 7). These results suggest that the age-related increase in bridging vein-associated SDH may especially affect women and those in frontal impacts.

Odds ratio analysis (Table 2) shows that the age-related increase in SDH in frontal crashes is present even after accounting for variables related to crash and head impact severity (ΔV, air bag deployment, skull fracture), especially for isolated SDH, and for women.

Assuming that isolated SDH are most likely to be associated with bridging vein bleeding, the current findings that the age-related increase in isolated SDH may be more frequent in frontal impacts are consistent with studies that have linked anterior-posterior motion to bridging vein failure [Depreitere et al., 2006, Gennarelli and Thibault, 1982, Löwenhielm, 1974, Ommaya et al., 1968] and consistent with the explanation that older individuals are more prone than younger individuals to SDH by bridging vein failure due to the increased relative brain motion and bridging vein tension induced by atrophy in the aging brain [Kleiven and von Holst, 2002, Meaney, 1991, Yamashima and Friede, 1984].

The case conditions for the SDH cases with contusion in the current study were compared to previous findings on cases with SDH with contusion [Maxeiner, 1998], or caused by bleeding sources that were intracerebral or on the surface of the brain rather than by bridging vein failure [Jamieson and Yelland, 1972]. In Jamieson and Yelland, the SDH cases with intracerebral or surface bleeds were more common among males. In the current study, SDH were accompanied by contusion more often among men than women, especially for *young* males under age 50 who sustained contusion with subdural more than twice as often as they sustained isolated SDH (Figure 2). Jamison and Yelland also reported that SDH caused by intracerebral or surface bleeding was *less*

common for adults over age 60. In the current study, although the injury rate for SDH with contusion increases for older occupants (Figure 6), the proportion of SDH that are accompanied by contusions decreases with age: only 20% of subdural cases among those age 70 and older are associated with contusion, compared to 38% of subdural cases for adults under age 50 (Figure 1). The reason for the reduction in the proportion of subdural injuries with contusion is that the age-related increase in rate of isolated SDH outpaces the age-related increase in rate of SDH with contusion. In previous studies, SDH associated with sources other than bridging veins were more frequently from lateral impact than those associated with bridging veins. In Jamieson and Yelland, 55% of complicated SDH cases were from lateral head impacts, while only 32% of isolated SDH cases were from lateral head impacts. Maxeiner reported 44% of SDH associated with contusion were confirmed to involve lateral head impacts while only 12% of bridging vein subdural hematoma were lateral head impacts. In the current study, 29% of cases with contusion were lateral vehicle impacts compared to 23% of isolated SDH cases which were lateral vehicle impacts.

Overall, the crash conditions most often associated with isolated SDH are different from those associated with SDH combined with contusion. While the rate of both types of subdural increases with age, the age-related increase is greater for isolated SDH, especially among women. For the oldest group of occupants, the rate of isolated SDH is almost twice as high in frontals as in side impacts, while SDH with contusions occur at a higher rate in side impacts than in frontals for all age groups. Isolated SDH occur bilaterally in only 7% of cases, compared to subdural with contusion cases which are bilateral in 41% of cases (Figure 4). Among the isolated subdural cases, the hematoma is contralateral to the vehicle impact side in 69% of cases, while contralateral SDH are documented in only 32% of subdural cases with contusion (Figure 5). These differences between cases with isolated SDH and SDH combined with contusion support that these two injury categories are representative of two different patterns of injury. Assuming that these injury categories correspond approximately to SDH caused by bridging vein failure and SDH caused by contusions or other bleeding sources, the results suggest that the mechanism of injury for these two types of SDH may be quite different.

The types of motion and forces required to produce SDH from bleeding sources on the surface of the brain have not been addressed. Although bleeding from cortical contusions or ruptured cortical vessels into the subdural border cell region would only be possible with rupture of the arachnoid, the loading required to produce this combination of bleeding injury and arachnoid damage has not been explored experimentally, nor have the effects of age on this process been explored. Research on the tolerance of occupants of all ages to SDH would benefit from a better understanding of the mechanism of SDH from sources other than bridging veins.

Older occupants appear to be particularly vulnerable to isolated SDH, which suggests that the increase in SDH rate in older occupants may be more dependent on decreased tolerance to SDH associated with bridging vein failure than to those associated with other bleeding sources. Further research on how tolerance to bridging vein failure changes with age may explain much of the increase in incidence of SDH among older occupants.

CONCLUSIONS

The rate of isolated SDH among crash occupants increases with age, potentially reflecting an increase in the frequency of SDH caused by bridging vein bleeding. This age-related increase is especially prominent among women and in frontal impacts. Determination of age-specific injury tolerance for SDH will require evaluation of the increasing risk of bridging vein failure in older occupants.

SDH accompanied by brain contusions or other potential bleeding sources are also common, especially in side impacts and among occupants younger than 70. These cases potentially represent injuries where subdural bleeding came from sources other than bridging veins. Estimation of the SDH tolerance for all adult occupants will require a better understanding of the mechanism of injury for SDH from these other bleeding sources.

ACKNOWLEDGEMENT

The authors are grateful to Drs. Peter Letarte and Bruce Donnelly for helpful comments and valuable discussions on the mechanism of SDH.

REFERENCES

Depreitere, B., C. Van Lierde, P. Verschueren, H. Delye, D. Berckmans, I. Verpoest, J. Vander Sloten, G. Van der Perre and J. Goffin. 2005. "Cerebral Bridging Vein Rupture in Humans: An Experimental Evaluation." Iutam Symposium on Impact Biomechanics, Gilchrist, M. D., ed., Springer, pp. 305-12.

Depreitere, B., C. Van Lierde, J.V. Sloten, R. Van Audekercke, G. Van der Perre, C. Plets and J. Goffin. 2006. "Mechanics of Acute Subdural Hematomas Resulting from Bridging Vein Rupture." J Neurosurg, 104(6), pp. 950-6.

Gennarelli, T.A. and L.E. Thibault. 1982. "Biomechanics of Acute Subdural Hematoma." J Trauma, 22(8), pp. 680-6.

Gennarelli, T.A. and D.I. Graham. 2005. "Neuropathology." Textbook of Traumatic Brain Injury, Silver, J. M., T. W. McAllister and S. C. Yudofsky, eds., American Psychiatric Publishing, Inc., Washington, DC.

Graham, D.I. 1996. "Neuropathology of Head Injury." Neurotrauma, Narayan, R. K., J. E. Wilberger and J. T. Povlishock, eds., McGraw Hill, New York, pp. 43-59.

Haines, D.E., H.L. Harkey and O. Al-Mefty. 1993. "The "Subdural" Space: A New Look at an Outdated Concept." Neurosurgery, 32(1), pp. 111-20.

Hanif, S., O. Abodunde, Z. Ali and C. Pidgeon. 2009. "Age Related Outcome in Acute Subdural Haematoma Following Traumatic Head Injury." Irish Medical Journal, 102(8), pp. 255-7.

Holbourn, A.H.S. 1943. "Mechanics of Head Injuries." Lancet, 2, pp. 438-41.

Hukkelhoven, C.W., E.W. Steyerberg, A.J. Rampen, E. Farace, J.D. Habbema, L.F. Marshall, G.D. Murray and A.I. Maas. 2003. "Patient Age and Outcome Following Severe Traumatic Brain Injury: An Analysis of 5600 Patients." J Neurosurg, 99(4), pp. 666-73.

Jamieson, K.G. and J.D. Yelland. 1972. "Surgically Treated Traumatic Subdural Hematomas." J Neurosurg, 37(2), pp. 137-49.

Jane, J.A. and P.C. Francel. 1996. "Age and Outcome of Head Injury." Neurotrauma, Narayan, R. K., J. E. Wilberger and J. T. Povlishock, eds., McGraw-Hill, pp. 793-804.

Kleiven, S. and H. von Holst. 2002. "Consqueences of Reduced Brain Volume Following Impact in Prediction of Subdural Hematoma Evaluated with Numerical Techniques." Traffic Injury Prevention, 3, pp. 303-10.

Lee, M.-C., J.W. Melvin and K. Ueno. 1987. "Finite Element Analysis of Traumatic Subdural Hematoma." 31st Stapp Car Crash Conference, SAE, pp. 67-77.

Lee, M.C. and R.C. Haut. 1989. "Insensitivity of Tensile Failure Properties of Human Bridging Veins to Strain Rate: Implications in Biomechanics of Subdural Hematoma." J Biomech, 22(6-7), pp. 537-42.

Löwenhielm, P. 1974. "Strain Tolerance of the Vv. Cerebri Sup. (Bridging Veins) Calculated from Head-on Collision Tests with Cadavers." Z Rechtsmed, 75(2), pp. 131-44.

Mallory, A. 2010. "Head Injury and Aging: The Importance of Bleeding Injuries." Ann Adv Automot Med, 54, pp. 51-60.

Maxeiner, H. 1997. "Detection of Ruptured Cerebral Bridging Veins at Autopsy." Forensic Sci Int, 89(1-2), pp. 103-10.

Maxeiner, H. 1998. "Subdural Hematomas in Victims with and without Cerebral Contusions - Comparision of Two Types of Head Injuries." Rechtsmedizin, 9(1), pp. 14-20.

Maxeiner, H. and M. Wolff. 2002. "Pure Subdural Hematomas: A Postmortem Analysis of Their Form and Bleeding Points." Neurosurgery, 50(3), pp. 503-9.

Meaney, D.F. 1991. "Biomechanics of Acute Subdural Hematoma in the Subhuman Primate and Man." Ph.D. Dissertation, University of Pennsylvania.

Miller, D.J., I.R. Piper and P.A. Jones. 1996. "Pathophysiology of Head Injury." Neurotrauma, Narayan, R. K., J. E. Wilberger and J. T. Povlishock, eds., McGraw Hill, New York, pp. 61-9.

Miller, J.D. and P.F.X.S. Statham. 2000. "Surgical Management of Traumtic Intracranial Hematomas." Operative Neurosurgical Techniques, Schmidek, H. H., ed., W.B. Saunders Company, Philadelphia, PA, pp. 83-90.

Monson, K.L. 2001. "Mechanical and Failure Properties of Human Cerebral Blood Vessels." Ph.D. Dissertation, University of California, Berkeley.

Ommaya, A.K., F. Faas and P. Yarnell. 1968. "Whiplash Injury and Brain Damage: An Experimental Study." JAMA, 204(4), pp. 285-9.

Perel, P., I. Roberts, O. Bouamra, M. Woodford, J. Mooney and F. Lecky. 2009. "Intracranial Bleeding in Patients with Traumatic Brain Injury: A Prognostic Study." BMC Emergency Medicine, 9(1), p. 15.

Raju, S., D.K. Gupta, V.S. Mehta and A.K. Mahapatra. 2004. "Predictors of Outcome in Acute Subdural Hematoma with Severe Head Injury - a Prospective Study." Indian Journal of Neurotrauma, 1(2), pp. 37-44.

Sawauchi, S. and T. Abe. 2008. "The Effect of Haematoma, Brain Injury, and Secondary Insult on Brain Swelling in Traumatic Acute Subdural Haemorrhage." Acta Neurochir (Wien), 150(6), pp. 531-6; discussion 6.

Seelig, J.M., D.P. Becker, J.D. Miller, R.P. Greenberg, J.D. Ward and S.C. Choi. 1981. "Traumatic Acute Subdural Hematoma: Major Mortality Reduction in Comatose Patients Treated within Four Hours." N Engl J Med, 304(25), pp. 1511-8.

Servadei, F. 1997. "Prognostic Factors in Severely Head Injured Adult Patients with Acute Subdural Haematoma's." Acta Neurochir (Wien), 139(4), pp. 279-85.

Stitzel, J.D., P.D. Kilgo, K.A. Danelson, C.P. Geer, T. Pranikoff and J.W. Meredith. 2008. "Age Thresholds for Increased Mortality of Three Predominant Crash Induced Head Injuries." Annu Proc Assoc Adv Automot Med, 52, pp. 235-44.

Taussky, P., H.R. Widmer, J. Takala and J. Fandino. 2008. "Outcome after Acute Traumatic Subdural and Epidural Haematoma in Switzerland: A Single-Centre Experience." Swiss Med Wkly, 138(19-20), pp. 281-5.

Toyama, Y., T. Kobayashi, Y. Nishiyama, K. Satoh, M. Ohkawa and K. Seki. 2005. "CT for Acute Stage of Closed Head Injury." Radiat Med, 23(5), pp. 309-16.

Yamashima, T. and R.L. Friede. 1984. "Why Do Bridging Veins Rupture into the Virtual Subdural Space?" J Neurol Neurosurg Psychiatry, 47(2), pp. 121-7.

Table A1.
CIREN cases with operative report documentation of bridging vein bleeding adjacent to surgically-evacuated subdural hematoma

Age, Sex & Seat Position	Impact Direction (PDOF)	Crash Severity	Head impact	SDH location	Adjacent Bleeding Source Identified in Operative Report	Other Serious Head Injuries (From AIS-codes with additional detail from diagnostic imaging where available)	AIS-based accompanying injury category as used in NASS CDS analysis
26 y.o. female driver	11 o'clock	BEV= 49 km/h	Roof/side rail with left head	Left panhemispheric and over tentorium	*Bridging vein:* Two lacerated bridging veins near midline	Left cerebral swelling AIS 4 Left subcortical hemorrhage AIS 4 Left subarachnoid hemorrhage AIS 3	Other serious injuries
85 y.o. female right front	12 o'clock	ΔV= 22 km/h	Passenger-side frontal air bag with left face	Left frontotemporal	*Bridging vein:* Torn bridging vein "was cause of hematoma"	**(Fatal)** Cerebral edema AIS 3	Other serious injuries
16 y.o. female right rear	3 o'clock	ΔV= 53 km/h	Left forehead to seatback, right occiput to unknown surface	Left temporal to convexity and over tentorium	*Bridging vein:* Hole in superior sagittal sinus from an evolved bridging vein	Right intracranial vessel laceration AIS 4	Other serious injuries
18 y.o. female driver	2 o'clock	ΔV= 59 km/h	Right door impact documented	Right	*Bridging vein:* Torn parasagittal vein	None	Isolated
46 y.o. female right front	3 o'clock	ΔV= 27 km/h	Right parietal / temporal to door interior or striking vehicle	Right frontal temporal and parietal	*Bridging vein & other:* Torn vein of Labbé, petrosal vein, and sylvian bridging vein	Subarachnoid hemorrhage AIS 3	Other serious injuries
27 y.o. female driver	1 o'clock	ΔV= 32 km/h	Left face and occiput to A-pillar and roof	Left frontal, parietal	*Bridging vein & other:* Bleeding from bridging vein and superficial cortical vein	None	Isolated

Table A2.
CIREN cases with operative report documentation of bleeding adjacent to subdural hematoma from sources *other than bridging veins*

Age, Sex & Seat Position	Impact Direction (PDOF)	Severity	Head impact	SDH location	Adjacent Bleeding Source Identified in Operative Report	Other Serious Head Injuries (From AIS-codes with additional detail from diagnostic imaging where available)	AIS-based accompanying injury category as used in NASS CDS analysis
76 y.o. female driver	2 o'clock, (rotated to 3 o'clock by time of head impact)	BEV= 38 km/h	Right passenger door with right forehead	Bilateral (surgery on left)	Left temporal/parietal intracerebral hematoma	**(Fatal)** Right temporal hinge fracture AIS 4 Right white matter hemorrhage and left temporoparietal intracerebral hematoma AIS 4 Right subarachnoid hemorrhage AIS 3	Other serious injuries
23 y.o. male driver	10 o'clock	ΔV= 28 km/h	B-pillar with left head, seat with right head	Right temporal and along tentorium	Temporal and parietal surface contusions and bleeders	Right epidural hematoma AIS 4 Basilar and right vault fractures AIS 4 Hemorrhagic contusions under SDH AIS 4 Right subarachnoid hemorrhage AIS 3	Contusion
21 y.o. female driver	4 o'clock	ΔV= 26 km/h	B-pillar with right occiput	Left frontal/ temporal	Temporal bleeders and bruises with contusions	Bilateral cerebral swelling AIS 5 Subarachnoid hemorrhage AIS 3 Left frontal-temporal hemorrhagic contusion AIS 4	Contusion
76 y.o. female driver	10 o'clock	ΔV= 12 km/h	B-pillar with left side of head	Left parietal/ occipital	Small arterial bleeder on the brain surface	No other head injuries coded	Isolated
29 y.o. male driver	2 o'clock	ΔV= 44 km/h	A-pillar-mounted handle with right head	Right convexity	Temporoparietal intracerebral hematoma with bleeders	Right parietal skull fracture AIS 4 Right cerebral edema AIS 3 Right intracerebral hematoma not coded	Other serious injuries
49 y.o. female driver	3 o'clock	ΔV= 44 km/h	Tree with right head and face	Left frontal/parietal/ temporal	Underlying hemorrhagic contusion	**(Fatal)** Cerebral hematoma/hemorrhage AIS 4 Fractures basilar skull, right vault and orbit AIS 3 Left subarachnoid hemorrhage AIS 3 Bilateral frontal lobe contusions AIS 3	Contusion

ASSESSMENT OF DUMMY MODELS BY USING OBJECTIVE RATING METHODS

Christian Gehre
PDB – Partnership for Dummy Technology and Biomechanics
Germany
Sebastian Stahlschmidt
DYNAmore GmbH
Germany
Paper Number 11-0216

ABSTRACT

The numerical simulation is an inherent process of the development of the passive vehicle safety. Robust and predictable computational models are the base of the successful application of numerical simulations. This study is focused on the assessment of the quality of dummy models used in occupant simulations. The progress of those models was remarkable over the past years. By increasing the quality, the potential of further improvements declines. Hence, the assessment of model improvements and their impact on the quality of simulations is getting more and more complicated. Major improvements of sub-parts do not necessarily improve the overall performance of a model. Therefore, a standardised objective evaluation of models would ease the definition of priorities of model updates.

Objective rating tools could help to solve this problem. These tools are calculating the level of correlation between two signals, usually coming from test and simulation. All signal ratings can be merged to a global rating of a loading case. However, the analysis of only one loading case is not sufficient to calculate a reliable and a robust quality score of a dummy model. A more comprehensive approach is required to provide a valid rating for all relevant loading conditions. Furthermore, it must distinguish between good and poor models and should correlate with user experiences.

This paper provides guidelines of defining boundary conditions of an overall quality rating of dummy models. The LS-Dyna ES-2 dummy model was used as a demonstrator of the new approach.

The study analyses the possibilities of an objective rating tool. Various tests with dummy parts, sled tests as well as dummy certification tests were analysed to define a set of characteristic loading conditions of the ES-2. Furthermore, the extraction of the most relevant dummy responses was an essential part of the evaluation, too. Finally, all defined scenarios were applied to different releases of the same dummy model. The calculated quality scores were verified with the experiences of users of the model.

The findings of this feasibility study are limited to the LS-Dyna ES-2 model. However, they can easily be transferred to other ES-2 models. If another side impact dummy or a dummy for a different crash scenario (e.g. frontal impact) is used, then the selection of loading cases and signals must be revised.

INTRODUCTION

The design of occupant safety systems by using numerical simulations became an essential part of the vehicle development processes. Especially the optimisation of safety systems as well as robustness studies of these systems benefit from the progress of the simulation. Hence, the requirements to computational dummy models increased over the past years significantly. By improving the predictability, the realisation of further improvements declines. A reliable quality rating could ease the assessment of these models.

However, increased requirements are not the only challenge. New suppliers entered the market of computational dummy models. Now there are models of different levels of detail and quality available. An objective evaluation of those models is required to find the appropriate ones.

OBJECTIVES

This paper is focused on a feasibility study on the definition and application of a rating procedure to assess the level of validation of dummy models.

The check of the correct implementation of geometry, mass and inertia as well as the use of appropriate modelling techniques were not part of this study. However, they must be verified before applying any rating scheme.

METHOD

The application of an objective rating tool was the base of this study. It calculates the correlation of responses obtained in test and simulation. Certification tests usually cover a limited range of loads but a quality rating of a dummy model should represent almost the complete range of loading conditions. Hence, component tests as well as sled tests, conducted to validate dummy models, were included in the data set. Validation tests usually cover a wider range of loads or are more representing loads in car crashes at least.

Objective rating method

A standardised method with reasonable scores is the basic principle of any rating. It enables an objective and reliable assessment of the level of validation of computational models. There are a few rating tools on the market and even more published in the literature. Each of the existing tools and algorithms has pros and cons. This study used the CORA approach [1]. However, the findings of this study should be valid if another rating tool is used.

Rating tool CORA CORA uses two different methods to assess the correlation of signals. While the corridor method calculates the deviation between curves by using corridors, the cross correlation method analyses specific curve characteristics like phase shift or shape of the signals. The rating results ranges from 0 (no correlation) to 1 (perfect match). More information is given in [1].

Interval of evaluation The recording time of signals in a crash or a simulation is typically slightly longer than actually required. So the length of a signal may influence the rating. CORA offers an algorithm to extract the relevant part of the signal for the analysis. This automatism was used in all evaluations. Solely the end of the interval was set manually for some pendulum accelerations of the lumbar spine component tests. A non-relevant secondary impact of the pendulum could not be handled by the algorithm automatically [1].

Filtering of signals As described in [1], the chosen filter influences the rating. The analysis and assessment of smooth signals is usually more robust than the analysis of oscillating curves. So the CFC180 filter was applied to all signals.

Peparation of the data T_0 was adjusted for each test to avoid wrong rating results because of accidental phase shifts. Additionally, all data were converted to the ISO-MME format.

Selection of responses and weighting factors

CORA calculates the correlation of each signal separately. Those single ratings were combined to a global rating by calculating the mean afterwards. Individual weighting factors are defining the significance of each signal. Those factors must be set by the user.

Certification tests Only the main signals were recorded in certification tests. Therefore, all evaluated signals were treated equally.

Component, sled and vehicle tests At first all signals were combined sensor-wise. So the sum of the weighting factors of every sensor is 1. The three abdominal forces, the three rib deflection and the three rib accelerations were treated as one sensor respectively.

Each minor axis of a sensor was assigned with a weighting factor of 0.1. A triaxial sensor with one major axis and two minor axes is using 1x 0.8 and 2x 0.1 as weighting factors.

Finally, all sensors were combined to the total rating by using the same weighting factor for every sensor.

If there were several load cases of a part or a sub-assembly available, then all load cases were treated equally.

DUMMY MODELS

The LS-Dyna FAT ES-2 model was used to demonstrate the feasibility of an objective quality rating. The quality score was calculated for three different releases of this model.

The FAT ES-2 model was developed by a consortium of German car makers and suppliers [2]. It is accepted and used all over the world.

Release 2.0

Version 2.0 was released in spring 2003 [3]. The model was derived from the EuroSID model, developed by the same consortium.

Additional material tests, pendulum tests with the whole dummy as well as sled tests were used to validate the model. The focus of the development was on a good overall performance of the model. In-depth validation of single parts of subassemblies was not in priority.

Release 4.5

Release 4.5 was published in summer 2009. The model was optimised by using the validation tests of release 2.0. Furthermore, the feedback of customers helped to improve the model. Com-

pared to its predecessor, the numerical robustness of this release increased significantly.

Release 5.0

It was decided by PDB in 2009 to start a major update programme of the ES-2 model to improve the quality significantly. Therefore, new material tests, component tests and sled tests were defined and conducted. The focus was on the improvement of the most crucial parts of the existing model such as shoulder, abdomen and lumbar spine. Particular attention was paid on the component and the sub-assembly level. Version 5.0 of the LS-Dyna model will be released in spring 2011. The model used in this study is not the finalised version 5.0 but very close to the final release.

In principle, this release can be compared to version 2.0 of the model. It is the first version after the completion of a new development or a major update programme. The full potential of the new test data will probably be realised with the successor of version 5.0

LOAD CASES

The quality of the three different releases was assessed by using certification, component and sled tests. Simulation runs with a vehicle environment were used as a final proof of the findings.

Certification tests

All certification tests of the ES-2 are described in [4]. Different test set-ups check the conformity of head, neck, shoulder, ribs, abdomen, lumbar spine and pelvis with the specs.

The assessment of head and neck was not included in this study. The focus was on thorax and pelvis.

Shoulder The longitudinal acceleration of the pendulum was used as the only signal to calculate the quality score.

41 dummy certifications were the basis of the evaluation.

Thorax The performance of the three ribs is tested in single rib tests. A pendulum impact against the complete thorax but without arm can be applied alternatively [5] which was used in this study. The deflection of the ribs as well as the longitudinal pendulum acceleration was assessed.

The data set used is less extensive compared to the other certification tests. Only four tests of two dummies were available.

Abdomen The abdomen is certified in a pendulum test. Usually, the sum of the three abdominal load cells is evaluated. To get a more reliable rating of the abdomen, the three abdominal forces were assessed separately. The pendulum acceleration completes the set of evaluated signals.

In total 41 certifications of three different dummies were used as base for all evaluations.

Lumbar spine The lumbar spine is tested in a pendulum test with mass substitute mounted on top. Three different bending angles were assessed.

40 certification tests coming from four specimens were taken as basis for the evaluation of the model.

Pelvis A pendulum test is used to certify the pelvis. The pubic force as well as the longitudinal pendulum acceleration was taken for the correlation assessment.

The reference data set included 40 certification tests of three different dummies.

Component tests

The programme to update release 4.5 of the ES-2 model started with extensive dynamic tests of several dummy parts and sub-assemblies. This study used pendulum tests with clavicle, abdomen and lumbar spine for the evaluation.

Clavicle The clavicle was fixed via shoulder load cell to the test rig and was loaded by a pendulum in different directions and energies. Figure 1 shows the test set-up of the vertical impact to the clavicle exemplarily.

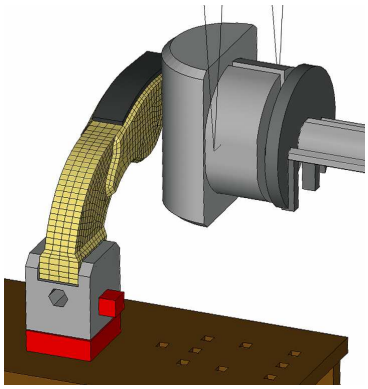

Figure 1. Impact z to the clavicle.

The forces of the shoulder load cell as well as the longitudinal and transverse accelerations of the pendulum were taken for the assessment of the correlation between test and simulation.

Abdomen Figure 2 shows the set-up of one abdomen pendulum test. The abdomen was loaded with different energies, at different impact locations and impact angles. The focus of the validation work was on the pure lateral impacts. So the weighting factors of the oblique tests were reduced.

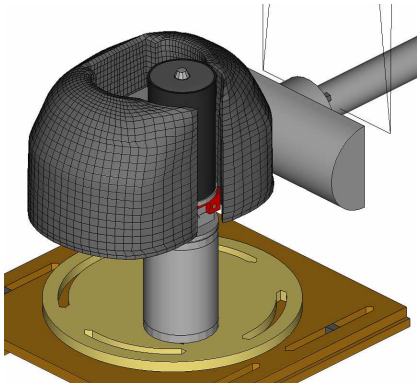

Figure 2. Lateral impact to the abdomen.

The three abdominal forces and pendulum accelerations were taken for the assessment.

Lumbar spine Three set-ups were used to identify the properties of the lumbar spine for pure torsion, shear and flexion bending loads. All modes were tested with different impact energies.

The signals of the pendulum, the T12 and the lumbar spine sensors were taken for the analysis of the shear and the bending mode. The torsion about the vertical axis of the lumbar spine was the only signal of the assessment of the torsion tests.

Sled tests

Sled tests with rigid bench and rigid barriers were used to validate the global kinematics of the dummy as well as the interactions between sub-assemblies. The different barrier faces induce kinematics and loadings observed in various vehicle crashes. Each barrier was assigned with a specific code (D1, D2 etc.) to differentiate between them. Tests with the D1, D3 and D4 barriers were used in this study. D1 and D4 are flat barriers. The upper edge of D4 is at the same level like the upper rib of the dummy, whereas the D1 barrier covers the whole shoulder. The D3 barrier is very similar to D1 but is equipped with an additional rigid pelvis pusher.

The dummy was placed on the WorldSID bench in all tests. Additional information is given in [6]. Figure 3 shows the set-up of a test with the D3 barrier exemplarily. These tests were conducted to develop the model release 5.0. Tests done during the development of the first ES-2 releases were not considered.

Head and neck loads were again not considered in the evaluation but the following signals were taken to calculate the correlation with the test data.

- Acceleration of T1, T12, ribs and pelvis
- Forces and moments of shoulder, T12, abdomen and pelvis
- Deflection of the ribs

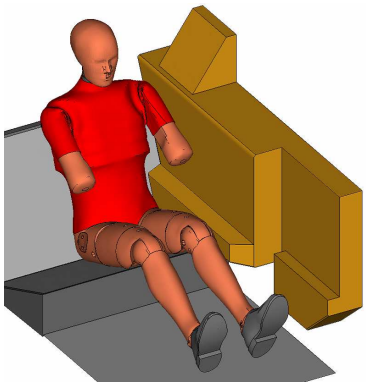

Figure 3. Sled test with D3 barrier.

Vehicle tests

A good validation in certification, component and sled tests is the base for successful application of the model in vehicle development processes. However, it is not a guarantee for high predictability in vehicle simulations. Additional simulation runs with a vehicle environment consolidate the findings.

A 90° pole impact of a mid-size vehicle without deployed side airbag and fired belt pre-tensioner was used as reference test. The selection of signals and the corresponding weighting factors was taken from the evaluation of the sled tests.

RESULTS OF THE RATING

The absolute classification of the CORA rating is complicated. Ratings close to 1 are easy to understand – the correlation is almost perfect. Unfortunately, many ratings are between 0.5 and 0.7. It is not clear yet, when a rating represents a good model. The significance of differences between ratings rises with the absolute deviation. However, a relative assessment by using the rating of one model as reference is preferred at this time.

The CORA algorithm is already used for a couple of years. Based on experiences made, some assumptions can be given. A good correlation can be assumed if the rating of a single signal is clearly better than 0.8. The situation is more

complicated in case of assessing a complete test of numerous signals. Correlations with a score of 0.7 or higher could be assumed as good.

Certification tests

Certification tests are part of most of the dummy validation programmes. The focus usually is to meet the requirements (e.g. corridors) of every test and not only an overall good correlation of the responses. This information might explain the rating results of some certification tests.

The results of the CORA rating of the dummy certifaction tests is shown in Table 1. Almost all tested body segments from release 2.0 to 5.0 were improved significantly. The new test data used for the ES-2 update programme enabled a more profound validation.

The limited improvement and even partly loss of correlation of release 4.5 compared to 2.0 is probably based on the development process of this version. As mentioned above, both releases used the same validation data set. Version 4.5 was mainly optimised for load cases in vehicle environments. So a loss of quality in some certification tests was an accepted side effect.

Table 1.
Evaluation of certification tests

	R2.0	R4.5	R5.0
Shoulder	0.562	0.645	0.825
Thorax	0.841	0.919	0.911
Abdomen	0.532	0.576	0.774
Lumbar spine	0.394	0.397	0.568
Pelvis	0.748	0.625	0.785

Thorax and shoulder of version 5.0 correlate very well to the hardware in this specific set-ups.

Component tests

Table 2 shows the assessment of clavicle, abdomen and lumbar spine. Only release 5.0 was validated against those tests. Consequently, its score is better than that of the previous model releases.

Anyhow, the rating indicates that the lumbar spine seems to be a crucial dummy part. By increasing the overall dummy performance of release 4.5, the quality of the lumbar spine decreased significantly. The lumbar spine of version 5.0 shows good correlation but the good results of the component tests seems to be in conflict with the rating of the certification tests.

Table 2.
Evaluation of component tests

	R2.0	R4.5	R5.0
Clavicle	0.551	0.594	0.776
Abdomen	0.690	0.714	0.750
Lumbar spine	0.675	0.562	0.731

Clavicle Detailed information of the evaluation of the clavicle is given in Table 3. The total rating of each impact (impact x, y and z) is calculated from the evaluation of two sub-load cases.

Table 3.
Evaluation of clavicle tests

	R2.0	R4.5	R5.0
Impact x	0.636	0.635	0.619
Impact y	0.752	0.820	0.793
Impact z	0.681	0.687	0.837
Mean	0.551	0.594	0.776

As mentioned before, the improvements of release 4.5 are achieved by optimising the clavicle without new component tests. So the progress is limited. Surprisingly, release 5.0 does not benefit from the new test data in longitudinal and lateral loadings. Solely the correlation of vertical impacts increased significantly.

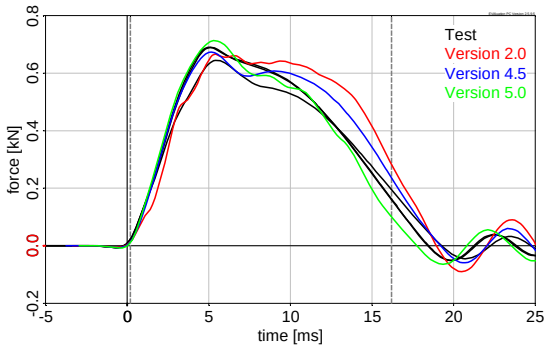

Figure 4. Impact y – shoulder force F_y.

Figure 4 shows the lateral shoulder forces of an impact y-test exemplarily. The corresponding CORA rating is shown in Table 4. The vertical dashed lines visualise the evaluated interval of the signals. In spite of the big differences of the CORA rating, the signals of the three models are close to the test data. Therefore, small differences (approx. <0.05) of the CORA rating should not be overestimated.

Table 4.
Evaluation of the shoulder force

	R2.0	R4.5	R5.0
Shoulder force (impact y)	0.710	0.878	0.963

Abdomen A summary of the abdomen tests is shown in Table 5. The weighting factor of the perpendicular impacts is 0.333 and 0.166 of the oblique tests. The quality score of both 90°-configurations is calculated from six sub-load cases respectively. Each oblique impact represents only one load case.

Table 5.
Evaluation of abdomen tests

	R2.0	R4.5	R5.0
90°, mid pos.	0.626	0.549	0.843
90°, upper pos.	0.400	0.567	0.784
60°, mid pos.	0.639	0.612	0.782
120°, mid pos.	0.614	0.719	0.618
Weighted mean	0.690	0.714	0.750

The new tests helped to improve the quality of the abdomen of release 5.0 under pure lateral load remarkably. The current state of version 5.0 is validated by using the pure lateral impacts only. So the oblique impacts could be used for further improvements.

The good correlation of release 4.5 in impacts at 120° is probably a side effect of the optimisation. In-depth analysis show that almost all signals of this model correlate slightly better with the tests. Finally, the numerous minor improvements result in a good overall rating.

Lumbar spine Table 6 shows more detailed information on the assessment of the lumbar spine. Each rating is a combination of the assessment of three sub-load cases.

Table 6.
Evaluation of lumbar spine tests

	R2.0	R4.5	R5.0
Flexion	0.735	0.709	0.844
Shear	0.685	0.617	0.899
Torsion	0.606	0.306	0.450
Mean	0.675	0.562	0.731

Flexion and shear of version 5.0 improved significantly by using the new test data. However, pure torsion seems to be a problem of version 4.5 and 5.0.

Sled tests

Table 7 gives an overview on the results of the evaluation of the barrier tests. The ES-2 version 2.0 could not be assess with barrier D4 because of numerical instabilities of the rib damping material. Consequently, the score was set to 0.

Table 7.
Evaluation of sled tests

	R2.0	R4.5	R5.0
D1 barrier	0.536	0.509	0.617
D3 barrier	0.634	0.616	0.724
D4 barrier	0.000	0.612	0.657

The dummy responses of model release 5.0 correlate clearly better with the test data than those of the previous model releases. In-depth analysis showed that the quality of almost all dummy parts is improved.

The rating of version 4.5 is remarkable. The improvement of the model's robustness and the tuning of the performance of sub-assemblies reduced the correlation of the complete model in those sled tests. However, it should be considered that the assessed tests were not part of the validation data of release 2.0 and 4.5.

Vehicle tests

The results of the quality rating of a vehicle test is shown in Table 8. The ranking of the models is identical to that of the sled tests. Solely the absolute difference between release 4.5 and 5.0 is reduced.

Table 8.
Evaluation of a vehicle test

	R2.0	R4.5	R5.0
Vehicle	0.655	0.671	0.739

Influence of signal weighting factors

The definition of the weighting factors of the signals has got an influence on the total rating. Table 9 shows the rating of the lumbar spine by using the same weighting factor for all major and minor signals. These results should be compared to the regular rating (Table 6).

Table 9.
Alternative rating of lumbar spine tests

	R2.0	R4.5	R5.0
Flexion	0.769	0.758	0.837
Shear	0.776	0.722	0.898

Uniform weighting factors improve the rating of the lumbar spines. The ranking between the models remains the same. It is an indication that reasonable weighting factors generate reasonable ratings. So the rankings shown in this study are valid.

Table 10.
Alternative rating of sled tests

	R2.0	R4.5	R5.0
D1 barrier	0.473	0.467	0.533
D3 barrier	0.517	0.534	0.620

Uniform weighting factors worsen the rating of the sled tests (see Table 10 and Table 7). Many minor signals of poor correlation got more influence on the total results. However, the general tendencies of the regular rating are confirmed. Solely release 2.0 and 4.5 are switching the order in test D3. The difference of the CORA rating between those models is minor in the regular rating as well as in the alternative rating.

DISCUSSION

The ratings of the different tests demonstrate the possiblities of an objective rating tool to assess the quality of a dummy model. The most relevant information have to be extracted to define a valid rating procedure of the complete model.

Definition of a model rating procedure

A dummy model rating procedure should be kept as simple as possible and the results should correlate with experiences of users.

Certification tests The assessment of a dummy model by using certification tests seems to be the easiest way to define a rating procedure.

The progress of dummy release 4.5 compared to its predecessor is noticeable but the clearly improved robustness of 4.5 cannot be assessed by CORA. Version 5.0 of the ES-2 model is a big step forward. The ratings of the certification tests are clearly better.

In spite of the good correlation between certification tests and model improvements, this simple procedure is not reliable. It is possible to tune a model to correlate well to the certification test by disregarding the overall performance. Table 11 shows results of the LSTC ES-2 model (release V0.000.4.ALPHA) exemplarily. Its validation is mainly based on certification tests [7], [8] and its internal geometry is modelled rudimentary. So this model cannot be compared to the FAT ES-2. However, the abdomen of the LSTC ES-2 model achieves a good rating (see Table 11 and Table 1) because of single point optimisation.

Table 11.
Evaluation of certification tests

	LSTC
Shoulder	0.444
Abdomen	0.784
Pelvis	0.479

In summary, a quality assessment based certification tests might only be helpful to assess the progress of a well-known model but it can fail when using it to benchmark different models of a dummy. Nevertheless, those tests should be part of a rating procedure.

Component tests Dynamic tests of parts or sub-assemblies might be an important supplement of any assessment procedure. However, they cannot replace tests of the complete dummy. Release 4.5 showed that the rating of the lumbar spine decreased (Table 6) but the overall performance remains almost constant (Table 7).

Furthermore, component tests of all relevant dummy parts and sub-assemblies should be available to define a well-balanced rating procedure based on component tests.

Sled tests Sled tests are probably a good base of a dummy rating procedure. However, the sample size of sled test configurations used in this study is too small. The tests should cover a wider range of loading conditions to define a robust and a reliable rating scheme.

Furthermore, sled tests might not recognise improvements of parts of a model. These minor updates may not relevant in sled tests but might help in vehicle tests. So the rating should be completed by results of component tests.

Vehicle tests Vehicle tests seem to be the best choice for the evaluation of a dummy model in theory. However, there are strong arguments against the inclusion of those tests in a dummy quality rating.

At first, each vehicle test is unique. There are specific restraint systems, seats and door trims used. So it is very difficult to distinguish be-

tween dummy effects and effects caused by the environment. Secondly, the validity of the interior models used is mostly unknown. Thirdly, it is almost impossible to share details of a vehicle simulation with third parties. A dummy model rating procedure requires a well described protocol including all relevant details of the tests used.

A generic test environment (e.g. sled tests) would solve these problems. It reduces the number of unknown or less controlled parameters. So the validity of the corresponding simulations is much higher. Finally, it is easier to publish details of generic tests.

Combined rating procedure The combination of the three kinds of tests is most likely the best base of a dummy model assessment. A mean rating and a weighted mean rating is shown in Table 12. The mean rating is using a weighting factor of 0.333 for each type of tests. Whereas the weighted mean assigns 0.500 to the sled tests and 0.250 to the certification tests as well as to the component tests. The different weighting factors do not change the ranking of the three models.

Table 12.
Evaluation by using various kinds of tests

	R2.0	**R4.5**	**R5.0**
Certification	0.616	0.632	0.773
Component	0.639	0.623	0.752
Sled	0.390	0.579	0.666
Mean	0.548	0.611	0.730
Weighted mean	0.509	0.603	0.714

Release 5.0 was developed by using new test data which covers a wider range of loads. So the CORA rating is clearly the best. Model release 2.0 lost some scores because of the not completed simulation run with the barrier D4. So the limited numerical robustness is covered by the rating procedure indirectly.

In summary, the combination of certification, component and sled tests seems to be the best approach of a dummy model assessment. However, more component tests and more sled tests should be included into the rating procedure. The chosen weighting factors seem to have only a minor influence on the results.

Build level of auxilary models

The models of the test environment such as pendulum and barriers are identical for the simulations in this study. All results can be compared to each other without any limitation.

These auxiliary models get improved like dummies by the time. It must be analysed and discussed if all simulations of a rating have to use the same auxiliary models. There is significant effort needed to run old dummy models in an updated environment just to update rating results. However, there are first indications that these updates are essential to get valid results. This problem needs further in-depth analysis.

CONCLUSION

This study gives a first impression on the possibilities of an objective dummy rating procedure. The rating results of the analysed certification, component, sled and vehicle load cases are reasonable. Furthermore, they mostly correlate to user's experiences. It is the base of the acceptance by users of the model.

The evaluation also shows that a rating procedure must combine different kinds of tests. Certification tests give a limited impression on the overall quality of a dummy model. Component tests can only be used to assess the performance of single parts or sub-assemblies. Sled tests are the right choice for the evaluation of the complete dummy but they might miss improvements of sub-assemblies. Vehicle tests are probably too complex to integrate them into a rating scheme. So finally, a combination of certification, component and sled tests seems to be right mix.

The number of validation tests used in this study is probably too small. There should be component tests for each relevant body region considered. Test data of arm, shoulder, thorax and pelvis is required to evaluate the quality of a side impact dummy. Furthermore, sled tests must cover a wider range of loading conditions to check all relevant load paths and impact energies.

The influence of the weighting factors of signals and loading cases on the ratings seems to be limited. However, reasonable values must be defined.

Geometry, mass, inertia as well as the application of adequate modelling techniques cannot be assessed by an objective rating tool. So it is essential to check these properties before applying any rating. Otherwise the rating is not valid.

LIMITATIONS

The data used in this study is not sufficient to propose a final procedure. All sled tests of the ES-2 model development programme and a lar-

ger set of component test should be included in the rating.

Furthermore, it would be helpful to run a full comparison of the FAT ES-2 model and the LTSC model to get a more funded classification on the absolute meaning of the CORA scores.

The responses of head and neck were not analysed in this study. However, a dummy rating should include these body segments.

ACKNOWLEDGEMENTS

The authors would like to thank Matthias Walz from DAIMLER AG for his support.

REFERENCES

[1] Gehre, C. et al; "Objective rating of signals using test and simulation responses"; 21st International Technical Conference on the Enhanced Safety of Vehicles Conference (ESV); Stuttgart; Germany; 2009; Paper 09-0407.

[2] Franz U. et al.; "Observations during validation of side impact dummy models - Consequences for the development of the FAT ES-2 model; 2nd European LS-Dyna User Conference; Gothenburg; Sweden; 2002.

[3] Franz U. et al.; "FAT Side impact dummy models – Remarks on usage and potential pitfalls"; 4th European LS-DYNA User Conference; Ulm; Germany; 2003.

[4] First Technology Safety Systems; "ES-2re, EuroSID-2 50th percentile side impact crash test dummy – User manual"; Part-No. 175-9900; Rev. D 2005-3-10; Plymouth, MI; USA; 2005.

[5] "ES–2re Side Impact Crash Test Dummy, 50th Percentile Adult Male"; Title 49, Part 572, Subpart U; USA; 2008.

[6] Stahlschmidt, S. et al.; "WorldSID 50th vs. ES-2. A comparison based on simulations."; 11th International LS-Dyna Users Conference; Dearborn, MI; USA; 2010.

[7] Maurath, C. et al.; "Overview of LSTC's LS-Dyna anthropometric models"; 11th International LS-Dyna Users Conference; Detroit, MI; USA; 2010.

[8] Mohan, P. et al.; "LSTC/NCAC dummy model development"; 11th International LS-Dyna Users Conference; Dearborn, MI; USA; 2010.

CHARACTERIZATION OF THE PEDIATRIC SHOULDER'S RESISTANCE TO LATERAL LOADING CONDITIONS

Brian Suntay
Transportation Research Center Inc.
USA
Kevin Moorhouse
National Highway Traffic Safety Administration
John Bolte IV
The Ohio State University
Paper Number 11-0038

ABSTRACT

Current efforts to prevent injury to children in car accidents involve the use of pediatric anthropomorphic test devices (ATDs) which are designed based on data from adult post-mortem human subjects (PMHS) and animal surrogates, rather than from data obtained directly from the pediatric population. In this study, the force-deflection characteristics of the pediatric and adult shoulder were measured directly using a combination of optical motion capture, resistive loading, and electromyography (EMG). The right shoulder of nine adult volunteers and ten pediatric volunteers was quasi-statically displaced using a hand-held force applicator in both medial and posteromedial directions. Each subject had reflective markers placed on the upper right arm, both acromions, the manubrium, and both epicondyles of the right elbow. The motions of the reflective markers were tracked using an eight-camera Vicon motion capture system. Surface EMG electrodes were applied to the latissimus dorsi, upper trapezius, anterior deltoid, posterior deltoid, biceps brachii, and pectoralis major to measure the level of muscle activity during loading. Three to five tests were performed for each loading direction and in both relaxed and tensed states. The resulting force-deflection curves were normalized and then shoulder stiffness was calculated. Shoulder stiffness in the medial direction could not be obtained since less than 2 mm of shoulder deflection was recorded in the medial loading direction prior to the data being truncated due to subject tilting. The shoulder stiffness in the posteromedial direction was found to be 3.8 N/mm for the 50th male, 2.4 N/mm for the 10 year old age group, and 3.7 N/mm for the 6 year old group in the relaxed condition. In the tensed condition, posteromedial shoulder stiffness was found to be 9.7 N/mm for the 50th male, 4.1 N/mm for the 10 year old age group, and 5.0 N/mm for the 6 year old age group. Statistical analyses were performed and it was found that adults had a significantly higher shoulder stiffness than the children. Tensed shoulder stiffness was found to be greater than relaxed shoulder stiffness for all age groups ($p < 0.001$).

INTRODUCTION

Motor vehicle crashes are a leading cause of death and disability to the pediatric population as they account for approximately 50% of pediatric trauma (Brown et. al., 2006). Even while properly restrained within a vehicle, hundreds of children are still killed or injured in motor vehicle crashes due to a lack of protection (Fildes et al., 2003; Simpson et al., 1992). This is especially true in side impacts where the risk of a child being killed was found to be much higher than frontal impacts due to the child's proximity to the side of the vehicle and the lack of available vehicle structure to absorb crash energy (Fildes et al., 2003; Franklyn et al., 2007; Simpson et al., 1992). This lack of protection is a possible explanation for why lateral impact crashes were found to represent the leading cause of injuries and fatalities to the pediatric population in motor vehicle accidents (Franklyn et al., 2007). Forty-two percent of children who were fatally injured in a motor vehicle accident were in a side impact collision (Arbogast et al., 2005). According to the Crash Injury Research Engineering Network (CIREN), children involved in side impact crashes were more likely to suffer severe injuries to the head and thorax. Of these severe injuries to pediatric crash victims, 34% were to the thorax, while approximately 43% of injuries were to the head (Brown et al., 2006).

It is important to note that the motions of the head and thorax during impact are heavily dependent on the response of the occupant's shoulder. During the event of a lateral impact, children in and out of car seats interact first with the side of the child restraint or the interior side of the vehicle, such as an intruding door. It has been observed that the shoulder is the

first part of the occupant to be struck. When loaded in this manner, the shoulder deflects medially towards the thoracic cage, which results in the distribution of the initial impact load to the thorax through the spinal column, and to the head (Thollon et al., 2001). It has therefore been theorized that the skeletal components of the shoulder girdle play an important role in absorbing impact energy and reducing the energy as it is transferred to the thorax and head of the occupant.

To improve vehicle safety for children, the Q-series of child dummies was developed to cover the child population up to age 12. The Q-series was designed not only to be biomechanically advanced, but also to be used in both frontal and side impacts making it the first multi-directional series of child dummies. Unlike adult dummy development, ethics has limited the amount of child subject data available for the development of biofidelic child dummies. Therefore, the scaling of adult data is used to establish biofidelity targets for the child dummies. The scaling that was applied to the Q-series of dummies was based on the differences between adult and child subjects in terms of geometry and stiffness. The scaling factors for geometry are based on a well established set of anthropometry data for the 50th percentile male and the child anthropometry database, and the scaling factors for stiffness are based on published tissue data. Damping is not scaled due to the lack of biomechanical data, implying equal damping characteristics for children and adults (van Ratingen et al., 1997).

However, the maturity and development of a child's musculoskeletal system differ greatly from those of an adult. The bones of children are not fully ossified and are composed of a large amount of cartilaginous tissue. The muscles of children are also not as developed as those of an adult. Therefore the method of scaling geometries and stiffness to define the biofidelity response of child dummies is debatable and the overall biofidelity of child dummies is questionable.

Previous research has successfully analyzed and measured the pediatric shoulder's range of motion (Dayanidhi et al. 2005; Duff et al. 2007; Endo et al. 2004; van Andel et al. 2008; Vermeulen et al. 2002). However, these studies are not useful for modeling the response of the pediatric shoulder to impact since only the relative motion of the shoulder during everyday tasks was observed. Stiffness measurements are needed in order to develop a biofidelic shoulder in ATDs since it is important to know the amount of force required to displace the shoulder. Therefore, instead of analyzing its range of motion, a medial and posteromedial loading of the shoulder should be analyzed (Kapandji, 1982). By measuring the forces required to displace the shoulder in a manner that is similar to impact conditions, the proper shoulder stiffness can be defined for the child population, which can lead to the development of more biofidelic child ATDs.

The purpose of this study was to investigate the response of the pediatric shoulder by quasi-statically and non-injuriously analyzing its resistance to lateral loading conditions, and compare it to the response of the adult shoulder. This study was conducted in two phases. Phase one consisted of defining and validating a new method for quasi-statically measuring the shoulder's stiffness, and then quasi-static non-injurious shoulder deflections were performed on adult volunteers to define the adult shoulder's stiffness. In phase two, quasi-static shoulder stiffness testing on pediatric volunteers was performed.

METHODS

Subjects

This study was reviewed and approved by The Ohio State University Institutional Review Board (IRB #2008H0202) and informed consent was obtained from all subjects. Nine adult volunteers (mean of 24 ± 3.6 years, 79 ± 10 kg) and ten pediatric volunteers (mean of 8 ± 2.3 years, 32 ± 12 kg) participated in this study. To be included, adult subjects had to be male, between the ages of 21-40 (a majority of the epiphyses have fused around the age of 21), and roughly meet the 50th percentile male requirements (78 kg, 175 cm). Children were either male or female (pediatric ATDs are representative of both male and female populations) and between 4-12 years of age. The age range of 4-12 years was chosen to correspond with the 6 year old and 10 year old ATDs. There were no height and weight requirements for pediatric subjects. The exclusion criteria for both groups were any history of injury or surgery to the shoulder, scapula, or clavicle. All male subjects were tested with their trunk bare and female subjects wore a tank-top so that the acromion was visible and to allow for non-restrictive shoulder movements.

Resistive Shoulder Loading

To measure the forces needed to displace the shoulder, a custom linear force applicator was developed utilizing a Honeywell Model 31 Mid-Range Precision Miniature Load Cell. A frame, with

translational motions in the x, y, and z-directions, was designed to allow for the proper alignment of the load cell with the subject's shoulder (Figure 1). A faceplate at the center of the fixture, on top of which a load cell guide was attached, was designed to allow for a medial and posteromedial (30° anterior to medial) loading direction (Figure 1).

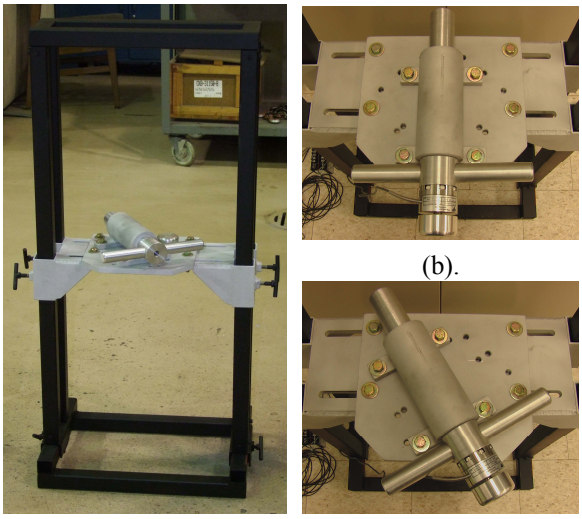

(a). (b). (c).

Figure 1. (a). Frame designed for the proper alignment of the shoulder force applicator with the subjects' shoulders; (b). Load cell attached to the tip of the force applicator and positioned in a medial loading direction; (c). Force applicator positioned in a posteromedial loading direction.

To measure shoulder girdle deflection and thoracic motion, an 8-camera, 100 Hz Vicon motion analysis system (Vicon Motion Systems, Oxford, UK) was used. Reflective markers were placed on the skin using double-sided adhesive tape over the subject's acromion process of both scapulas, manubrium of the sternum, lateral and medial epicondyles of the right humerus, and around the mid-shaft of the humerus as an 8-marker cluster with a 2x1x2x1x2 configuration (Figure 2). In addition, reflective markers were placed on the load cell guide and the bench on which the subjects were seated.

To measure muscle activity during the tests, surface electrodes were applied to the superficial muscles that play an important role in the movement and stabilization of the shoulder. The muscles documented and analyzed were the latissumus dorsi, upper aspect of the trapezius, anterior and posterior portions of the deltoid, biceps brachii, and pectoralis major of the displaced shoulder.

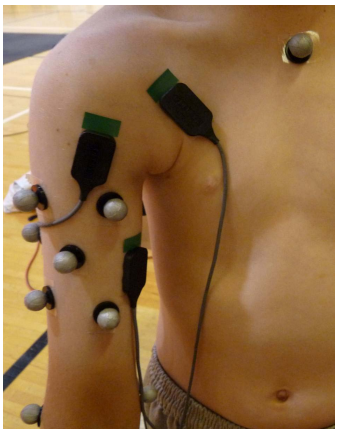

Figure 2. Placement of reflective markers and surface electrodes.

The subject bench and shoulder apparatus were placed at the center of the 8-camera Vicon optical motion capture setup. Each subject was seated on the right edge of the bench with the right side of the seatback along the subject's spine, allowing for a free range of motion of the shoulder. With the subject in position, a hip brace was applied to the subject's left hip and clamped onto the bench to prevent any translational motion of the subject's pelvis during the various loading conditions (Figure 3).

Figure 3. Image of an adult test setup. The custom linear force applicator and frame are seen to the subject's right side. A special bench with Teflon backing was used to allow for a free range of motion of the shoulder. A hip brace was placed to the subject's left to prevent total body sliding during testing.

Prior to the positioning of the load cell, the maximum voluntary contractions (MVCs) of the muscles were recorded. With the aid of a researcher, the subject's right arm was placed at prescribed positions and then the subject was told to move his or her arm in various directions with as much force as possible while the

researcher provided resistance such that each relevant muscle was maximally contracted. The subject maintained each maximal contraction for five seconds, was told to relax for five seconds, and then told to repeat the movement and maintain for another five seconds while recording the signal. Upon completion of the recording of the MVCs, the shoulder loading apparatus was placed next to the subject. The height of the load cell was adjusted and centered at the lateral portion of the subject's deltoid muscle covering the glenoid fossa of the scapula. For each test, a researcher would manually push the load applicator and slowly displace the subject's shoulder. As the subject began to tilt, the application of the force was terminated and the load applicator was retracted back to its starting position. Three to five tests were performed with the subject's muscles relaxed, and three tests were performed with the subject's muscles tensed. The sequence of relaxed tests followed by tensed tests was performed for both medial and posteromedial loading directions.

Data Reduction and Analysis

Marker data acquisition was performed at 100 Hz and processed using Vicon Nexus software. Forces from the load cell were acquired at 1000 Hz and filtered using a low-pass butterworth filter at 100 Hz. EMG signals were acquired at 1000 Hz, rectified, filtered using a bandpass filter between 10 and 400 Hz, and then filtered using a low-pass filter at 25 Hz for analysis. The deflection of the shoulder was calculated using the Vicon marker data as the change in distance between the acromion of the shoulder being displaced and both the manubrium (half-girdle deflection) and non-displaced acromion (full-girdle deflection), and was plotted against the applied load. Half-girdle and full-girdle shoulder deflections were used interchangeably since initial analysis of the two measurements found them to be near identical. Therefore, for each test the deflection measure that produced the largest linear region in the force-deflection curve was chosen, since ultimately the linear region of the curve would be used to calculate stiffness values. Additionally, if either the manubrium or opposite acromion were lost during motion tracking, the deflection measure that was used for the test was the one that had the available markers.

The resulting force-deflection curves were to be used to determine shoulder stiffness for each subject, loading direction, and relaxed or tensed test condition. In all cases, the force-deflection curves displayed a relatively linear response until the force became large enough to cause the subject to start tilting away from the loading. Once the subject began tilting away the force-deflection response became nonlinear and unpredictable, thus the data was effectively meaningless at that point. In some instances the subject's response to a force high enough to cause them to tilt away was to avoid it by leaning into the load, also resulting in nonlinear and meaningless force-deflection responses. Therefore in order to calculate the shoulder stiffness for each test, a linear portion of each curve had to be defined. First, data was truncated at the point where four degrees of subject tilt was observed, where tilt was defined as the change in angle between a line going through both acromions and the horizontal plane (Bolte et al., 2000; 2003) Next, the linear portion of the curve was determined by evaluating the central portion of the force-deflection curve (20-80%) and finding the range in which the slope of each point remained within one standard deviation of the average of the slopes of the previous points (Margulies & Thibault, 2000). Once the slope exceeded one standard deviation (i.e., became nonlinear) the data was truncated at that point and the data that remained exhibited a relatively linear force-deflection response that could be used for calculating stiffness.

Example force-deflection curves for the medial and posteromedial loading conditions of adult subject 7 are shown in Figures 4 and 5. The curves show the repeatability and linearity of the test trials as the curves follow similar, linear trends. Note that less than 2 mm of shoulder deflection was recorded in the medial loading direction prior to the data being truncated due to subject tilting. This was found to be the case for all pediatric and adult subjects in the medial direction and indicates that the clavicle is stiff enough that no appreciable shoulder deflection can be achieved in this quasi-static manner before the subject begins to tilt. Since the average human skin thickness ranges from 0.5 mm (eyelids) to 4 mm (soles of hands and feet), the 2 mm of deflection observed in these tests is on the order of what would be required simply to compress the skin on the shoulder. In addition, the resolution of accuracy for the Vicon motion capture system is on the order of 0.1 mm which means a minimum of 5% error would immediately be introduced into the deflection measurements. For these reasons, only the posteromedial stiffness is reported and discussed in this paper since it is the opinion of the authors that 2 mm of shoulder deflection is not suitable for calculating shoulder stiffness. Similarly, data from any test trials in the posteromedial loading direction in which the shoulder deflection did not exceed 2 mm was also excluded from analysis. Future testing will

incorporate a load wall positioned at the subject's non-loaded shoulder to prevent immediate tilting and allow for more shoulder compression. Preliminary pilot studies have demonstrated that much more shoulder deflection can in fact be achieved in the medial loading direction using an opposing load wall, and will be presented in a future publication.

In order to calculate stiffness for each subject the repeated trials in each test condition were reduced to one representative mean force-deflection curve for each subject and test condition. However, since the quasi-static load for each test was applied manually, the loading rate was not controlled resulting in different loading rates for each test. Therefore, the typical calculation of the mean and standard deviation of a set of curves using the time-histories is invalid since forces and deflections from each trial used to calculate the mean were reached at different times. Since a representative mean curve was still desired for each subject and test condition, the repeated trials within each group were interpolated onto common values of deflection and then a mean curve was calculated in "force-deflection space" instead of using the time-histories. It should be noted that since the data was interpolated on common levels of deflection, and no extrapolation of the data was performed, the mean curve could only be calculated up to the smallest value of maximum shoulder deflection of each trial since force data was not available at any further values of deflection for that trial. Once the force-deflection curve was reduced in this manner to a single mean curve for each subject and test condition, a linear fit could be obtained, taking the slope to be the shoulder's stiffness.

Normalization

All adult data were normalized to the anthropometry of a 50th percentile male, data from pediatric subjects age 8 to 12 were normalized to the anthropometry of the 10 year old ATD, and data from pediatric subjects age 4 to 7 were normalized to the anthropometry of the 6 year old ATD.

The underlying basis of the normalization procedure was a spring-mass model first introduced by Mertz (1984) which incorporates a mass ratio and a stiffness ratio. In Mertz (1984), the mass ratio was comprised of effective mass values calculated from the subject response data using an impulse-momentum analysis. The denominator of the ratio was the effective mass calculated for each individual subject. The numerator was determined by calculating the percentage of each subject's effective mass to their total body mass, averaging the percentage across subjects, and multiplying by the total body mass of the population to which the data was to be normalized (e.g., 76 kg for 50th percentile male). The stiffness ratio was simply a ratio of characteristic lengths (e.g., chest depth) where the denominator was the characteristic length of the subject and the numerator was the characteristic length of the population to which the data was to be normalized. Moorhouse (2011; 2008) took this methodology a step further by also incorporating the response data into the determination of the stiffness ratio. Using a procedure analogous to the effective mass ratio described above, the denominator was determined by calculating the effective stiffness of each subject from the response data, and the numerator was determined by calculating the percentage of each subject's effective stiffness to a characteristic length of the subject, averaging the percentage across subjects, and multiplying by the characteristic length of the population to which the data was to be normalized.

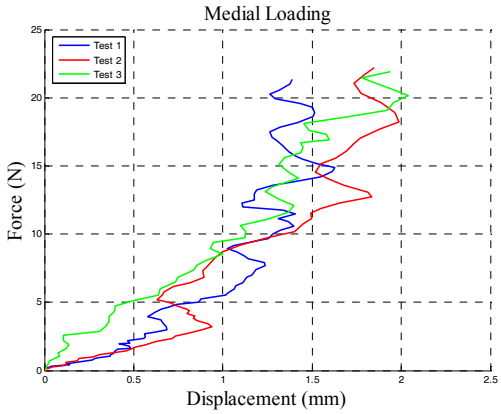

Figure 4. Force-deflection curves for adult subject 7 in the medial loading condition.

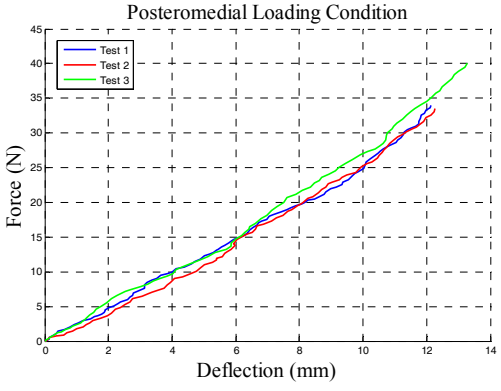

Figure 5. Force-deflection curves for adult subject 7 in the posteromedial loading condition.

For the data from the current study, the impulse-momentum procedure used to calculate the effective mass of each subject is not valid since the quasi-static loading rate does not represent impulse loading. Therefore it was decided to calculate the mass ratio (λ_m) using the total body mass of the subject for the denominator and the total body mass of the population to which the data was to be normalized for the numerator (Equation 1). To determine the stiffness ratio in this study, first an effective stiffness (k_{eff}) for each subject and test condition was calculated using Equation 2. Then a percent stiffness ratio (%Stiff) was calculated by dividing the subject's effective stiffness by their shoulder breadth, where the shoulder breadth was deemed the most appropriate characteristic length for this study. Within each test condition the values for %Stiff were averaged across subjects (Avg %Stiff), and finally the stiffness ratio (λ_k) was calculated using Equation 3.

$$\lambda_m = \frac{Mass_{50th,10yo,6yo}}{Subject\ Mass} \quad (1).$$

$$k_{eff} = \frac{2\int F dx}{x_{max}^2} \quad (2).$$

$$\lambda_k = \frac{Avg\ \%Stiff \times Shoulder\ Breadth_{50th,10yo,6yo}}{k_{eff}} \quad (3).$$

Normalizing factors for force (λ_F) and deflection (λ_D) were then calculated from the resulting mass and stiffness scaling ratios (Equations 4 and 5), the normalized force and deflection were cross-plotted, and the normalized shoulder stiffness determined via the slope of a linear fit.

$$\lambda_F = \sqrt{\lambda_m \times \lambda_k} \quad (4).$$

$$\lambda_D = \sqrt{\lambda_m / \lambda_k} \quad (5).$$

RESULTS

Important subject information taken from anthropometric measurement sheets are listed in Table 1. Subjects were divided into three age groups corresponding to the 50th percentile male, 10 year old ATD, and 6 year old ATD, as described in the normalization section above.

Force-deflection plots of the repeated trials for each subject and test condition which were used to generate the non-normalized mean force-deflection curves are provided in Appendix A. Appendix B contains the six sets of the non-normalized mean force-deflection curves for each age group and test condition.

After normalizing the data, biomechanical targets were created for each age group and test condition to represent the force-deflection response of the adult, 10 year old, and 6 year old shoulder to quasi-static posteromedial loading in relaxed and tensed conditions (six total biomechanical targets). For the same reasons described in the methods, mean and standard deviation curves for each age group and test condition could not be calculated using the time-histories. Instead, data from all subjects within a test condition were first interpolated onto common values of deflection and a mean curve and force standard deviations were calculated. Next the data was interpolated onto common values of force so that the deflection standard deviations could be calculated. The resulting deflection standard deviations were then interpolated onto the mean curve so that the force standard deviations and deflection standard deviations occurred at common points. Finally, ellipse targets were developed using the force and deflection standard deviations by calculating an ellipse at each point along the mean force-deflection curve as previously described in Shaw (2006).

Relaxed and tensed biofidelity targets for each of the age groups are plotted in Figures 6 and 7, respectively, along with the normalized mean force-deflection curve for each individual subject.

A summary of normalized shoulder stiffness for the 50th male, 10 year old, and 6 year old in both relaxed and tensed conditions is shown in Table 2. Statistical analysis using a two sample t-test assuming unequal variance was performed on both the relaxed and tensed stiffness data. The resulting p-values are tabulated in Table 3 and show that all three age groups demonstrate statistically significant differences in shoulder stiffness for both relaxed and tensed conditions (adult >> 6YO >> 10YO). In addition, tensed shoulder stiffness was found to be greater than the relaxed stiffness in all three age groups ($p < 0.001$).

Table 1.
Subject age and anthropometry data

	Subject #	Age	Gender	Mass (kg)	Seated Height (cm)	Shoulder Breadth (cm)
Adult	1	23	M	82	84	43
	2	24	M	77	91	48
	3	23	M	80	91	43
	4	23	M	73	94	39
	5	32	M	79	93	40
	6	22	M	70	95	44
	7	25	M	73	91	39
	8	20	M	74	90	40
	9	28	M	102	91	39
	Average	24 ± 4		79 ± 10	91 ± 3	42 ± 3
10YO	P1	10	M	50	74	34
	P4	8	M	39	73	36
	P7	9	M	34	74	29
	P8	11	M	43	82	35
	P10	8	F	25	68	29
	P11	10	F	43	80	39
	Average	9 ± 12		39 ± 8	75 ± 5	33 ± 4
6YO	P3	7	M	26	68	28
	P5	5	F	16	56	22
	P9	4	F	18	70	20
	P12	6	F	23	66	28
	Average	6 ± 1		21 ± 5	65 ± 6	24 ± 4

Table 2.
Normalized posteromedial shoulder stiffness (N/mm) for the 50th male, 10 year old, and 6 year old age groups

	Relaxed	Tensed
50th Male	3.84	9.69
10YO	2.44	4.11
6YO	3.67	4.98

Table 3.
Statistical significance between normalized shoulder stiffness for the three age groups (two sample t-test assuming unequal variance)

p-Values		
Age Group Comparison	**Relaxed**	**Tensed**
Between 10YO and 6YO	< 0.001	< 0.05
Between 10YO and Adult	< 0.001	< 0.001
Between 6YO and Adult	< 0.05	< 0.001

DISCUSSION

This study investigated the response of the shoulder to lateral loading by quasi-statically and non-injuriously analyzing its resistance to lateral loading conditions. A total of 9 adult and 10 pediatric volunteers were tested, and the stiffness of the shoulder in a posteromedial loading direction in both relaxed and tensed conditions was obtained.

A cursory examination of Tables 2 and 3 reveals that for both relaxed and tensed conditions the shoulder stiffness in the posteromedial direction of all three age groups are statistically different from one another (i.e., adult >> 6YO >> 10YO), and that for all three age groups the tensed shoulder stiffness is greater than the relaxed shoulder stiffness. However, examination of Table 4 which lists the individual stiffness values (both non-normalized and normalized) for each age group and test condition reveals that the normalization procedure drastically reduces the variance in stiffness within each age group, potentially resulting in inflated statistical significance between age groups.

If the non-normalized stiffness for each age group is evaluated for statistical significance (Table 5), it can be observed that in the relaxed condition there is still

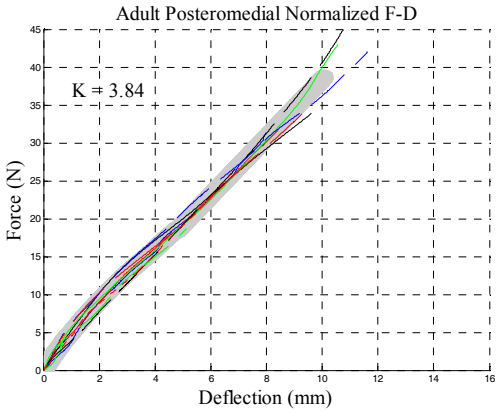

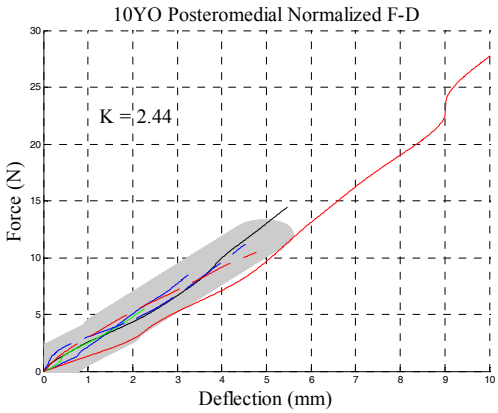

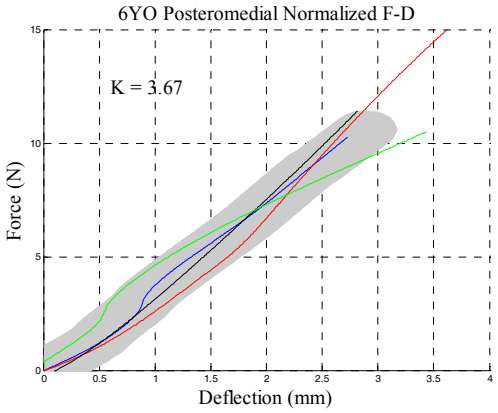

Figure 6. Normalized force-deflection curves and biofidelity targets (grey) for the 50th percentile adult male, 10 year old, and 6 year old in the relaxed posteromedial loading condition. The targets were created by forming one standard deviation ellipses around the mean force-deflection response.

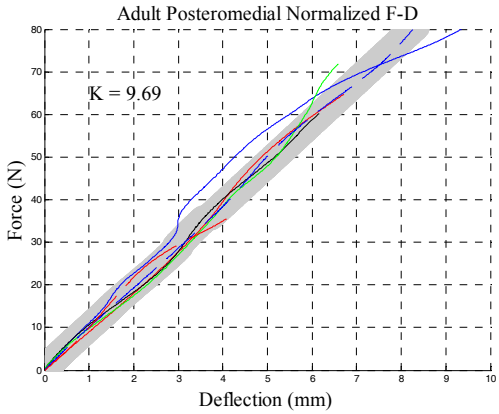

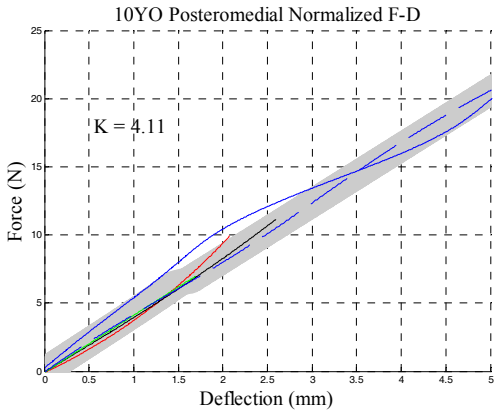

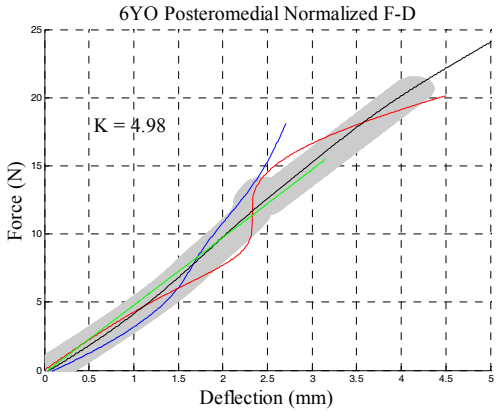

Figure 7. Normalized force-deflection curves and biofidelity targets (grey) for the 50th percentile adult male, 10 year old, and 6 year old in the tensed posteromedial loading condition. The targets were created by forming one standard deviation ellipses around the mean force-deflection response.

Table 4.
Shoulder stiffness in the posteromedial loading direction in both relaxed and tensed conditions. Adult subjects 3, 4 and pediatric subject 1 were not included in the tensed condition due to shoulder deflections that were less than 2 mm.

	Subject #	Relaxed		Tensed	
		Non-Normalized	Normalized	Non-Normalized	Normalized
Adult	1	6.10	3.88	9.58	9.34
	2	5.50	3.84	6.23	9.86
	3	3.14	3.78	--*	--*
	4	3.35	3.88	--*	--*
	5	3.22	3.79	10.07	9.74
	6	1.37	3.79	7.61	9.91
	7	2.36	3.96	15.58	9.74
	8	2.63	3.80	4.79	9.57
	9	4.67	3.86	--*	--*
	Mean	**3.59**	**3.84**	**8.98**	**9.69**
	Std. Dev.	**1.45**	**0.06**	**3.47**	**0.19**
10YO	P1	2.70	2.50	--*	--*
	P4	2.15	2.57	3.35	3.97
	P7	1.98	2.47	3.73	4.26
	P8	3.28	2.41	4.99	4.13
	P10	2.65	2.37	3.21	4.10
	P11	1.91	2.35	8.98	4.07
	Mean	**2.45**	**2.44**	**4.85**	**4.11**
	Std. Dev.	**0.48**	**0.08**	**2.16**	**0.10**
6YO	P3	2.16	3.69	3.41	5.30
	P5	2.35	3.80	7.34	4.90
	P9	3.97	3.76	4.35	4.85
	P12	3.40	3.42	1.65	4.87
	Mean	**2.97**	**3.67**	**4.19**	**4.98**
	Std. Dev.	**0.74**	**0.15**	**2.06**	**0.19**

a significant difference between adults and the 10 year old age group, but not between adults and the 6 year old age group, or between the 6 year olds and 10 year olds. However, in the tensed condition there is a significant difference between adults and both child age groups, but no significant difference between the two child populations. As with the normalized shoulder stiffness, all three age groups demonstrate a significantly higher shoulder stiffness in the tensed condition than in the relaxed condition ($p < 0.001$).

Table 5.
Statistical significance between non-normalized shoulder stiffness for the three age groups (two sample t-test assuming unequal variance)

p-Values		
Age Group Comparison	**Relaxed**	**Tensed**
Between 10YO and 6YO	0.16	0.35
Between 10YO and Adult	< 0.05	< 0.05
Between 6YO and Adult	0.19	< 0.05

Despite the difference in potential conclusions drawn from the normalized stiffness values versus the non-normalized stiffness values, both analyses produce clear evidence that there is a difference in shoulder stiffness between children and adults. The specific details of the difference likely lie somewhere between, and further testing with a much larger sample from each age group should help elucidate those details.

In addition, it is important that the shoulder stiffness in the medial loading direction is determined for each age group to supplement the results from the posteromedial loading direction, as it is expected that much more variation between children and adults would be seen in the medial direction. Whereas in the posteromedial direction where the stiffness of soft tissue contributing to the anterior-posterior resistance may differ to some degree between children and adults, the resistance to medial loading is primarily provided by the clavicle so bone maturity may play a large role in the response. In adults, the clavicle and other bony structures of the shoulder are fully ossified. However, in children, especially those

under the age of 12, a larger portion of bones are still cartilaginous. The presence of cartilage can lead to a more compliant shoulder and result in a lower stiffness in the younger age groups. The intent of this study was to evaluate both loading directions but the combination of the quasi-static loading and the stiffness of the clavicle caused there to be no appreciable shoulder deflection (< 2 mm) before the subject began to tilt away from the loading. This could be avoided by using an opposing load wall on the non-loaded shoulder and investigation of the force-deflection response of the shoulder in the medial loading direction using an opposing load wall is currently underway and will be presented in a future publication.

The importance of the medial loading direction can be seen to some extent in the data obtained from this study in the posteromedial loading direction if the resultant force and deflection is broken down into its medial-lateral (y-direction) and anterior-posterior (x-direction) components. As expected, all three age groups demonstrate that the shoulder is much less stiff in the x-direction due to the lack of bony structures to impede the motion of the joint posteriorly. When moving in this direction, the shoulder pivots at the sternoclavicular joint and there are no bony structures that directly inhibit the shoulder's motion, thus soft tissue, rather than hard bony tissue, contributes more to the stiffness. In contrast, the shoulder has higher stiffness in the y-direction because the clavicle serves as a strut to hinder the medial motion of the shoulder, thus hard tissue contributes more to the stiffness.

The shoulder stiffness comparisons between age groups in this study yielded two unexpected findings that warrant some further discussion. First, for the normalized stiffness in both the relaxed and tensed conditions the shoulder stiffness of the 6 year old is significantly larger than the 10 year old. Due to the fact that this result did not hold for the non-normalized stiffness values, this may be an artifact of variance reduction in the normalization process which inflates the statistical significance between stiffness values from each population. The other unexpected finding was that both the non-normalized and normalized shoulder stiffness of the six year old was not significantly different from the adult in the relaxed condition, although it was significantly lower (as expected) in the tensed condition. Although these phenomena should be better understood after future studies involving a larger sample of children (only four 6YO subjects and six 10YO subjects in this study), and when stiffness data for medial loading is available, they still may be worth some consideration. It is possible that these results could be due to a lack of muscle control in younger subjects. Even when relaxed, younger subjects in the 6 year old group may involuntarily activate their muscles as a shoulder protection mechanism, which can lead to higher stiffness values than the subjects in the 10 year old group. This could also explain why in the relaxed condition the shoulder stiffness of the 6 year old group was similar to adults since their relaxed stiffness was higher due to muscle activation.

Evidence for this can be found upon close examination of the EMG data. Appendix C contains a plot of the EMG signals for a subject from each age group in both relaxed and tensed test conditions, along with a table showing the maximum %MVC obtained during each test. It can be seen that the adults demonstrate a much higher difference in %MVC between the relaxed and tensed conditions than either of the child age groups. Also, as the age of the group decreases from adult down to six year old, the %MVC in the relaxed condition increases (3%, 9%, 17%, respectively) whereas in the tensed condition is remains relatively consistent (22%, 16%, 20%).

One definitive conclusion from this study is that for all three age groups, and for both the normalized and non-normalized stiffness values, that the stiffness of the shoulder is greater with muscle tensing than when relaxed. This result is not surprising for this quasi-static loading condition because tensing of the muscles should result in stabilization of the shoulder joint and less movement for a given applied force. However, as the applied force becomes very large (i.e., well above the increase in stabilizing force of the tensed muscles) with a much higher severity of loading as seen in a crash-scenario, the relative effect of tensing on the resistance to loading would be expected to decrease. Therefore, the relevance of this result to a crash-scenario where an occupant's muscles may be relaxed or tensed depending on if they are aware of an oncoming accident is unknown. This could potentially be investigated by applying crash-level loading to the shoulder of PMHS in both tensed and relaxed conditions, where the tensed condition could be simulated using muscle stimulation to cause the muscles to contract upon loading.

Although the statistical significance of the normalized stiffness values should be taken with caution, it should be pointed out that the normalized data is very important for creating biomechanical targets for assessing the biofidelity of existing child ATD shoulders and for designing new ATD

shoulders based on measured differences between children and adults. The extreme amount of variation seen in the non-normalized force-deflection response of the shoulder (Appendix B), particularly in the adults, must be reduced so that an ATD is held to higher standard when trying to match a biofidelic mean response.

LIMITATIONS

There are several factors to consider when interpreting the results of this study. First, only a limited amount of subjects (9 adults and 10 children) were tested in this study. More volunteers will need to be tested in the future in order to increase the statistical significance of the conclusions. Since completion of this study, approximately twenty additional pediatric subjects have been recruited, and testing is currently ongoing to obtain shoulder stiffness data to supplement the current study. This ongoing study will also obtain meaningful data in the medial loading direction by utilizing an opposing wall on the non-loaded shoulder so that differences in the response of the clavicle between children and adults can be taken into account

Also, the test procedure and analysis itself proved to be very challenging. Quasi-static shoulder deflections such as were performed in this study had not previously been conducted. The shoulder joint is complicated to study due to the fact that it is a floating joint and relies mostly on muscles for stabilization. Since muscle mass and muscle tone vary greatly between individuals due to their body shapes and the types of activities they take part in, the motions of the shoulder can vary greatly. Also, performing tests on volunteers provided additional challenges and introduced several factors that were hard to control in the study, especially with the younger age groups. Even though steps were taken to try and control the posture of each individual, no two volunteers sat on the bench in precisely the same manner. Subjects' shoulders were hunched or arched back; heads were leaning forward or backward; backs were straight, arched, or hunched; and the younger age groups would sometimes move around between tests and even during some tests. Another factor that was difficult to control was the amount of voluntary and involuntary muscle activation during both the relaxed and tensed testing conditions. Even when relaxed, an individual may involuntary activate some of their muscles, especially with the younger age groups who do not have full control over their muscles and may reflexively guard their shoulders. It is even very difficult for individuals to activate the same muscles, and to the same degree of activation, from test to test. Furthermore, the muscles naturally activated during "tensing" can vary greatly between individuals. All of these variables undoubtedly introduced some test-to-test variation and may have affected the results.

Despite these limitations, these results are still important in trying to understand and characterize the difference in the pediatric shoulder's resistance to various loading conditions with respect to the resistance of the adult shoulder.

CONCLUSION

Based upon the research presented in this paper, the following observations were made:

- Despite the difficulty in controlling the test conditions using volunteer subjects, the method presented for quasi-statically displacing the shoulders of adult and pediatric volunteers was repeatable as demonstrated by the similarity of repeated trials for each subject and test condition.
- The shoulder stiffness of the 50th percentile adult male is significantly larger than the shoulder stiffness of children.
- Relative shoulder deflection measured from acromion-to-sternum is very similar to measured shoulder deflection from acromion-to-acromion.
- The tensing of the shoulder muscles causes an increase in shoulder stiffness
- Improvements to the test procedure were identified in this study, particularly the use of an opposing load wall on the non-loaded shoulder to prevent subject tilting. This should allow for appreciable shoulder deflection to be measured in the medial loading direction in future testing.
- The statistical power of the results could be improved by obtaining more pediatric subjects, and a study involving approximately 20 more pediatric subjects using an opposing load wall is already underway.
- Despite the limitations, the results are a good start to understanding the differences in shoulder stiffness between pediatric and adult subjects, which can hopefully lead to improved methods for developing pediatric ATDs.

ACKNOWLEDGEMENTS

This research was supported by the National Highway Traffic Safety Administration's Vehicle Research and Test Center. We gratefully acknowledge and thank the students of The Ohio State University's Injury Biomechanics Research Laboratory for all their hard work and involvement. We would like to thank Dr. Ajit Chaudhari and Steve Jamison of the Sports Biomechanics Laboratory and Dr. John Borstad of the Human Movement and Performance Lab. We would also like to thank all the volunteers for their contribution to the study.

REFERENCES

Arbogast, K.B., Kallan, M.J., Durbin, D.R. (2005). Effectiveness of high back and backless belt-positioning booster seats in side impact crashes. *Ann Pro Assoc Adv Automot Med*, 49, 201-213.

Bolte, J. H., Hines, M. H., Herriott, R. G., McFadden, J. D., & Donnelly, B. R. (2003). Shoulder impact response and injury due to lateral and oblique loading. *Stapp Car Crash Journal, 47*, 35-53.

Bolte, J. H., Hines, M. H., McFadden, J. D., & Saul, R. A. (2000). Shoulder response characteristics and injury due to lateral glenohumeral joint impacts. *Stapp Car Crash Journal, 44*.

Brown, J. K., Jing, Y., Wang, S., & Ehrlich, P. F. (2006). Patterns of severe injury in pediatric car crash victims: Crash Injury Research Engineering Network database. *Journal Of Pediatric Surgery, 41*(2), 362-367.

Dayanidhi, S., Orlin, M., Kozin, S., Duff, S., & Karduna, A. (2005). Scapular kinematics during humeral elevation in adults and children. *Clinical Biomechanics (Bristol, Avon), 20*(6), 600-606.

Duff, S. V., Dayanidhi, S., & Kozin, S. H. (2007). Asymmetrical shoulder kinematics in children with brachial plexus birth palsy. *Clinical Biomechanics (Bristol, Avon), 22*(6), 630-638.

Endo, K., Yukata, K., & Yasui, N. (2004). Influence of age on scapulo-thoracic orientation. *Clinical Biomechanics (Bristol, Avon), 19*(10), 1009-1013.

Fildes, B., Charlton, J., Fitzharris, M., Langwieder, K., & Hummerl, T. (2003). Injuries to children in child restraints. *International Journal of Crashworthiness, 8*(3), 277-284.

Franklyn, M., Peiris, S., Huber, C., & Yang, K. H. (2007). Pediatric material properties: a review of human child and animal surrogates. *Critical Reviews in Biomedical Engineering, 35*(3-4), 197-342.

Kapandji, I. A. (1982). The shoulder. *Clinics in Rheumatic Diseases, 8*(3), 595-616.

Margulies, S.S. & Thibault, K.L. (2000). Infant skull and suture properties: Measurements and implications for mechanisms of pediatric brain injury. *Journal of Biomechanical Engineering*, 122, 364-371.

Mertz, H.J. (1984). A Procedure for Normalizing Impact Response Data. SAE 840884. Society of Automotive Engineers, Warrendale, PA

Moorhouse, K.M. (2008). An improved normalization methodology for developing mean human response curves. *Injury Biomechanics Research. Proceedings of the Thirty-Sixth International Workshop.*

Moorhouse, K.M. (2011). An improved normalization methodology for developing mean human response curves. *Journal of Biomechanical Engineering (in review)*

Shaw J.M., Herriott, R.G., McFadden, J.D., Donnelly, B.R., and Bolte, J.H. (2006). Oblique and Lateral Impact Response of the PMHS Thorax. *Stapp Car Crash Journal.* 50, 147-67.

Simpson, D. A., Scott, G., McLean, A. J., & Blumbergs, P. C. (1992). Head injuries in infants and children: measures to reduce mortality and morbidity in road accidents.

Thollon, L., Cavallero, C., Pu, M., & Brunet, P.C. (2001). The thoracic member under side impact: an experimental approach. *International Journal of Crashworthiness*, 6(3), 307-319.

van Andel, C. J., Wolterbeek, N., Doorenbosch, C. A. M., Veeger, H. E. J., & Harlaar, J. (2008). Complete 3D kinematics of upper extremity functional tasks. *Gait & Posture, 27*, 120-127.

van Ratingen, M.R., Twisk, D., Schrooten, M., & Beusenberg, M.C. (1997). Biomechanically based design and performance targets for a 3-year old child crash dummy for frontal and side impact. *Society of Automotive Engineers.*

Vermeulen, H. M., Stokdijk, M., Eilers, P. H. C., Meskers, C. G. M., Rozing, P. M., & Vliet Vlieland, T. P. M. (2002). Measurement of three dimensional shoulder movement patterns with an electromagnetic tracking device in patients with a frozen shoulder. *Annals of The Rheumatic Diseases, 61(2), 115-120*

APPENDIX A

Relaxed Adult Posteromedial F-D Curves

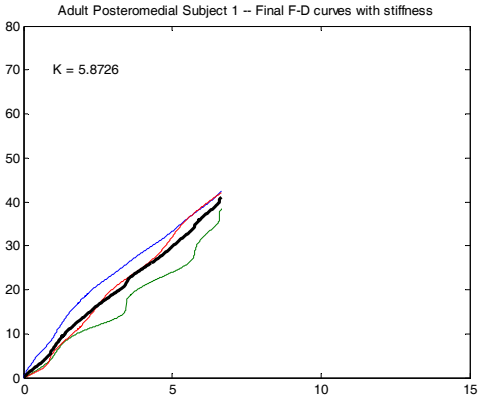

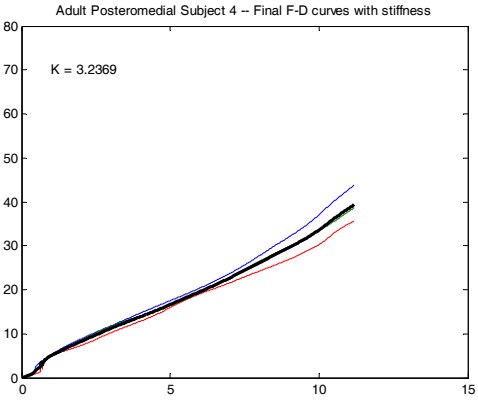

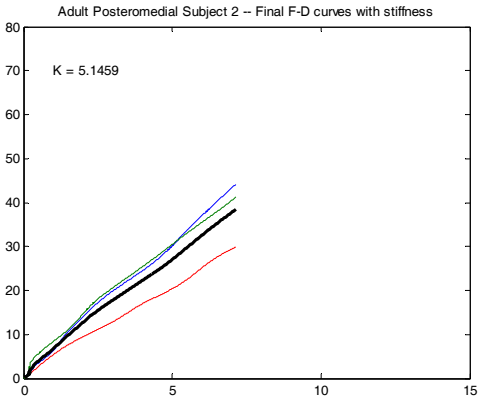

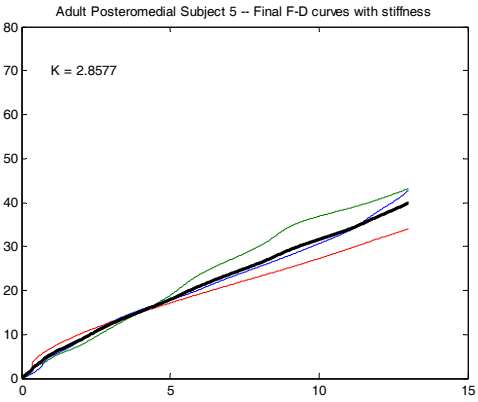

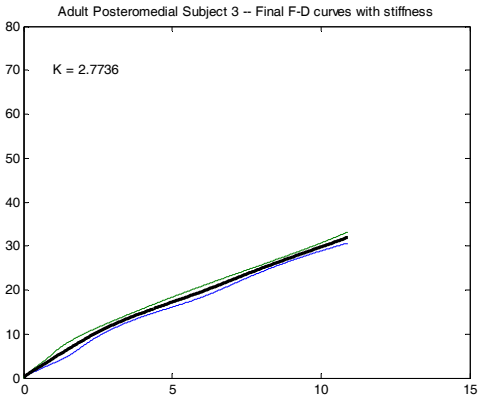

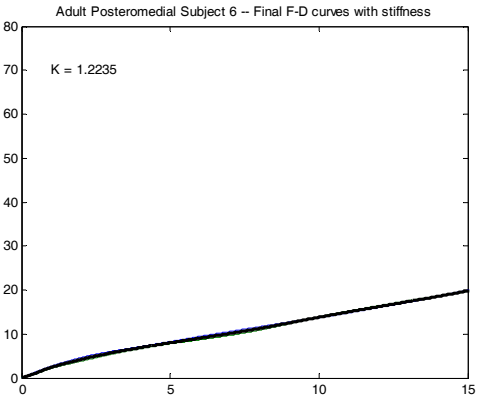

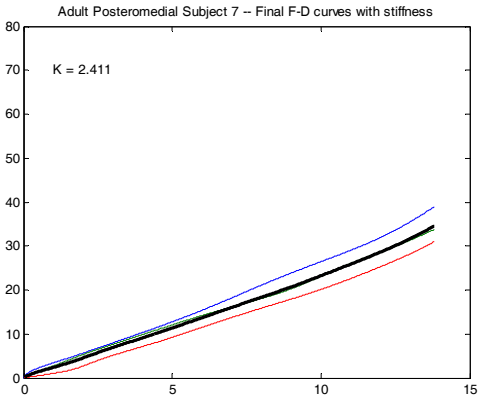
Adult Posteromedial Subject 7 -- Final F-D curves with stiffness
K = 2.411
80
70
60
50
40
30
20
10
0
0
5
10
15

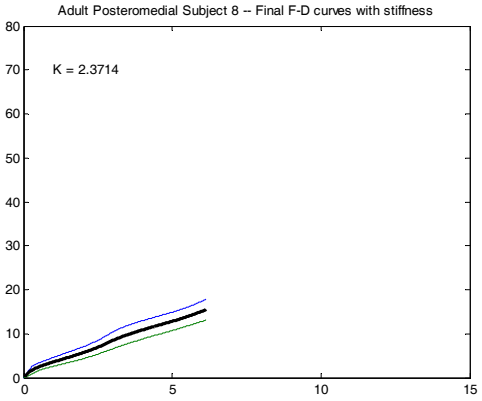
Adult Posteromedial Subject 8 -- Final F-D curves with stiffness
K = 2.3714
80
70
60
50
40
30
20
10
0
0
5
10
15

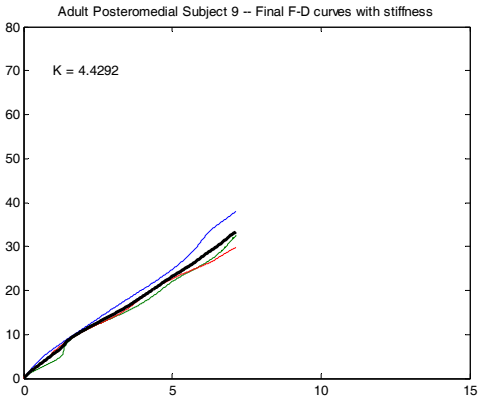
Adult Posteromedial Subject 9 -- Final F-D curves with stiffness
K = 4.4292
80
70
60
50
40
30
20
10
0
0
5
10
15

Relaxed 10YO Posteromedial F-D Curves

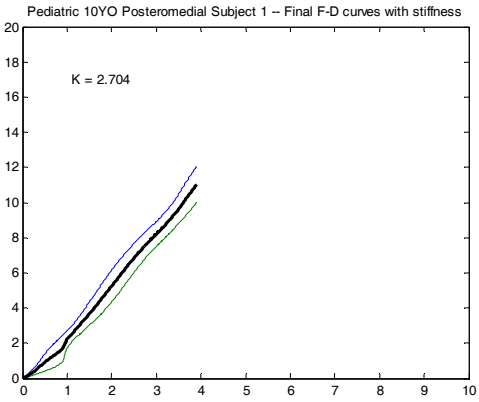

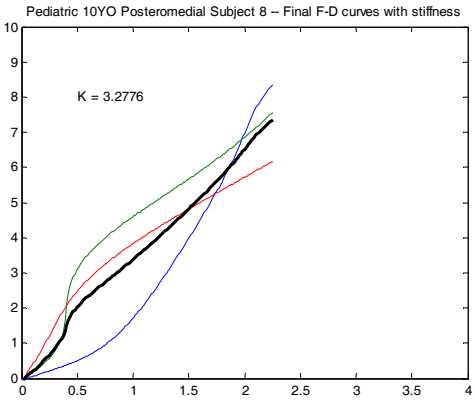

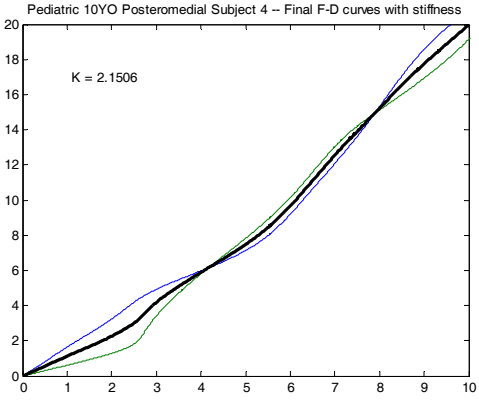

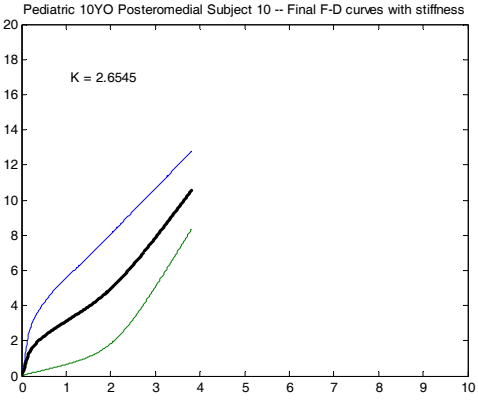

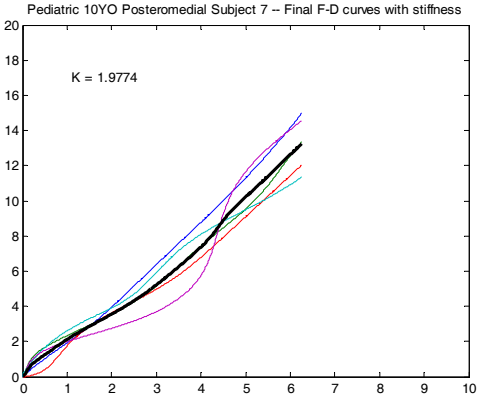

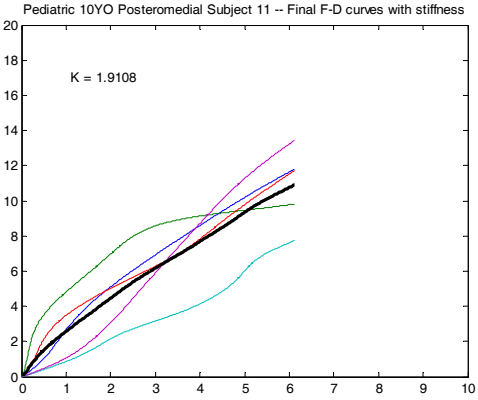

Relaxed 6YO Posteromedial F-D Curves

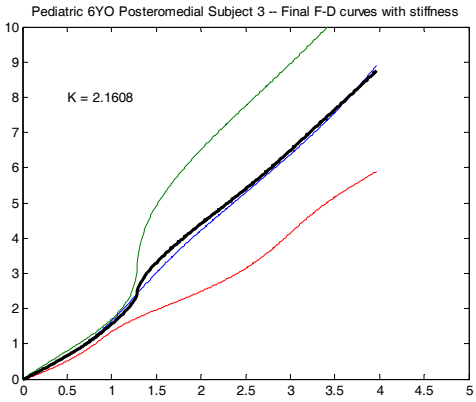

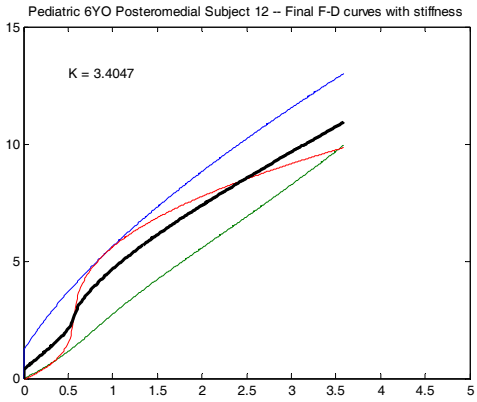

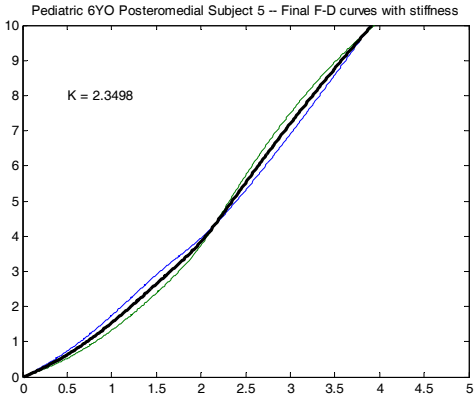

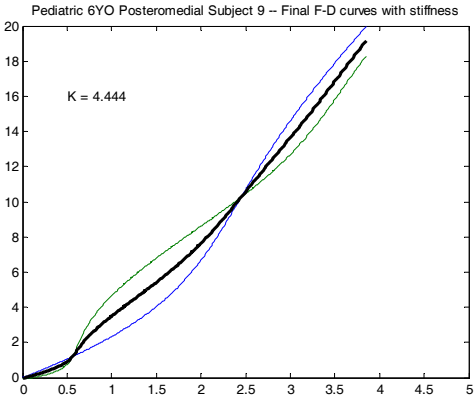

Tensed Adult Posteromedial F-D Curves

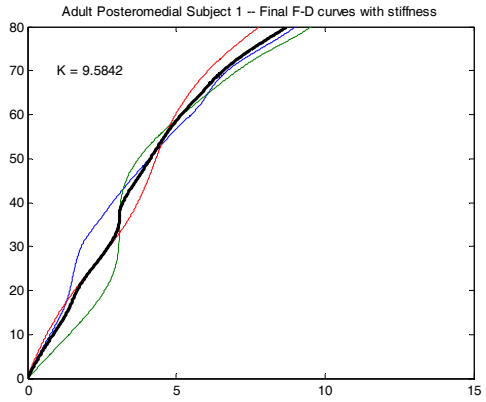

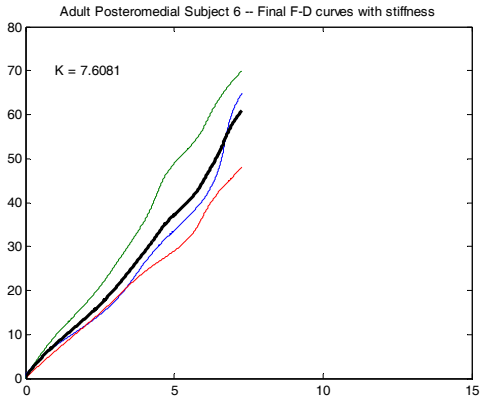

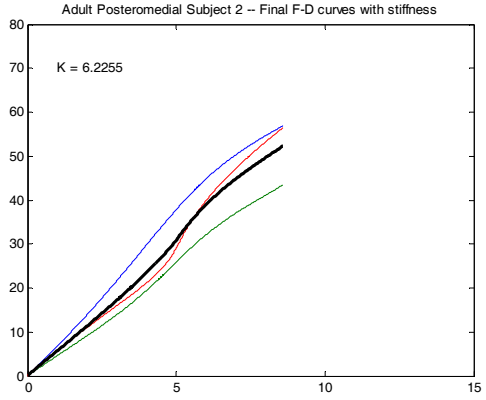

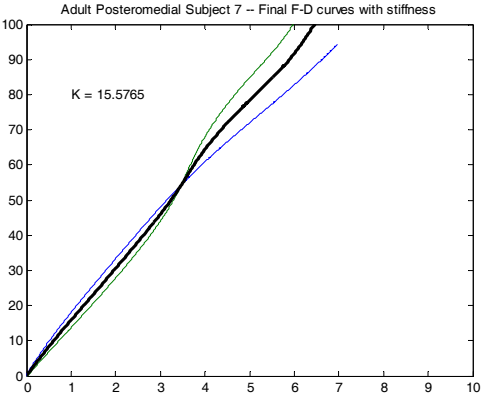

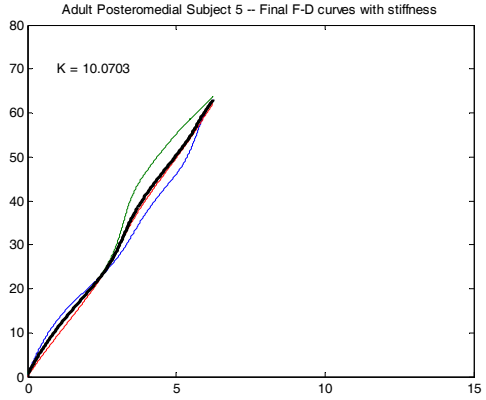

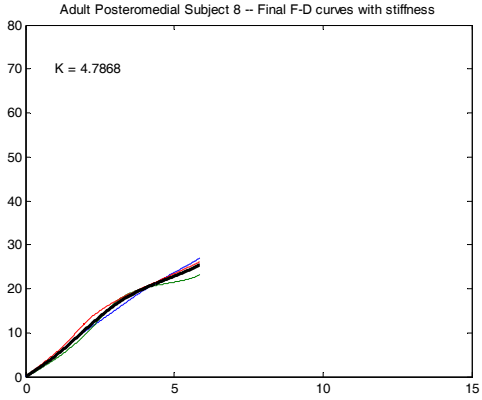

Tensed 10YO Posteromedial F-D Curves

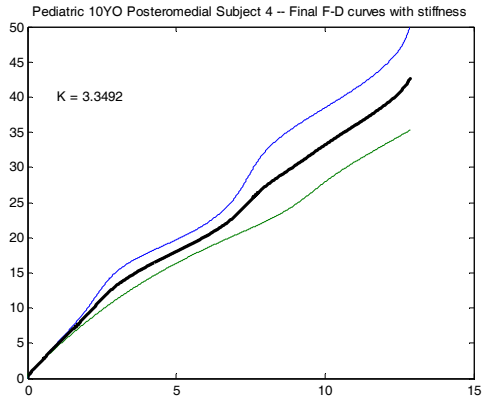

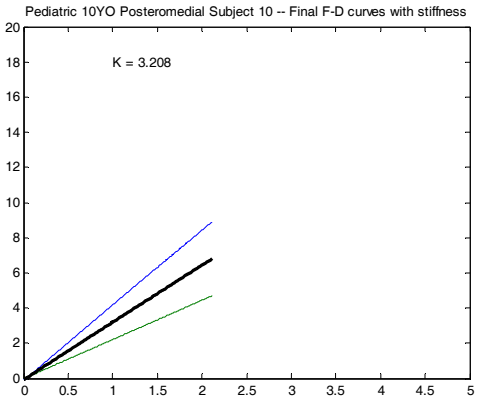

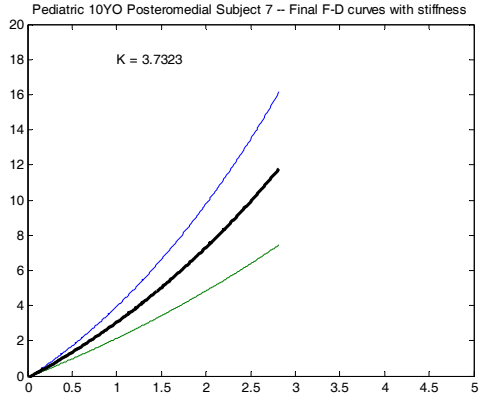

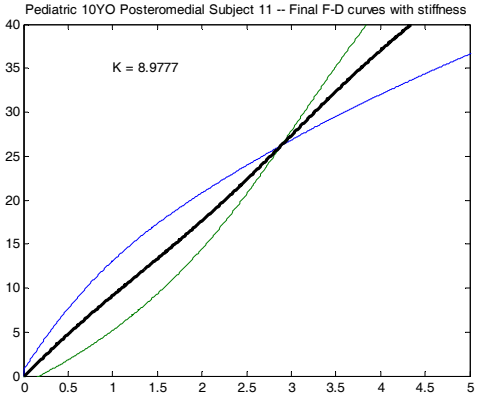

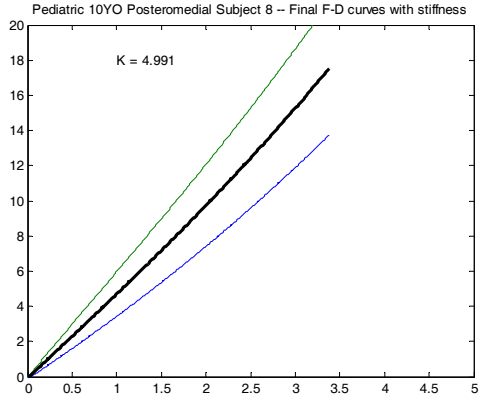

Tensed 6YO Posteromedial F-D Curves

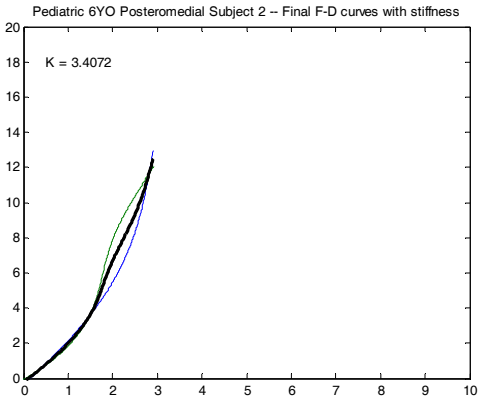

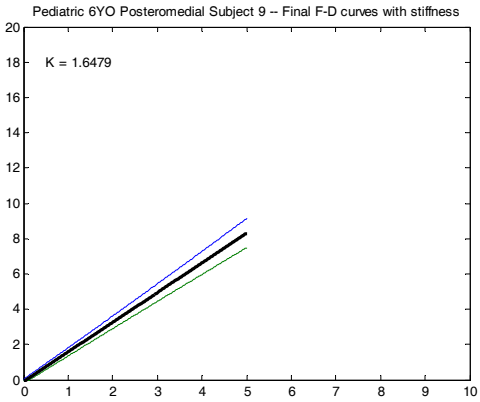

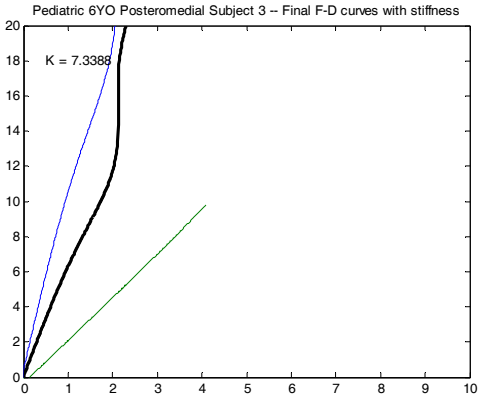

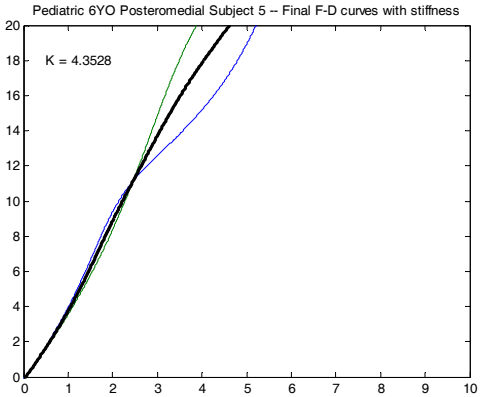

APPENDIX B

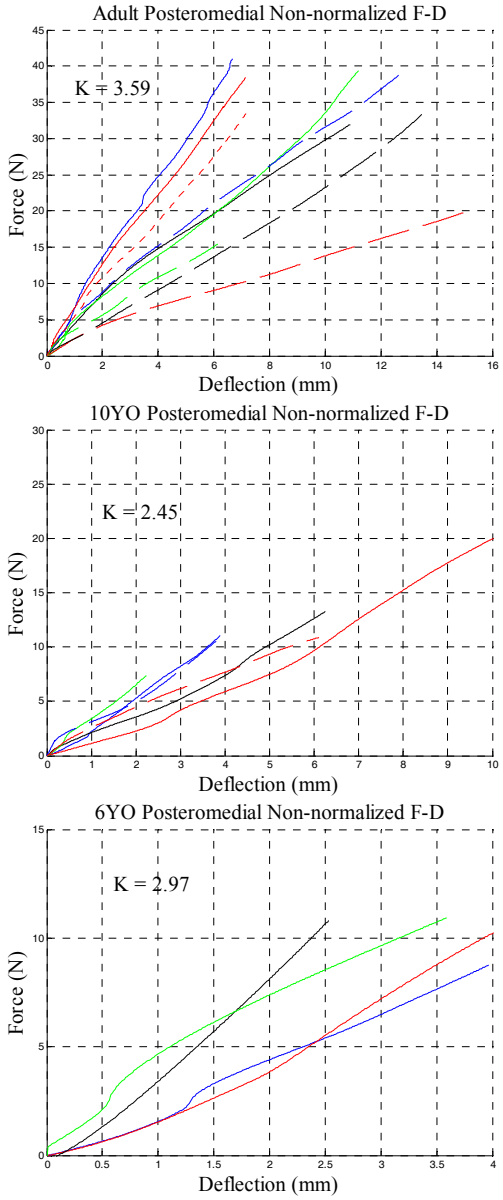

Figure B1. Non-normalized force-deflection curves for the 50th percentile adult male, 10 year old, and 6 year old in the relaxed posteromedial loading condition.

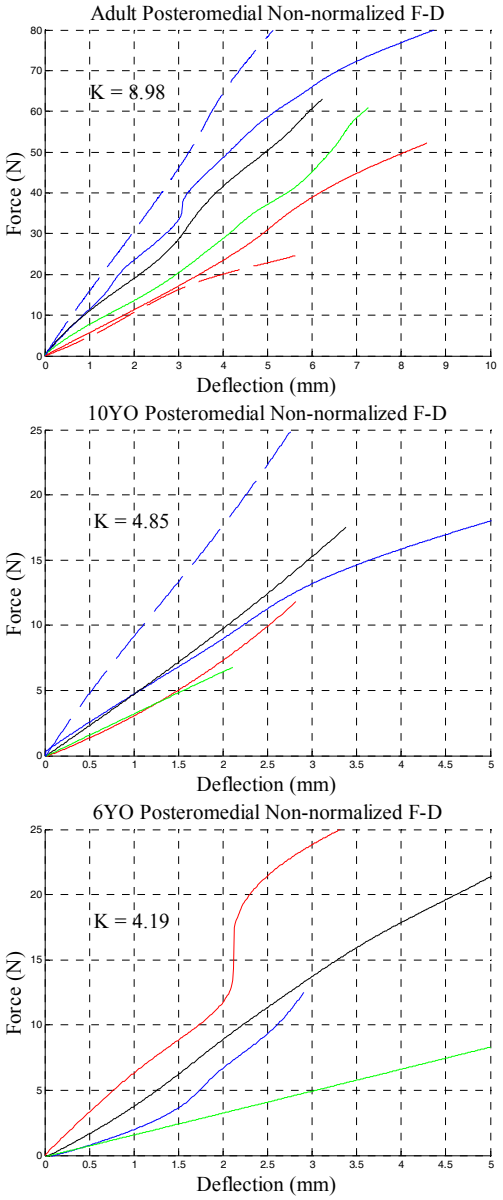

Figure B2. Non-normalized force-deflection curves for the 50th percentile adult male, 10 year old, and 6 year old in the tensed posteromedial loading condition.

APPENDIX C

Table C1.
Maximum %MVC values for a subject in each age group in both the relaxed and tensed test conditions

	Adult		10YO		6YO	
	Relaxed	**Tensed**	**Relaxed**	**Tensed**	**Relaxed**	**Tensed**
Latissimus Dorsi	6.29	37.29	11.62	41.15	30.92	14.05
Upper Trapezius	2.35	29.90	13.36	3.32	2.55	2.98
Anterior Deltoid	1.15	13.57	13.80	4.24	46.91	51.36
Posterior Deltoid	2.37	27.74	5.47	26.04	4.27	7.62
Biceps Brachii	1.40	10.96	3.35	3.37	4.55	3.22
Pectoralis Major	5.49	14.12	8.26	17.21	11.97	41.11
Average %MVC	**3.18**	**22.26**	**9.31**	**15.89**	**16.86**	**20.06**

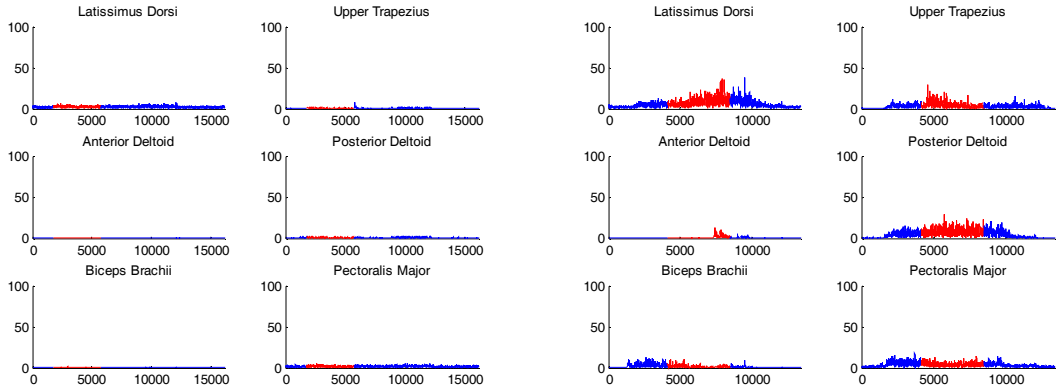

Figure C1. Plot of relaxed (left) and tensed (right) EMG signals for an adult subject. The y-axis represents a percentage of maximum voluntary contraction. The x-axis represents time (ms). The area highlighted in red is the interval in which a load was applied to the shoulder.

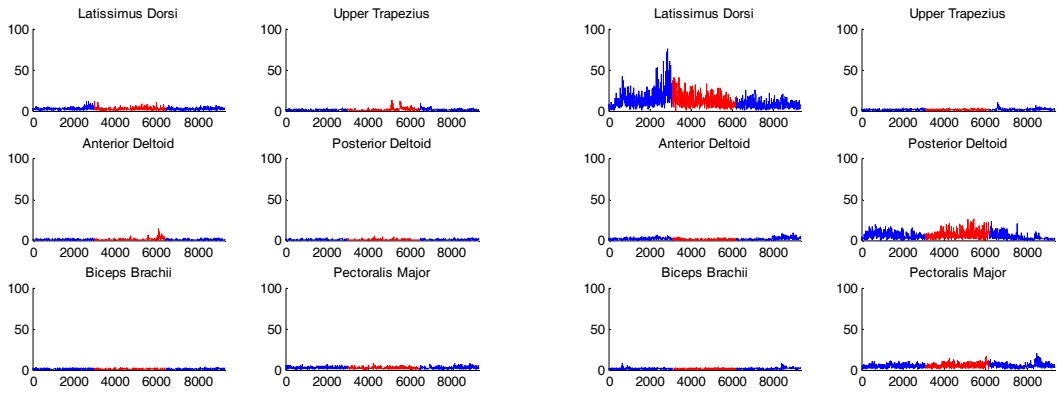

Figure C2. Plot of relaxed (left) and tensed (right) EMG signals for a subject in the 10 year old age group. The y-axis represents a percentage of maximum voluntary contraction. The x-axis represents time (ms). The area highlighted in red is the interval in which a load was applied to the shoulder.

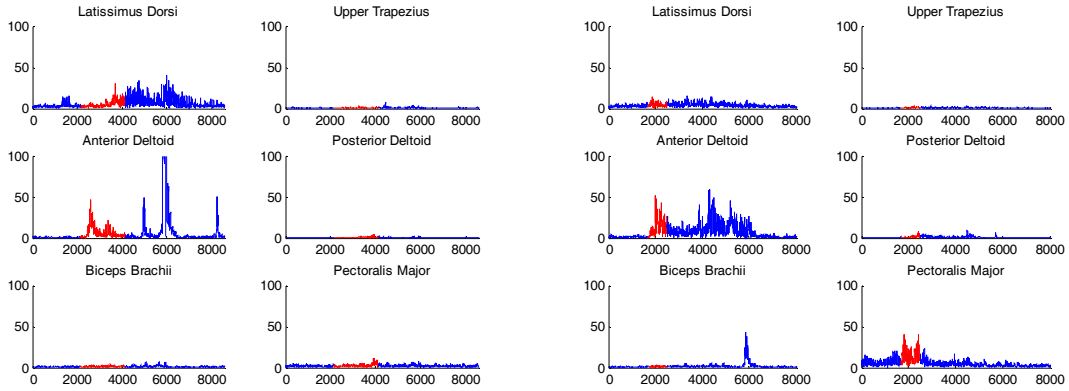

Figure C3. Plot of relaxed (left) and tensed (right) EMG signals for a subject in the 6 year old age group. The y-axis represents a percentage of maximum voluntary contraction. The x-axis represents time (ms). The area highlighted in red is the interval in which a load was applied to the shoulder.

DETAILED ANALYSIS OF 3D OCCUPANT KINEMATICS AND MUSCLE ACTIVITY DURING THE PRE-CRASH PHASE AS BASIS FOR HUMAN MODELING BASED ON SLED TESTS

Stefan Kirschbichler
Wolfgang Sinz
Graz University of Technology, Vehicle Safety Institute, Austria
Adrian Prüggler
Philipp Huber
Kurt Steiner
Virtual Vehicle Research and Test Center, Austria

ABSTRACT

Today, human models are frequently used for improvements in occupant and pedestrian protection. The models have been carefully prepared with respect to anthropometric and biomechanical validity but do not include muscle activity.

Hence, primary safety issues cannot be addressed by the model, since during low loading the model is not stabilized by muscles. Therefore, the OM4IS ("Occupant Model for Integrated Safety") project was initiated by a large consortium including scientific (Virtual Vehicle Research and Test Center, Graz University of Technology, Bundesanstalt für Straßenwesen BASt) and industry (PDB, Bosch, Toyoda Gosei Europe, TRW, DYNAmore GmbH) to examine muscle activity from volunteer tests and implement the results in a human model. The second aim is to find movement patterns which will be integrated in the simulation to develop active restraint systems.

The main focus in this project is set on two different driving maneuvers. The first one is an emergency braking maneuver the second one is a lane change maneuver. In a first step these two maneuvers were simulated with sled tests and later these maneuvers had been carried out with a real vehicle on a test track. The purpose of the sled tests was to generate first input data for the numerical simulation and to check if it is possible to measure necessary information without vehicle tests. A seat was fixed on a sled and accelerated longitudinally to simulate the emergency braking maneuver and afterwards turned by 90 degrees to simulate lateral loading.

In total eleven volunteers, weight and height correlated to the 50% male, were tested and analyzed. Kinematic analyses were performed using two different motion capturing systems, one infrared based system and one high-speed video system. Two different systems were chosen to evaluate the adaptability for vehicle tests.

Additionally muscle activity was measured with surface EMG (Electromyography) for upper body muscles.
First results showed a significant difference among volunteers. Repeated tests with the same volunteer showed minor differences. Movement patterns varied significantly between different tests. Detailed information concerning simulation is presented in a separate paper [7].

INTRODUCTION

Today`s restraint systems are developed with different crash tests and simulations. Mostly these tests are evaluated with dummies and dummy models. Integrated vehicle safety is also a challenge for simulation models. Human models like THUMS [9], HUMOS [10] or as included within MADYMO [11] are used increasingly for these research purposes. THUMS for example is used for pedestrian and occupant safety. But the improvement of occupant safety and pedestrian safety is an ongoing challenge to update existing human models. Furthermore different crash scenarios need to be analyzed and for the development of new active restraint systems the kinematics of occupants before the crash is interesting. To obtain correct position information of occupants it is necessary to assess typical movements of humans for various scenarios. For these patterns the function of muscles is a relevant part.
Most of the currently available human models are validated by means of high impact PMHS tests neglecting muscle activation and low impact situations [1]. But for the above mentioned movement patterns the muscle activity is a necessary component. A common measurement system for muscle analysis is surface EMG which is often used for biomechanical topics [2]. Praxl et al. [3] showed significant differences in the kinematics during a rollover scenario comparing the behavior of a dummy model with the overall kinematics of a passive human deformable facet model provided by MADYMO. Also Adamec et al. [4] showed differences between different dummies

and volunteer sled tests. Ejima et al. [5] conducted sled tests with five volunteers, three male and two female. They analyzed the kinematics and muscle characteristics and found that the difference in muscle activity governs the motion based on the acceleration and EMG electrodes. The study showed that depending on the location of the muscle the reflextime varied. M. latisimus dorsi and paravertebral muscles were mainly activated and reflex time of head, neck and torso muscles was around 70 ms to 200 ms. Begeman et al. [6] also did a study with low impact tests. He identified a reaction time from 50 ms to 150 ms and that the tone of the lower extremity muscles changed the occupant's dynamics.

TEST SETUP

The main focus was on the pre-crash phase for two different driving maneuvers. To cover the basic movement directions the emergency braking maneuver and lane change maneuver were simulated with sled tests.

Sled Design

For these tests a test vehicle (Figure 1) was constructed. The vehicle had standard car tires and a hydraulic braking system. On the vehicle a frame for the camera systems was mounted.

Figure 1. Sled design for the lane change simulation

Also a simplified seat without cushion was fixed on the vehicle (referred to as sled). The seat frame was taken from a serial production seat, only the cushion was removed. For the seating area wooden plates covered with leather were used. These modifications were done in order to eliminate the influence of the seat cushion and therefore simplify the boundary conditions for the simulation.

Realization

The sled was accelerated longitudinally to simulate the emergency braking maneuver. Due to the fact that the sled could only be controlled in one direction the seat had been mounted backwards for this maneuver (Figure 2). Afterwards the seat was turned perpendicular to the acceleration direction to simulate the lateral loading.
In order to constrain the movement a fixed lap belt was used, such that there was minimal movement in the pelvis area. This procedure was chosen to provide well defined boundary conditions for the simulation. Additional support by a 3 point belt complicates the identification of movement patterns, which was another reason for choosing the lap belt.
Furthermore the volunteer did not get any information about the start of the maneuver because the task was to measure the pure reaction of the volunteer during unanticipated acceleration.

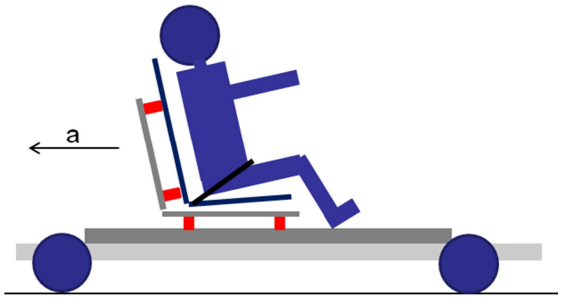

Figure 2. Principle test setup with direction of acceleration a

The acceleration was measured in the center of the vehicle and was analyzed from the start point up to the point where the acceleration started to decrease. This interval was used as input for the simulation. The acceleration characteristic depends on the automatic control of the crash test facility and the decrease of the acceleration was significant after 500 ms. The acceleration data after 500 ms was not important for the analysis.
Three frontal tests with a maximum acceleration of 0.8 g (Figure 3) and three lateral tests with a maximum acceleration of 0.5 g (Figure 4) were performed with each volunteer. Each test was repeated twice because the influence of the anticipated maneuver also was interesting for the project.

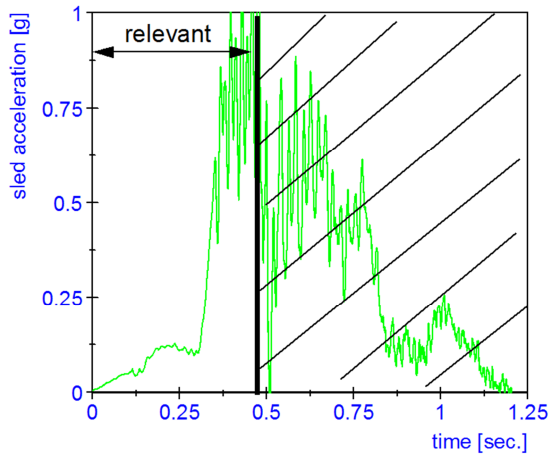

Figure 3. Sled acceleration frontal test

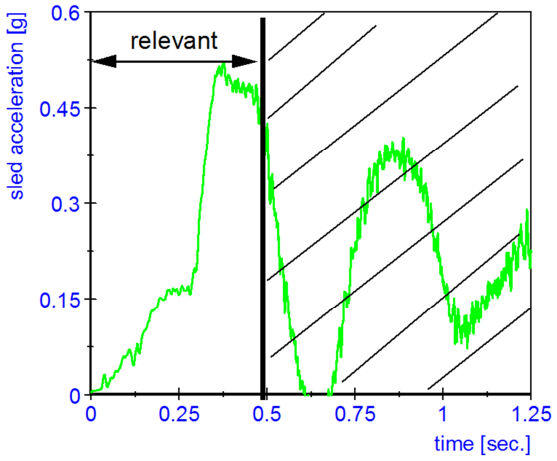

Figure 4. Sled acceleration lateral test

The specific acceleration characteristics were chosen due to safety reasons and to mimic accelerations in the full vehicle tests.

Volunteer

The body size and anthropometric data of the volunteers corresponded to the 50% male (175cm height, 78kg weight, Table 1).

volunteer	height [cm]	weight [kg]
volunteer 1	178	75
volunteer 2	186	75
volunteer 3	175	74
volunteer 4	173	69
volunteer 5	180	75
volunteer 6	183	80
volunteer 7	172	70
volunteer 8	185	80
volunteer 9	174	71
volunteer 10	180	70
volunteer 11	181	71
average	179 (+/-5)	74 (+/- 4)

Table 1. Volunteer height and weight

Measurement Systems

The kinematic analysis was performed using two different 3D motion capturing systems. An infra-red based system (VICON [14]) and a standard optical high-speed video system (WEINBERGER [15]) were used. Four volunteers were measured with the infrared based system and seven volunteers with the standard high-speed video system.

Infrared based motion capturing system Cameras with infrared strobes recorded images of passive markers, small spherical objects, wrapped with retro-reflective foil, attached to the subject's body and to the surrounding structure. A calibration process was performed prior to the experiments, where a known geometric structure was recorded by all cameras. Thereby the camera positions, orientations and lens parameters could be determined. The system consisted of 8 cameras set to a strobe frequency of 100 Hz. The advantage of the infrared system is that there is no need for additional lighting. The system allowed capturing around 50 markers simultaneously. A very tight suit was used, which led to marginal displacements due soft tissue movement. The same markers were used for frontal test and lateral tests (Figure 5).

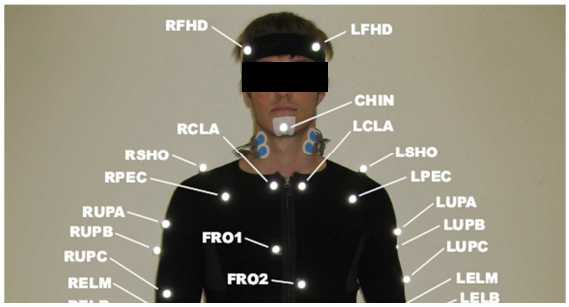

Figure 5. Targets infrared system (frontal and lateral tests)

One handicap of the system is that only the trajectories of the targets are recorded and can therefore be visualized. For a real video an additional digital camera is necessary.

High-speed video system In this system two high-speed cameras have been used. The system allows the use of more cameras but due the fact that the sled was only accelerated in one direction and the upper part of the body was of interest two cameras were sufficient. The captured frequency was 1000 Hz. A calibration process was performed prior to the experiments, with the so called FALCON CamFolder procedure [12]. To record 3D kinematics it was necessary that each target was recorded by both cameras. Targets were only put on the most important points of the body. For the frontal and the lateral test two sets of targets were used. Three targets on the head, one on the

shoulder, elbow, wrist joint, hip and the knee were measured in the frontal test, see Figure 6 and 7.

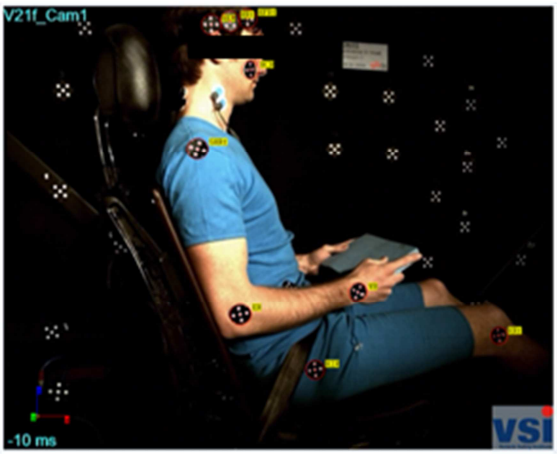

Figure 6. Targets high-speed video system frontal tests

In addition to these two more targets in the thorax area were recorded for the lateral test (Figure 7).

Figure 7. Targets high-speed video system lateral tests

An advantage of this system is that a real video is generated, while the drawback is that powerful additional lighting is needed.

Surface EMG Muscle activity was measured with a TeleMyo 2400T surface EMG measurement system by NORAXON [13]. The system transmitted real-time EMG by wireless transmission. The recorded frequency was 1000 Hz. Seven different upper body muscles were chosen to be captured, the same ones on the left and right side of body. The same set of muscles was recorded for the braking and the lane change simulation.
On the frontal side the muscles Sternocleidomastoideus, Rectus abdominis and the Obliquus externus abdominis were analyzed, see Figure 8.

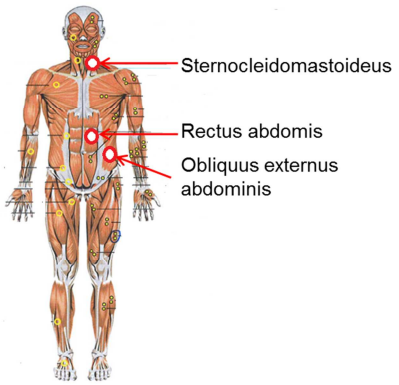

Figure 8. Muscle frontal view (mod. from [8])

On the dorsal side the muscles Neck extensors, Trapezius p. descendez, Latissimus dorsi and the Erector spinae (lumbar region) were measured (Figure 9).

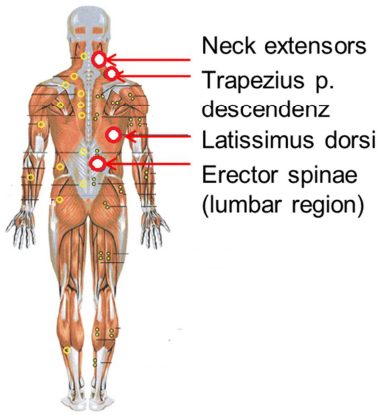

Figure 9. Muscle dorsal view (mod. from [8])

The main purpose of these sled tests was to get first kinematic information of the volunteer's movement for the two maneuvers. Additionally the muscle activities during the different maneuvers were analyzed. Another task was to decide which motion capturing system was the more efficient one to use in a full vehicle test.

RESULTS

High-speed video system In the following figures the motions of different targets and volunteers are represented. In Figures 10-14 the red graph shows the relative trajectory of the volunteer with the largest movement, while the green graph is the relative trajectory of the volunteer with the smallest movement. The gray graphs show the trajectories of the remaining volunteers.
In Figure 10 the motion of the head target of all seven volunteer can be seen. A big difference in the movement among the volunteers was noted. A

maximum amplitude of 500 mm (x-direction, parallel to the acceleration direction) and 140 mm (z-direction, parallel to gravity) was recorded during the frontal test, while the minimum amplitude was 118 mm (x) and 10 mm (z).

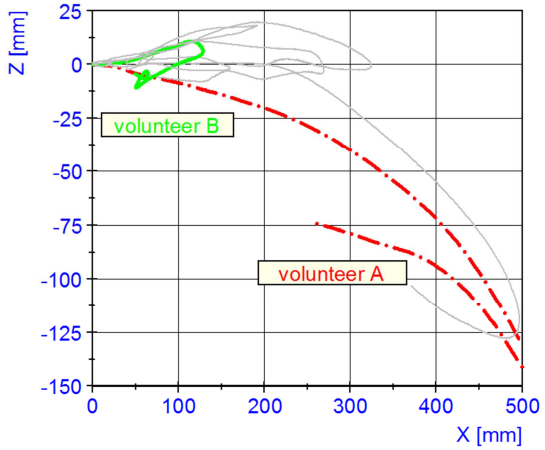

Figure 10. Head trajectory frontal test

Also the shoulder target movement (Figure 11) showed a large difference among the subjects. A maximum amplitude of 390 mm (x) and 47 mm (z) was recorded, while the minimum amplitude was 100 mm (x) and 22 mm (z).

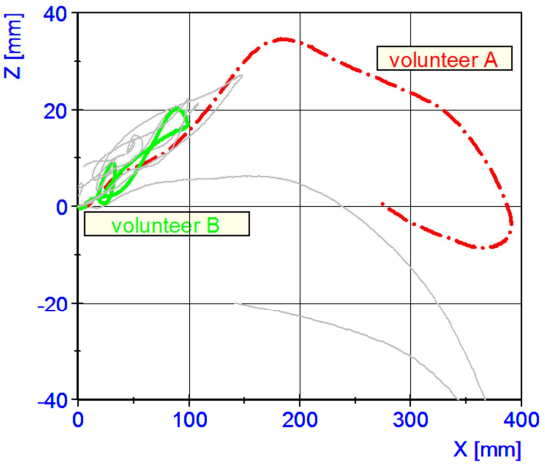

Figure 11. Shoulder trajectory frontal test

For the lateral test three targets were analyzed. The head target (Figure 12) showed amplitudes between 175 mm (x), 30 mm (z) and 90 mm (x) and 5 mm (z).

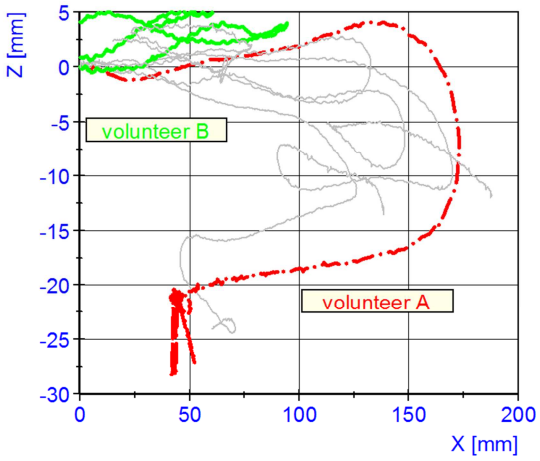

Figure 12. Head trajectory lateral test

Figure 13 shows the relative shoulder marker trajectories. Measured amplitudes ranged between 130 mm (x), 30 mm (z) and 65 mm (x), 15 mm (z).

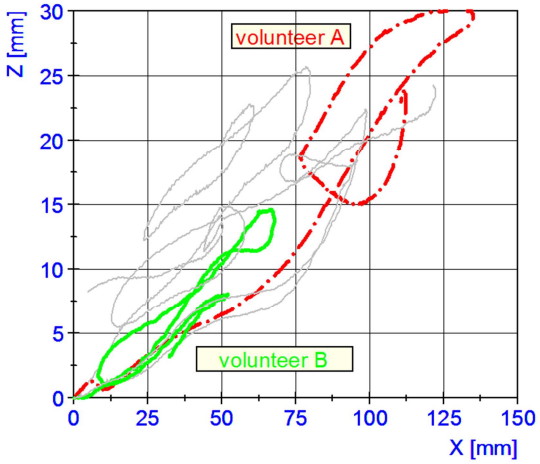

Figure 13. Shoulder trajectory lateral test

For the lateral test additional sternum targets (Figure 14) were recorded. Here a maximum amplitude of 125 mm (x) and 12 mm (z) was recorded, while the minimum amplitude was 55 mm (x) and 3 mm (z).

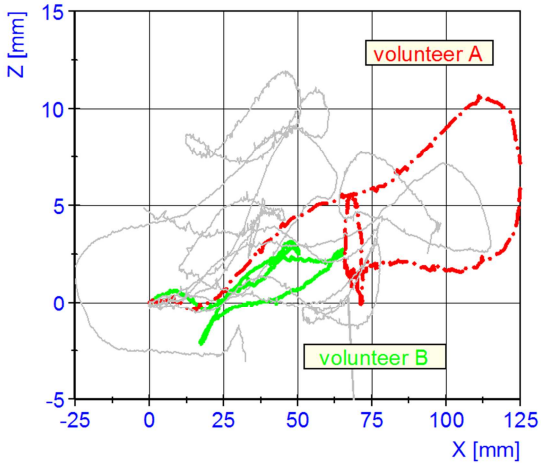

Figure 14. Sternum trajectory lateral test

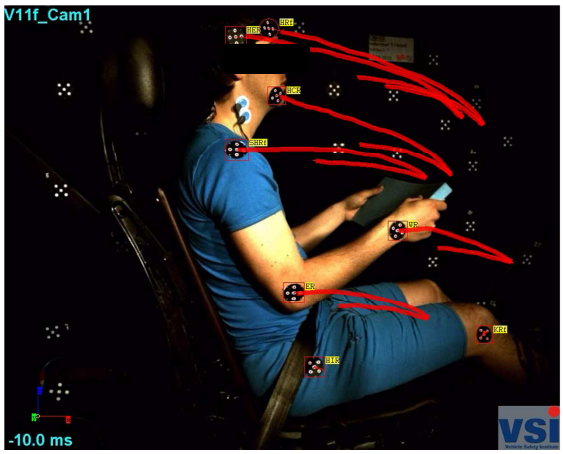

Figure 15. Trajectories high-speed video system

In Figure 15 the movement of the different targets during the first trial can be seen. Although three trials per volunteer per test were recorded, the analysis concentrated on the initial recording of each test due to time constraints.

Infrared based motion capturing system Four volunteers were captured with this system. As more targets were attached and recorded, there was more information about the volunteer's movement available. In order to visualize the movement positions of adjacent targets were connected by lines.

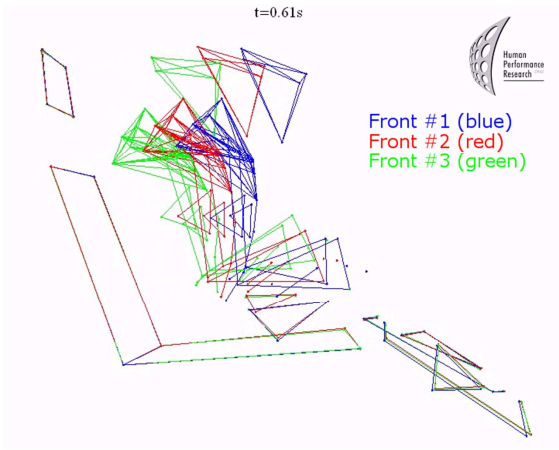

Figure 16. Infrared system frontal test

Figure 16 shows the position of one volunteer during repeated emergency braking simulations at the same time after the maneuver started. For this volunteer the amplitudes of the forward motion decreased with each repetition. An underlying reason for this might be an exercise effect, although not all volunteers showed the exactly same behavior.
Figure 17 displays the three lateral load cases for one volunteer. Unlike the frontal case no significant differences in amplitudes were found among the volunteers. This hints to a different countermovement mechanism than in the frontal case.

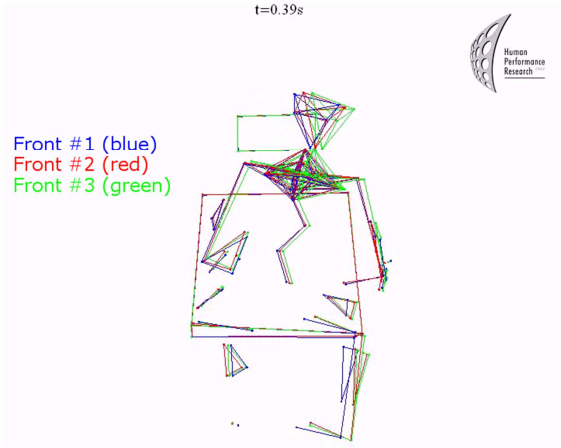

Figure 17. Infrared system lateral test

Using an inverse kinematic model the 3D marker data was used to estimate hip and neck angles, which were then input into the simulation model [7].

Surface EMG In addition to the kinematic measurement EMG data was recorded.

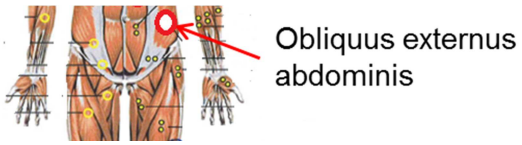

Figure 18. Muscle Obliquus externus abdominis (mod. from [8])

In Figure 19 signals from one selected muscle (Obliquus externus abdominis, see Figure 18) are displayed for the three frontal trials of one volunteer. The peak signal of each repetition is marked in the graph.

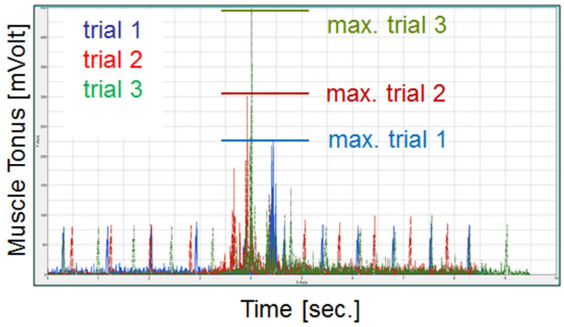

Figure 19. EMG signal of muscle Obliquus externus abdominis

For this volunteer a correlation between the peak signal in the muscle Obliquus externus abdominis (Figure 18) and the movement amplitudes (see Figure 16) is observed.
Such a correlation cannot be found for each muscle. In Figure 21 the recorded signal of the muscle neck

extensor (Figure 20) is displayed. Again the peak signals of each trial are marked in the graph (Figure 21), but here no correlation to the movement (Figure 16) can be established.

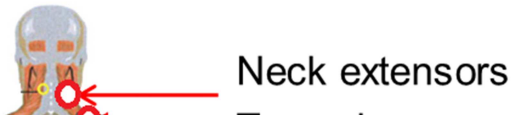

Figure 20. Muscle neck extensors (mod. from [8])

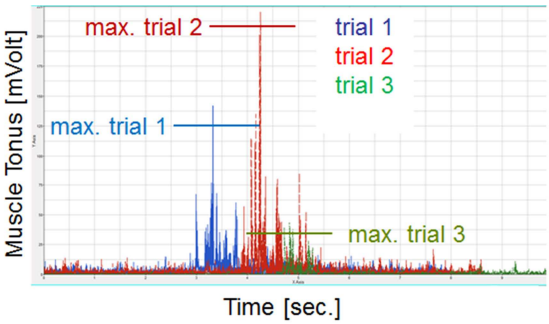

Figure 21. EMG signal of muscle neck extensors

In summary for eleven volunteers no significant correlation between EMG peak signals and movement amplitudes was detected. For further analysis activation onset and duration will be considered.
The character of the movement varies between the volunteers. Note that only the kinematic information from the first frontal and lateral test was used because the analyzed videos showed differences by repeating the load case and the simulation model should reflect the reaction of volunteer.

CONCLUSIONS

In the conducted sled test kinematic data was recorded with two 3D motion capturing systems. The captured data of both systems was of sufficient accuracy to act as input data for the simulation. Due to the additional lighting needed for the high-speed video system the infrared-based system was preferred for the full vehicle tests performed later on.
The first analysis of target trajectories showed large inter-subject differences, not only in the amplitudes, but also in the characteristics of the entire movement. Furthermore significant intra-subject differences in the movement amplitudes were detected for the frontal tests, while for lateral tests no such observation was identified. Due to these findings no movement patterns could be defined with the analyzed quantities.
The quality of EMG-signals was also adequate but for the sled test a correlation between movement and EMG peak signals could not be detected.

OUTLOOK

Volunteer tests with a real vehicle as part of the project were conducted and will be presented in a separate publication later on. Like in the sled tests two different maneuvers, an emergency braking and a lane change maneuver, were performed. The body size of the volunteers corresponded to the 50% male (175cm height, 78kg weight). Kinematic data was measured with the infrared based system and additional EMG data was recorded. Maneuvers with a large number of volunteers were recorded and the experienced loads were closer to real world driving situations than the sled test. Thereby the pool of available data for the numerical simulation was extended significantly. Analysis of the full vehicle experiments is in progress and will be presented in the future.

ACKNOWLEDGEMENT

The authors would like to acknowledge the financial support of the "COMET K2 - Competence Centres for Excellent Technologies Programme" of the Austrian Federal Ministry for Transport, Innovation and Technology (BMVIT), the Austrian Federal Ministry of Economy, Family and Youth (BMWFJ), the Austrian Research Promotion Agency (FFG), the Province of Styria and the Styrian Business Promotion Agency (SFG).
We would furthermore like to express our thanks to our supporting industrial and scientific project partners, by names in alphabetical order: Bundesanstalt für Straßenwesen-BASt (DI Andre Eggers), Robert Bosch GmbH (Dr.-Ing. Gian Antonio D'Addetta), DYNAmore GmbH (Dr.-Ing. Dirk Fressmann), Daimler AG (DI Christian Mayer), BMW Group (Dr. Katja von Merten; DI Philipp Wernicke), TRW Automotive (DI(FH). Thomas Herpich; DI Simon Kramer), Toyoda Gosei Europe (Dr.-Ing. Jörg Hoffmann; DI Michael Freisinger), Partnership for Dummy Technology and Biomechanics (Dr. Norbert Praxl); Graz University of Technology, Vehicle Safety Institute (Univ.-Prof. Dipl.-Ing. Dr. techn. Hermann Steffan), Institute of automotive engineering (Univ.-Doz. Dr. techn. Arno Eichberger), Ludwig-Maximilians-Universität Munich (Dr.-Ing. Steffen Peldschus).

REFERENCES

[1] H. Muggenthaler, J. Adamec, N. Praxl, M. Schönpflug (2005). The Influence of Muscle Activity on Occupant Kinematics. International

IRCOBI Conference on the Biomechanics of Impact, Prague (Czech Republic) September 2005.

[2] De Luca C.J. (1997). The Use of Surface Electromyography in Biomechanics. Journal of Applied Biomechanics, 13 (2): 135-163.

[3] N. Praxl, M. Schönpflug, J. Adamec (2003). Application of Human Models in Vehicle Rollover.: 18th International Technical Conference on the Enhanced Safety of Vehicles (ESV), Montreal (Canada) June 2003.

[4] Adamec J., Praxl N., Miehling T., Schönpflug M.(2005). The Occupant Kinematics in the first Phase of a Rollover Accident – Experiment and Simulation. International IRCOBI Conference on the Biomechanics of Impact, Prague (Czech Republic) September 2005.

[5] Ejima S., Ono K., Holcombe S., Kaneoka K., Fukushima M. (2007). A Study on Occupant Kinematics Behavior and Muscle Activities during Pre-Impact Braking Based on Volunteer Tests. International IRCOBI Conference on the Biomechanics of Impact, Maastricht (Netherlands) September 2007.

[6] Begeman P.C., King A.I., Levine R.S. (1980). Biodynamic Response of the Musculoskeletal System to Impact Acceleration. SAE World Congress.

[7] Prüggler et al. (2011) Manuscript to be submitted to the 22nd International Conference on ESV, June 13-16. Washington, USA

[8] Konrad Peter EMG – FIBEL. Eine praxisorientierte Einführung in die kinesiologische Elektromyographie. Version 1.0 September 2005.

[9] Article published on March 15, 2011. "Total Human Model for Safety (THUMS)." URL-http://www.toyota.com/esq/articles/2010/THUMS.html

[10] Stéphane Robin. HUMOS - Human Model for Safety – A Joint Effort towards the Development of Refined Human-like Car Occupant Models
LAB PSA Peugeot-Citroën RENAULT, France
Paper Number 297.

[11] MADYMO Product Suite URL-http://www.tass-safe.com/en/products/madymo. Accessed on March, 15 2011.

[12] FalCon extra CamFolder URL-http://www.falcon.de/falcon/ger/camfolder.htm. Accessed on March 15, 2011.

[13] Surface EMG system NORAXON. URL-http://www.noraxon.com/index.php3. Accessed on March, 15 2011.

[14] Motion Capture Systems from Vicon. URL-http://www.vicon.com/. Accessed on March 15, 2011.

[15] Weinberger High Speed Camera. URL-http://www.weinberger-service.com. Accessed on March 15, 2011.

DEVELOPMENT OF A FINITE ELEMENT PAM-CRASH MODEL OF HYBRID III ANTHROPOMORPHIC TEST DEVICE WITH HIGH FIDELITY

Xinghua Lai[1]
Yongning Wang[2]
Qing Zhou[1]
Zhe Lin[1]
Pierre Culiere[2]
[1]State Key Laboratory of Automotive Safety and Energy,
Department of Automotive Engineering, Tsinghua University, China
[2]ESI Group, France
Paper Number 11-0031

ABSTRACT

Prior studies indicate that a majority of Hybrid III dummy models are validated over a limited range of loading velocities in accordance with the specification of CFR 49 Part 572. The shortcoming is that the dummy model response, based on validation at regulatory velocities, may not correlate well with experiments when loaded at different velocities. The fidelity of models at an extended range of velocities is important, as in car crash tests dummies are frequently exposed to a variety of loading conditions in terms of loading type and loading velocity, which are differing from that of the Hybrid III standard certification tests.

In this study, a finite element model of Hybrid III 50th percentile dummy with high-fidelity response is developed using the non-linear finite element code PAM-CRASH. The methodology implemented for the model development is presented, with particular focus on material calibration and validation of the model against experimental data at different structure levels (component level, sub-system level, and system level), under a wide range of loading velocities. In addition to compliance with the typical certification requirements, the developed model has reasonable correlations with the physical dummy for a series of loading conditions. The model response has proven to be robust and reliable while maintaining computational efficiency, showing good potential to be used for accurate prediction of occupant injury numbers in crash simulation.

INTRODUCTION

Anthropomorphic test devices (ATDs) are designed to approximate human physical characteristics and mechanical response under impact loading[1]. Vehicle safety related regulation requires use of crash test dummies for the evaluation of vehicle crashworthiness and occupant protection within the automotive industry. Among various dummies meeting diverse need, the Hybrid III 50th percentile male dummy is the most commonly used ATD. In 1986, the Hybrid III dummy was specified as the standard front impact test dummy for FMVSS 208 by the National Highway Traffic Safety Administration (NHTSA). Currently, the dummy is extensively used worldwide for front impact tests on evaluation of restraint-system effectiveness to protect occupants and meet regulations[2].

With growing performance of computer hardware and analytical software, finite element (FE) simulations play a significant role in the field of automotive crash safety research and development. Use of finite element modeling approach provides fast insight into the performance of systems in great detail, and thus largely shortens the development period of the vehicle model. At present, diverse computer models of test devices (dummies, barriers, …) are already developed and routinely used for crash simulation[3][4]. The dummy models, as an indispensible part of a car crash model, allow efficient evaluation of restraint-system effectiveness. To date, crash simulation users demand increasingly higher dummy model quality, for accurate prediction of the injury risk to occupants. An essential feature for such dummy models is the fidelity, which means to what extent the model response is correlated to the hardware.

In the practice of dummy model development, the minimum requirement for the Hybrid III model is compliance with the standard certification tests as specified in the CFR 49 Part 572. However, the loading velocities in the regulatory certification tests are within a very limited range. The shortcoming is that the performance of the model, based on validation at limited range of regulatory velocities, may not always give satisfactory results in simulations at different velocities[5]. It was suggested that validation tests should be conducted under wide range of strain rates and in deformation ranges typical of loading conditions for dummies in vehicle crash[6]. Therefore, in addition to

compliance with the regulation, the performance of the dummy model could be further improved through a larger scale validation against experiments with the physical dummy tested at different structural levels under wide range of loading velocities. Previous studies indicate that, a majority of dummy models are merely validated in accordance with the dummy regulation[7][8][9]. While there is the practice of validation of the dummy model under multiple loading velocities, the velocity range at the sub-system level is not wide enough[10][11].

In this paper, a finite element model of Hybrid III dummy with high fidelity and robust response is developed using the nonlinear finite element code PAM-CRASH[12][13]. The dummy model is constructed in great detail in terms of physical characteristics to accurately represent the hardware. Material properties of the model are optimized to represent the mechanical behavior of the hardware through validations at different structure levels and loading velocity levels. The dummy model developed in this study has shown reasonable correlations with the hardware for a variety of loading conditions. The model has proven to be of good fidelity to the hardware, robust, reliable, computationally efficient, and is a reasonable basis for further work to reach accurate prediction of occupant injury numbers in automotive crash simulations.

MODEL CONSTRUCTION APPROACH

Prior to the project, an extensive literature survey was conducted to gather the Hybrid III related information. Then, a three dimensional finite element model of the Hybrid III torso is constructed from measurements on a disassembled physical dummy. Limbs and head models from an existing ESI commercial BioRID model are connected to the the torso model with joints leading to generation of a full dummy assembly.

Geometry Acquisition

Rather than relying on nominal geometries from dummy drawings, a realistic geometry is developed from measurements on a physical dummy torso structure, totally disassembled for the purpose of the project. In acquiring the geometry of individual components, the parts with regular shapes are directly measured. The skin parts that feature complex three dimensional surfaces are digitized by CT scan. The CAD models and subsequent assembly are constructed in CATIA. Weight of parts including small accessories is measured, while the exterior dimension and moment of inertia of Hybrid III can be directly referred to the dummy user manual and public literature.

Mesh Construction

Most parts are meshed with hexahedral elements in order to reduce the number of elements. For complex surface parts, like pelvis and abdomen, meshes are made of tetrahedral elements. In meshing rigid body of complex structure with hexahedral elements, a slight gap of 1.1 mm is maintained between internal adjacent sub-parts for easier contact interface management. As compared with the more classical method of solid meshing with shared nodes, the total element number for a given part is largely reduced. As a result, the model size is comparable to existing commercial dummy models, meanwhile the mesh quality of flexible parts is rigorously ensured.

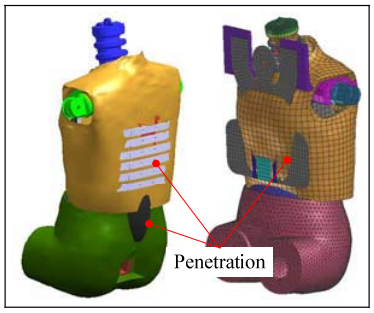

Figure 1. Penetration issues in preliminary model assembly.

Model Assembly

When individual CAD models are assembled together, there are many penetrations in the chest model, as shown in Figure 1. The main reason for these penetrations is that the dummy hardware has pre-deformations that are released when its parts are disassembled. For example, without the assembling constraint, urethane bib is flat and not accommodated in the chest structure. Therefore, enforcing certain pre-deformation to the pre-stressed parts is necessary to make them assume their ultimate shape during the chest assembly process. Simulation runs of six rib components, the bib and jacket are performed to capture the pre-deformed shapes of the assembled dummy hardware. With all the pre-deformation to the parts in place, the torso model is properly assembled, as illustrated in Figure 2. Limbs and head obtained from an existing ESI commercial BioRID model are connected to the torso model using joint definition. Figure 3 shows the

assembled full dummy model. It should be noted that pre-stresses from assembly are not included in the model.

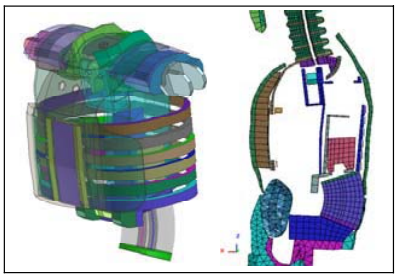

Figure 2. Adapted mesh for model assembly.

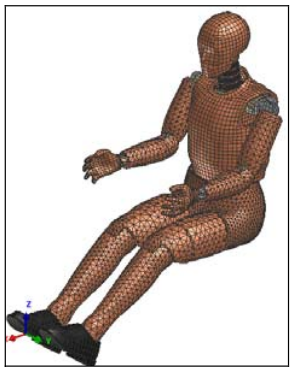

Figure 3. Developed Hybrid III 50th percentile PAM-CRASH FE model.

MODEL DESCRIPTION

The full dummy model consists of 160 parts, 42518 nodes and 87764 elements. The entities are regularly numbered for clear organization.

The model geometry complies with the specifications of Hybrid III in terms of external dimension, mass and inertia. Instruments of Hybrid III are properly modeled in accordance with the hardware and SAE J211. Load cells and accelerometers are commonly modeled as joints and nodal local time history, respectively. Chest potentiometer is realistically modeled using a joint at the base of the transducer and a general kinematic joint at the sternum. The rotational angle of the transducer arm about y-axis can be easily converted to chest frontal compression with a simple formula.

Material properties of different parts are defined using different material types in PAM-CRASH. Rigid bodies and null material (types 99, 100), elastic plastic material (types 1, 103) are frequently used to model metal parts that undergo small elastic deformations. Linear visco-elastic material (type 5) and nonlinear strain rate dependent foam (type 45) are used to model typical flexible parts, like vinyl skin and flesh foam, respectively. In addition, types 301 and 221 are used to model tied link and generalized spherical joint.

EXPERIMENTAL DATABASE AND MODEL VALIDATION

A variety of tests are carried out at different levels in terms of structure complexity and loading velocity. Experiments at the component level include single rib drop test and abdomen drop test. Dummy calibration tests at the sub-assembly level include head drop test, neck flexion and extension test as well as chest frontal impact test. In addition to above tests on local response of the dummy, a sled test with a belted full dummy at the system level is conducted, recording dummy kinematics and injury numbers.

Most tests at different structural levels are conducted for a series of loading velocities. To prevent damage of the dummy or segments in high-velocity impacts, tests are in general conducted at progressive loading velocities. During the tests, the sampling rate for data channels and high speed movie is set at 20,000 samples/s and 1,000 frames/s, respectively. Test ambient temperature and relative humidity are recorded.

Besides, above experimental data, publicly available test conditions and results, e.g., lumbar spine bending and the dummy calibration curves from the hardware owner's manual[15], are also referred to expand the experimental database for the model validation purpose. Therefore, the accumulated experimental data for the model validation are derived from three major sources, i.e., tests conducted in this project, the hardware owner's manual and public literature. In this paper, most test curves selected for comparison against the model response are from the tests in this project, unless otherwise noted. It should also be noted that the test data and the model response are both filtered with protocols in accordance with SAE J211.

In the dummy modeling, the most challenging work is material characterization through validation of the model at different levels. In order to enhance the fidelity of the model response, critical material parameters are identified using optimization techniques, as schematically shown in Figure 4.

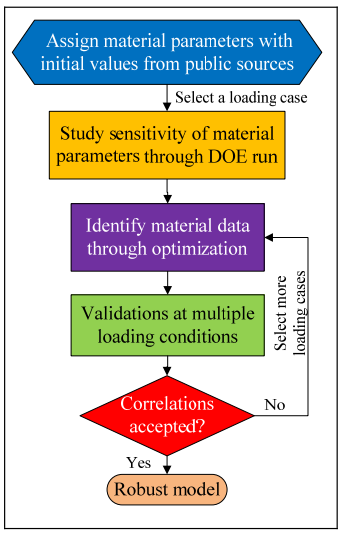

Figure 4. Technical approach used in material parameters identification.

Material data available from public literature[5][7][10], serving as a good starting point for the model validation, are first assigned to various material parameters. Design of experiments (DOE) analysis is then performed to investigate the sensitivity of different material parameters at a selected loading condition, during which critical material parameters are determined. This is followed by launching an optimization run in which values of the afore-identified critical material parameters are iteratively adjusted until convergence is reached. The model with optimized material data is subsequently validated at remaining loading conditions. If correlation of the model with tests is not accepted, the material data will be re-calibrated through optimization by simultaneous simulation at two or more loading conditions. The optimized model is again validated at multiple loading conditions and this process continues until adequate correlations between simulation and tests at a series of loading conditions are achieved. Using the optimization protocol, the material properties of the dummy model are calibrated at component and sub-system levels, then validated at the system level.

Material Calibration and Model Validation at Component Level

The material properties of rib component, abdomen and lumbar spine are calibrated at the component level through optimization using respectively single rib impact, abdomen impact, and lumbar spine bending load cases.

Single rib impact In frontal impact, ribs play a dominant role in chest response. A dummy rib is composed of a spring steel plate bonded with a damping material for providing proper dynamic response. Each rib is supported at the rear by a stiffener.

A series of single rib impact tests is carried out using a drop tower, as shown in Figure 5. The rib is positioned in a configuration that loads the rib in a similar way as in the dummy in a frontal crash situation. Rib ends are rigidly constrained to ensure stability of rib deformation during impact. Impact load and rib compression are calculated by acceleration signal and high speed movie, respectively. Nominal velocity of loading is ranging from 2.0 m/s to 6.7 m/s.

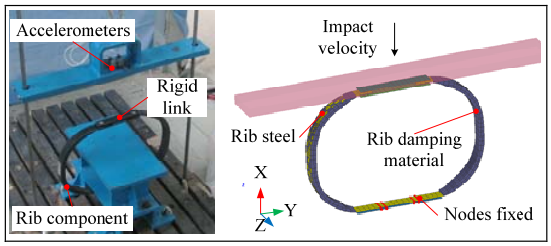

Figure 5. Setup for rib drop test and simulation.

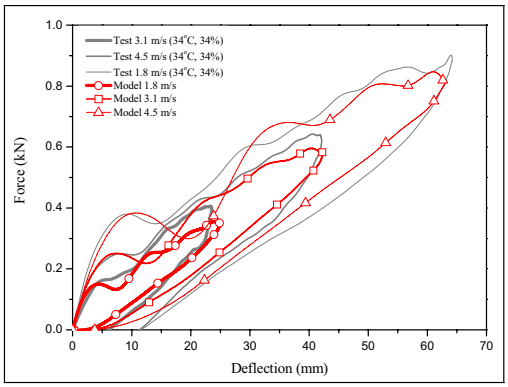

Figure 6. Correlations between rib model response and test data.

In the single rib model, sharing nodes is applied to simulate the bond on the interface between the rib steel and the damping material. The rib steel and the stiffener are modeled as elastic material. The damping material is modeled as linearly visco-elastic. Figure 6 gives the correlations results indicating that the simulated structural response shows good agreement with the tests at different loading velocities. Note that correlation at 6.7 m/s is not shown as the effective test data is rather limited.

Abdomen impact Impact tests with the abdomen, composed of vinyl-encased foam, are also conducted with the drop tower, as shown in Figure 7. The abdomen is properly positioned to best spread the load. Although the loading direction is not identical with that experienced by dummy in a typical car crash, it still can serve the component validation purpose as the abdomen component is quite homogeneous and isotropic. Impact load and abdomen compression are calculated by acceleration signal and double integration of the signal, respectively. Nominal impact velocities are ranging from 2 m/s to 4 m/s, which is sufficient to generate substantial compression of the abdomen.

In the abdomen model, the vinyl skin is meshed with shell elements that share nodes with the solid tetrahedral elements of the interior foam mesh. The vinyl skin and the interior foam are modeled as elastic plastic material and general strain rate dependent foam, respectively. Figure 8 shows the simulation results, indicating that the model correlates reasonably with tests at different loading velocities, except for the hysteresis of the high speed loading. Since good correlations in loading stage are reached under different velocities loading, the model behavior is adequate for injury prediction at this stage.

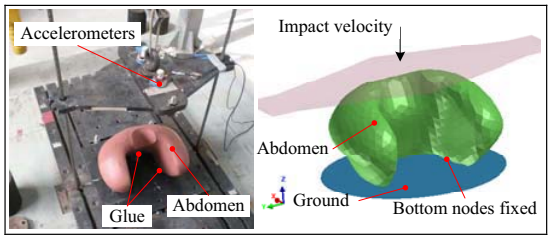

Figure 7. Setup for abdomen drop test and simulation.

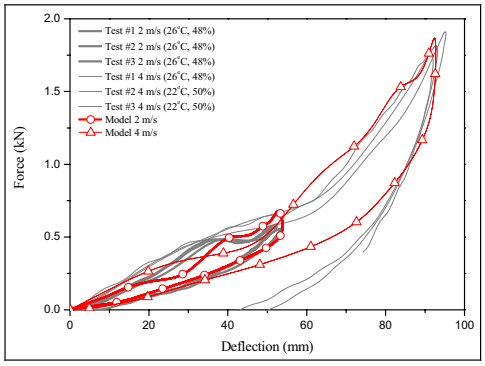

Figure 8. Correlations between abdomen model response and test data.

Lumbar bending Material characterization of the lumbar spine is performed with reference to the lumbar bending test in the literature[2]. The lumbar spine is modeled as linear visco-elastic solid rubber clamped by two rigid-body steel plates on each end. The two cables are modeled as a number of bar elements going through the lumbar spine. A rotational angle-time function with a constant loading velocity of 0.13 s^{-1} is applied at the upper end of the loading beam while keeping the lower end of the lumbar spine constrained. The moment-rotation history of the lumbar spine is calculated. Simulation result shows an approximate linear representation of the experimental data, considered accurate enough at this stage in the absence of measurements on the available hardware. The lumbar spine can be further improved by validation against the test under dynamic loading.

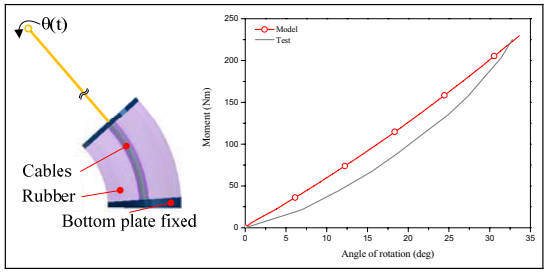

Figure 9. Setup for lumbar bending simulation and correlation of the model with test.

Material Calibration and Model Validation at Sub-System Level

Typical certification tests of Hybrid III at the sub-system level are carried out, including head drop test, neck flexion and extension test and chest pendulum test, as shown in Figure 10. Configuration for the tests and the performance target is briefly presented below. Readers are referred to CFR 49 Part 572 subpart E for more detailed information[16].

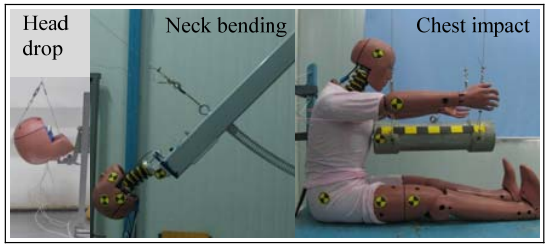

Figure 10. Setup for Hybrid III calibration tests.

Head drop test The test measures Hybrid III

forehead response to frontal impact with a hard surface. The head assembly is suspended at a height of 376 mm and dropped freely on a smooth and hard steel plate, according to the regulation. The peak resultant acceleration of the head center of gravity should lie between 225 g and 275 g. In the project phase 1, we carry out head certification test at the regulatory drop height of 376mm, corresponding to the impact velocity of approximately 2.7 m/s. Mechanical response of the hardware segment at other impact velocities can be found in the literature[10][11]. With the Hybrid III head model, the material properties of head skin that is modeled as linearly visco-elastic are calibrated. Figure 11 shows the correlations between simulation and tests. It is clearly observed that the head model response is in conformity with the regulatory performance requirement at 2.7 m/s. In addition, the model also correlates properly with the test data at velocities ranging from 2.2 m/s to 3.1 m/s. As for the high velocity of 4.2 m/s, however, the head model shows 10% lower peak value than test data.

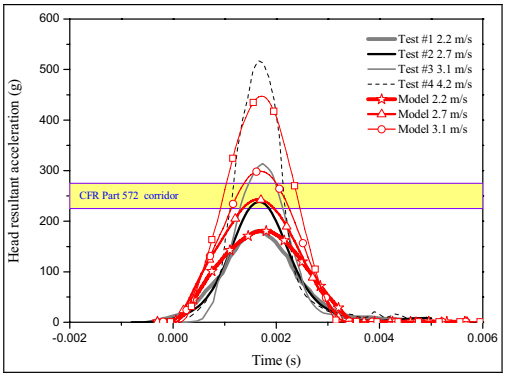

Figure 11. Correlations between head model response and test data; Test 2.2 m/s and 3.1 m/s from reference[11]; Test 4.2 m/s from reference[10].

Neck flexion and extension test This test measures structural response of the head-neck assembly subjected to forward bending and rear bending, respectively. The head-neck sub-assembly is mounted at the bottom of a pendulum, as shown in Figure 12, which is released from a given height to achieve the impact velocity of about 7 m/s for flexion and approximate 6 m/s for extension, as specified in the certification test specification. A block of honeycomb material is used to stop the pendulum at the lowest point. Rotation angle of the D-plane is recorded by the combined use of head potentiometer and neck potentiometer. In the project phase 1, neck tests are carried out with a drop velocity range of 3 m/s to 6 m/s for both flexion and extension.

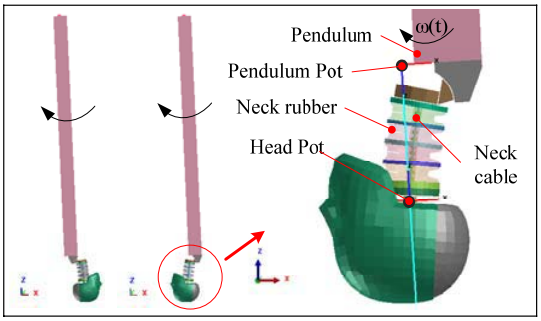

Figure 12. Setup for neck extension and flexion simulation.

The head-neck bending tests are realistically simulated through construction of the neck model in detail and true loading condition applied to the model, as illustrated in Figure 12. The simulation starts at the time of contact between the pendulum and the honeycomb. An angular velocity time history, converted from the crash pulse, is applied to the pendulum to avoid the difficulty in modeling the honeycomb material. Motion of the head-neck sub-assembly during impact is schematically shown in Figure 13. Material properties of the neck are optimized for the flexion at 7 m/s and validated at other loading conditions, including extension at 6m/s and 3m/s, and flexion at 3m/s. Results indicate that the optimized neck model has responses of high fidelity at high velocities (Figure 14, 15) and shows reasonable correlation with tests at low velocities (Figure 16).

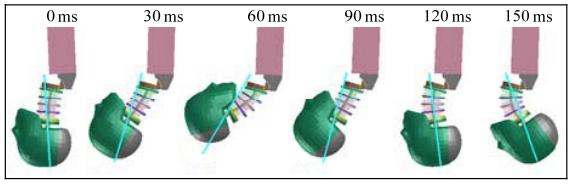

Figure 13. Head-neck sub-assembly kinematics, flexion at 7 m/s.

Thorax impact test In this test, chest response at the system level under frontal impact loading is measured. The dummy regulation specifies that a rigid pendulum with a mass of 23.4 kg is released from a given height to achieve the chest impact velocity of approximate 6.7 m/s. In the project phase 1, the impact speeds are ranging from 3.0 m/s to 5 m/s. Experimental data at 6.7 m/s is referred to public literature and the dummy owner's manual.

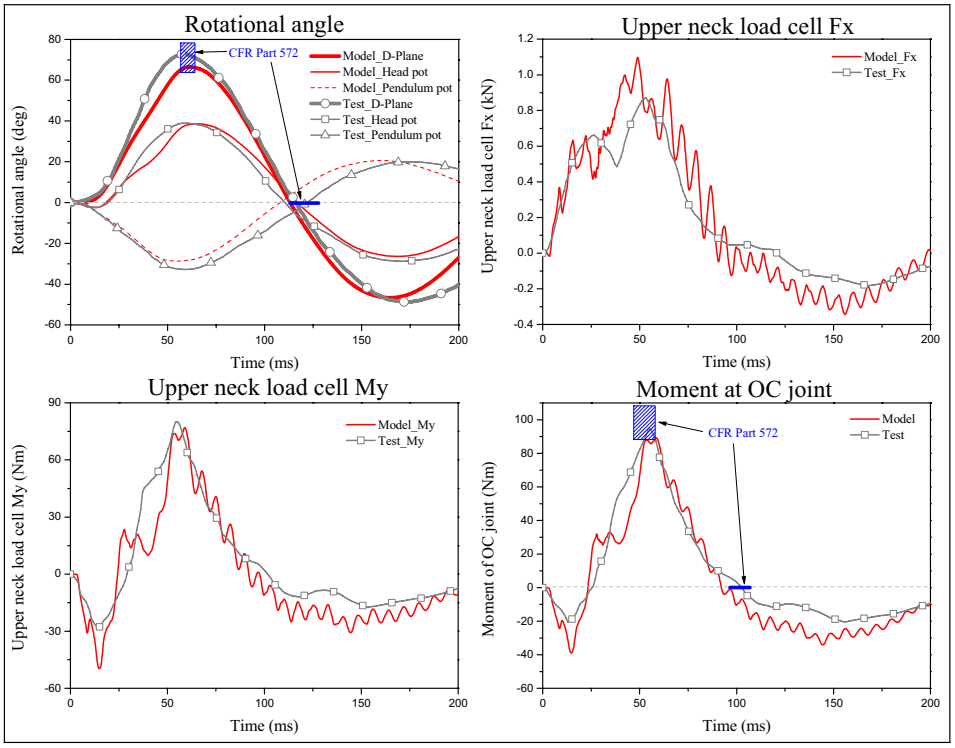

Figure 14. Optimization for flexion at 7 m/s, test data from the dummy owner's manual[15].

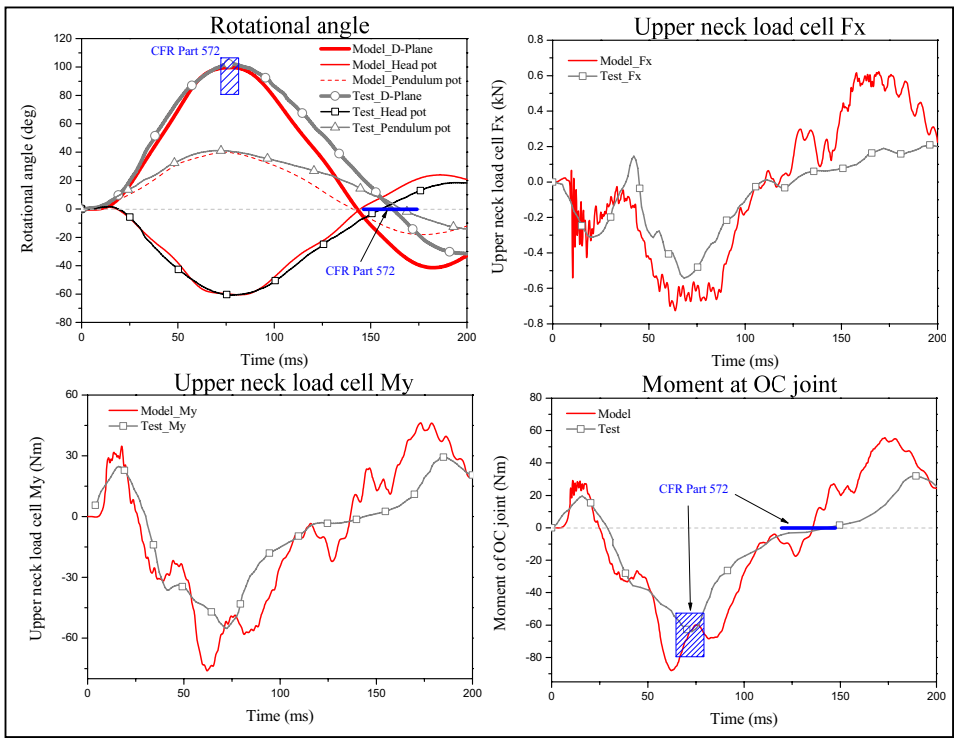

Figure 15. Validation for extension at 6 m/s, test data from the dummy owner's manual[15].

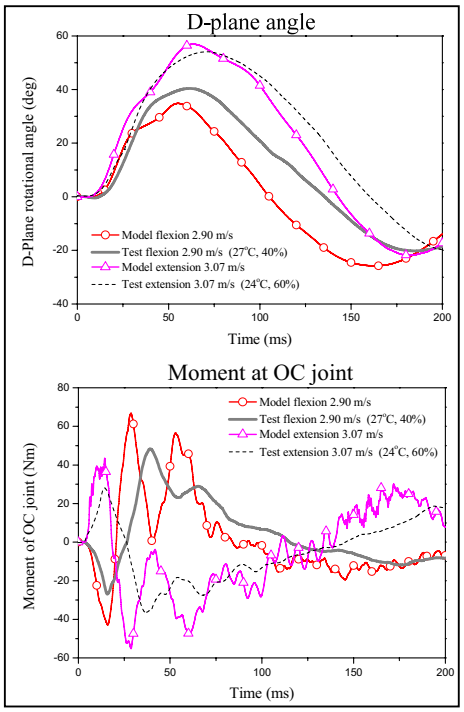

Figure 16. Validation for neck flexion and extension at low velocities.

Figure 17 shows the initial positioning of the chest impact model, in which impact force and chest deflection are recorded from the impactor contact, and the simulated internal chest potentiometer. Note that rib material properties optimized at single rib level are further adapted at the chest assembly level. Figure 18-21, show correlations between the model and test data at a series of loading velocities.

It is observed that the mechanical behavior of the chest model is in conformity with SAE standard performance target at 3 m/s (Figure 18) and the regulatory requirements at 6.7 m/s (Figure 21). The model response agrees well with that of Hybrid III dummy and cadaver corridors both at velocities of 4.3 m/s and 6.7 m/s, as observed in Figure 19 and Figure 21. Additionally, the model shows reasonable correlation with test data at 3 m/s and 5.1 m/s, as respectively shown in Figure 18 and 20, in which relatively larger chest deflection and lower peak force in conducted tests in the project is observed. This is likely to be caused by the non compliance of test ambient temperatures.

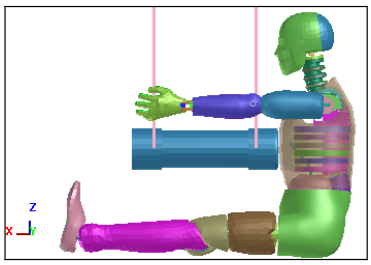

Figure 17. Setup for chest impact simulation.

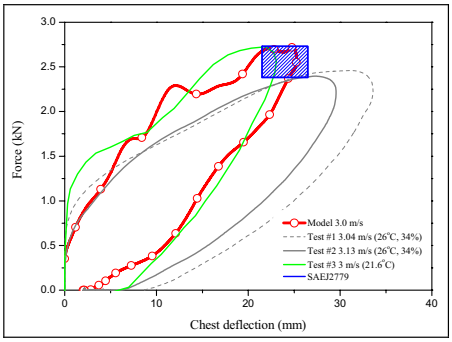

Figure 18. Correlation between chest model and tests at 3 m/s, test #3 from reference[17].

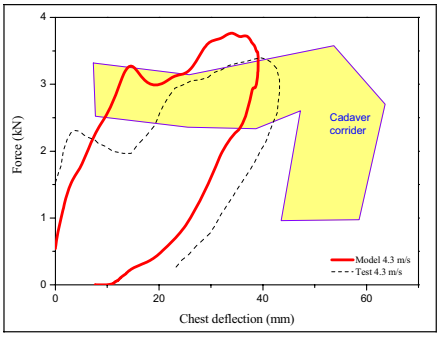

Figure 19. Correlation between chest model and tests at 4.3 m/s, test data from references[1][17].

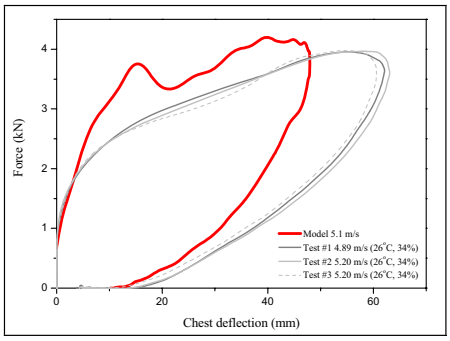

Figure 20. Correlation between chest model and tests at 5.1 m/s.

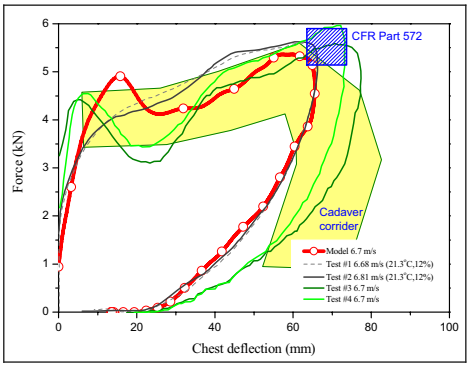

Figure 21. Correlation between chest model and tests at 6.7 m/s, test #1 & #2 from reference[15], test #3 & #4 from references[1][17].

Full Dummy Validation at System Level

Model validation against a sled test A sled test is conducted to evaluate the belted dummy response in an environment close to a 50 km/h real car crash situation. A hard seat associated with a piece of TNO child seat testing foam is used to approximate a typical car seat. The knee bolster is removed to avoid any possible complex interaction during the impact. Feet are properly rested on the inclined toe panel. Figure 22 shows the sled test setup and the model configuration.

Simulation is performed by inversely applying a velocity-time history, integral of the crash pulse, to the sled. Validation results of the dummy model against typical test data is given in Figure 23, as well as comparison of their kinematic motion as illustrated in Figure 24. It is clearly examined that good correlation between simulation and experiment is achieved in terms of dummy kinematics and [illegible]. Further improvements [illegible]tion of chest deflection.

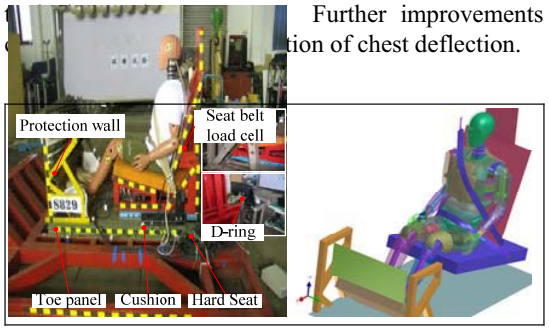

Figure 22. Setup for sled test with a belted full dummy and simulation.

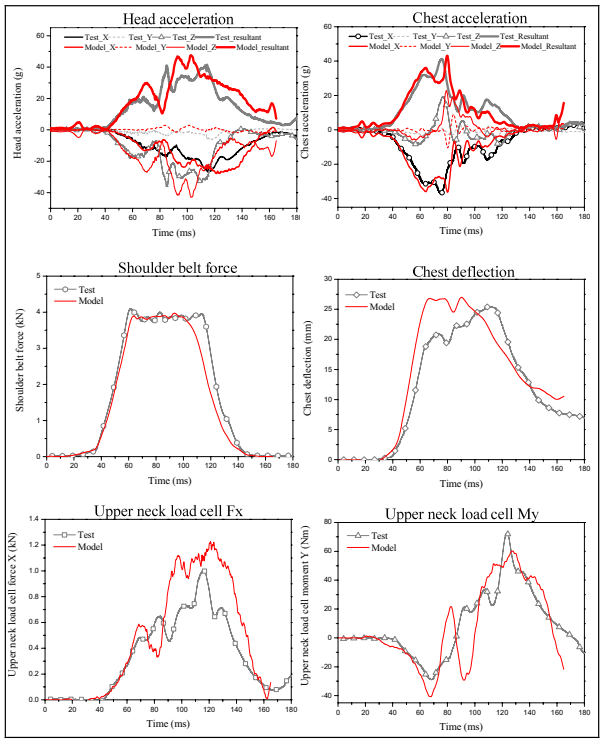

Figure 23. Correlations between model response and test data at system level.

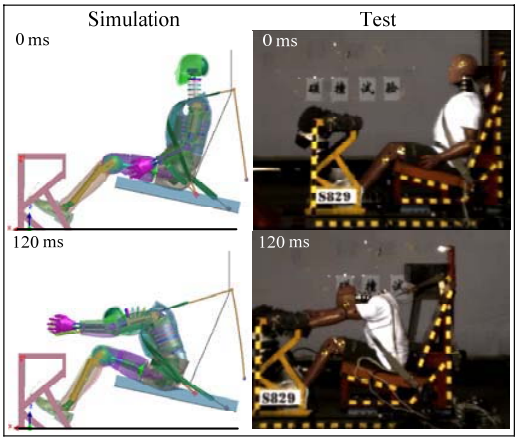

Figure 24. Comparison of dummy kinematics.

CONCLUSIONS

The automotive industry requires high quality dummy models for crash safety simulation in the design of new vehicle models. This paper has introduced a new platform for research and development on the Hybrid III dummy model with PAM-CRASH. It attempts to represent with a reasonable accuracy of the mechanical response of the hardware under loading conditions at various velocities, in addition to compliance with the

regulatory requirements. It also uses a new method to approach the real geometry of the assembled dummy, consisting in simulating the assembly of the thorax. In this paper, the current status of the Hybrid III FE model shows reasonable correlation between simulation and experiments. Further developments are still needed to reach a highly realistic model, in particular correlations against a wider range of experiments, statistics on actual dummy properties, further material modeling, and finer account of manufacturing details.

REFERENCES

[1] Foster J, Kortge J, Wolanin M. Hybrid III-A biomechanically-based crash test dummy. SAE Technical Paper No. 770938, 1977

[2] Deng Y C. Analytical study of interaction between belt and HIII dummy in sled tests. SAE Technical Paper No. 880648, 1988

[3] Franz U, Stahlschmidt S, Schelkle E, et al. 15 years of finite element dummy model development within FAT, 2009

[4] Rieser A, Nußbaumer C, et al. A development process for creating finite-element models of crash test dummies based on investigations of the hardware. The 21st International Technical Conference on the Enhanced Safety of Vehicles Conference, ESV 09-0368, 2009

[5] Yu H, Zhou Q, Neat G W. Three-dimensional finite element modelling of the torso of the anthropomorphic test device THOR. International Journal of Vehicle Safety 2(1-2): 116-140, 2007

[6] Arnoux P J and Joonekindt S, et al. RADIOSS finite element model of the Thor dummy. International Journal of Crashworthiness 8(6): 529-541, 2003

[7] Noureddine A, Eskandarian A, Digges K. Computer modeling and validation of a Hybrid III dummy for crashworthiness simulation. Mathematical and Computer Modelling (35): 885-893, 2002

[8] Naravane A, Deb A.Validation of a Hybrid III dummy model and its application in simulation of vehicle frontal NCAP tests. Altair CAE Users Conference, 2005

[9] Mohan P and Marzougui D, et al. Development and Validation of Hybrid III Crash Test Dummy. SAE Technical Paper No. 2009-01-0473, 2009

[10] Khalil T B, Lin T C. Simulation of the Hybrid III dummy response to impact by nonlinear finite element analysis. SAE Technical Paper No. 942227, 1994

[11] Moss S and Huang Y, et al. Development of an advanced finite element model database of the Hybrid III crash test dummy family. SAE Technical Paper No. 971042, 1997

[12] ESI Group. Virtual Performance Solutions-Explicit Solver Notes Manual, 2008

[13] ESI Group. Virtual Performance Solutions-Explicit Solver Reference Manual, 2008

[14] FTSS Inc. User's manual for the 50th percentile male Hybrid III test dummy, April 2005

[15] FTSS Inc. Owner's manual for the 50th percentile male Hybrid III test dummy, SN. 1113

[16] NHTSA 49 CFR 49 572.31 Subpart E-Hybrid III Test Dummy

[17] Kai W, Xiangrong L, Haitao Z, Xianglei Z. Research on the low speed thorax calibration test for Hybrid III 50th Male Dummy. The Twelfth Conference of Automotive Safety Technology, 2010

Development of An Advanced Finite Element Model for A Pedestrian Pelvis

Miwako Ikeda
Shunji Suzuki
Yasuaki Gunji
Yukou Takahashi
Honda R&D Co.,Ltd. Automobile R&D Center
Yasuki Motozawa
Masahito Hitosugi
Dokkyo Medical University School of Medicine
Japan

Paper Number 11-0009

ABSTRACT

Because of a highly complex three-dimensional geometry of the pelvis, a variety of load transmission inside the pelvis exists. Due to the variation in pelvis internal load transmission, some of the previous studies revealed a variety of pelvis fracture patterns to pedestrians.

In order to predict pelvis fractures accurately, human finite element (FE) models have been developed in past studies. However, the biofidelity of these pelvis models has not been evaluated sufficiently in terms of pelvis internal load transmission due to the lack of biomechanical data from the literature. In order to address different load paths within the pelvis when subjected to lateral impact load, a recent experimental study investigated the reaction forces at the anterior (i.e., pubic rami) and posterior (i.e., sacrum) sides separately in acetabulum and iliac impacts.

The aim of this study was to improve the biofidelity of a pelvis model by performing additional validations against the published experimental data.

The pelvis model used in this study was based on the FE pelvis model developed in a previous study. The structure and geometry of the baseline pelvis model were further improved. The geometry of the pubic symphysis was newly created by using CT images, and the articular cartilage was added at the acetabulum and SI joint to better represent overall compliance of the pelvis. The overall width of the pelvis was scaled in order to accurately represent the anthropometry of a mid-sized male.

In addition to the response validations performed in the previous study, the pelvis model was subjected to further validations to confirm enhanced biofidelity. Four force-deflection response corridors from the combinations of the impact locations (acetabulum or iliac crest) and reaction forces (anterior or posterior) were developed in the current study from the published experimental data for dynamic lateral compression of isolated human pelves. Material parameters of the cortical and trabecular bones were modified to better match the response corridors. The results of the response comparisons showed that the modified pelvis model is capable of representing different load paths within a human pelvis in various loading configurations.

INTRODUCTION

The analysis of the distribution of AIS 2+ injuries by region and vehicle type from NASS-PCDS (National Automotive Sampling System, Pedestrian Crash Data Study, 1994-1998) showed that in pedestrian accidents, leg injuries are most frequent with sedans, while pelvis injuries are most frequent with SUVs [Kikuchi et al., 2008]. In addition, the distribution of injured body regions in pedestrian serious injuries from Japanese accident statistics shows that the number of head injuries in 2009 was dropped by 38.2% compared with that in 1999, while the number of pelvis injuries was only reduced by 7.7%. This suggests that pelvis protection is one of the important issues in pedestrian protection.

Pelvis fractures are classified into several fracture patterns. Among those, the pubic rami are the most frequently injured region in the pelvis. Edwards et al. [1999] investigated the data containing 316 injured pedestrians obtained from the Major Trauma Outcome Study (MTOS), and showed that 61.5% of pedestrian pelvic fractures were pubic rami fractures, of which 17.5% were associated with acetabulum fracture. Ryan [1971] investigated 387 patients admitted to St. Vincent's Hospital in Australia with pelvic fractures due to traffic accidents, and showed

that 78.8% suffered pubic rami fracture, 23.3% suffered acetabulum fracture, and 20.4% suffered iliac fracture. Teresinski et al. [2001] investigated data from the autopsies of 371 pedestrian victims in road traffic accidents in the Department of Forensic Medicine, Medical Academy in Lubin, and showed that fracture of the upper ramus of the pubic bones was observed in 29.6%.

Due to the complex and highly three-dimensional nature of the geometry of the pelvis, it is crucial to represent both anterior and posterior load paths of the pelvis for predicting pelvis fracture accurately. A pelvis FE model can be an appropriate tool for predicting fracture, because it is capable of representing the precise geometrical characteristics of the pelvis. For this reason, many pelvis FE model have been developed in past studies [Renaudin et al., 1993; Dalstra et al., 1995; Plummer et al., 1996; Konosu et al., 2003; Song et al., 2006; Kikuchi et al., 2006; Kikuchi et al., 2008]. However, almost all of these models have only been validated against the experiments conducted by Guillemot et al. [1998], where total reaction forces of the contralateral side of the pelvis were investigated in lateromedial compressive loading into the acetabulum. Since the load distributions of anterior and posterior sides of the pelvis cannot be identified from this experiment, those models needed to be further validated in terms of pelvis internal load distributions.

Salzar et al. [2008] conducted the experiment for the responses of isolated pelves, where the fixed side of the pelvis was separated such that anterior and posterior loads can be measured individually in acetabulum and iliac crest loadings. Untaroiu et al. [2010] developed a pelvis FE model and validated it against this experiment, however, the model was validated only in acetabulum loadings.

The aim of this study was to improve the biofidelity of a pelvis FE model by means of validating the model against average responses and corridors of anterior and posterior reaction forces in lateromedial compression of the pelvis due to loadings to the acetabulum and the iliac crest.

MODEL DESCRIPTION

In this study, the model development was performed by using PAM-CRASH™ Version 2008.

Geometry

The model used in this study was based on the pelvis FE model developed by Kikuchi et al. [2006] representing a mid-sized male anthropometry (Figures 1, 2). Since the geometry of the baseline model was created using CT images of the pelvis from a specific human subject that may not be a representative of a mid-sized male, the overall width of the pelvis was scaled to 262 mm taken from the anthropometric data developed by the University of Michigan Transportation Research Institute [Robbins, 1983] to accurately represent the anthropometry of a mid-sized male. Although the pelvis model was geometrically scaled, the thickness of the pelvis cortical bone was kept the same as that of the baseline model because the average thickness of the cortical bone of approximately 0.9 mm used in the baseline model was close to the average thickness of 0.936 mm investigated by Ostertag et al. [2009].

The sacrum was modeled using deformable shell elements, which had been modeled as a rigid body in the baseline model. It was difficult to clearly identify the thickness distribution of the cortical bone of the sacrum from the medical images, and no data for the material property of the sacrum were found in the literature. Therefore, the average thickness of 0.9 mm for the pelvis cortical bone was used for the sacrum. Due to geometrical complexity, the trabecular bone inside the cortical layer was not modeled, and mechanical characteristics were lumped into the cortical layer.

Although the width of the pubic symphysis increases from posterior to anterior [Vix et al. 1971], a uniform width was applied in the baseline model. Therefore, the geometry of the pubic symphysis was modified referring to the CT images taken in the Dokkyo Medical University School of Medicine, University Hospital (Figure 3). The use of the CT images in this study has been approved by the Ethics Committee of the Dokkyo Medical University School of Medicine. The width of the symphysis pubis was set at 5.6 mm and 4.0 mm on the anterior and posterior sides, respectively.

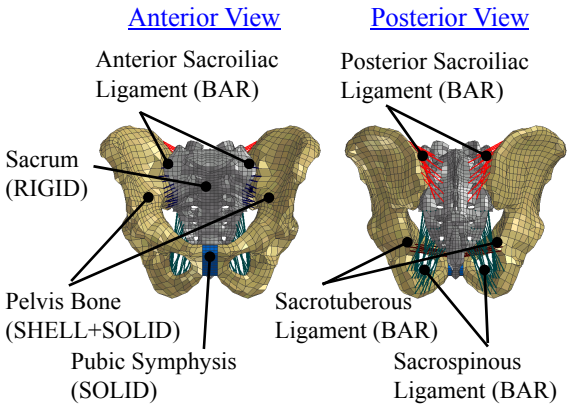

Figure 1. Baseline Pelvis FE Model.

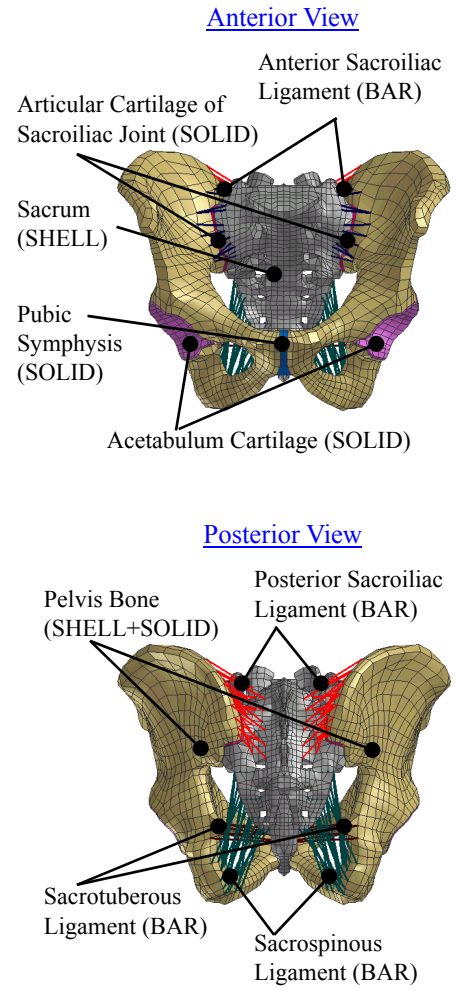

Figure 2. Modified Pelvis FE Model.

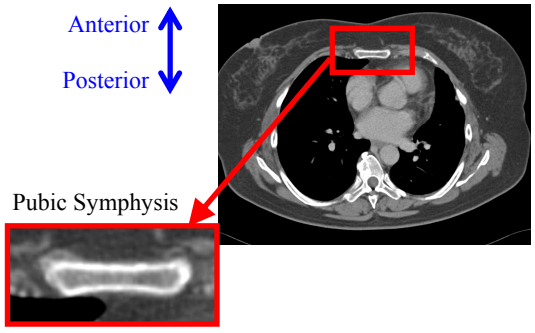

Figure 3. CT Image of Pubic Symphysis.

The articular cartilage represented by solid elements was added to the surfaces of the SI joint and the acetabulum. The thicknesses of the cartilaginous layers at the SI joint and the acetabulum were set at 2.5 mm and 2 mm, respectively, by referring to the anatomical book (Grey's Anatomy [1995]) and the research conducted by Walker [1992] and McLauchlan et al. [2002]. The compressive response of the SI joint was represented by the cartilage modeled using solid elements, and the tensile response of this joint was represented by the ligaments modeled using tension-only bar elements. The orientations of these ligaments were also modified by referring to the CT images.

Material Property

Pelvis Bone and Sacrum The material parameters of the pelvis bone were tuned based on those of the baseline model so as to match the force-deflection responses of the experiment by Salzar et al. Since the cortical bone is the main component for the stiffness of the pelvis, the parameters chosen in this study were compared to the published data to ensure validity of the tuned parameters. Kemper et al. [2008] conducted tensile tests of the coupon of the cortical bone of the pelvis, and showed that the elastic modulus is 10.9±1.8 GPa, the ultimate stress is 86.4±26.8 MPa, the ultimate strain is 0.016±0.010. It was found that the parameters chosen in this study (elastic modulus: 9.75 GPa, ultimate stress: 76.9 MPa, ultimate strain: 0.016) were within the range of the experimental data. Because of the lack of data for the sacrum, the same stress-strain curves as those of the pelvis bone were applied, and bone fracture was not simulated, since no complete fracture of the sacrum was seen in the dynamic loadings of the experiment by Salzar et al.
Similar to the baseline model, the stress-strain curves of both cortical and trabecular bones were configured so that the strength and stiffness were approximately proportional to the strain rate raised to the 0.06 power referring to the research by Carter et al. [1970]. Bone fracture was represented by using the element elimination option with a total strain criterion except the sacrum. McElhaney et al. [1976] shows the stress-strain curves of human femur in compression in different strain rate (Figure 4). From the figure, the relationship between the ultimate strain and the strain rate was identified for the femur (Equation 1). Due to the lack of data for the pelvis bone, the identical property to that of the femur was applied to the pelvis bone.

$$\varepsilon_u = -0.0012 \log_{10} \dot{\varepsilon} + \varepsilon_{static} \quad (1).$$

$$\varepsilon_u : Ultimate\ \ Strain,\ \ \dot{\varepsilon} : Strain\ \ Rate$$

$$\varepsilon_{static} : Ultimate\ \ Strain\ \ at\ \ \dot{\varepsilon} = 1$$

In order to represent the nonlinear stress-strain relationship, strain rate dependency, and the element elimination, MAT143 (elastic-plastic with elastic

stiffening and failure for shell elements) was chosen for the cortical bone and MAT36 (elastic/stiffening-plastic with failure for solid elements) was chosen for the trabecular bone.

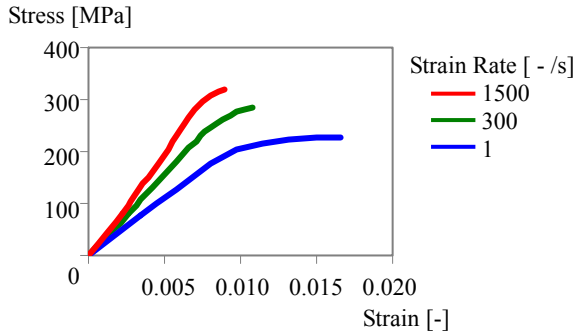

Figure 4. Stress-strain Curves of Human Femur in Compression in Different Strain Rates. [McElhaney et al., 1976].

Pubic Symphysis Due to the lack of information on the material property of the pubic symphysis available from the literature, the material parameters for the pubic symphysis were also tuned during a validation process. Since major loading pattern to the pubic symphysis is compressive loading, the material parameters were determined through the validation against compressive response of the isolated pubic symphysis from the experiment conducted by Dakin et al. [2001]. However, only one compressive response curve was presented in the paper, where the load was applied up to 0.8 mm compression. For this reason, only the initial toe region was determined by validating the model against Dakin et al., and the successive region of the stress-strain curve was determined by validating the model against the force-deflection response of the anterior side of the pelvis in acetabulum impact from the experiment performed by Salzar et al. It was found from these validations that the stiffness of the toe region validated against low speed tests by Dakin et al. was similar to that of the successive region validated against high speed tests by Salzar et al. Therefore, it was decided not to incorporate strain rate dependency. Since complete disruption of the pubic symphysis occurred in only one out of six cases in the dynamic loading to the acetabulum in the experiment performed by Salzar et al., it was decided not to represent failure of the pubic symphysis. In order to represent the nonlinear behavior of the pubic symphysis, MAT36 in PAM-CRASH^{TM} was used and the modulus of the first phase of the material characteristics was set to 1.2 MPa.

Acetabulum Cartilage and Articular Cartilage of Sacroiliac Joint Due to the lack of information available from the literature, the same material property as that of the pubic symphysis was applied to these cartilaginous layers except the stiffer region representing the bottoming. The stiffness of the stiffer region of these layers was determined by validating force-deflection response against the experiment performed by Salzar et al. The strain rate dependency and the rupture were not modeled in the material of these layers. MAT36 in PAM-CRASH^{TM} was chosen for modeling the material of the acetabulum cartilage. As for the articular cartilage of the SI joint, nodes were shared at the interface between the bones (ilium and sacrum) and the cartilage for numerical stability. For this reason, MAT21 in PAM-CRASH^{TM} (elastic foam with hysteresis for solid elements) was chosen in order to provide no tensile resistance from the cartilage.

Sacroiliac Ligaments In order to represent the nonlinear tension-only response of the SI joint, MAT205 (nonlinear tension-only bar element) was chosen for these ligaments. Trilinear stress-strain curve was specified to represent initial toe region as well as less stiff region with high strain. Other ligaments contained in the pelvis model were modeled using the same material models and parameters as those of the baseline model.

AVERAGE RESPONSE AND CORRIDOR FOR PELVIS VALIDATION

Response Curves for Validations

In order to provide validation data for the modified pelvis model, average force-deflection response and corridors were developed based on the test results from Salzar et al. Figure 5 shows the schematics of the test setup. A 76.6 kg drop impactor impacted a transfer beam to which a loading surface to a pelvis specimen was attached. Loads were applied to either the iliac wing or the acetabulum, and load paths through the sacrum and the pubis were separated by cutting the contralateral side of the pelvis to measure posterior (through the sacrum) and anterior (through the pubis) reaction forces individually. As a loading surface, a metallic ball and a padded rigid plate were used for acetabulum and iliac loading tests, respectively. Six dynamic and two quasi-static tests were run for each of the two loading configurations. Due to the limited number of quasi-static tests, the pelvis model was validated against dynamic tests

only. The average impact velocities were 2.8 and 1.9 m/s for the acetabulum and iliac loading tests, respectively. The pubic rami fractured in all of the dynamic acetabulum loading tests. In the dynamic iliac loading tests, two specimens sustained pelvis fracture (at the SI joint and the sacrum) and four subjects sustained laxity or dislocation of the SI joint.

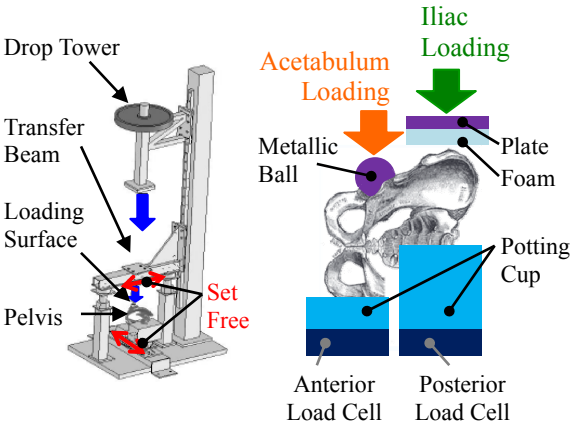

Figure 5. Setup of Experiment Conducted by Salzar et al. [2008].

The average responses and corridors of the anterior or posterior loads in acetabulum and iliac dynamic loadings were developed in this study, using geometrically scaled response curves to average mid-sized male using the standard width of the pelvis (262 mm obtained from the anthropometric data developed by the University of Michigan Transportation Research Institute [Robbins, 1983]). Displacement time histories of the impact surface were calculated by double integrating the acceleration of the transfer beam, and twelve force-deflection curves of the experiment were geometrically scaled in order to represent the response of the mid-sized male.

In the experiment performed by Salzar et al., no direct measurement was done as to the timing of initial contact. For this reason, the force-deflection curves were aligned such that the curves start from certain levels of reaction forces. In case of the acetabulum loading, the force level was set at 100 N for both anterior and posterior reaction forces. In case of iliac loading, 600 N was used for the posterior reaction force because a padded loading surface was used for the iliac loading. The curves for the anterior reaction force were aligned at the timing when posterior reaction force reached 600 N. A video analysis showed that the first peak of the force well correlated with the initiation of pelvis fracture or SI joint dislocation. Based on this finding, it was decided to interpret the timing of the first peak as the timing of failure, and use the curves up to this timing for response corridor development. Since no peaks were apparent from the anterior reaction force in iliac loading, the timing of failure identified for the posterior reaction force was applied to the anterior reaction force. From the six dynamic iliac loading tests, two of them (#011 and #016) were not used when developing force-deflection corridors because visual inspection showed that the shape of the pelvis was extremely different from others. Figures 6 through 9 show force-deflection curves obtained by following the procedure described above for the four combinations of the loading locations (acetabulum and iliac loadings) and the reaction forces (anterior and posterior reaction forces).

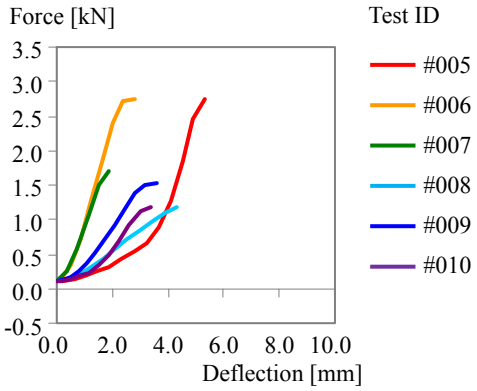

Figure 6. Force-Deflection Response for Anterior Reaction Force in Acetabulum Loading (Scaled to Mid-sized Male).

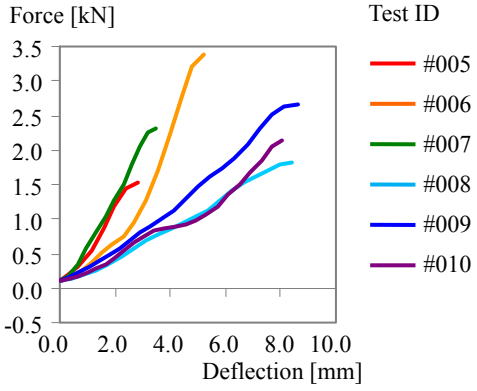

Figure 7. Force-Deflection Response for Posterior Reaction Force in Acetabulum Loading (Scaled to Mid-sized Male).

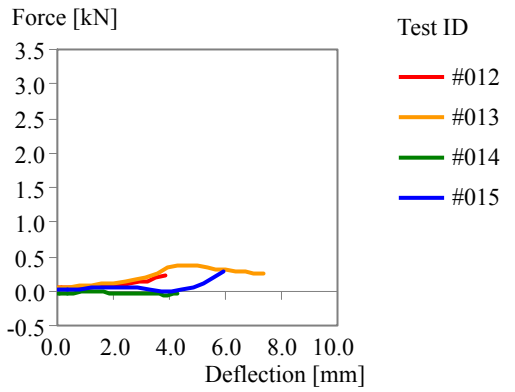

Figure 8. Force-Deflection Response for Anterior Reaction Force in Iliac Loading (Scaled to Mid-sized Male).

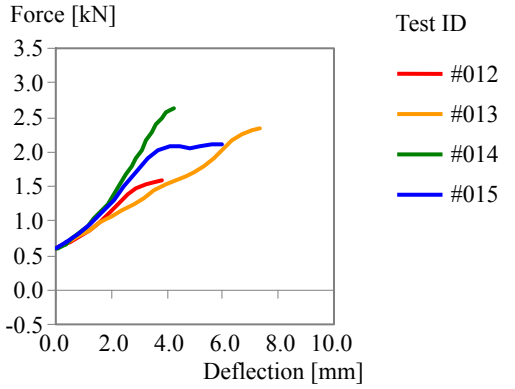

Figure 9. Force-Deflection Response for Posterior Reaction Force in Iliac Loading (Scaled to Mid-sized Male).

Development of Average Response and Corridor

Referring to the scheme for developing corridors proposed by Lessley et al. [2004], the average force-deflection responses and corridors were developed. As an example, the procedure for making them for the anterior reaction force in acetabulum loading is shown below. The same procedure was applied for the posterior reaction force in acetabulum loading and the anterior and posterior reaction forces in iliac loading.

1. For each force-deflection curve, normalize deflection by maximum deflection. (Figure 10)
2. For each force-deflection curve, apply linear interpolation to obtain force values for all normalized curves at every 2 % of the normalized maximum deflection (1.0). (Figure 11)
3. Calculate average and standard deviation of the force values at every 2% of the normalized maximum deflection to obtain an average curve and upper and lower bounds (average ± one standard deviation (S.D.)) for normalized deflection. (Figure 12)
4. For the average curve and upper and lower bounds, multiply the normalized deflection values by the average maximum deflection of the raw curves. (Figure 13)
5. Calculate the average and the S.D. of the deflection at the end point of each raw response curves to obtain a 'box' representing a failure point variation estimated from one standard deviation of the force and deflection. (Figure 14)

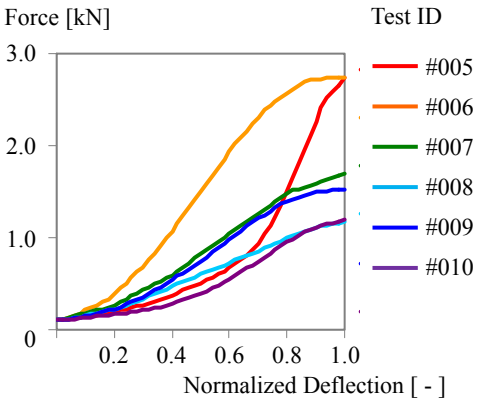

Figure 10. Step 1: Force-Normalized Deflection Responses.

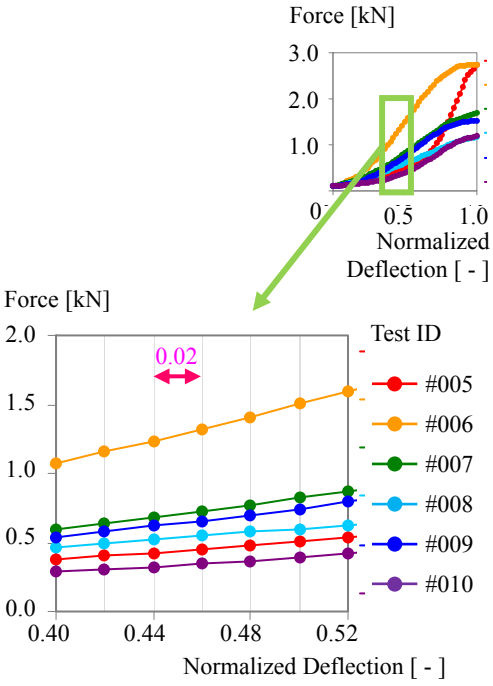

Figure 11. Step 2: Interpolation of Deflection for Force-Normalized Deflection Responses.

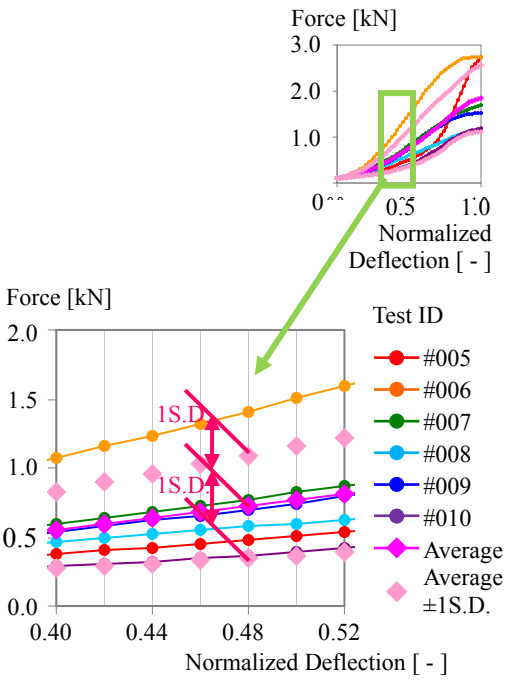

Figure 12. Step 3: Average and Upper and Lower Bounds of Force-Normalized Deflection Responses.

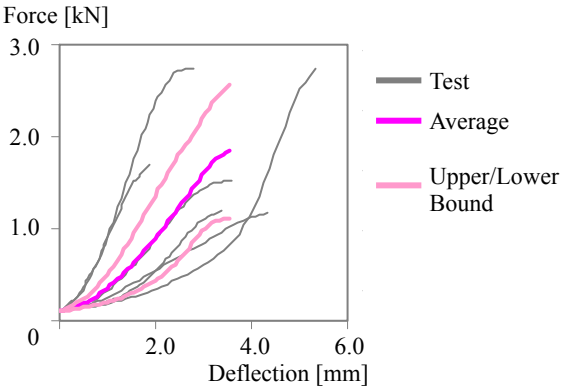

Figure 13. Step 4: Average and Upper and Lower Bounds of Force-Deflection Responses.

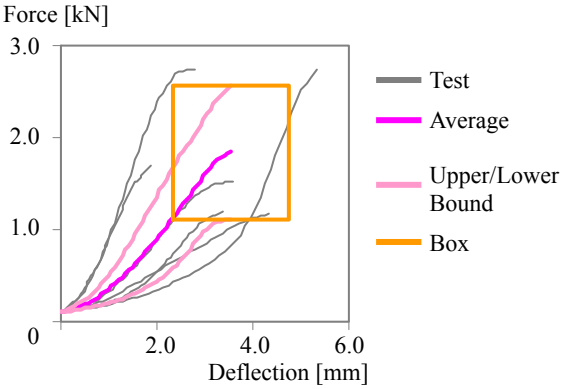

Figure 14. Step 5: 'Box' Representing Failure Point Variation.

MODEL VALIDATION

Pelvis-1: Validation against the experiment by Salzar et al.

Model Setup The modified pelvis model was validated against the dynamic loading tests conducted by Salzar et al. The model setup simulating the experiment is shown in Figure 15.

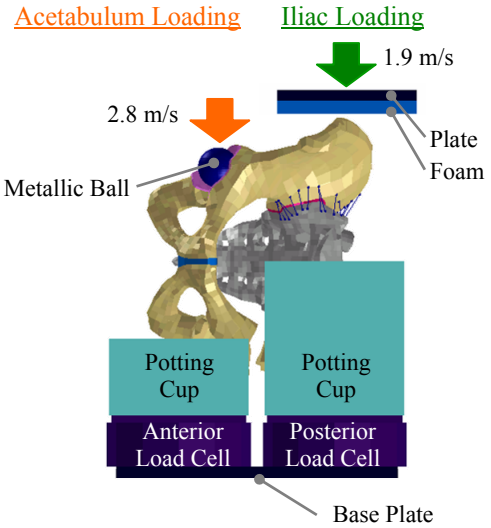

Figure 15. Model Setup Simulating Experiment by Salzar et al. for Pelvis Validation.

Similar to the experimental setup, the translational degree of freedom of the impact surface in anterior-posterior direction and the translational degree of freedom of the base plate to which potting cups are connected via load cells in superior-inferior direction were both set free. As the impact surface, the metallic ball (for acetabulum impact) or the plate (for iliac impact) was modeled as rigid, and the average time history of the displacement of the impact surface calculated from the test results was applied to them. At the surface of the plate, a layer of foam was modeled using solid elements (MAT21). The material property of this foam was determined from dynamic compression tests of CF-45 Confor® Foam at the loading rate of 35 km/h and the temperature of 20 °C. On the non-impact side, the elements of the pelvis model along a line defined from the mid distance of the two anterior iliac spines and the top of the greater sciatic notch were removed. The elements within the potting cups on the non-impact side of the pelvis were rigidly connected to the corresponding potting cups modeled as rigid. Each potting cup was connected to the load cell,

which was fixed to the base plate modeled as rigid. Kinematic joint elements were specified at the interfaces between the potting cups and the load cells in order to obtain time histories of the reaction forces.

Results In acetabulum loading, pubic rami fracture was predicted as a result of this simulation (Figure 16). This prediction well matched the results of the experiment, where pubic rami fracture was observed in 5 out of 6 cases. In iliac loading, dislocation of the SI joint was predicted, followed by fracture of the ilium near the SI joint (Figure 17), while SI joint dislocation and bone fracture near the SI joint were observed in 2 and 2 out of 4 cases in the experiment, respectively.

The predicted force-deflection response was compared to the average curve and corridor determined from the results of the experiment (Figures 18 through 21). This comparison showed that the model prediction well matched the average curve for the anterior response in acetabulum loading and the posterior response in iliac loading, which were the major load paths compared to others for both loading configurations.

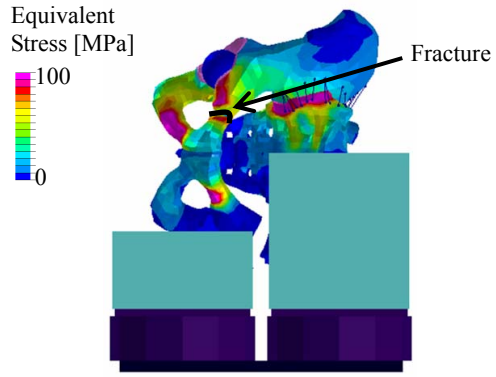

Figure 16. Injury Prediction in Acetabulum Loading.

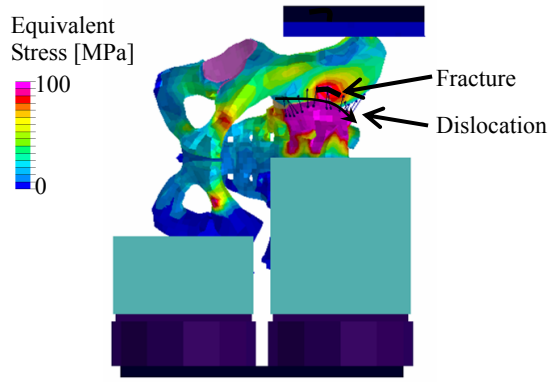

Figure 17. Injury Prediction in Iliac Loading.

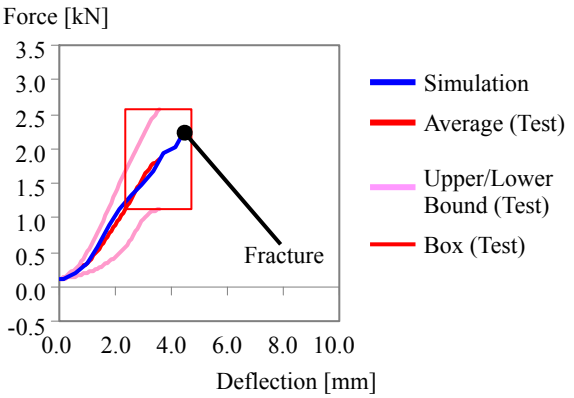

Figure 18. Comparison of Force-Deflection Response for Anterior Reaction Force in Acetabulum Loading.

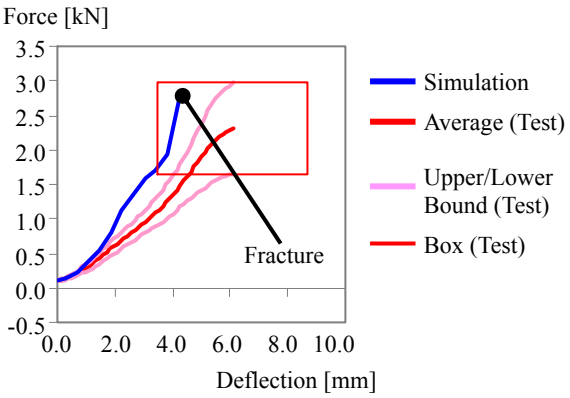

Figure 19. Comparison of Force-Deflection Response for Posterior Reaction Force in Acetabulum Loading.

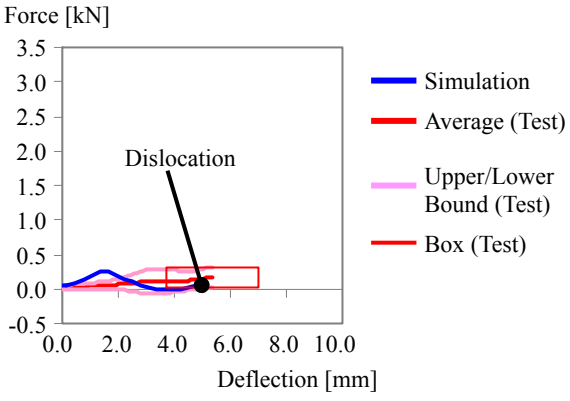

Figure 20. Comparison of Force-Deflection Response for Anterior Reaction Force in Iliac Loading.

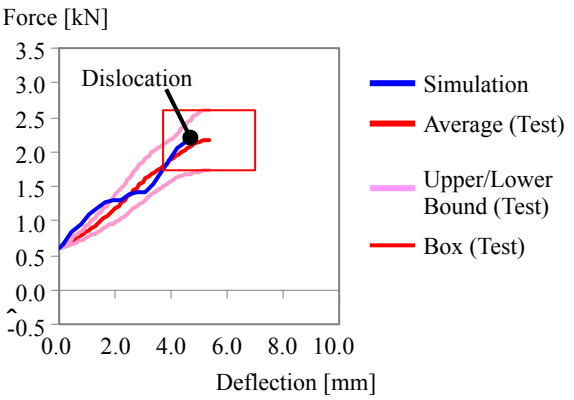

Figure 21. Comparison of Force-Deflection Response for Posterior Reaction Force in Iliac Loading.

Pelvis-2: Validation against the experiment by Guillemot et al.

Model Setup The validation using the results from Guillemot et al. performed in the previous study [Kikuchi et al. 2006] was also done using the modified pelvis model. As shown in Figure 22, one side of the pelvis bone was fixed to the bone fixing box, and a metallic ball inserted into the acetabulum was impacted by the impactor covered with the silicon padding. The material property of the silicon padding was derived from the data used in the previous study. The padding with a dropping mass of 3.68 kg impacted the metallic ball at a speed of 4 m/s.

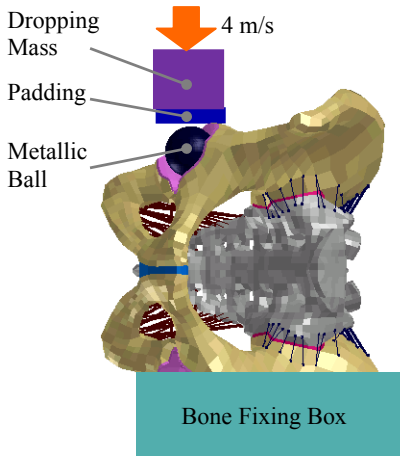

Figure 22. Model Setup Simulating Experiment by Guillemot et al. for Pelvis Validation.

Results The injury prediction from the simulation was shown in Figure 23. Complete fracture of the superior pubic ramus was predicted by the model. The relationship been the maximum force and the maximum displacement from the results of the test and simulation was shown in Figure 24. Six out of twelve tests were performed using female pelves. However, since the height of the specimen was not described in the paper, the value of the tests was unable to be scaled to a mid-sized male. The test results are classified into 3 groups depending on injury patterns, and the simulation results fell within the variation range of the maximum force and the maximum displacement for the group sustaining pubic fracture, which was predicted by the model.

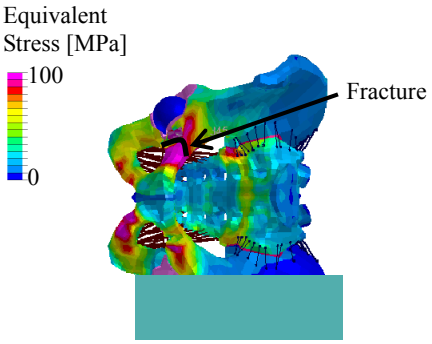

Figure 23. Injury Prediction in Pelvis Validation against Guillemot et al.

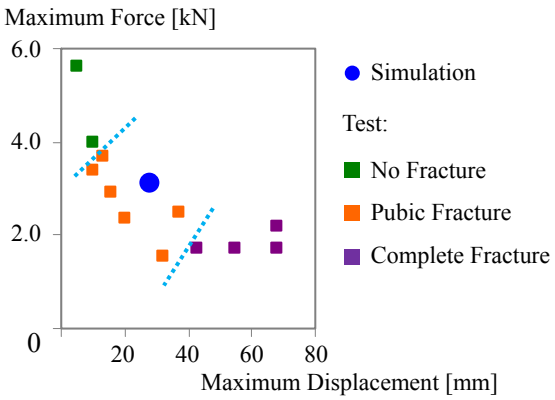

Figure 24. Comparison of Relationship between Maximum Force and Maximum Displacement.

Pubic Symphysis

Model Setup The pubic symphysis model was validated against the compressive loading tests conducted by Dakin et al. [2001] for the compression up to 8 mm. The model setup representing the experiment is shown in Figure 25. The pubic symphysis model along with bony parts on both sides of the pubic symphysis was extracted from the modified pelvis model, and both edges of the pubis were rigidly fixed to the bone fixing boxes. In the simulation, one side of the bone fixing box was fixed

to the space, and enforced displacement in compression at the speed of 1 mm/s was applied to the other side.

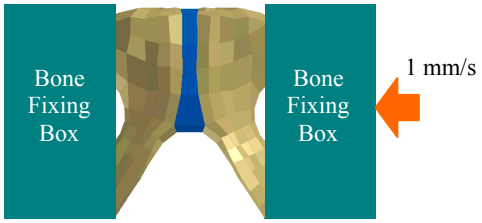

Figure 25. Model Setup Simulating Experiment by Dakin et al. for Pubic Symphysis Validation.

Results The comparison of force-deflection response between the test and the simulation is shown in Figure 26. The model response showed good correlation with that of the test.

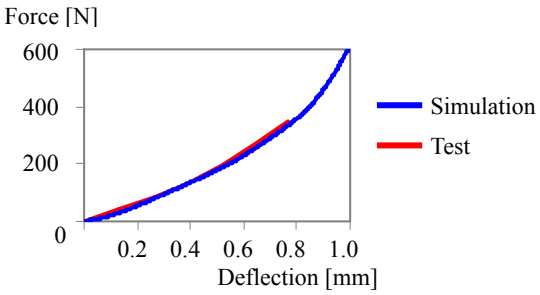

Figure 26. Comparison of Force-Deflection Response of Pubic Symphysis in Compression.

DISCUSSION

The baseline pelvis model developed in a previous study by Kikuchi et al. [2006] incorporated a relatively wider pubic symphysis than that of an actual human. In addition, the model lacked cartilaginous layer at the SI joint. In contrast, the modified model developed in the current study incorporated the pubic symphysis with its geometry taken from CT images, and a layer of cartilage was added at the SI joint. Figures 27 through 30 compare force-deflection responses for the anterior and posterior reaction forces in acetabulum and iliac impacts, respectively, obtained from pelvis lateral loading simulations representing the experiment by Salzar et al. using the pelvis models from the previous study (baseline model) and the current study (modified model). The results of the comparisons showed that the baseline model failed to accurately represent responses on both the anterior and posterior sides in terms of stiffness and failure characteristics, while the responses from the modified model matched those from the experiment on both the anterior and posterior sides. The mechanical characteristics of the pelvis are determined by a combination of those from the cartilaginous layer and the bony structure in series on both anterior and posterior sides. For this reason, it can be concluded that it was necessary to improve geometric and material characteristics of the cartilaginous layers at the pubic symphysis, acetabulum and SI joint to accurately represent force-deflection responses on both the anterior and posterior sides in a certain impact configuration. This suggests that it is crucial for a human pelvis model to incorporate accurate geometric and material properties of cartilaginous layers along with bony structures in order to accurately reproduce pelvis injuries in car-pedestrian collisions.

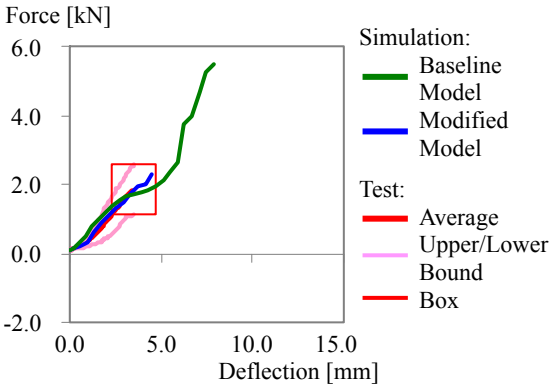

Figure 27. Comparison of Force-Deflection Response for Anterior Reaction Force in Acetabulum Loading between Baseline and Modified Pelvis Models.

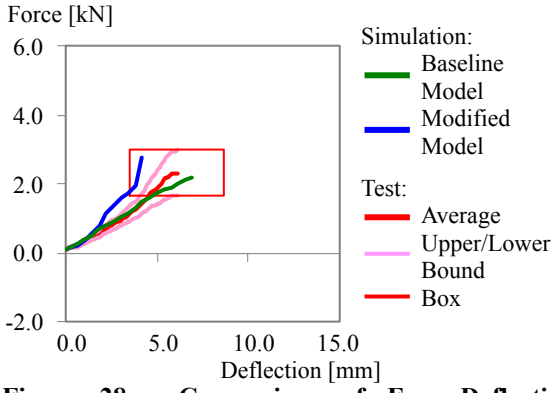

Figure 28. Comparison of Force-Deflection Response for Posterior Reaction Force in Acetabulum Loading between Baseline and Modified Pelvis Models.

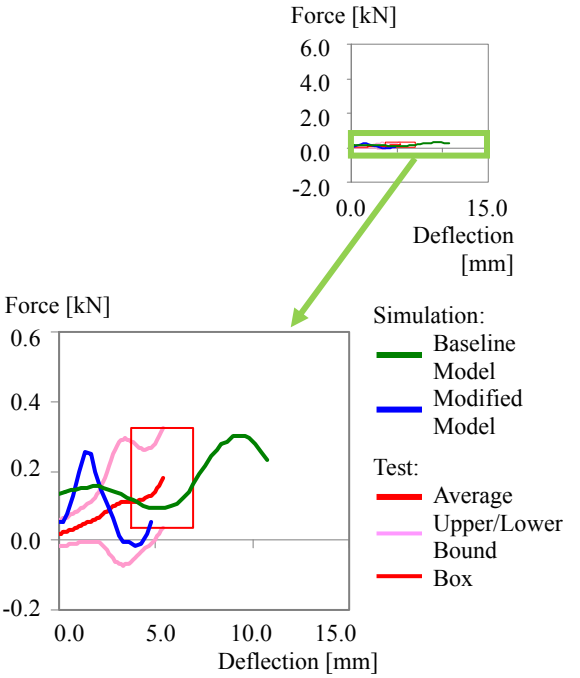

Figure 29. Comparison of Force-Deflection Response for Anterior Reaction Force in Iliac Loading between Baseline and Modified Pelvis Models.

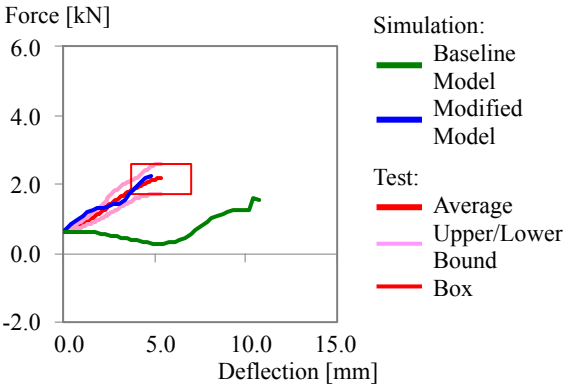

Figure 30. Comparison of Force-Deflection Response for Posterior Reaction Force in Iliac Loading between Baseline and Modified Pelvis Models.

Although the current study extensively validated the modified pelvis model against human response data available from the literature, the model still has some limitations in model validation.

1. The material property of the cartilage of the acetabulum and the SI joint were estimated through the validations, rather than using biomechanical data at the tissue level, because of the lack of data available from the literature. The material parameters for the cartilage used in the modified model need to be further validated once such data becomes available in the future.
2. The sacrum was modeled as a ductile structure with shell elements representing only the cortical layer, and no trabecular bone inside the sacrum was modeled, due to geometrical complexity. Although the biomechanical data used in the model validations do not include fracture to the sacrum, this would be an issue when predicting sacral fracture and requires further improvement as necessary.
3. The pelvis model was validated primarily in lateromedial direction. Accident statistics in Japan shows that in the year 2009, 59.9% of pedestrian accidents occurred when a pedestrian was walking across the road, and 16.5% of them occurred when a pedestrian was walking toward or parallel to the vehicle. Although the accident data suggest that primary loading direction to a pedestrian pelvis would be in lateral direction, the model needs to be further validated in other directions as well, in order to allow application of the model to prediction of injuries in various real-world situations.

CONCLUSION

In this study, the finite element model for the pedestrian pelvis developed in a previous study was modified by adding layers of cartilage at the acetabulum and the SI joint, and improving the geometry of the pubic symphysis and the orientation of the SI ligaments using the CT images.

The biofidelity of the modified pelvis model was evaluated by performing additional validations against published data, including individual validation of reaction forces at the anterior and posterior sides in acetabulum and iliac impacts.

The results of this study provide a tool for accurate prediction of the load distribution inside the pelvis when the pelvis is subjected to lateral impact.

ACKNOWLEDGEMENTS

The authors would like to thank Nobuhiro Tsukamoto, M.D., of Saitama Medical University for his technical support in collecting CT images.

REFERENCES

[1] Carter, D.R. and Hayes, W.C. 1977. "The Compressive Behavior of Bone as A Two-Phase Porous Structure" The Journal of Bone and Joint Surgery, 59(7): 954-962

[2] Dakin, G.J., Arbelaez, R.A., Molz, F.J., Alonso, J.E., Mann, K.A. and Eberhardt, A.W. 2001. "Elastic and Viscoelastic Properties of the Human Pubic Symphysis Joint: Effects of Laterla Impact Joint Loading" Journal of Biomechanical Engineering, 123(3): 218-226

[3] Dalstra, M., Huiskes, R. and van Erning, L. 1995. "Development and Validation of a Three Dimensional Finite Element Model of the Pelvis Bone" Journal of Biomechanical Engineering, 117: 272-278

[4] Edwards, K.J. and Green, J.F. 1999. "Analysis of the Inter-Relationship of Pedestrian Leg and Pelvis Injuries" Proceeding of 1999 International IRCOBI Conference on the Biomechanics of Impacts, 355-369

[5] Gray, H. 1995. "Gray's Anatomy: The Anatomical Basis of Medicine and Surgery, Thirty-eighth Edition" Churchill Livingstone

[6] Guillemot, H., Got, C., Resnault, B., Lavaaste, F., Robin, S., Le Coz, J. and Lassau, J. 1998. "Pelvis Behavior in Side Collisions; Static and Dynamic Tests on Isolated Pelvic Bones" Proceedings of the 16th International Technical Conference of the Enhanced Safety of Vehicles, 1412-1424

[7] Institute for Traffic Accident Research and Data Analysis 2009. "Traffic Accident Statistics" (in Japanese)

[8] Kemper, A.R., McNally, C. and Duma, S.M. 2008. "Dynamic Tensile Material Properties of Human Pelvic Cortical Bone" Biomedical Science Instrumentation, 44:417-418

[9] Kikuchi, Y., Takahashi, Y. and Mori, F. 2006. "Development of a Finite Element Model for a Pedestrian Pelvis and Lower Limb" SAE Paper #2006-01-0683

[10] Kikuchi, Y., Takahashi, Y. and Mori, F. 2008. "Full-Scale Validation of a Human FE Model for the Pelvis and Lower Limb of a Pedestrian" SAE Technical Paper #2008-01-1243

[11] Konosu, A. 2003. "Development of a Biofidelic Human Pelvis FE-Model with Several Modifications onto a Commercial Use Model for Lateral Loading Conditions" SAE paper #2003-01-0163

[12] Lessley, D., Crandall, J., Shaw, G., Kent and R., Funk, J. 2004. "A Normalized Technique for Developing Corridors from Individual Subject Responses" SAE Technical Paper #2004-01-0288

[13] McElhany, J.M., Roberts, V.L. and Hilyard, J.F. 1976. "HANDBOOK OF HUMAN TOLERANCE" Japan Automobile Research Institute, Inc.

[14] McLauchlan, G.J. and Gardner, D.L. 2002. "Sacral and Iliac Articular Cartilage Thickness and Cellularity; Relationship to Subchondral Bone End-Plate Thickness and Cancellous Bone Density" Rheumatology, 41(4): 375-380

[15] Ostertag, A., Cohen-Solal, M., Audran, M., Legrand, E., Marty, C., Chappard, D. and de Vernejoul, M. 2009. "Vertebral Fractures are Associated with Increased Cortical Porosity in Iliac Crest Bone Biopsy of Men with Idiopathic Osteoporosis" Bone, 44: 413-417

[16] Plummer, J.W., Bidez, M.W. and Alonso, J. 1996. "Parametric Finite Element Studies of the Human Pelvis: The Influence of Load Magnitude and Duration on Pelvis Tolerance During Side Impact" SAE Technical paper #962411

[17] Renaudin, F., Guillemot, H., Lavaste, F., Skalli, W., Lesage, F. and Pecheux, C. 1993. "A 3D Finite Element Model of Pelvis in Side Impact" SAE Technical Paper #933130

[18] Robbins, D.H. 1983. "Anthropometric Specifications for Mid-sized Male Dummy, Volume 2, the University of Michigan Transportation Research Institute" Report Number UMTRI-83-53-2

[19] Ryan, P. 1971. "Traffic Injuries of the Pelvis at ST.Vincents Hospital, Melbourne" The Medical Journal of Australia, 1(9): 475-479.

[20] Salzar, R.S., Genovese, D., Bass, C.R., Bolton, R., Guillemot, H., Damon, A.M. and Crandall, J.R. 2008. "Load Path Distribution within the Pelvic

Structure under Lateral Loading" International Crashworthiness Conference, 14(1): 99-110

[21] Song, E., Trosseille, X. and Guillemot H. 2006. "Side Impact: Influence of Impact Conditions and Bone Mechanical Properties on Pelvic Response Using a Fracturable Pelvis Model" SAE Technical Paper #2006-22-0004

[22] Teresinski, R. and Madro, R. 2001. "Pelvis and Hip Joint Injuries as a Reconstructive Factors in Car-to-Pedestrian Accidents" Forensic Science International, 124: 68-73

[23] Untaroiu, C.D., Salzar, R.S., Guillemot, H. and Crandall, J.R. 2008. "The Strain Distribution and Force Transmission Path Through Pubic Rami During Lateral Pelvic Impacts" International Mechanical Engineering Congress and Exposition, IMECE2008-67791, 79-88

[24] Vix, V.A. and Ryu, C.Y. 1971. "The Adult Symphysis Pubis: Normal and Abnormal" Acerican Journal of Roentgenology, Radium Therapy, and Nuclear Medicine, 112(3): 517-525

[25] Walker, J.M. 1992. "The Sacroiliac Joint: A Critical Review" Physical Therapy, 72(12): 903-916

DYNAMIC PROPERTIES OF THE SHOULDER COMPLEX BONES

Sudipto, Mukherjee
Anoop, Chawla,
Saurabh, Borouah
Debashish, Sahoo
Mike W. J. Arun
Department of Mechanical Engineering, IIT Delhi
India
Girish, Sharma
Parthiv Shah
Christophe Ageorges
Mercedes Benz R&D India
India
Paper Number 11-0428

ABSTRACT

This paper reports a characterization of stress-strain response of the humerus, clavicle and scapula through impact studies followed by property estimation. For the humerus, the modulus obtained for quasi-static tests varies between 0.4 to 18 GPa while the modulus obtained from the drop height of 0.5m varies from 0.7 to 40.5 GPa, that obtained from a drop height of 1m varies from 0.8 to 40.95 GPa and that from the 1.5m drop tests varies from 1.8 to 53 GPa. The increase in modulus with strain rate is consistent with earlier studies including McElahney [[5]].

INTRODUCTION

Safety measures have traditionally been evaluated by full-scale crash testing. The high cost and that it can be conducted only after a prototype is available has been a barrier in investigating alternatives for limiting injuries. Computer simulations are cost effective as compared to full-scale crash tests, and also provide a great deal of information that is frequently unavailable from full-scale crash testing. Unlike full-scale crash tests that normally yield data for only predetermined points where sensors have been mounted, computer simulations can be used to track all areas where a design needs additional reinforcement or areas where a component has excess capacity. For example, finite element modeling provides designers with an accurate picture of the stress distributions in critical components of a safety device throughout the impact event. Sicking and Mak [[6]] note that After a computer simulation has been developed and successfully validated against full-scale crash tests, the cost associated with conducting parametric studies to investigate the effects of installation details, impact conditions, road furniture, and vehicle characteristics is relatively inexpensive.

Computer simulations of vehicle collisions have improved significantly over the past few years. With advances in computer technology and non-linear finite element (FE) codes, full scale models and simulations of sophisticated phenomena like in biological systems are becoming ever more possible. Finite element crash simulations have been primarily focused on the vehicle models and their crash characteristics. Recently, refined FE models of airbags and dummies have been added to the simulations. This allows assessment of occupant injury and restraint system performance. Specifically, a well-developed human body model helps in understanding injury mechanisms and also helps to know the effect of modifications made to vehicles.

Efficient human body model development requires detailed modeling of the geometry of the human body and extensive tissue and bone properties beyond those already available in literature, such as dynamic properties of bones. Mechanical properties of human shoulder bones at strain rates expected in automotive related crashes are reported here. The outboard shoulder is in close proximity to the side door. Shoulder bones characteristics are hence critical in analyzing side impact crashes. As shown in Table 1, the percentage of casualties with AIS (Abbreviated Injury Scale) 3+ injuries to Upper extremities are 12.1 % Holt and Vassey [[4]] to 14.3 % in Dalmotas

[[1]], highlighting the large incidence in the Upper extremities.

Table 1. Percent of three point belted casualties with AIS >=3 in side impacts

	Percentage of injuries with AIS>=3	
BODY REGION	HOLT and VASSEY (1977)	DALMOTAS (1983)
Head/face	46.6	48
Neck	1.7	7.1
Shoulder/chest	48.3	40.8
Pelvis	24.1	13.3
Abdomen	10.3	11.2
Upper extremities	12.1	14.3
Back	0	1

Attempts have been made earlier to study bone properties at high strain rates, often using Split Hopkinson Pressure Bars. Shima et al. [[8]] characterized the dynamic compressive mechanical properties of cancellous bone from the human cervical spine using SHPB. The static and dynamic compressive responses of cancellous bone specimens from the human cervical spine were studied.

Ferreira et al. [[2]] characterized the mechanical properties of bovine cortical bone at high strain rate using SHPB. The study evidenced that bone is a highly heterogeneous structure and scattering of results is significant. It was observed that for an increase of strain rate the resistance properties increased and stiffness properties decreased. Westhuizen et al. [[7]] characterized the strain rate dependent mechanical properties of bovine bone in axial compression by quasi-static and dynamic tests.

Human cadavers (right and left shoulder) in age group 40 — 60 yrs have been tested. Cadaveric bone specimens were tested in three point bending with impact speeds up to 20 kmph. Piezoelectric impactor-force sensor data was acquired in excess of 400 KHz through a digital oscilloscope. A strain gauge mounted at the point opposite to point of impact was used to measure longitudinal strain data. A REDLAKE MotionXtra HG-LE was used to record displacements at points of interest and locate the time of visible crack initiation at a frame rate of 30,000 frames/s.

Using pre-impact CT images, FE meshes were developed for each individual bone, and material density was estimated using Materialise MIMICS software. The spectrum of material density is clustered into groups, and elastic-plastic properties are initially assigned to each group on the basis of the CT grey values. Impact simulation in LS-DYNA were used to estimate material properties.The region dependant parameters for Cowper Symonds material model for bones are then optimized to match the experimental results. Further, a roadmap to building accurate bone models, through CT scans and assignment of material properties based on grey values to account for nonhomogeniety of bones has been investigated.

In this paper, we will describe the results of the test done on the humerus. The optimized material properties for each bone that resulted in the best fit will be presented as the final result.

The Quasi-Static Test Setup

Three point bending tests with the impactor moving at constant velocity has been used. Figure 1shows the schematic arrangement for the static three point bending set up.

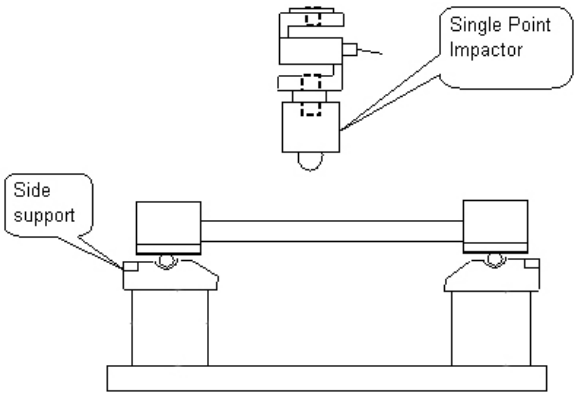

Figure 1. A schematic of the three Point Bending Setup

Figure 2 shows the pre-loading setup for the humerus. The ends are potted using bone cement and

a jig designed especially to maintain the desired alignment during the potting process.

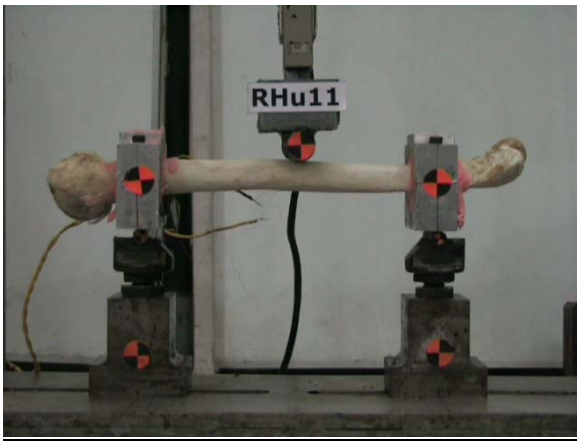

Figure 2. Initial setup of the quasi-static loading on the humerus

The Dynamic Test Setup

The freefall impactor rig, shown in Figure 3, comprises of an impactor of mass 30.5kg constrained to move between two vertical rails. A cable winch is used to raise the mass to desired height and a sprocket and cowl mechanism is used to hold and release the impactor. The drop height can be set to a maximum of 2m. A load cell in line with the impactor is used to record the impactor force and foam padding is used to arrest the impactor at the end of the stroke to protect the instrumentation. The specimen is positioned so that the bone fractures before the falling impactor comes in contact with the arresting foam.

The base plate, shown in Figure 3, supports the specimen through load cells. The specimen, set in the potting mounts, rests on these rollers mounted on top of the load cells to achieve simply supported boundary conditions.

The average mass of the humerus bones was 204.6 gms, that of the clavicle bones was 30.4 gms and that of the scapula bones was 86.55 gms. For testing the scapula which is not by structure amenable to bending tests, thin strips suitable for bending tests were extracted by milling. These bones were scanned using commercially available CT scanner and then tested.

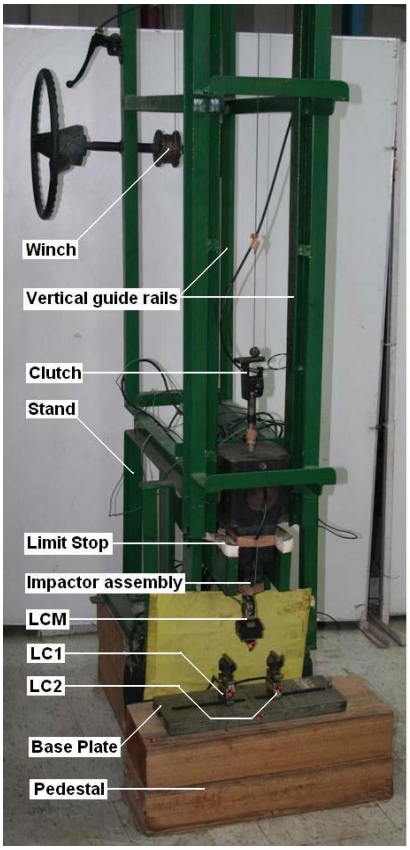

(a)

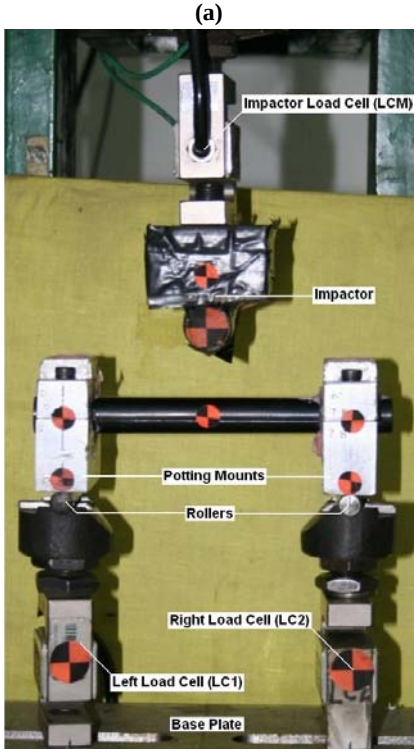

(b)

Figure 3. Freefall rig and base plate with supports (a) Full view (b) Close-up of Base Plate and mounts

Table 2. Test matrix

Type of test	Humerus	Clavicle	Scapula (spine)	Scapula (lateral border)
Quasi-static	4	4	5	5
0.5m drop	5	6	5	5
1.0m drop	5	6	5	5
1.5m drop	8	8	5	5
Total	22	24	20	20

Results of testing on Humerus

The quasi static response is presented in **Figure 4**. Four tests and the average of the tests with the ± 1σ band are shown. Dispersion of the stiffness and the failure point between specimens is large. The average stiffness has been projected to the largest displacement seen by the humerus to failure. The bones with higher stiffness have progressively higher force to failure but lower displacement to failure. This has not been reported by earlier researchers like Schriber [[7]]. Though the increase in failure force with increase of stiffness is consistent in the scapula and clavicle tests, the phenomenon of increased displacement to failure with increasing compliance is not observed in the clavicle or scapula tests.

Tests were conducted on four specimens at a drop height of 0.5 m, four specimens at a drop height of 1.0 m and six specimens at a drop eight of 1.5 m. The maximum strain rate achieved at a drop height of 1.5m is about 33/s. An average response was defined at each drop height with a spread. The point of failure was identified post-facto based on the high speed camera data and the earliest failure for a particular height was used to determine the time to which the averaging was done. The fracture point was all occasions after the first peak though this is not obvious from the average data for 1.5 m drop. It is seen that for larger drop heights, the peak forces are higher and the failure occurs earlier. It may be pointed put that the average response is not indicative of probable bone response for that drop height, but the probable bone response at that drop height before crack initiation.

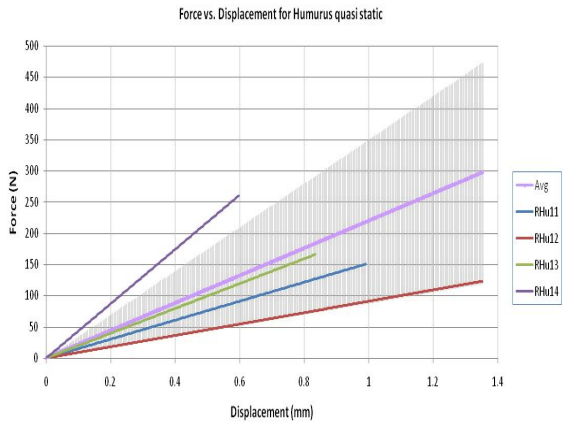

Figure 4. Force vs displacement response for humerus in three point bending.

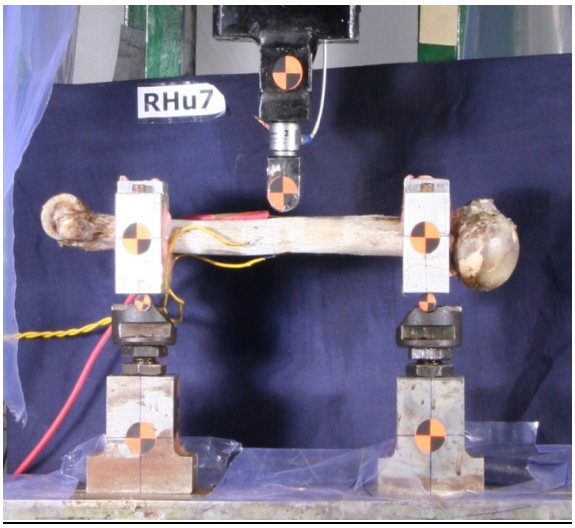

Figure 5. Initial setup of the impact test on the humerus

Figure 5 shows the pre-impact setup for the humerus. In dynamic tests, the mass and moment of inertia properties of the end fixation devices modify the response. These have hence been engineered to leave as small a footprint as possible and have been accurately estimated so that they can be reproduced in the simulations.

Finite element modelling and property extraction

The CT scan data of the bone with the response closest to the average curve obtained was used to

develop a bone model. The loading setup was modeled to mimic the tests in quasi-static as well as impact tests. The setup is shown in Figure 7 below.

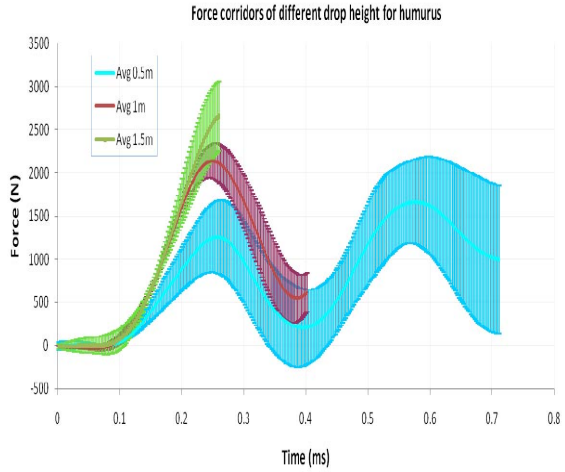

Figure 6 Force corridors for tests done with different drop heights on the humerus

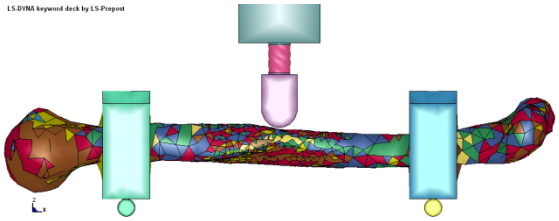

Figure 7. Typical FE model for drop test

The bone models are made of approximately 8500 linear tetrahedral elements made from about 2500 nodes. In order to decide the mesh size a convergence analysis was done by varying the mesh size in various regions of the bone. The bone FE model was finalized with two zones of different mesh density. Elements in mid-diaphysis region have an edge length of approximately 3.5 mm. This fine element region extends to 25mm on either sides of the point of impact. This is done to increase the accuracy of Hertzian contact stress approximation. The rest of the bone is meshed with elements whose edge lengths are approximately 7 mm. In the mesh, the minimum warpage was 5 and the minimum Jacobian was 0.7. Only 1% of the total elements had an aspect ratio more than 5. The average run time of a simulation was approximately 90 seconds when solved using 4 CPUs which clocks data at the rate of 2.33 GHz on a Core 2 Quad processor with 4Gb RAM.

Relationships between CT Hounsfield number, apparent density and elastic modulus were used to assign an *initial* density-dependent modulus for each tetrahedral element [[2]] in ten groups. The net mass of the bone was compared with the measured mass and if needed (variation was usually less than 5%) the density was scaled linearly to match the mass.

The dynamic tests were simulated in LS Dyna and the static tests were simulated in Abaqus. The RMS between the two responses was taken to be the objective function to be minimized by tuning the stiffness. The mapping between the Hounsfield number and modulus is taken to be bilinear with the transition occurring at Hounsfield number of 600 based on a histogram analysis. The parameters of the linear relationship along with yield strain and the maximum plastic strain were altered in the GA run in order to match the simulation response with the average experimental response. In addition, the C & P parameters in the Cowper Symmond's Model were altered in order to capture the shift in the yield stress with strain rate. This was seen to affect only a small set of elements near the point of impact. The optimized responses are shown alongside the average values in Figure 8, Figure 9, Figure 10 and Figure 11 respectively.

The correlations obtained through simulations are listed in Table 3 and have a average fit of 0.897. The quasi static tests consistently have very high fits and the 1.5 m humerus drop has fits of 0.684, which could be said not to be strongly correlated. The match between simulation and experiment for the lateral border of the scapula is not as strong as the rest of the tests. This could be due to problems in idealizing the boundary conditions of the test in the simulation.

Table 4 summarises the estimated properties for the humerus. The modulus obtained for quasi-static tests varies between 0.4 to 18 GPa while the modulus obtained from the drop height of 0.5m varies from 0.7 to 40.5 GPa, that obtained from a drop height of 1m varies from 0.8 to 40.95 GPa and that from the 1.5m drop tests varies from 1.8 to 53 GPa. The increase in modulus with strain rate is consistent with earlier studies including McElahney [[5]].

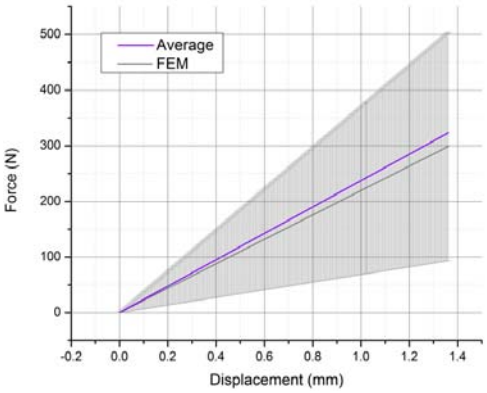

Figure 8 The average experimental and the FEM response for quasi-static test.

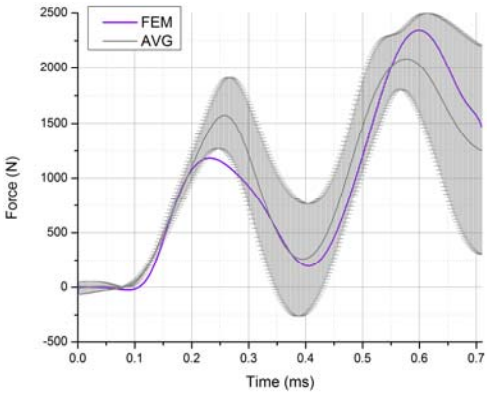

Figure 9 The average experimental and the FEM response for 0.5mtr drop height.

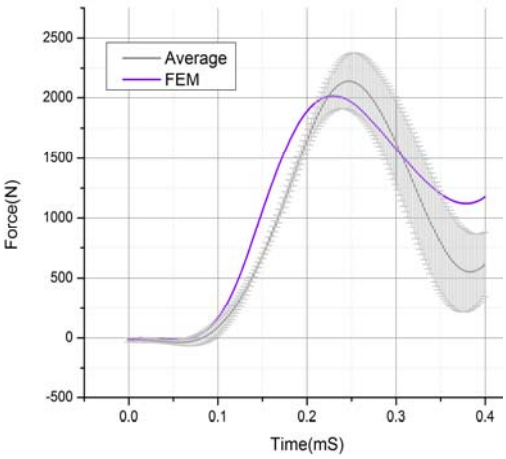

Figure 10. The average experimental and the FEM response for 1 m drop height.

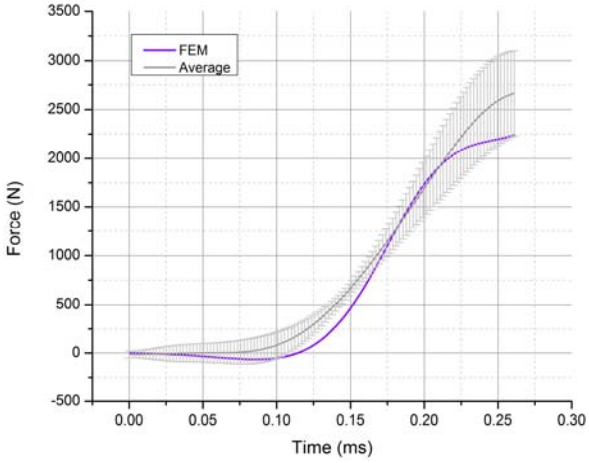

Figure 11. The average experimental and the FEMresponse for 1.5mtr drop height.

Table 3 Correlations against average experimental value

Humerus 0.5 m drop	0.85752
Humerus 1.0 m drop	0.90481
Humerus 1.5 m drop	0.68421
Humerus quasi-static	0.99963
Clavicle 0.5 m drop	0.94860
Clavicle 1.0 m drop	0.8011
Clavicle 1.5 m drop	0.92337
Clavicle quasi-static	0.99921
Scapula 0.5 m drop	0.99892
Scapula 1.0 m drop	0.99537
Scapula 1.5 m drop	0.70772
Scapula quasi-static	0.99949
Scapula(lat border) 0.5 m drop	0.68553
Scapula(lat border) 1.0 m drop	0.99952
Scapula(lat border) 1.5 m drop	0.85877
Scapula(lat border) quasi-static	0.99952

The response for clavicle and the corresponding estimates of properties have not been listed here for brevity. There are some different trends observed for the scapula which have been listed in the conclusion.

CONCLUSION

A procedure and instrumentation has been established to estimate region based bone properties that reproduce dynamic impact in FE based simulations.

For the same material densities, the modulus for the scapula is much lower than that for the humerus and

the clavicle. For the spine of the scapula, the modulus under dynamic conditions is lower than that under static conditions which is unexpected. It is also noted that in the dynamic tests, the spine of the scapula has a very different failure mode which seems to be similar to a shear failure. This could be resulting from the variance between the microstructure of the scapula and that of the other bones.

Table 4. Estimated modulus and yield stress

				Materials									
				Cancellous			Cortical						
				1	2	3	4	5	6	7	8	9	10
			Density	132	394	657	918	1181	1443	1705	1968	2230	2492
$\dot{\varepsilon}_{max}$			Hounsfield No	1 to 200	200 to 399	399 to 600	600 to 871	871 to 1142	1142 to 1413	1413 to 1684	1684 to 1955	1955 to 2226	2226 to 2500
0	ε_y	1.8	Young's Moudulus (Gpa)	0.413	2.98	5.55	5.55	7.61	9.69	11.76	13.82	15.9	17.96
	ε_{pf}	0	Yield Stress (Mpa)	7.44	53.7	100.1	100.1	137.1	174.5	211.68	248.89	286.24	323.5
13.5	ε_y	1.2	Young's Moudulus (Gpa)	0.7	2.4	4.06	4.06	10.1	16.2	22.3	28.3	34.4	40.5
	ε_{pf}	0.9	Yield Stress (Mpa)	8.91	28.8	48.77	48.77	121.3	194.4	267.2	340	413.12	486
20.5	ε_y	0.51	Young's Moudulus (Gpa)	0.807	3.76	6.729	6.729	12.41	18.13	23.83	29.53	35.26	40.95
	ε_{pf}	0.92	Yield Stress (Mpa)	4.11	19.2	34.31	34.31	63.28	92.47	121.54	150.62	179.8	208.9
33	ε_y	1.59	Young's Moudulus (Gpa)	1.8	6.2	10.6	10.6	17.6	24.7	31.7	38.8	45.9	53.01
	ε_{pf}	1.05	Yield Stress (Mpa)	29.31	98.8	168.6	168.6	280.5	393.3	505.56	617.87	730.61	842.9

It is our understanding that though the initiation of the fracture is predicted accurately, the propagation is not predicted accurately by the current method. This needs further refinement. The study is not extensive enough to characterize the full spectrum of crash victims. More tests are planned in the near future to normalize the specimen to specimen variation in the samples and evolve age and gender trends.

The process of optimizing the distribution of bone properties has been limited by the computing resources. A larger number of clusters than currently used could in principle be considered, leading to better fits. Similarly, instead of averaging the response, fitting the properties to individual geometry and estimating an average of properties may be considered as an alternative given more computational and manpower resources.

REFERENCES

[1] Dalmotas,D.J., (1983), Injury mechanisms to occupants restrained by three point seat belts in side impact, SAE transactions, 92(2), 2.328-2.354, SAE paper 830462, 1983.

[2] Dalstra, M., Huiskes, R., Odgaard, A., and van Erning, L., 1993, "Mechanical and Textural Properties of Pelvic Trabecular Bone," J Biomech, 26, pp. 523-35.

[3] Ferreira F, Vaz MA, Simoes JA, (2005), "Mechanical properties of bovine cortical bone at high strain rate", Materials Characterization, 2005.

[4] Holt, B.W. & Vazey, B.A, (1977), In depth study of seriously injured seat belt wearers, Report number 1/77, Traffic Accident Reasearch unit, Department of motor transport,1977.

[5] McElhaney J.H. (1966) Dynamic response of bone and muscle tissue. Journal of Applied Physiology 21, 1231-1236

[6] Sicking, D.L and K.K. Mak, Improving Roadside Safety by Computer Simulation, Transportation in the New Millenium, Transportation Research Board, Washington, D.C., January 2000

[7] Schreiber P., Crandall J., Micek T., Hurwitz S., Nusholtz G. S., "Static and Dynamic bending strength of the leg", IRCOBI Conference - Hannover, September 1997

[8] Shima V.P.W., Yanga L.M., Liua J.F., Leeb V.S., (2005), "Characterisation of the dynamic compressive mechanical properties of cancellous bone from the human cervical spine", International Journal of Impact Engineering, Volume 32, Pages 525-540, 2005.

[9] Westhuizen V.D., Cloete T.J., Kok S., Nurick G.N., (2007), "Strain rate dependent mechanical properties of bovine bone in axial compression", IRCOBI Conference, 2007.

EVALUATION OF BIOFIDELITY OF ECE REGULATION NO. 22 INJURY CRITERIA

Paul Rigby
Brett Juhas
Jessica Wong
Philemon Chan
L-3/Jaycor, San Diego CA
USA

Paper Number 11-0366

ABSTRACT

The biofidelity of the injury criteria of the European standard for motorcycle helmets (ECE Regulation No. 22, Section 7.3 Impact-absorption tests), were examined against biomechanically based injury metrics. Using a method to measure the helmet contact pressure on the headform during impact, twenty helmets were dropped according to ECE R22 free drop specifications. A total of 76 impacts to the front, crown, rear, right and left side of the helmet were examined using finite element simulations to predict skull fracture. The ECE R22 criteria, peak head acceleration and HIC, were correlated with these injury metrics.

It was found that ECE R22 criterion of peak headform acceleration is the best correlate with all injuries. HIC was an acceptable correlate for brain injury metrics but a very poor correlate to skull strain. The current peak headform acceleration limit of 275 g resulted in a 20% probability of skull fracture.

This research has shown that peak head acceleration can be an acceptable injury metric for skull fracture using the ECE R22 test method. The current ECE R22 linear acceleration limit of 275 g is slightly higher than the calculated thresholds of injury used in this study for skull fracture, 252 g for 15% probability of skull fracture. Even though a free head drop method was used, the resultant translational acceleration trace at the center of gravity of the headform proved no better at predicting concussion than the rigidly mounted FMVSS No. 218 headform. When headform rotation was measured and used in the SIMon analysis, an increase in the concussion injury metric was seen. In order to use SIMon as a brain injury analysis tool, unconstrained free drops with headforms instrumented to record angular motion are necessary.

A comparison of test results for helmets which were tested using both FMVSS No. 218 and ECE R22 methods was conducted. It was found that the peak head acceleration was an acceptable injury metric for skull fracture in both studies. Although FMVSS No. 218 and ECE R22 test protocols are different, both have a pass/fail criterion based on the peak head acceleration. Since peak head acceleration correlates to skull fracture, any future modification of the peak head acceleration criterion can be based on acceptable probability of skull fracture analysis.

INTRODUCTION

The National Highway Traffic Safety Administration (NHTSA) of the US Department of Transportation (DOT) estimated that motorcycle helmet use has increased from 48 percent in 2005 to 67 percent in 2009 (NHTSA 2009). However, in a 2007 NHTSA report, it was found that a motorcyclist is 34 times more likely to die than a person riding in a car. By wearing a helmet the likelihood of death decreases by 37 percent. In total cost, NHTSA has estimated that wearing a motorcycle helmet has saved $1.3 billion dollars in medical expenses in 2002 alone (NHTSA 2007). If everyone that was injured was wearing a helmet, a further $835 million would have been saved.

The objective of this study was to evaluate the biomechanical basis of the impact absorption requirements of United Nations Economic Commission for Europe (ECE) Motorcycle Helmet Regulation No. 22.05 versus known biomechanically-based injury criteria in the context of the ECE R22 test protocol. This study will also compare the biofidelity results with that of a previous study investigating the biofidelity of the U.S. helmet standard FMVSS No. 218.

ECE R22 Motorcycle Helmet Standard

The latest revision of ECE R22 was adopted in 2000. ECE R22 requires impact absorption, friction, rigidity, and retention system tests. This study will focus on the impact absorption test.

Impact-Absorption Test The underlying principle of the impact-absorption test is to "determine by recording against time the acceleration imparted to a headform fitted with the helmet, when dropped in guided free fall at a specific impact velocity upon a fixed steel anvil" (UNECE R.22 2000). To perform this test, the helmet is fitted to an ISO full faced headform. The ISO headform is defined by the EN960 standard. A single triaxial accelerometer is mounted at the center of gravity of the headform.

Unlike FMVSS No. 218 in which the headform is firmly attached to the rail, ECE R22 uses a free fall system that allows the helmet to freely move during impact. The helmet is set on a mobile system which supports the helmeted headform during free fall. The support system can either be guided using wires or attached to a rail system.

There are two types of anvils used, a flat steel anvil with a flat impact face (130 mm diameter) and a steel kerbstone anvil (Figure 1). The impact velocity against either anvil is 7.5 (+0.15 / -0.0) m/sec. The velocity of the moving mass is measured between 1 and 6 cm before impact and must be accurate within 1%.

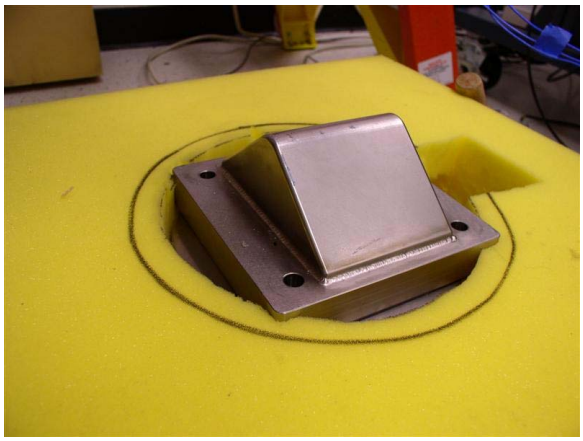

Figure 1. Kerbstone anvil used in ECE R22

Each helmet is impacted in four locations; the front (B), either side (x), rear (B) and crown (P). Each location is only hit one time. ECE R22 specifies the front visor to be impacted, however this was not performed for this study. The ECE R22 protocol also calls for impacts under ambient, heated, low temperature and ultraviolet radiation and moisture conditions. Each condition has an anvil type associated with it. Drops were restricted to ambient temperatures for this study (temperature 25°C ± 5°C, relative humidity 65% ± 5% for four hours).

To pass the impact-absorption requirement of ECE R22, the criteria

$$A_{max} \leq 275 \text{ g, and}$$
$$HIC_{36} \leq 2400,$$

must be satisfied for all drops on the helmet. A_{max} is the peak resultant acceleration of the headform. HIC is calculated as the maximum of the equation

$$HIC = \left[\frac{1}{t_2 - t_1}\int_{t_1}^{t_2} a(t)dt\right]^{2.5}(t_2 - t_1)$$

where a is the resultant acceleration in g and t_1 and t_2 are any two points in time during the impact.

HIC was developed in 1971 from modifications of the Wayne State University Tolerance Curve and Gadd Severity Index (Newman 1980). HIC was incorporated into FMVSS No. 208 and is widely used in the automobile industry. HIC is calibrated to be used with an unhelmeted Hybrid III head and as such does not characterize any one particular type of injury, but is a general measure for head injury. A HIC_{15} of 700 correlates to a 11% probability of an AIS 3+ injury (NHTSA 2008). When investigating how HIC correlates to a specific head injury criterion, Vander Vorst et al. (Vander Vorst, Stuhmiller et al. 2003) demonstrated that HIC correlates poorly with skull strain due to its high sensitivity to target compliance. Although, when the contact area is considered, HIC correlates well with strain. It is unknown how a helmet affects the HIC injury-risk function. It is also unknown how using a rigid metal headform instead of a Hybrid III head affects HIC.

The authors could not find documentation showing how the ECE R22 criteria of 275 g peak head acceleration and HIC_{36} of 2400 was decided upon. In March 1995, the original ECE Regulation No. 22 was amended to add in the 275 g and HIC_{36} of 2400 criteria. Previous to this amendment, ECE R22 drop tests were done at 7.0 and 6.0 m/s (depending on the anvil) with the following criteria, "the resultant acceleration measured at the centre of gravity of the headform is less than 150 g for any 5 msec continuously and at no time exceeds 300 g." FMVSS No. 218 is structured similarly in that it contains requirements limiting the dwell time of acceleration over 150 g to 4.0 msec and acceleration over 200 g to 2.0 msec.

For skull fracture, ECE R22 will be compared against the generalized linear skull fracture criteria. Vander Vorst (Vander Vorst, Stuhmiller et al. 2003; Vander Vorst and Chan 2004) first presented the linear skull fracture criteria called skull fracture correlate (SFC). SFC is the average headform acceleration over the HIC_{15} time interval. The HIC_{15} time interval is the

time duration, up to 15 msec, during which the peak HIC value is found. SFC was validated using post mortem human specimens (PMHS) data from the historical Hodgson and Thomas tests (Hodgson and Thomas 1971; Hodgson and Thomas 1973) and recent data from Medical College of Wisconsin (MCW). The PMHS data were correlated with Hybrid III headform tests and finite element model simulations. The first work (2003) demonstrated that the skull strain calculated by a finite element model (FEM), the fracture data and SFC all correlated well with one another with well defined confidence bands, hence validating the biofidelity of SFC. The following work (2004) expanded the validity of SFC to lateral impact using more newly obtained PMHS data. Chan et al. (Chan, Lu et al. 2007) developed a generalized linear skull fracture correlate using frontal and side impact PMHS data. The head impacts in this study involved side, frontal, and crown hits; therefore, the generalized SFC injury curve is used.

In the previous study on FMVSS No. 218, brain injuries were evaluated using the NHTSA SIMon finite element head model version 1 (Takhounts, Eppinger et al. 2003). It was found that driving SIMon using only translational acceleration did not produce significant injury metrics. It was concluded that both translational and rotational motion was necessary to achieve meaningful results from SIMon. Zhang et al. has shown that rotational motion contributes significantly to strain in the brain during impacts compared to translational acceleration (Zhang, Yoganandan et al. 2006). In this study, the rotation of the headform during impact and how it affects SIMon injury metrics will also be investigated. This will be achieved using a new nine accelerometer package system for the ISO headform. NHTSA released a newer version of SIMon in 2009 (Takhounts et al., 2008). The current study continued using the original version to be consistent with prior work done in evaluating the biofidelity of the injury limits in FMVSS No. 218 (Rigby et al., 2009).

METHODS

Instrumentation for Measuring Headform Pressure To predict the efficacy of a particular helmet using finite element calculations coupled with the head would require a validated structural model of the helmet. This task is impractical for each helmet model to be tested. However, if during a drop test, the pressure applied by the helmet to the headform were measured, and this pressure applied to the anatomical finite element model to compute the skull strain, then the probability of skull fracture could be predicted for the specific helmet. To accomplish this, instrumentation to measure the pressure contours on the headform was developed.

TekScan's FlexiForce sensors were chosen to measure the contact pressure between the helmet liner and the headform. Extensive tests were conducted to characterize the FlexiForce force sensors. The sensors were found to have acceptable drift, repeatability, and linearity when a normal force was applied. A drop in signal voltage was observed when the sensor was subjected to shear force. This negative voltage was proportional to the normal force acting on the sensor and was repeatable.

During the impact absorption test, the FlexiForce sensors attached to the headform would be subjected to shear forces, causing error in the experimental data. In order to get the true force from the sensors, the shear force experienced by the sensors was reduced by applying petroleum jelly directly to each FlexiForce sensor and then covering them with Teflon strips. Once the best method for reducing shear error was found, an array of sensors was glued to a Cadex (type J) medium size ISO headform. The sensors were attached using silicon adhesive sealant then the petroleum jelly and Teflon strips were applied. A total of 36 FlexiForce sensors were used to cover the impact area of the headform. A fully treated and instrumented headform is shown in Figure 2.

The FlexiForce sensors were distributed in a regular grid pattern, and it was assumed that the pressure measured by a sensor was uniform over the sub-grid area with the sensor at the center. For each impact configuration (crown, right side, left side, back, or frontal drop), it was assumed that the contact load would primarily be borne by the impact side of the headform and tangential loads were negligible. Therefore, the sensors were placed only out to the edge of the impact side of the headform. The total impact area was estimated for each impact configuration and distributed evenly to each sensor sub-grid area for inputs to the anatomical finite element model for skull fracture prediction.

Figure 2. Fully instrumented headform for crown drops.

Impact Absorption Tests One hundred drop tests were conducted to gather input data for the finite element model simulations. Impact absorption tests were performed according to specifications given in the ECE R22 document. The helmets were dropped in a guided free fall onto either a flat or a kerbstone anvil at a speed of 7.5 m/sec (ECE R22 Sec# 7.3). Half the tests were conducted against the flat anvil; the other half used the kerbstone anvil. There were four impact sites selected for each helmet: crown, front, right and left side (ECE R22 Sec# 7.3.4.2).

The acceleration of the headform was measured using a triaxial accelerometer placed at the center of gravity of the headform. The anvils were bolted onto a Kistler 925M113 load cell connected to a Kistler 5118B2 power supply/coupler which was in turn bolted to the cement floor. Headform acceleration, load cell force, and FlexiForce pressure data was taken by LabView version 7.0 on a BSI FieldGo Pentium 4 computer.

Twenty helmets were used in the tests. Helmet types consisted of a mixture of full face helmets, open face helmets, and half helmets. All helmets were designed and certified to HMVSS No. 218. No documentation on certification to ECE R22 was found. Each helmet was struck at all five of the impact locations. For each impact location, ten helmets were randomly selected to impact the flat anvil while the other ten helmets were then impacted against the kerbstone anvil. As per ECE R22 protocol (Sec# 7.4.2.1.2.1), the chin strap on each helmet was tightened as much as possible to secure the headform so that it did not shift before impact. In order to achieve a guided free fall, the helmet/headform assembly was placed onto the aluminum ring attached to the drop tower (Figure 3). A mesh bag was secured to the ring to catch the helmet after impact. All absorption tests were conducted at ambient conditions. The impact absorption test was the only type of test conducted; all of the other test procedures identified by ECE R22 (Sec# 7) were not done.

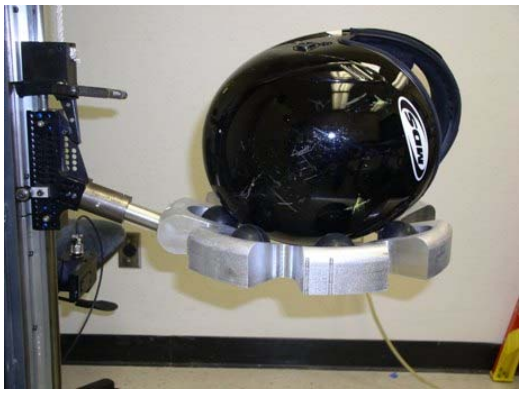

Figure 3. Impact absorption test setup.

Skull Fracture Finite Element Model The maximum principal skull strain was calculated for each impact absorption test using a refinement of the anthropomorphic, medical imaging-based, finite element model of Vander Vorst, et al.(Vander Vorst, Chan et al. 2004). The baseline model was composed of 24,000 elements and resolved the outer and inner tables, diploe, brain, scalp, and face. The mass of the baseline model was 4.54 kg. The skull components were modeled using fully integrated thick shells and the brain, scalp, and face were modeled with fully integrated bricks. Since this model was based on CT imaging of a PMHS, the skull shape and thickness are anatomically correct. The thickness of the compact skull tables was set to be 1 mm uniformly, since they were too thin to be resolved from the CT scan. The 1-mm value was based on measurements of photographic cross-sections from the Visible Man project (NIH 2000). The properties of the biological materials were taken from the open literature. The elastic properties of compact skull bone were from Wood (Wood 1971). Diploe was taken to be linear elastic (Khalil and Hubbard 1977). The linear viscoelastic properties of the brain were from Takhounts et al. (Takhounts, Eppinger et al. 2003). Scalp was assumed to be viscoelastic with properties calibrated by Vander Vorst et al. (Vander Vorst, Stuhmiller et al. 2003).

The sensor locations on the headform were mapped directly to the scalp elements of the skull fracture FEM (Figure 4). For example, if the headform had a line of seven sensors equally spaced from the anterior to posterior reference line, the location of the reference plane on the skull fracture FEM would be

determined and the seven sensor locations would be equality spaced similar to the headform. The maximum strain in either the inner or outer table of the skull for each test was found and used in the statistical analysis.

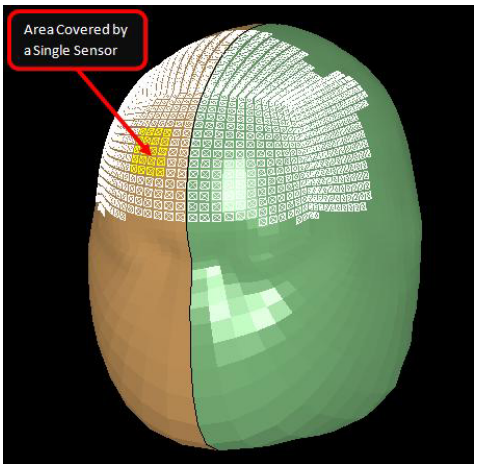

Figure 4. LS-Dyna finite element model showing the sensor locations for front impacts.

Headform Rotation Analysis In a parallel helmet study sponsored by the U.S. Army Medical Research and Material Command, a method for calculating the rotational motion of an ISO headform was developed. These methods from the HMSS study have been adopted into this study to more fully evaluate the ECE R22 helmet standard.

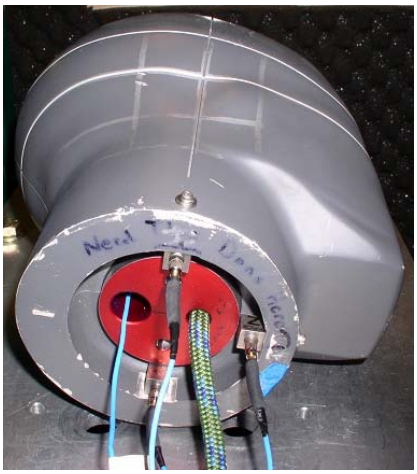

Figure 5. Picture of the headform equipped with linear accelerometers.

SIMon Methods and Results using Angular Velocity Data Four extra helmet drops were conducted on the front, crown, right and left side of a helmet using the NAP configured ISO headform in order to determine the effect rotation during impact has on SIMon brain injury results. Two SIMon cases for run for each impact. The first case was using only the translational acceleration data taken from the CG of the helmet. This is the same method used when examining ECE R22 in this study. The second case was to use both the translational acceleration and the rotational velocities for each impact. The three SIMon injury metrics (CSDM, DDM, and RMDM) were then plotted against each other in order to observe the effect of rotation.

Each test was computed out to 20 msec. Although helmets continued to move after 20 msec, both the translation and rotational acceleration due to the impact were over. The injury measures recorded were: cumulative strain damage measure (CSDM), dilatational damage measure (DDM), and relative motion damage measure (RMDM). SIMon reports CSDM values at various tolerances of strain. Takhounts et al., reports that a CSDM with a tolerance of 15% strain in the brain achieved the best correlation with diffuse axonal injuries compared to other tolerances. Therefore, CSDM with a tolerance of 15% strain was used in this study. The RMDM threshold for injury was established using only sagittal impact data. Data from side hits were not used to evaluate RMDM, only crown, front and rear impact results are reported as suggested in the SIMon documentation.

RESULTS

Impact Attenuation Tests A total of 20 helmets were used in this study. Each helmet was dropped once on the crown, front, right side, left side, and back in locations specified by ECE R22 protocol. Out of the 80 impacts performed, 59 tests were used in analysis. This was split up between 14 crown hits, 17 front hits, 14 right and 14 left side hits. A test was removed if 1) there was a misfire of the data acquisition trigger and the data for the drop was not recorded, 2) if it was found that more than 3 FlexiForce sensors were broken during impact, or 3) if the impulse of the head computed with the FlexiForce was more than 50% off from that calculated using the headform accelerometer. The majority of the tests removed were due to misfires of the data acquisition software.

Thirty percent of the helmets passed the current criteria for ECE R22. Helmets that failed to pass, failed both the peak acceleration limit and the HIC limit for the majority of the cases. There was significantly more failures when the flat anvil was used compared to the kerbstone anvil. For all drops

combined, drops against the flat anvil had a 47.5% pass rate and drops against the kerbstone anvil had an 87.5% pass rate. There was not a single case where identical helmets passed on a flat anvil but failed on the kerbstone anvil. However, there are multiple cases where identical helmets failed on a flat anvil but passed on the kerbstone. The majority of the failures happened on the crown against the flat anvil, achieving a 20% pass rate.

Since the FlexiForce sensors did not cover the entire contact area between the helmet and the headform, it was unknown if the sensors would pick up the entire load delivered to the headform. In order to determine if the correct loading was applied, the FlexiForce force data was validated against the headform accelerometer data. The total vertical component of the force from the FlexiForce sensors was computed and divided by the mass of the headform to get the resultant head acceleration. Each FlexiForce sensor was assumed to cover both its area and a portion of the surrounding area. This provided complete surface area coverage in the finite element model. The impulse of the headform was also calculated using both the FlexiForce and accelerometer data (Figure 6).

If the measured accelerometer impulse and the calculated FlexiForce impulse were not equal, a factor was applied to the FlexiForce pressures to preserve the accelerometer measured impulse at the peak acceleration. This was to assure a conservation of impulse between the acceleration data and the FlexiForce data. Since the FlexiForce sensors were assumed to cover its own area and the area around it the impulse calculated from the FlexiForce sensors could be slightly off, especially if only a few sensors recorded the majority of the impact force. This impulse factor ranged from 0.80 to 1.50 with an average of 1.17. This factor was applied to the pressures at each sensor for the finite element calculations. The headform acceleration and impulses data measured by the accelerometer and those calculated from the scaled FlexiForce data were in good agreement, as shown in Figure 6. All FEM calculated peak head acceleration values were within 10% of the experimental values.

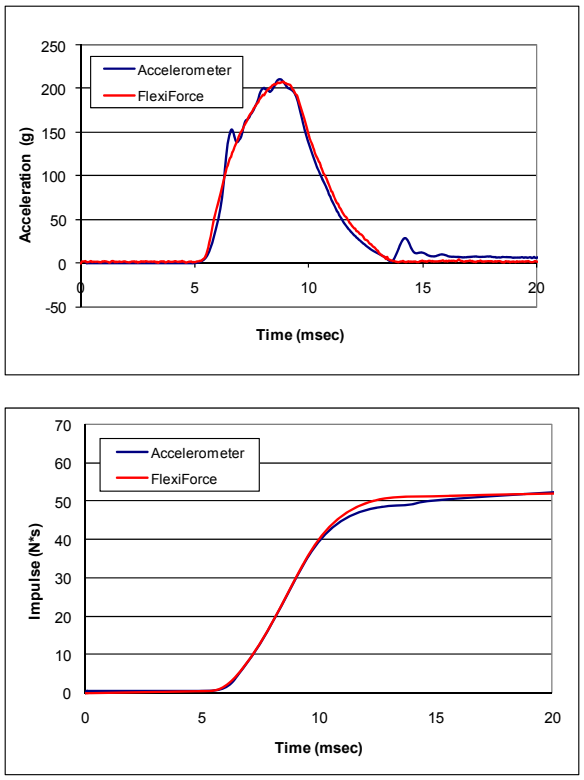

Figure 6. Head Acceleration and Impulse Data Comparison

Skull Fracture Evaluation A finite element simulation was performed for each impact attenuation test which passed the headform impulse criterion. The FlexiForce pressure measurements were used as inputs in to the model. Each simulation was analyzed out to 20 msec. After the drop simulation was completed, the maximum principle strain in either the outer or inner table of the skull was determined. The peak strain for the test was determined by averaging the strain-time history of the element in the model with the peak strain with all of its neighbors. By averaging a group of elements, single element anomalies can be avoided. The headform acceleration was also calculated by the FEM and compared to the experimental values. In each case, the FEM-calculated head acceleration trace closely matched the experimental results. Characteristic contour plots of the pressure applied to the scalp and the resulting pressure transmitted to the skull are shown in Figure 7.

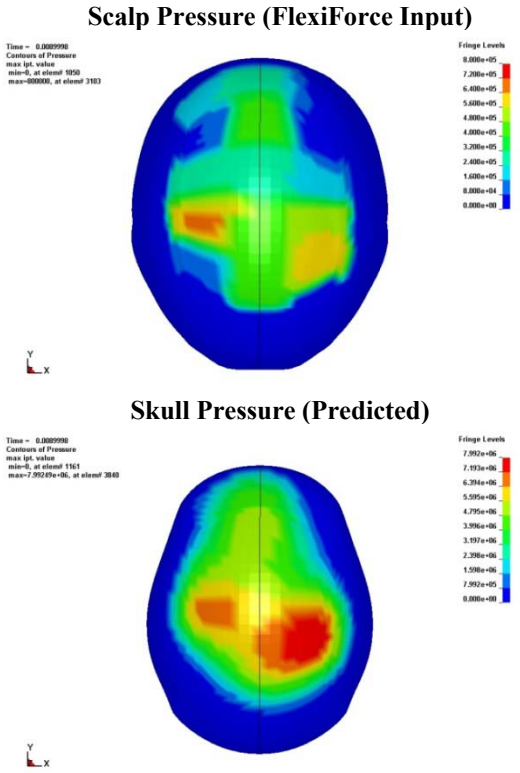

Figure 7. Pressure Contour Plots of Scalp and Skull

The finite element model did not reach the termination time of 20 msec for a few of the side impact cases. This was due to excessive deformation of the scalp from the very high pressures recorded during these drop tests. In these cases, the model was run out until failure and the last recorded skull strain was used. Failure usually occurred within a millisecond of the peak input pressure; therefore, it was assumed that the strain values are close to the actual values.

An adjustment of the SFC risk curve for the rigid ISO EN960 full faced headform was made using the finite element results. The standard SFC risk curve was originally established for the Hybrid III headform with an outer rubber skin, with 15% probability of skull fracture predicted by SFC=124 g (Chan, Lu et al. 2007), but this value will change for the rigid headform with no skin. Fortunately, skull fracture can be predicted using the skull strain calculated from the anthropomorphic FEM. Therefore, the SFC risk curve was adjusted for the ISO full faced headform by correlating the SFC values calculated from the headform acceleration with the skull strain calculated from the FEM (Figure 8). For 15% probability of skull fracture, which corresponds to 0.19% of skull strain, the SFC value will be 189 g for the ISO full faced headform. However, as can be seen in Table 1, the correlation for all ECE R22 tests combined was R^2=0.39. This is lower as compared to the correlation observed in the previous Rigby and Chan FMVSS No. 218 study (R^2 = 0.66). Different from the FMVSS No. 218 study where correlation was relatively consistent in the three drop conditions with R^2 values of 0.48, 0.65 and 0.69, there was a much broader range of R^2 values in the current study with values as low as 0.39 in left side drops to 0.81 in crown drops.

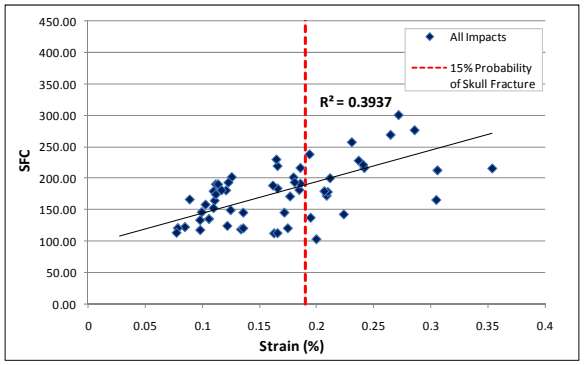

Figure 8. Correlation between SFC and Skull Strain for ISO Headform

Table 1. Strain Correlates

	Strain vs. Acceleration			
	22-05		218	
Condition	R^2	15% Prob Value	R^2	15% Prob Value
All	0.518	251.790	0.675	208.155
Left Side	0.555	202.660	0.738	274.929
Right Side	0.822	213.734		
Front	0.513	297.923	0.507	262.954
Crown	0.904	310.897	0.638	178.827
	Strain vs. SFC			
	22-05		218	
Condition	R^2	15% Prob Value	R^2	15% Prob Value
All	0.394	189.448	0.656	149.793
Left Side	0.392	166.296	0.690	193.325
Right Side	0.530	167.431		
Front	0.463	225.555	0.476	200.670
Crown	0.813	218.241	0.651	128.219

	Strain vs. HIC			
	22-05		218	
Condition	R^2	15% Prob Value	R^2	15% Prob Value
All	0.213	2576.84	0.616	1417.152
Left Side	0.043	2506.36	0.690	1923.354
Right Side	0.415	1672.34		
Front	0.500	3205.50	0.425	2115.330
Crown	0.795	3034.14	0.627	2258.890

SFC Correlation Using the ECE R22 injury criteria, peak head acceleration and SFC have a correlation value of $R^2 = 0.91$ (Figure 9a). SFC and HIC have a correlation value of $R^2 = 0.87$ (Figure 9b). Using the adjusted SFC for 15% probability of skull fracture of 212 g, an adjusted peak acceleration of 238 g is given. A HIC of 2265 g would correspond to a 15% probability of skull fractures based on the SFC limit of 189 g.

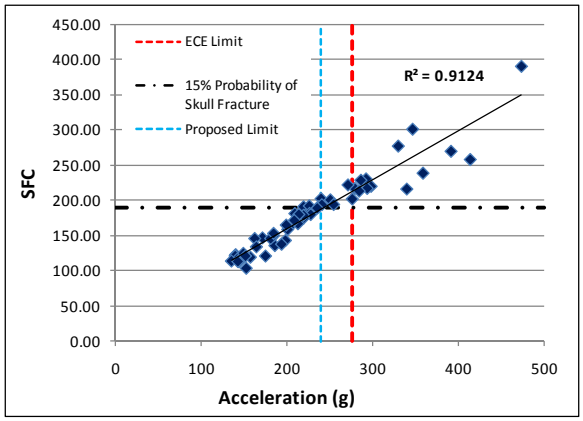

(a) SFC vs. Peak Head Acceleration

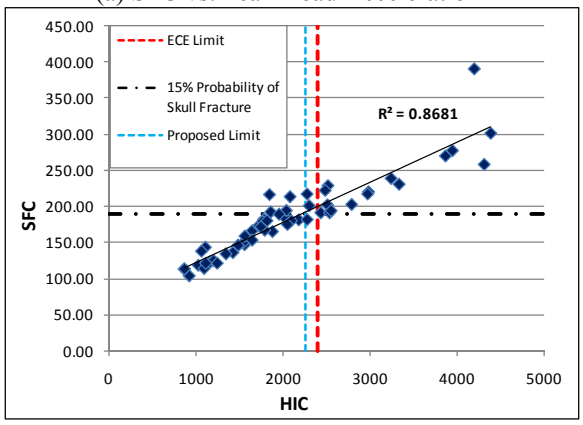

(b) SFC vs. HIC.

Figure 9. SFC comparison.

Strain Correlation The correlation of peak head acceleration and peak skull strain was $R^2 = 0.52$. However, the correlation was higher when looking at individual drop conditions with R^2 ranging from 0.51 in frontal drops to 0.90 in crown drops (Table 1). However, if the linear regression is banded by one standard deviation limits, 83% of the data points are within one standard deviation error. Using the linear regression equation, a peak head acceleration of 252 g correlates to a 15% probability of skull fracture. This acceleration limit is close to the 238 g value based on the SFC comparison. The correlation between HIC and peak skull strain was $R^2 = 0.22$. Given the low correlation between peak strain and HIC, no adjusted HIC limit was determined (Figure 10).

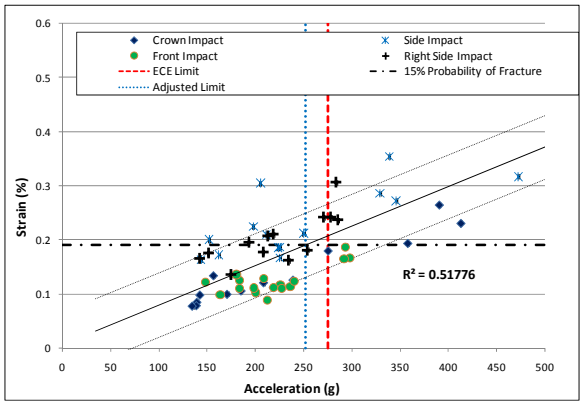

(a) Skull Strain vs. Peak Head Acceleration

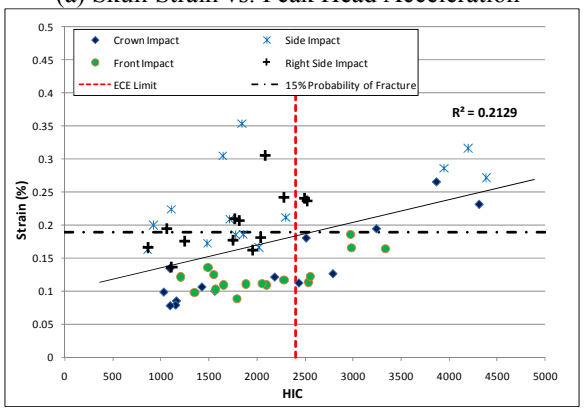

(b) Skull Strain vs. HIC

Figure 10. Skull Strain Comparison

HIC Correlation The correlation between HIC and peak head acceleration is $R^2 = 0.82$ as seen in Figure 11. The ECE R22 HIC limit of 2400 g corresponds to a peak head acceleration of 261 g.

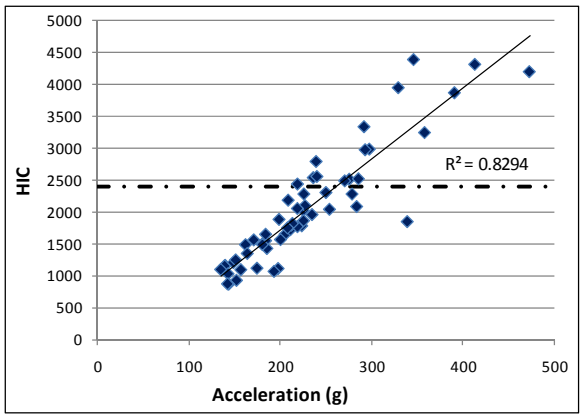

Figure 11. HIC Comparison

The overall results show that peak head acceleration appears to be the better correlate with the biofidelic injury metric strain, especially if impact direction is examined instead of looking at all directions as a whole. While HIC correlates well with other injury metrics (peak acceleration and SFC), it is a poor correlate to strain. A summary of the peak head acceleration comparison results are shown in Table 2, which also indicates the peak acceleration adjustments according to the published limits for the various damage measures. The current ECE R22 acceptable peak head acceleration of 275 g is slightly higher than the adjusted peak head accelerations to meet the published injury criteria for skull strain and SFC.

Table 2. Summary of Damage Measures based on Finite Element Models

Damage Measure	**Injury at 275g (ECE limit)**	
	Measure	Probability
Skull Strain	0.19%	15.0%
SFC	212	33.0%
	Published Injury Limit	
	Measure	Probability
Skull Strain	0.19%	15%
SFC	189	15%
	Headform acceleration at published injury risk levels	
Skull Strain	252g	
SFC	238g	

Comparison to FMVSS No. 218 Helmet Study Sixteen out of the twenty helmets used in this study are the same or a very similar model helmet that was used in the previous study evaluating the biofidelity of FMVSS No. 218. The peak headform acceleration, peak strain, and HIC values computed in this study were plotted against the values determined in the FMVSS No. 218 study to determine any correlation between the standards. It must be noted that helmets in the FMVSS No. 218 study were dropped at 6.0 and 5.2 m/s against flat and hemispherical anvils, respectively. Helmets in the ECE R22 study were dropped at 7.5 m/s against flat and kerbstone anvils. FMVSS No. 218 helmets were also dropped twice at the same location compared to once in the ECE R22 study. The injury metrics from the FMVSS No. 218 study are plotted against the same helmet's injury metrics from the ECE R22 study in Figure 12. Although FMVSS No. 218 requires two drops on the same location, only the first impact was used with ECE R22 comparison. No injury metrics show correlation between FMVSS No. 218 and ECE R22 for drops on the same helmet. This is probably due to the significant differences between headforms, test apparatus and testing protocol. FMVSS No. 218 uses a DOT half headform that is rigidly mounted to the drop tower assembly. ECE R22 used an ISO full faced headform that is dropped and allowed to freely bounce upon impact. While both protocols impact against flat anvils, FMVSS No. 218 tests against a hemispherical anvil and ECE R22 tests against a kerbstone anvil. ECE R22 also has a higher impact velocity than FMVSS No. 218. The combination of differences results in injury criteria which are not able to be correlated between the two standards.

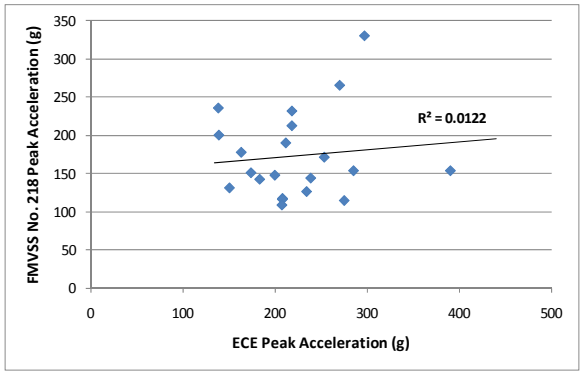

(a) Peak Acceleration

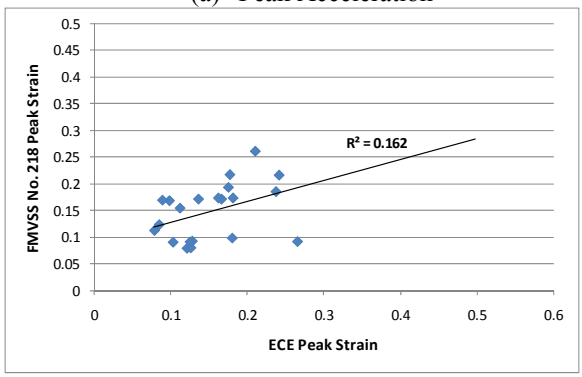

(b) Peak Strain

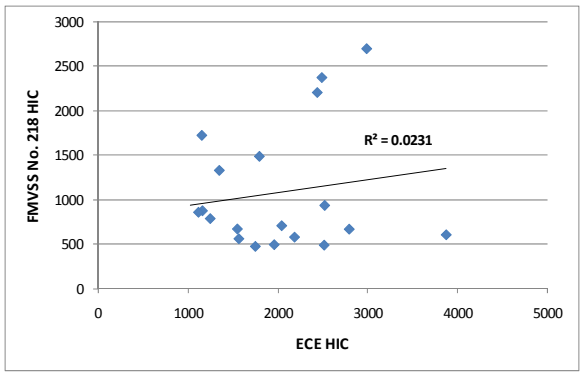

(c) HIC

Figure 12. Comparison of ECE R22 and FMVSS No. 218 Results

One commonality between the ECE R22 and FMVSS No. 218 tests were the use of a flat anvil. Of the helmets that were used in both studies, a comparison of data where drops were made against flat anvils was conducted to determine if the trends of both experimental methods agree. For both studies, helmets were randomly assigned to impact a flat or non-flat anvil for each impact direction. Due to the small number of helmets that fit the criteria of being used in both studies and impacted in the same orientation on a flat anvil, a comparison of the linear regression trend for all impacts against the flat anvil for both studies was conducted.

As seen in Figure 13a, the peak strain vs. peak acceleration trend line for both the FMVSS No. 218 study and the ECE study are similar. The ECE linear regression equation is y = 560.06x + 153.93, while the FMVSS No. 218 linear regression equation is y = 658.51x + 117.36. The similarity of slopes and a slight offset in the y-intercept demonstrates that when a common impact surface is employed, both test methodologies predict very similar peak strains.

Figure 13b shows that there is a difference in the trends between HIC and peak strain for the two standards. The ECE R22 trend predicts a higher HIC value and the same strain percentage when compared to the FMVSS No. 218 data. Also the correlation coefficient of $R^2 = 0.1689$ is much lower than that of the FMVSS No. 218 study.

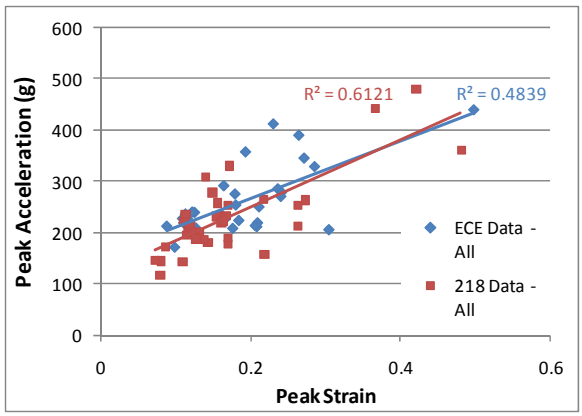

(a) Peak Acceleration

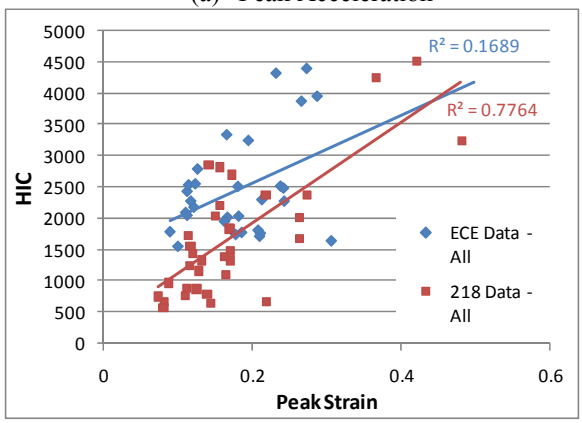

(b) HIC

Figure 13. Comparison of correlation trends using only flat anvil data

SIMon Results using Rotational Data

Four drops were made separate of the previous tests conducted to evaluate ECE R22 to investigate the affect rotation has on the brain injury correlates calculated by SIMon. The drops were all conducted on different helmets with one drop to the front, one to each side and one to the crown. A sample angular velocity used as inputs for SIMon is shown in Figure 14. From this plot, it can be seen that the headform experiences a large angular velocity on side drops and little rotation from crown drops.

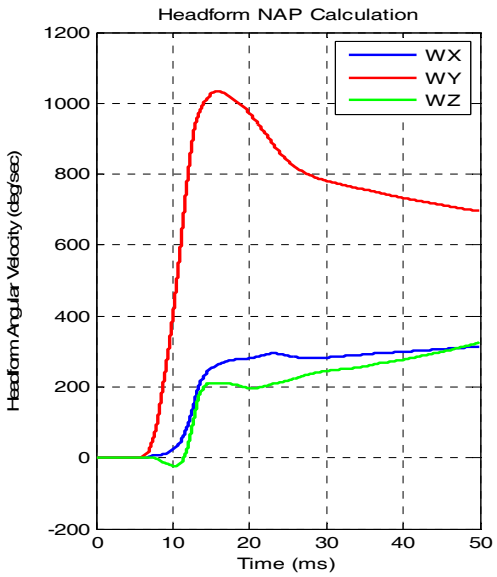

Figure 14. ISO Headform NAP Calculation for Front Drop.

Figure 15 through Figure 16 show the SIMon results for the four drops. SIMon was first run only using the headform center of gravity translational acceleration data. It was then repeated using the CG translational acceleration and the headform rotational velocity calculated by the NAP. In all cases except the crown impact, there was an increase in the CSDM result. However, only the right side impact case showed an increase of the CSDM result near the 50% probability of concussion range. DDM also increased for each hit location, although DDM results approached the threshold for 50% probability of injury. Finally there was a large 41% and 33% increase to the RMDM metric due to rotation. The side impact RMDM was not calculated due to RMDM not being validated for side impacts.

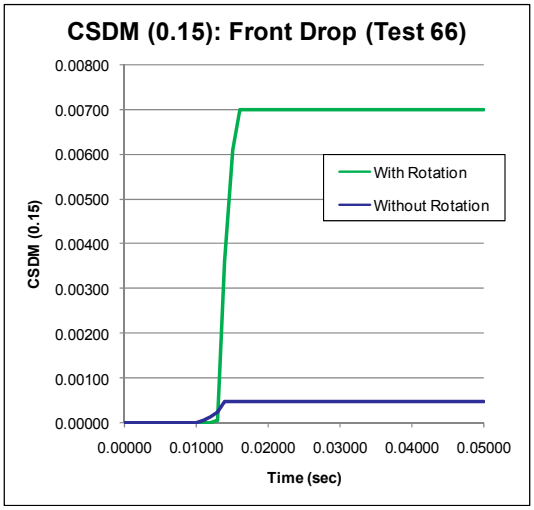

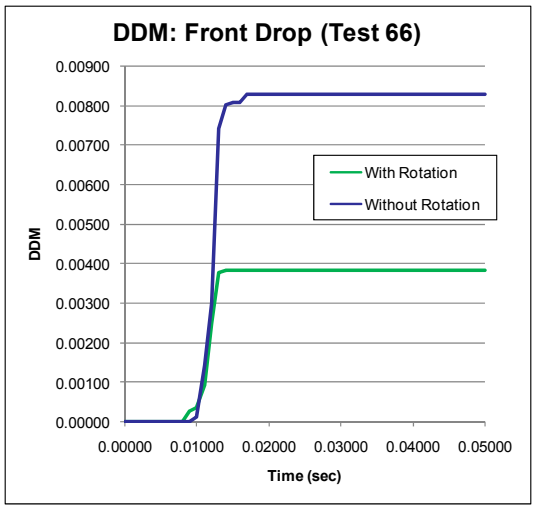

Maximum RMDM	
With Rotation	0.5539
Without Rotation	0.3928
Increase with Rotation	41%

Figure 15. SIMon Results for Front Drop with Rotation

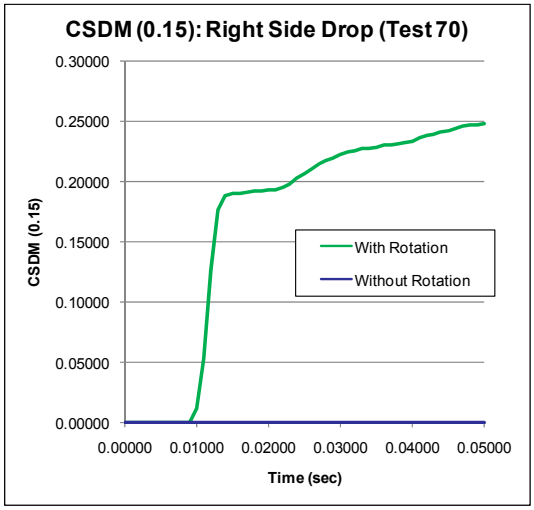

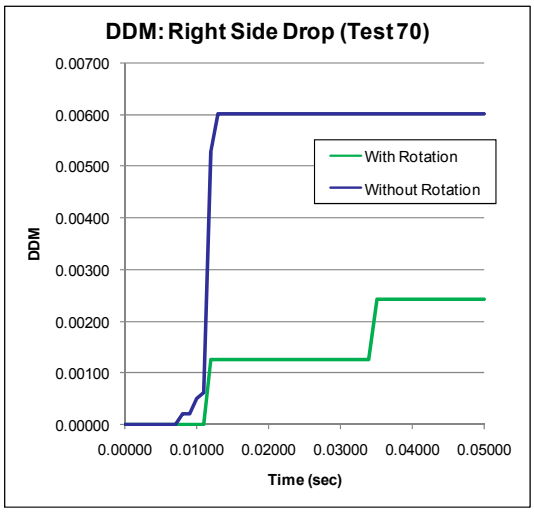

Figure 16. SIMon Results for Right Side Drop with Rotation

DISCUSSION

There are significant differences between the ECE R22 and the FMVSS No. 218 testing methods and pass/fail criteria. FMVSS No. 218 uses a headform constrained to the drop rail traveling at either 6.0 or 5.2 m/sec, against flat and hemispherical anvils respectively. ECE R22 uses a free headform traveling at 7.5 m/sec against both flat and kerbstone anvils. Both standards use resultant peak head acceleration as one of the criterion although FMVSS No. 218 allows peak accelerations up to 400 g while ECE R22 limits the threshold to 275 g. FMVSS No. 218 also uses the time duration of the impact above 150 g and 200 g as pass/fail criteria. ECE R22 uses a HIC36 threshold of 2400.

There was a wide range of correlation values between impact locations in the ECE R22 tests when compared to the FMVSS No. 218 set of experiments (Table 1). The crown had the highest correlation for all injury metric. This is probably due to less rotation, symmetrical loading, a greater surface area on the head interacting with the helmet and the least amount of designed objects on the helmet (visors, etc.) causing different helmet responses. In contrast, the back of the helmet had the lowest correlation coefficient in all cases. Side impacts also had visor mounts which could interfere with the contact dynamics.

The FMVSS No. 218 tests had similar correlation values for all impact directions. This discrepancy between standards could be due to the different dropping mechanisms (one fixed and one free). There could be an effect caused by rotation on the measured pressures that was unforeseen. The sensors are designed to measure normal forces and special care was taken to reduce all shear forces on the sensors.

As in the FMVSS No. 218 tests, there were a number of side impacts where single or small group of FlexiForce sensors reported very high impact forces. However, Table 1 shows that for ECE tests, there was a lower peak head acceleration needed to cause a 15% probability of skull fracture for side impacts than other impacts. The FMVSS No. 218 data showed that the peak acceleration in side impacts and front impacts are similar but that crown impacts have a lower acceleration limit for 15% probability of skull fracture.

There are a number of factors that complicate the experiments and can cause the discrepancies shown. The helmet visor location and connection point of the visor on the helmet vary among helmets and can cause impacts loads to be distributed differently depending on exact impact location. The loading and rotation of the helmet when impacting a flat or kerbstone anvil can vary against tests on a hemispherical anvil.

The impact loading on the skull can also change due to the contact area between the helmet and the headform. Table 3 shows the average contact surface area for impacts from three different directions.

Table 3. Approximate Impact Area According to Location

Impact Direction	Surface Area (cm^2)
Crown	194.6
Front	146.2
Right Side	109.2

By comparing the contact area for the different impact locations and assuming the total load for each drop will be equal, localized parts of the skull will see nearly twice as much force in side impacts than crown impacts. The figure below shows the FlexiForce pressure traces during a side impact for a distributed and focused loading case. Figure 17a shows the pressure on the scalp distributed over 110 cm^2 with peak pressures near 2300 kPa. Figure 17b shows a small number of FlexiForce experiencing the loading over a 30 cm^2 contact area. As a comparison, a typical crown impact is shown in Figure 17c. The peak pressures seen in the crown impact are half of those seen in the side impact (a). The duration of loading is also longer in the crown impact when compared to the side impact, 12 msec duration compared to 7 msec.

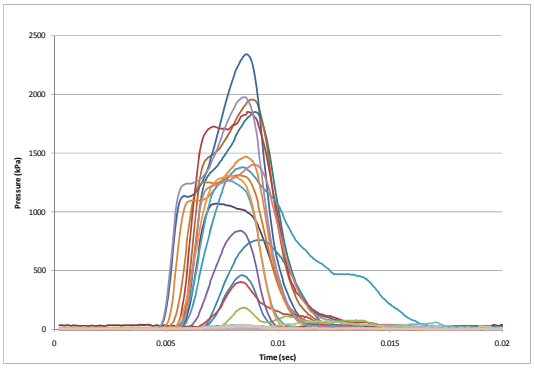

Distributed Side Load

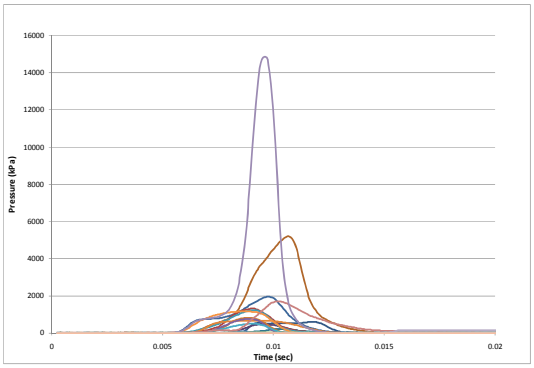

Focused Side Load

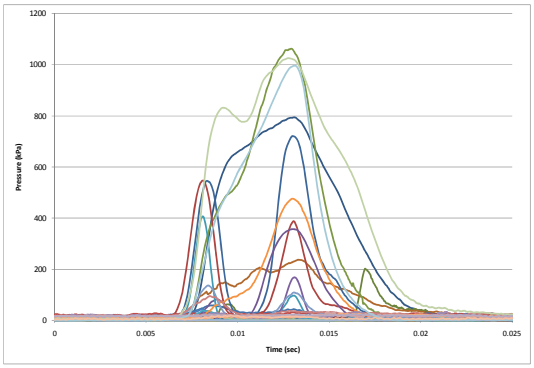

Distributed Crown Load

Figure 17. Distribution of Load During Impact

As with the FMVSS No. 218 study, the skull fracture analysis results show that peak acceleration is a good indicator for skull fracture, especially if impact orientation is examined. The front, crown and back impacts all had similar correlation trends and the side impacts correlated together. It is when all impacts are correlated together that the R^2 value drops.

The correlation between SFC and skull strain was low ($R^2 = 0.24$) and therefore SFC should not be used as a biofidelic injury metric in this case. The SFC correlate could be significantly off if there were areas of local high pressure on the skull. SFC assumes that forces are applied over the whole impact area and the fractures that occur are linear skull fractures. SFC will not be able correlate well with peak strains calculated from the FEM under these circumstances.

The adjusted peak head acceleration using peak skull strain as the injury metric should be 278g. This recommended limit is higher than that proposed in the FMVSS No. 218 study (214 g) in Rigby et al. (2009). This could be due to the method of impact (rail constrained head vs. free head) and the difference in shape of the half-head DOT headform and the full-faced ISO headform. As shown in Figure 12, there are significant differences between injury metrics determined using the same helmet but different test protocol and test equipment. The peak accelerations determined using peak strain which correlate with 15% probably of skull fracture are very close to the current ECE R22 peak head acceleration limit of 275 g.

HIC did not correlate well with the most biofidelic skull fracture metric, peak skull strain. It did correlate well with other injury correlates which were also calculated from the headform acceleration trace, SFC and peak head acceleration. The HIC value of 2400 correlates with a peak acceleration value of 261 g. This value also happens to be close to the peak acceleration value at 15% probability of skull fracture (Table 2). Based on peak acceleration limits, the 2400 HIC limit is appropriate. Using the SFC – HIC analysis, the HIC that correlates to 15% probability to skull fracture (2403) is very close to the current HIC criterion of 2400. However, as stated before, HIC is calibrated for the Hybrid III dummy head and not a rigid headform.

The COST 327 study concluded that HIC correlated better with the Abbreviated Injury Scale (AIS) for the head than peak acceleration or impact speed (COST 327 2001). Consistent with previous research, COST 327 found a HIC of 1000 predicted an AIS of 2 and a HIC of 1500 predicted an AIS of 3. It is still unknown what the transfer function (if any) is between a HIC calculated on a Hybrid III and that calculated on an ISO headform.

As shown in the previous FMVSS No. 218 study, only using the translational acceleration of the headform is not adequate for predicting concussion using the SIMon model. The ECE R22 results were very similar to those seen in the FMVSS No. 218 study for CSDM when only translation acceleration was used in the model. Even with a free headform, not accounting for rotation causes a prediction of just 1% probability of concussion. When rotational data is used along with translational acceleration in SIMon, the CSDM value greatly increases, especially for

large angular velocity cases such as side impacts. The right side impact test case showed a CSDM value of 25% which correlates to approximately a 20% chance of concussion. However, for almost every impact in this study, the peak head acceleration was above the published limits for concussion. Given these results, the use of CSDM as calculated in SIMon is not recommended to be used as a measure for concussion.

The Wayne State Tolerance Curve, based on a linear acceleration criterion, predicts a threshold of 60 to 80 g for concussion. Pellman et al. (Pellman, Viano et al. 2003) found the peak acceleration in concussion-causing impacts in professional American football to be 98 ± 28 g. Using small primates data obtained from Ono et al (Ono, Kikuchi et al. 1980) with scaling to humans, Vander Vorst et al. (Vander Vorst, Ono et al. 2007) estimated a 175 g peak linear acceleration limit for 10% probability of concussion. By conducting tests that measure pressure load transmitted to the headform and both translation and angular acceleration of the headform, the injury models can be used to their full potential providing more accurate skull fracture and brain injury predictions.

Thresholds for subdural hematoma injury are usually correlated with rotational acceleration. In order to fully analyze the subdural hematoma, the rotation of the head needs to be measured. A headform integrated with rotational motional sensors, such as a NAP system, should be used. Using PMHS, critical thresholds for injury have been suggested to be 4500 rad/s^2 for durations 15 to 50 msec (Lowenhielm 1974) and 10,000 rad/s^2 for durations under 10 msec (Depreitere, Van Lierde et al. 2006). The right side impact test case using the NAP equipped ISO headform had a peak angular acceleration of 14,400 rad/s^2. The rotational acceleration was above 10,000 rad/s^2 for 2 msec and above 4,500 rad/s^2 for 4 msec. The ECE R22 test conditions can provide the conditions to produce subdural hematoma.

The ECE R22 and FMVSS No. 218 contusion results are also similar. ECE R22 results suggest a 15% probably of contusion at the current criterion of 275 g peak head acceleration. FMVSS No. 218 reported a 23% probability at 400 g. Both results agree with other real world estimates detailed in the previous FMVSS No. 218 study (COST 327 2001; Vander Vorst, Ono et al. 2007). The trend in the DDM results varied when the rotation was added to the analysis. For some impacts the DDM value increased due to rotation, while in others it decreased. As detailed in the SIMon documentation (Takhounts, Eppinger et al. 2003), DDM is based on the percentage of the brain tissue experiencing a -100 kPa pressure and undergoing cavitation. It is expected that the addition of rotational data will not overly influence this due to cavitation being primarily linked to translational acceleration. While DDM is less influenced by rotational movement, the fact that DDM values did change given the inclusion of rotational data indicates that drawing conclusions from the DDM values calculated from the drops on the 20 helmets tested in the current study may not be appropriate.

If skull fracture is the primary metric in which a standard would base its pass / fail criteria on, either the rail drop system used by FMVSS No. 218 or the free head drop of ECE R22 are acceptable. Both test methodologies showed peak head acceleration and SFC to correlate highest with skull strain. However, the current study results of ECE R22 tests did show lower correlation between peak head acceleration and SFC to peak strain with R^2 values of 0.52 and 0.39, respectively versus 0.68 and 0.66 in the FMVSS No. 218 study. The R^2 value of 0.52 is low and additional tests using ECE R22 certified helmets could be used for further refinement.

If rotationally induced brain injury metrics are to be considered then a test protocol that allows for headform rotation should be considered. The ECE R22 method will also need to be modified to accept additional NAP sensors on the headform. Otherwise, as demonstrated in this study, there is no benefit to free head drops. All brain injury metrics calculated by SIMon in this and the previous FMVSS No. 218 study were very similar when only the translational acceleration at the CG of the headform is used.

When the results from the same helmets used in the FMVSS No. 218 study were compared to those in the ECE R22 study, there was little correlation between them. The best correlate was peak skull strain followed by peak head acceleration. This is probably due to a number of factors in the way the tests were conducted. The speeds of the FMVSS No. 218 impacts were not consistent between anvils as were the ECE R22 impacts. By having some FMVSS No. 218 impacts at 5.2 m/s and others at 6.0 m/s depending on the anvil being hit, the correlation could be disrupted. The anvil type is also thought to influence the results. It was noted in the FMVSS No. 218 study that hemispherical impacts to the side of the helmet caused local areas of significant high pressure, this in turn then causes a large skull strain. The use of free drops with a fully instrumented headform able to measure angular velocities is

necessary if both skull fracture and brain injury evaluation are of interest.

Limitations The correlation between injury measures based on CG accelerometer data (peak acceleration and SFC) and peak skull strain was quite low compared to the same correlation in the FMVSS No. 218 experiments. However, when broken down into the various impact orientations, the correlation coefficients increased. For the ECE R22 experiments, the side impacts correlations between peak head acceleration and HIC versus peak skull strain was quite different than that of the other impact orientations. This is seen by the low injury metric values for 15% probably of skull fracture in Table 1. For the FMVSS No. 218 study, the crown impacts had injury metrics for 15% probability of skull fracture at lower values compared to other impact sites.

CONCLUSION

The biofidelity of the injury criteria used by ECE R22 were examined against biomechanically based injury metrics. Helmet drop tests were conducted using the ECE R22 protocol to obtain acceleration and pressure data on the headform during impact attenuation tests. The data was used in finite element models to predict injuries for skull fracture, concussion, brain contusion, and subdural hematoma. The predicted damage measures were then correlated against the injury criteria used in ECE R22 (peak head acceleration and HIC). Below are a summary of the findings from this research:

- Peak head acceleration was the best correlate to skull fracture injury measures identified in this study. HIC was only a good correlate to other acceleration based injury metrics.
- The current ECE R22 linear acceleration limit of 275 g is slightly higher than the calculated thresholds of injury used in this study for skull fracture, 252 g for 15% probability of skull fracture.
- ECE R22 tests with NAP instrumentation allowing for assessment of translational and rotational movement of the headform and subsequent SIMon analysis with and without rotational movement indicates that to evaluate brain injury measures in the ECE R22 protocol, both rotational and translational movement of the headform needs to be collected.
- While the FMVSS No. 218 method of helmet evaluation gives differing results when compared to ECE R22 tests, both testing methods show that peak head acceleration is the best correlate to skull strain. Both standards demonstrate that by using an appropriate threshold of peak head acceleration, skull fracture can be protected against.

ACKNOWLEDGEMENTS

This study was funded by NHTSA through an interagency agreement (DTNH22-07-X-00073) with the U.S. Army Medical Research and Materiel Command (MRMC) under contract W81XWH-06-C-0051. The previous study evaluating the biofidelity of FMVSS No. 218 (Rigby et al., 2009) was also funded by NHTSA through an Interagency Agreement with the U.S. Army MRMC. The views expressed in both papers are those of the authors and do not represent the views of NHTSA.

REFERENCES

Chan, P., Z. Lu, P. Rigby, E. Takhounts, J. Zhang, N. Yoganandan and F. Pintar (2007). Development of Generalized Linear Skull Fracture Criterion. 20th International Technical Conference on the Enchanced Safety of Vehicles, Lyon, France.

COST 327 (2001). COST 327, Motorcycle Safety Helmets. B. Chinn, European Commission.

Depreitere, B., C. Van Lierde, J. V. Sloten, R. Van Audekercke, G. Van der Perre, C. Plets and J. Goffin (2006). "Mechanics of acute subdural hematomas resulting from bridging vein rupture." J Neurosurg. **104**(6): 950-6.

Hodgson, V. and L. Thomas (1971). Breaking strength of the human skull vs. impact surface curvature., Wayne State University.

Hodgson, V. and L. Thomas (1973). Breaking strength of the human skull vs. impact surface curvature., Wayne State University.

Khalil, T. and R. Hubbard (1977). "Parametric Study of Head Response by Finite Element Modeling." J. Biomechanics **10**: 119-132.

Lowenhielm, P. (1974). "Dynamic properties of the parasagittal bridging veins." Z Rechtsmed. **74**(1): 55-62.

Newman, J. (1980). Head Injury Criteria in Automotive Crash Testing. 24th Stapp Car Crash Conference. Troy, Michigan, USA, Society of Automotive Engineers, Inc.**:** 703-747.

NHTSA (2007). Motorcycle Helmet Use Laws. Traffic Safety Facts, National Highways Traffic Safety Administration.

NHTSA (2008). "Consumer Information; New Car Assessment Program." Federal Register **73**(14): 4006-50.

NHTSA (2009). Motorcycle Helmet Use in 2009 - Overall Results. Traffic Safety Facts, National Highways Traffic Safety Administration.

NIH (2000). Visible Human Project. Bethesda, Maryland, National Library of Medicine.

Ono, K., A. Kikuchi, M. Knakamura, H. Kobayashi and N. Nakamura (1980). "Human head tolerance to sagittal impact reliable estimation deduced from experimental head injury using subhuman primates and human cadaver skulls." Stapp Car Crash Journal: 105-160.

Pellman, E. J., D. C. Viano, A. M. Tucker, I. R. Casson and J. F. Waeckerle (2003). "Concussion in professional football: reconstruction of game impacts and injuries." Neurosurgery. **53**(4): 799-812; discussion 812-4.

Takhounts, E. G., R. H. Eppinger, J. Q. Campbell, R. E. Tannous, E. D. Power and L. S. Shook (2003). On the development of the SIMon finite element head model. Proceedings of the 47th Stapp Car Crash Conference, San Diego, California, USA.

UNECE R.22 (2000). Regulation No. 22. www.unece.org/trans/main/wp29/wp29regs21-40.html

Economic Commission for Europe.

Vander Vorst, M., P. Chan, J. Zhang, N. Yoganandan and F. Pintar (2004). "A new biomechanically-based criterion for lateral skull fracture." Annu Proc Assoc Adv Automot Med. **48**: 181-95.

Vander Vorst, M., K. Ono, P. Chan and J. Stuhmiller (2007). "Correlates to traumatic brain injury in nonhuman primates." J Trauma. **62**(1): 199-206.

Vander Vorst, M. J. and P. Chan (2004). Biomechanically-based criterion for lateral skull fracture. 48th Annual Proceedings of the Association for the Advancement of Automotive Medicine.

Vander Vorst, M. J., J. H. Stuhmiller, K. Ho, N. Yoganandan and P. F. (2003). Statistically and biomechanically based criterion for impact-induced skull fracture. 27th Annual Proceedings of the Association for the Advancement of Automotive Medicine. Lisbon, Portugal.

Wood, J. (1971). "Dynamic response of human cranial bone." J Biomech **4**(1): 1-12.

Zhang, J., N. Yoganandan, F. A. Pintar and T. A. Gennarelli (2006). "Role of translational and rotational accelerations on brain strain in lateral head impact." Biomed Sci Instrum. **42**: 501-6.

EVALUATION OF STATISTICAL METHODS FOR GENERATING INJURY RISK CURVES

Vikas Hasija
Bowhead Systems Management, Inc
Erik G. Takhounts
Stephen A. Ridella
NHTSA
United States
Paper Number: 11-0331

ABSTRACT

Statistical methods such as survival analysis (parametric and non-parametric) and logistic regression, along with other non-parametric methods such as Consistent Threshold Estimate and Certainty method are used for generating injury risk curves from biomechanical data. Recently, much attention has been drawn to the question of which statistical methodology is more appropriate in the construction of risk curves for biomechanical datasets. Most of the papers and reports focus on existing biomechanical datasets for which they generate various risk curves using parametric and non-parametric methods and then suggest the use of one method over another based on some sort of criteria. The purpose of this paper is to look at the same statistical methods, but from the "inverse perspective", e.g. evaluate different statistical methods using non-correlated, randomly generated data and to see if any of the widely used methods would yield a "good" risk curve when they are supposed to yield a "bad" risk curve. The "goodness" of a risk curve was evaluated based on 95% confidence intervals, the shape of the curve, and "goodness of fit" statistics. If the risk curve had a well pronounced S-shape, narrow confidence intervals and good "goodness of fit" statistics, then the method was concluded to be inappropriate for non-correlated datasets as it was expected to yield poor S-shape, wide confidence intervals and poor "goodness of fit" statistics. A well-correlated, randomly generated dataset was also evaluated using the various statistical methods. It was observed that logistic regression was able to clearly identify both the non-correlated and well-correlated datasets but suffered because of the underlying distribution that sometimes resulted in non-zero injury probability at zero stimulus level. Survival analysis with different types of censoring and underlying distributions was closely studied. Survival Analysis with a Weibull/ Log-Logistic/ Log-Normal underlying distribution and left- right censored data was not only able to clearly identify both non-correlated and well-correlated datasets, but also gave zero injury probability at zero stimulus level. This paper presents a new perspective of judging the applicability of the various statistical methods and recommends the statistical method, censoring technique, and the distributions that may be used for generating injury risk curves from biomechanical datasets.

INTRODUCTION

Injury risk curves are developed by statistically analyzing experimental data (human and/or animal data) to find an injury criterion and then developing a relationship between this criterion and the type of injury (Kuppa et al [1]). In essence, injury risk curves define the probability of injury to a certain body region as a function of a predictor variable like force, deflection etc. Injury risk curves are used to establish Injury Assessment Reference Values (IARV) (Eppinger et al [2], Mertz et al [3]) that are used for assessing occupant injuries in crash tests. Depending on the IARV's, a car can get an acceptable, good, or poor rating. Thus the importance of correctly generating the injury risk curves cannot be overstated. Various statistical methods such as survival analysis (parametric and non-parametric) and logistic regression, along with other non-parametric methods such as Consistent Threshold Estimate and Certainty method are used for generating injury risk curves from biomechanical data (Kuppa et al [1], Eppinger et al [2], Mertz et al [4], Petitjean et al [5], , McKay et al [6], Yoganandan et al [7], Kent et al [8], Banglmaier et al [9], Banglmaier et al [10], Nusholtz et al [11], Domenico [12], Wang et al [13], Domenico et al [14]). Much of attention has been drawn recently to the question of which statistical methodology is more appropriate in the construction of risk curves for biomechanical datasets (Petitjean et al [5], Kent et al [8], Nakahira et al [15]). Some of the papers generate various risk curves using parametric and non-parametric methods and then suggest the use of one method over another based on some criteria (e.g. McKay et al [6], Kent et al [8], Banglmaier et al [9], Nakahira et al [15], Domenico [12], and Wang et al [13]).

The method used for risk curve generation should be properly evaluated. For example McKay et

al [6] obtained uncensored data from their experiments using acoustic sensors and generated a tibia axial force injury risk curve using survival analysis with uncensored/right censored technique assuming logistic distribution. A "good" risk curve was generated using survival analysis even when most of the injury points were to the left of the non-injury points (McKay et al [6], Figure 14, Page 243). Also their risk curve had non-zero injury probability at zero tibia axial force. Since McKay et al [6] assumed logistic distribution, they obtained non-zero injury probability at zero stimulus. For datasets such as McKay's, other variables and confounding factors should be considered. Such datasets indicate that more testing needs to be done to add more points to the dataset before generating the risk curve. Instead McKay et al [6] have generated a "good" risk curve using uncensored survival analysis. Also Kent at el [8] studied the different data censoring schemes and distributions for injury risk curve generation. They concluded that uncensored/right censored survival analysis is an appropriate method for generating risk curves when logistic regression and left/right censored survival analysis are not able to generate a relevant risk curve. This paper evaluates uncensored survival analysis with various distributions, in addition to other statistical methods, to assess the usefulness of this technique.

Wang et al [13] concludes that interval censored injury data (*when an observation is an injury, it is treated as interval censored from zero to the observed stimulus value instead of left censored where injury could occur anywhere from $-\infty$ to observed stimulus value*) improves the risk curve generation. In their study, one of the methods used was survival analysis with normal distribution and interval censoring as mentioned above. This paper also evaluates interval censored survival analysis with normal distribution to assess its effectiveness for risk curve generation.

This paper evaluates statistical methods based on an "inverse perspective" where non-correlated datasets are used for evaluation purposes. Based on the results of non-correlated datasets, further study is carried out on well-correlated dataset and appropriate statistical methods are identified that may be used to generate injury risk curves.

METHODOLOGY

Prior to describing the methodology, a few definitions used in this paper are given below:

a. Correlation: Relationship between independent (X) and dependent variable (Y). Correlation is computed using R^2, Pearson correlation coefficient, Point Biserial correlation coefficient and the p-value. A p-value of > 0.05 was defined to have no statistically significant correlation.
b. Non-correlated dataset: The independent and dependent variables have no or very poor correlation as determined by R^2, Pearson correlation coefficient, Point Biserial correlation coefficient and the p-value
c. Well-correlated dataset: The independent and dependent variables have strong correlation as determined by R^2 , Pearson correlation coefficient, Point Biserial correlation coefficient and the p-value
d. Point (0, 0): indicates zero injury probability at zero stimulus level.
e. "Goodness of Fit" for Logistic Regression*: is tested using Receiver Operating Characteristic (ROC) curve, Hosmer-Lemeshow statistic [16], and "Max Loglikelihood". Greater area under the ROC curve, lower value of Hosmer-Lemeshow statistic and lower value of "Max Loglikelihood" indicate better fit to data. A ROC plot shows the false positive rate (1-specificity) on the X axis and the true positive rate (sensitivity or 1 - the false negative rate) on the Y axis. The accuracy of a test is measured by the area under the ROC curve. The closer the curve follows the left-hand border and then the top border of the ROC space, the more accurate the test; the true positive rate is high and the false positive rate is low. Statistically, more area under the curve means that it is identifying more true positives while minimizing the number/percent of false positives.
f. "Goodness of Fit" for Survival Analysis*: is computed using "Max Loglikelihood". Lower value of "Max Loglikelihood" indicates better fit.
   * *The "goodness of fit" statistics described above can only be compared for different models on the same dataset and not across datasets.*
g. "Good" risk curve: Good S-shape curve, narrow 95% confidence intervals, and good "goodness of fit" statistics.
h. "Bad" risk curve: Poor S-shape curve or near flat/flat curve, wide 95% confidence intervals, and poor "goodness of fit" statistics.
   **Shape of the risk curve is purely a qualitative factor.*
i. Left censored: An injury point (x, 1) is defined as left censored when the injury threshold lies in the interval $[-\infty, x]$.

j. Right censored: A non-injury point (x, 0) is defined as right censored when the injury threshold lies in the interval $[x, +\infty]$.
k. Interval censored: An injury point (x, 1) is defined as interval censored when the injury threshold lies in the interval [k, x], where k is the point when subject is uninjured and x is a point when subject is injured.
l. Uncensored: An injury point (x, 1) is defined as uncensored when the injury threshold is equal to x.

The methodology for evaluating various statistical methods is shown in Figure 1.

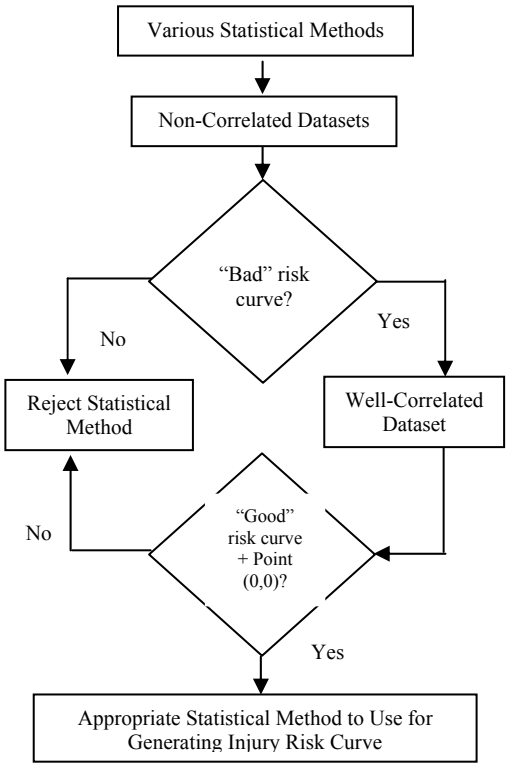

Figure 1. Methodology flow chart

Both the non-correlated datasets and the well-correlated dataset are considered for the purpose of evaluation. For the non-correlated datasets, various statistical methods mentioned in Table 1 are used to generate risk curves. In addition to the four distributions i.e. Weibull, Normal, Logistic and Log-Normal commonly used for biomechanics risk function (Kent et al [8], Banglmaier et al [9], Banglmaier et al [10], Wang et al [13]), other distributions were also studied (Table 1). It is also observed that risk curves are generated using survival analysis with Normal distribution where injury data is interval censored [*0, failure*] (Banglmaier et al [9], Banglmaier et al [10], and Wang et al [13]). This special case of interval censoring was also studied.

Table 1.
Statistical methods used for Non-correlated datasets

Method	Distribution	Injury	Non-Injury
Survival Analysis	Non-parametric	Uncensored	Right censored
Survival Analysis	Normal	Uncensored	Right censored
Survival Analysis	Normal	Left censored	Right censored
Survival Analysis	Weibull	Left censored	Right censored
Survival Analysis	Weibull	Uncensored	Right censored
Survival Analysis	Log-Logistic	Uncensored	Right censored
Survival Analysis	Log-Logistic	Left censored	Right censored
Survival Analysis	Log-Normal	Left censored	Right censored
Survival Analysis	Log-Normal	Uncensored	Right censored
Survival Analysis	Logistic	Left censored	Right censored
Survival Analysis	Logistic	Uncensored	Right censored
Survival Analysis	Extreme Value	Left censored	Right censored
Survival Analysis	Extreme Value	Uncensored	Right censored
Survival Analysis	Normal	Interval Censored	Right censored
Other Methods			
Logistic Regression			
Consistent Threshold Estimate Method			
Certainty Method			

The various distributions mentioned in Table1 are shown in Figures 2-6.

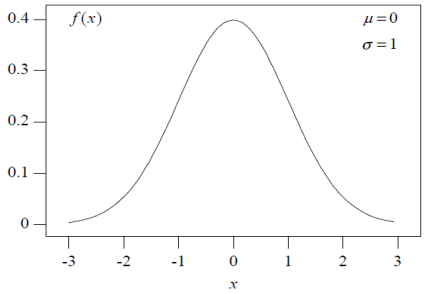

$$f(x) = \frac{1}{\sqrt{2\pi}\,\sigma} \exp\left[\frac{-(x-\mu)^2}{2\sigma^2}\right] \qquad -\infty < x < \infty \qquad (1).$$

Figure 2. Normal Distribution

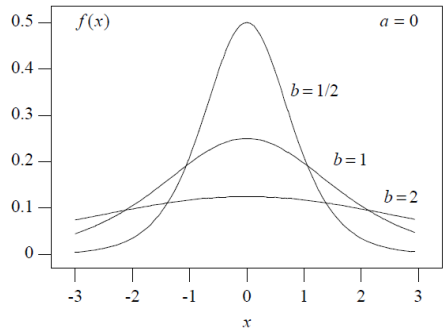

$$f(x) = \frac{1}{b}\frac{e^{(x-a)/b}}{[1+e^{(x-a)/b}]^2} \quad -\infty < x < \infty \qquad (2).$$

Figure 3. Logistic Distribution

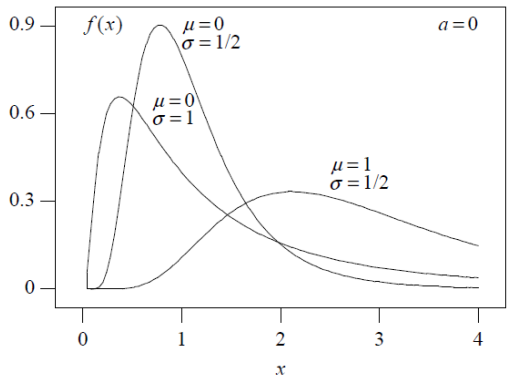

$$f(x) = \begin{cases} \dfrac{1}{\sqrt{2\pi}\,\sigma(x-a)} \exp\left[-\dfrac{[\ln(x-a)-\mu]^2}{2\sigma^2}\right] & x > a \\ 0 & \text{otherwise} \end{cases} \qquad (3).$$

Figure 4: Log-Normal Distribution

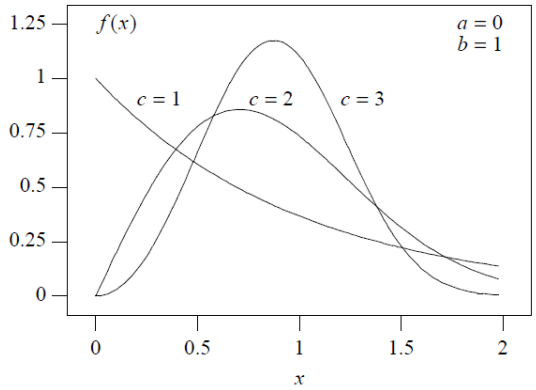

$$f(x) = \begin{cases} \dfrac{c}{x-a}\left(\dfrac{x-a}{b}\right)^c \exp\left[-\left(\dfrac{x-a}{b}\right)^c\right] & x > a \\ 0 & \text{otherwise} \end{cases} \qquad (4).$$

Figure 5: Weibull Distribution

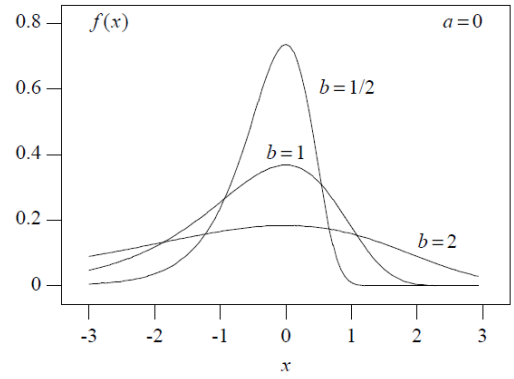

$$f(x) = \frac{1}{b}\, e^{(x-a)/b} \exp[-e^{(x-a)/b}] \quad -\infty < x < \infty \qquad (5).$$

Figure 6: Extreme Value Distribution

First, the statistical methods as listed in Table 1 are used for generating injury risk curves for non-correlated datasets. For non-correlated datasets, the shape of the risk curve, the 95% confidence intervals and "goodness of fit" statistics are checked for each statistical method. If the risk curve looks "good", the corresponding statistical method is rejected as it should have generated a "bad" risk curve for the non-correlated dataset. Second, analysis is carried out to test the applicability of survival analysis with uncensored data for risk curve generation. It is our understanding that survival analysis with uncensored data has an effect of adding extra points to the analysis. To show this, two examples are presented (1) how uncensored analysis works by adding extra points (example 1) and (2) how as few as two injury data points and no non-injury points are enough to generate a good S-shape risk curve using uncensored survival analysis (example 2).

Finally, the statistical methods that pass the non-correlated dataset are used for generating injury risk curves for the well-correlated dataset. For the well-correlated dataset, the shape of the risk curves, 95% confidence intervals, "goodness of fit" statistics and the injury probability at zero stimulus level are considered. The statistical methods that satisfy the conditions of a "good" risk curve and point (0, 0) are accepted and identified as appropriate methods that may be used for generating injury risk curves from biomechanical data.

Datasets

Three datasets were used for evaluation purposes:

Dataset 1 and Dataset 2 (Non-Correlated)

The first dataset was obtained from the cadaver tests conducted by University of Virginia, where the number of rib fractures was used as a dependent

variable and the body mass index (BMI) given for each tested cadaver was used as an independent variable. Therefore our first dataset (Dataset 1) was number of rib fractures vs. BMI. The linear regression line given on Figure 7 shows the poor correlation between the two selected variables.

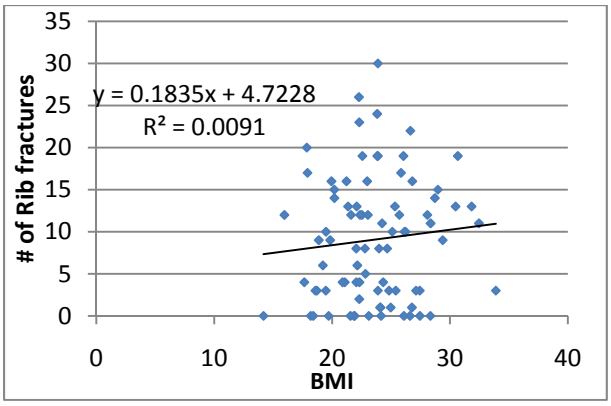

Figure 7. Dataset 1 (BMI vs. # of Rib Fx's)

Since Dataset 1 had the problem of limited range for the independent variable (BMI), a random independent variable was generated with the values bounded between 0 and 50 as shown in Figure 8 to obtain Dataset 2. Again the regression line on Figure 8 shows the poor correlation between the dependent and independent variable.

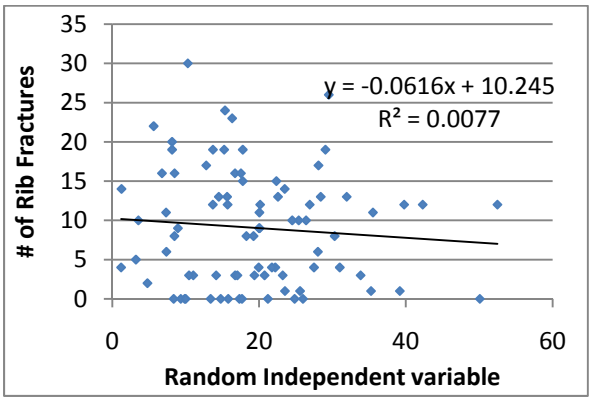

Figure 8. Dataset 2 (Random Variable vs. # of Rib Fx's)

For each dataset (Dataset 1 and Dataset 2) the following injury scenario was considered:

- Injury =1 when the number of rib fractures were greater than six (Fx >6).

For both Dataset 1 and Dataset 2, the Pearson correlation coefficient, Point Biserial correlation coefficient and p-value (Table 2) were calculated between the independent variable (X) and the dependent variable (Y).

Table 2.
Correlation Coefficients and p-value for Dataset 1 and Dataset 2

Dataset	N	Pearson Corr. Coefficient	Point Biserial Coefficient	p-value
1	83	0.147	0.146	0.185
2	83	0.0084	0.0084	0.94

Both Dataset 1 and Dataset 2 have a very low Pearson correlation coefficient and Point Biserial Correlation coefficients indicating very weak or no correlation between the independent variable and binary outcome. Dataset 1 and Dataset 2 also show p-values > 0.05 indicating that the correlation is not statistically significant.

Dataset 3 (Well-Correlated)

For the well–correlated dataset, the independent variable (X) was randomly generated between zero and sixty and dependent variable (Y) was calculated by multiplying the independent variable by a random number. The regression line on Figure 9 shows that Dataset3 has strong correlation between the dependent and independent variable as compared to Dataset1 and Dataset 2.

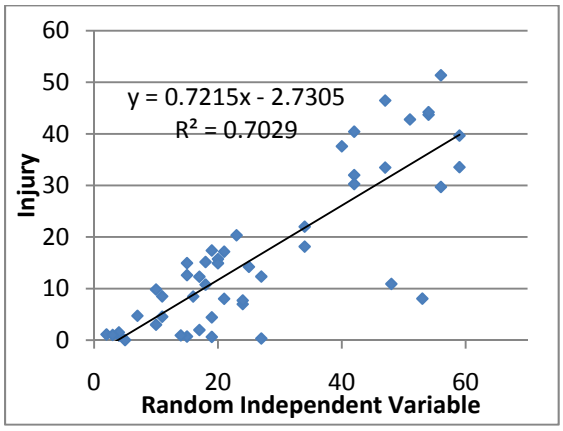

Figure 9. Dataset 3

For the purpose of injury analysis, the dependent variable was assumed as injured (equal to 1) when its value was greater than six (equivalent to the other datasets with Fx>6). For Dataset 3, the Pearson correlation coefficient, Point Biserial correlation coefficient and p-value (Table 3) were also calculated.

Table 3.
Correlation Coefficients and p-value for Dataset3

Dataset	N	Pearson Corr. Coefficient	Point Biserial Coefficient	p-value
3	50	0.597	0.597	<0.0001

Dataset 3 shows relatively high Pearson correlation coefficient and Point Biserial correlation coefficient as compared to Dataset 1 and Dataset2 indicating moderate to reasonably strong correlation between the independent variable and binary outcome. Also, Dataset 3 shows p-value of < 0.0001 indicating that the correlation is statistically significant.

Break-Down Data for Example 1

For evaluating example 1, Dataset 3 was used to generate Break-Down data as follows:

- Injury data is uncensored i.e. it is exactly known at what stimulus the sample breaks. So, for each injury point, ten extra injury points are added to the right of the corresponding data point and ten extra non-injury points are added to the left of the corresponding data point as shown in Table 4 (original point in red).

Table 4.
Break-Down data

1	60
1	57.4
1	54.8
1	52.2
1	49.6
1	47
1	44.4
1	41.8
1	39.2
1	36.6
1	**34**
0	30.6
0	27.2
0	23.8
0	20.4
0	17
0	13.6
0	10.2
0	6.8
0	3.4
0	0

- For each non-injury point, ten additional non-injury points are added to the left of the corresponding data point as shown in Table 5 (original point in red).

Table 5.
Break-Down of data

0	**15**
0	13.5
0	12
0	10.5
0	9
0	7.5
0	6
0	4.5
0	3
0	1.5
0	0

A program was written to add extra points to the dataset. The interval at which additional injury points were added is given by Equation 6.

$$\frac{60 - stimulus}{10} \quad (6).$$

where *60* represents the maximum stimulus.

The interval at which additional non-injury points were added is given by Equation 7.

$$\frac{stimulus - 0}{10} \quad (7).$$

where 0 represents the minimum stimulus.

Break-Down of Dataset 3 in this manner led to a total of 900 data points from 50 points.Statistical analysis was conducted on Dataset 3 (original data) and Break-Down data as shown in Table 6.

Table 6.
Statistical Methods used for Break-Down Data

Methods
Survival analysis on original data with normal distribution + uncensored injury points and right censored non-injury points.
Logistic regression on Original data
Logistic regression on Break-Down data.

Dataset for Example 2

For evaluating example 2, a hypothetical dataset (Table 7) was generated where three different laboratories test a sample and come up with their set of injury points

Table 7.
Injury points

Lab	Injury	Stimulus Value

Lab1- Set1	1	40
	1	45
Lab2-Set 2	1	35
	1	40
Lab3-Set 3	1	45
	1	50

Uncensored survival analysis is studied with this dataset (Table 7)

SAS [17] was used to run the statistical analysis. The PROC RELIABILITY procedure in SAS was used to run survival analysis with different data censoring schemes and with various distributions as listed in Table 1. PROC LOGISTIC was used to run logistic regression and generate ROC curves. Non-parametric Survival analysis was carried out in SAS using PROC LIFETEST Apart from the statistical methods mentioned in Table 1; other non-parametric methods i.e. Certainty method and Consistent Threshold Estimate method were also used for risk curve generation. These methods were programmed in Visual Basic and interfaced with MS Excel.

RESULTS

Dataset1: This dataset was evaluated using all statistical methods (Table 1) and showed a similar trend as Dataset 2. For more clarity, all results are presented for Dataset 2 but only the injury risk curves generated using Certainty and CTE methods are shown for Dataset 1. Figure 10 and Figure 11 show the injury risk curves obtained using the Certainty and Consistent Threshold Estimate (CTE) methods respectively.

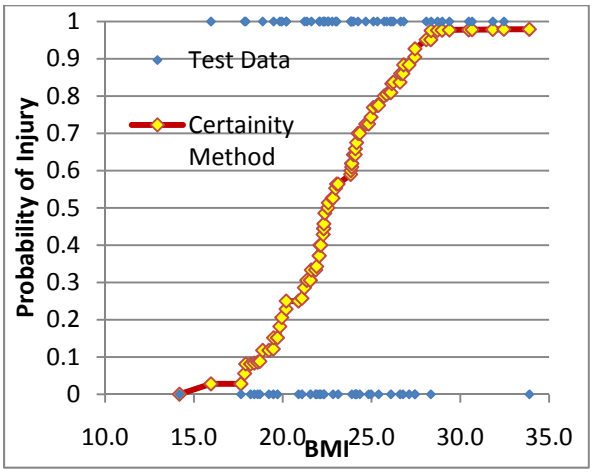

Figure 10. Certainty method

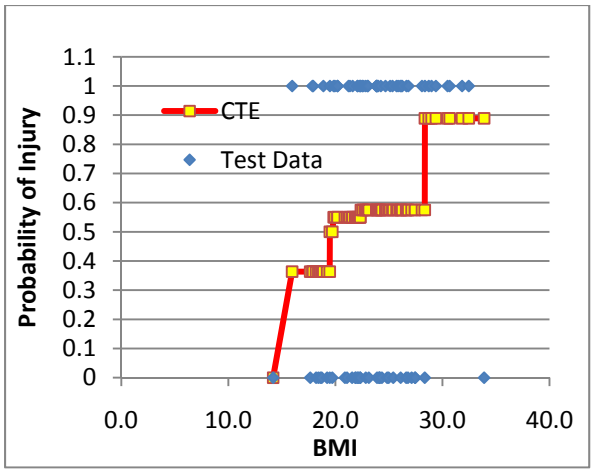

Figure 11. CTE method

Dataset 2: Figures 12-27 show the injury risk curves for dataset 2 using statistical methods mentioned in Table1.

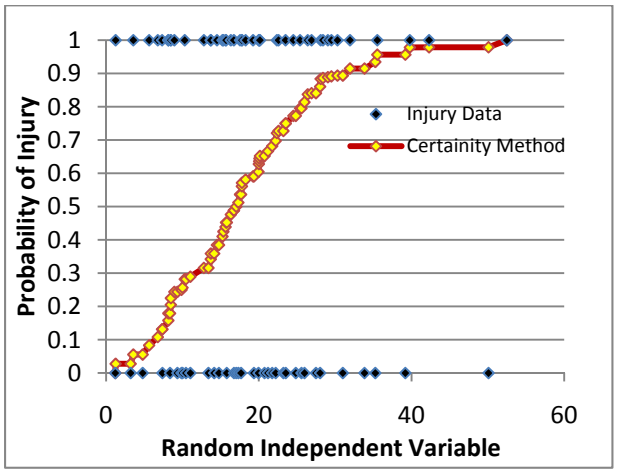

Figure 12. Certainty method

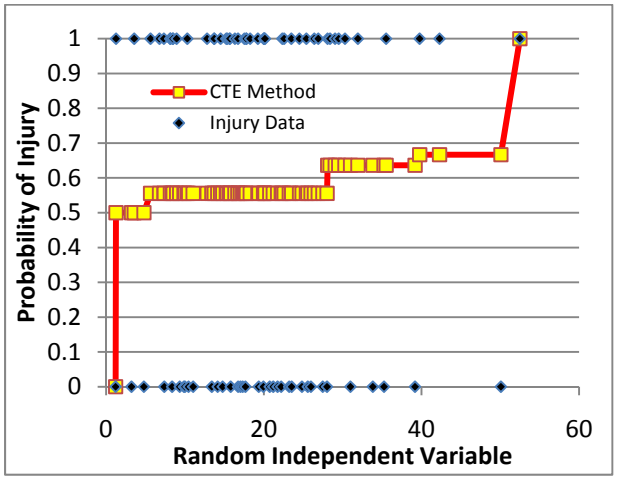

Figure 13. CTE method

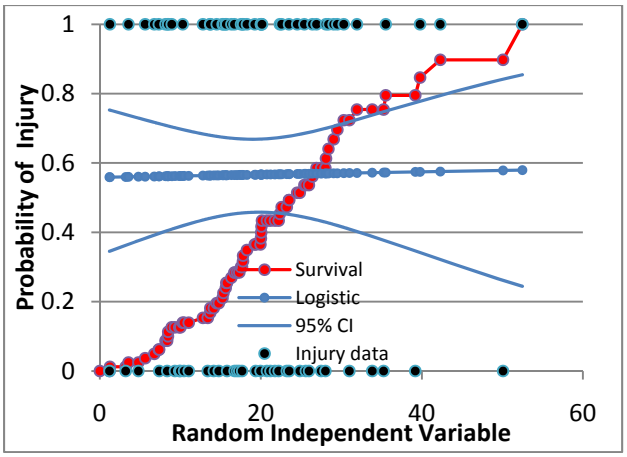

Figure 14. Logistic regression and non-parametric survival analysis

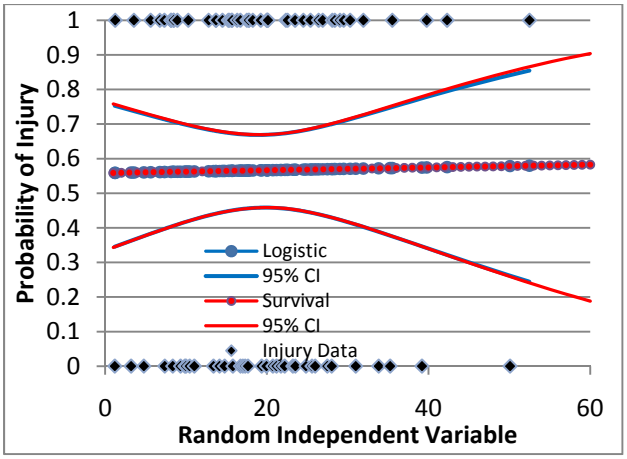

Figure 15. Logistic regression and survival analysis (Left/Right censoring +Normal Distribution)

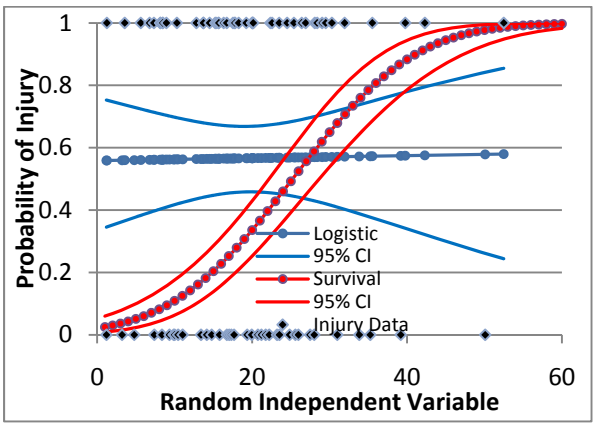

Figure 16. Logistic regression and survival analysis (Uncensored/Right Censored +Normal Distribution)

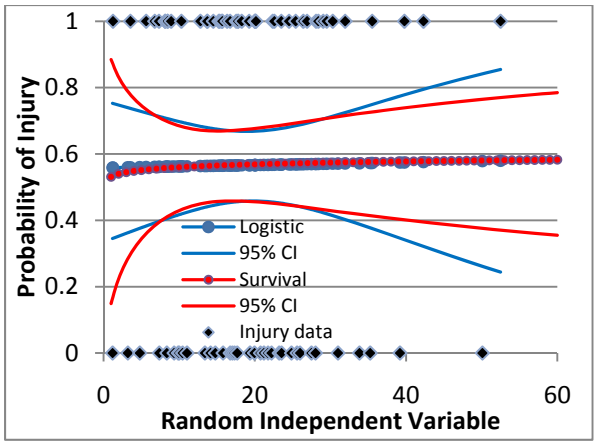

Figure 17. Logistic regression and survival analysis (Left/Right censoring +Log-Normal Distribution)

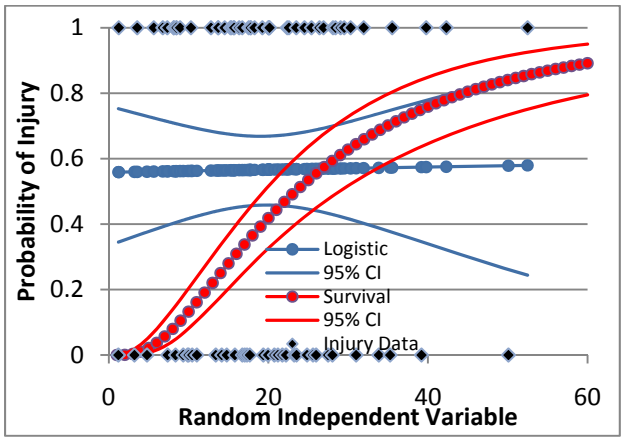

Figure 18. Logistic regression and survival analysis (Uncensored/Right Censored + Log-Normal Distribution)

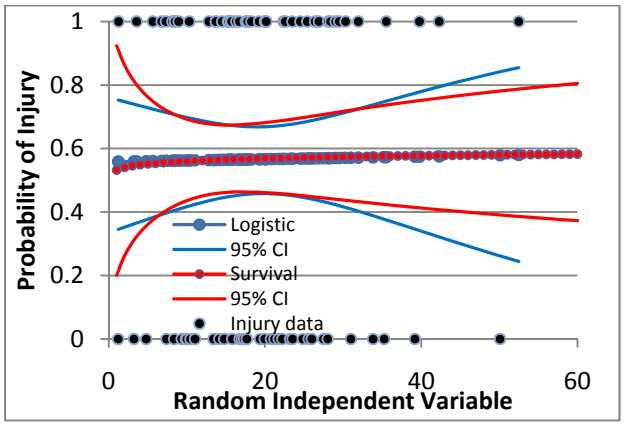

Figure 19. Logistic regression and survival analysis (Left/Right Censoring +Weibull Distribution)

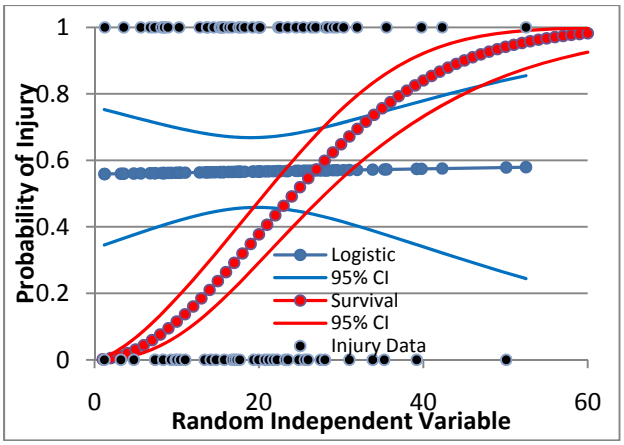

Figure 20. Logistic regression and survival analysis (Uncensored/Right Censored +Weibull Distribution)

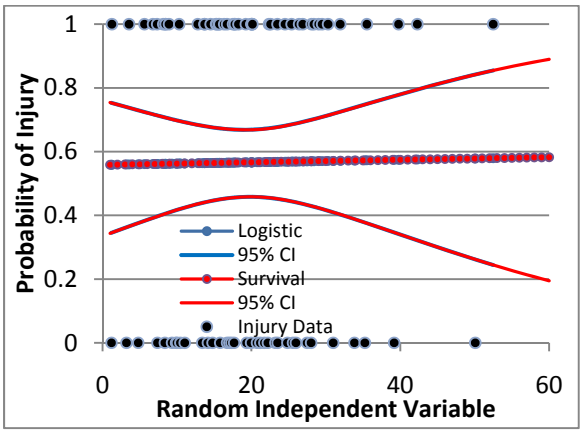

Figure 21. Logistic regression and survival analysis (Left/Right Censoring +Logistic Distribution)

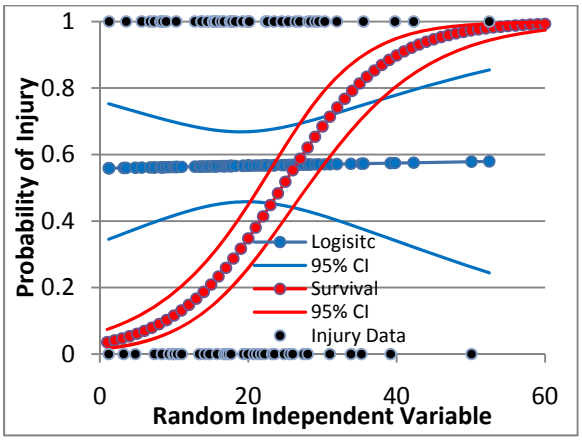

Figure 22. Logistic regression and survival analysis (Uncensored/Right Censored +Logistic Distribution)

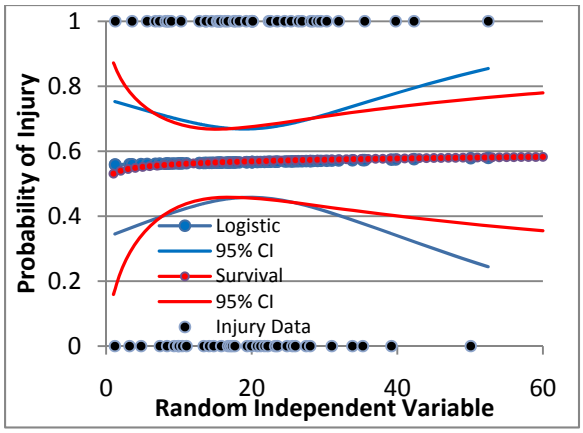

Figure 23. Logistic regression and survival analysis (Left/Right Censoring +Log-Logistic Distribution)

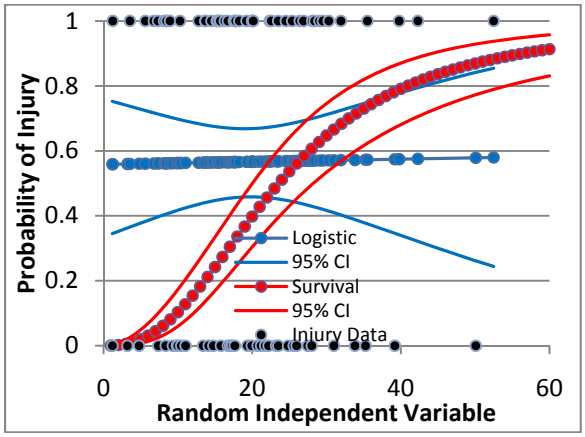

Figure 24. Logistic regression and survival analysis (Uncensored/Right Censored + Log-Logistic Distribution)

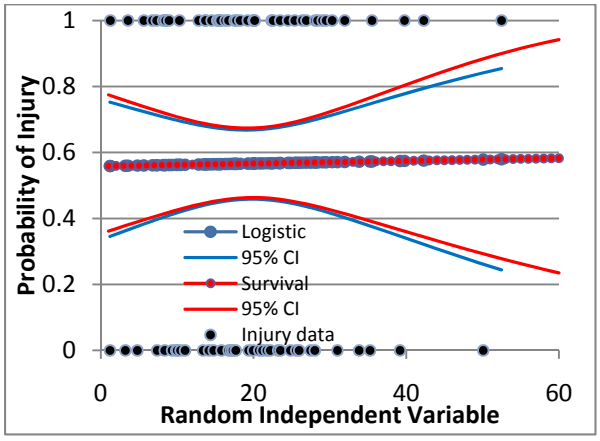

Figure 25. Logistic regression and survival analysis (Left/Right Censoring +Extreme Value Distribution)

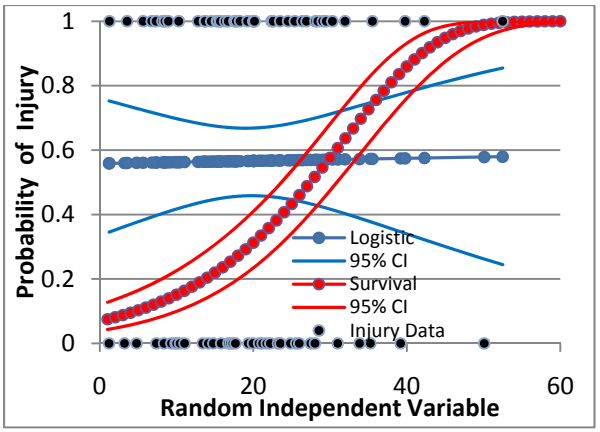

Figure 26. Logistic regression and survival analysis (Uncensored/Right Censored + Extreme Value Distribution)

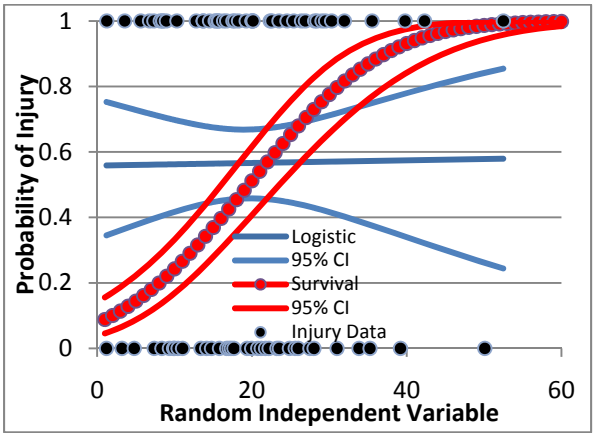

Figure 27. Logistic regression and Survival analysis (Interval Censored /Right Censored + Normal distribution)

Figure 28, Table 8 and Table 9 show the fit statistics for logistic regression and survival analysis corresponding to Figures 14-27.

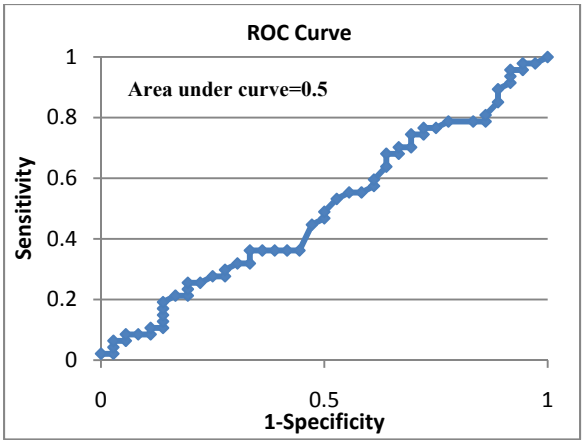

Figure 28. ROC Curve for Dataset 2.

Table 8.
Fit Statistics for Dataset 2 (Logistic Regression)

	Hosmer-Lemeshow Goodness-of-Fit	Max Loglikelihood
Logistic Regression (Figures 14-27)	7.27	-56.797

Table 9.
Fit Statistics for Dataset 2 (Survival Analysis)

Survival Analysis	Max Loglikelihood
Figure 15 Normal +LC/RC	-56.79
Figure 16 Normal + UC/RC	-203.76
Figure 17 Log-Normal +LC/RC	-56.78
Figure 18 Log-Normal +UC/RC	-73.38
Figure 19 Weibull +LC/RC	-56.78
Figure 20 Weibull +UC/RC	-69.25
Figure 21 Logistic +LC/RC	-56.79
Figure 22 Logistic +UC/RC	-204.57
Figure 23 Log-logistic +LC/RC	-56.78
Figure 24 Log-logistic +UC/RC	-70.5
Figure 25 Extreme Value +LC/RC	-56.79
Figure 26 Extreme Value +UC/RC	-212.12
Figure 27 Normal +IC/RC	-84.85

Based on the results of non-correlated datasets, the uncensored/right censoring scheme was eliminated from contention for risk curve generation as the uncensored analysis generates "good" risk curves even for non-correlated data (Figures 16, 18, 20, 22, 24 and 26). The interval censoring scheme (with injury interval defined from [0, failure]) with normal distribution also was not considered for further study for the same reason (Figure 27).

Example 1: The results obtained using statistical methods (Table 6) on original data (Dataset 3) and Break-Down data are shown in Figure 29. It can be seen that logistic regression on Break-Down data converges to survival analysis on original data i.e. analyzing data using survival analysis with uncensored injury points and right censored non-injury points is equivalent to logistic regression with additional points manually added. This example shows that uncensored analysis has the effect of adding more points to the analysis and therefore changes the distribution of the original population.

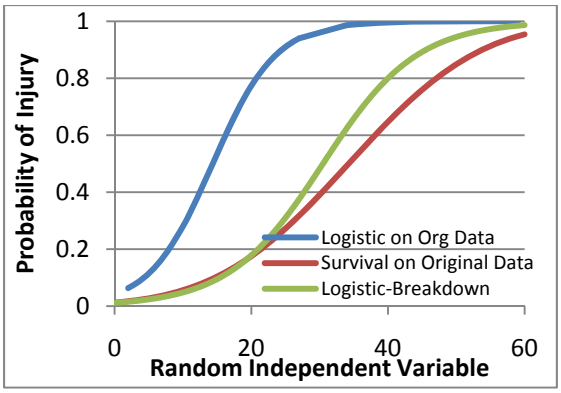

Figure 29. Statistical analysis on Original and Break-Down data.

Example 2: As shown in example 1, uncensored analysis has the effect of adding extra points to the analysis. Thus uncensored analysis allows for risk curve generation based on just two injury points and no non-injury points. As a result each laboratory can come up with its own risk curve as shown in Figure 30.

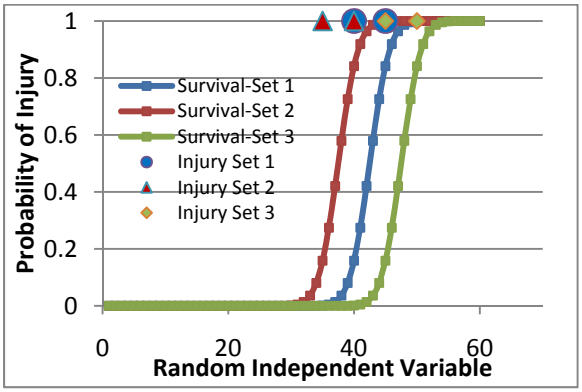

Figure 30. Risk curves using two injury points

Dataset3: Based on the results of non-correlated datasets (Dataset1 & Dataset 2) and the uncensored survival analysis examples, Dataset 3 was studied in detail using only logistic regression and left / right censored survival analysis with various distributions. For completeness, Dataset3 was evaluated using uncensored survival analysis with Weibull distribution only and non-parametric survival analysis. The injury risk curves generated for Dataset3 are shown in Figures 31-37.

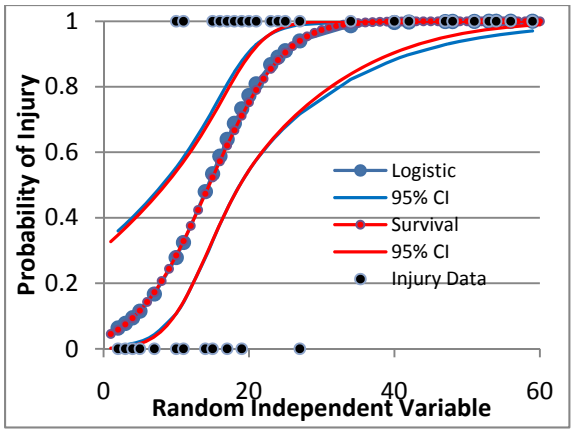

Figure 31. Logistic regression and survival analysis (Left/Right censored + Normal Distribution)

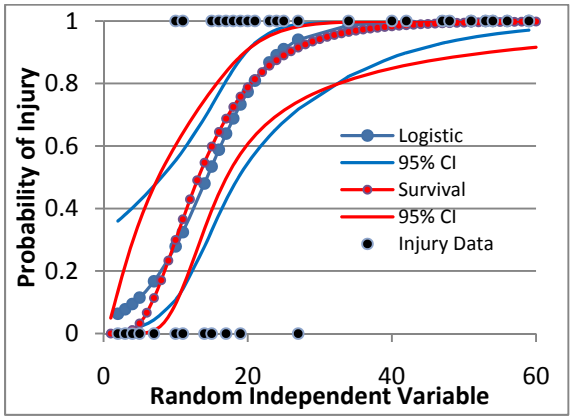

Figure 32. Logistic regression and survival analysis (Left/Right censored + Log-Normal Distribution)

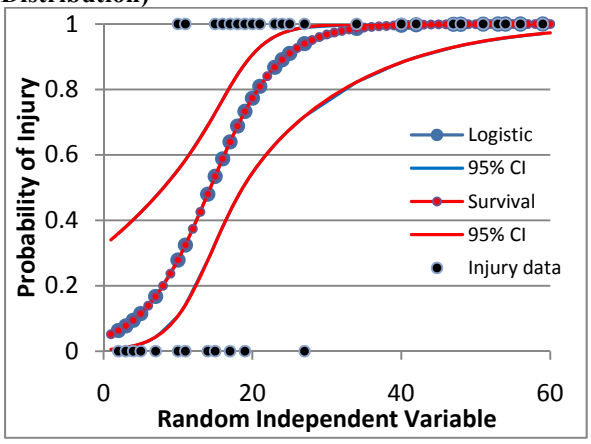

Figure 33. Logistic regression and survival analysis (Left/Right censored + Logistic Distribution)

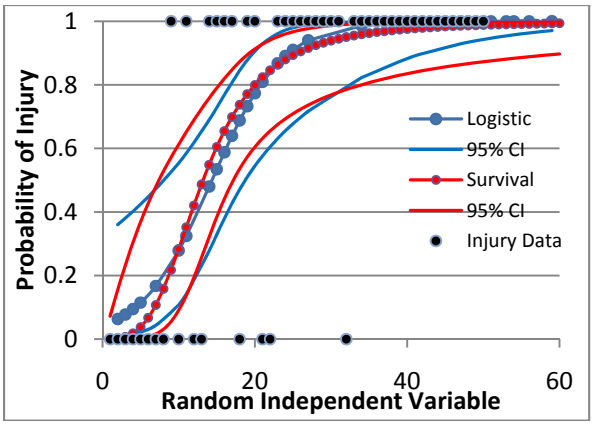

Figure 34. Logistic regression and survival analysis (Left/Right censored + Log-Logistic Distribution)

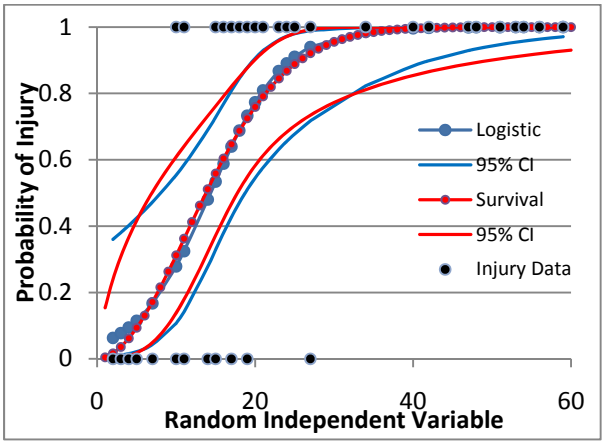

Figure 35. Logistic regression and survival analysis (Left/Right censored + Weibull Distribution)

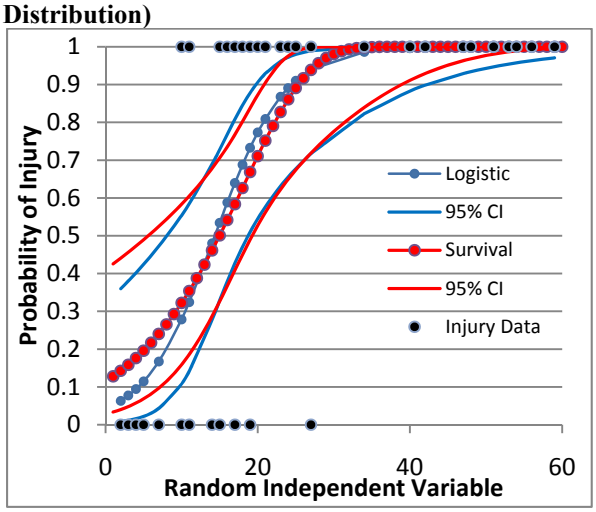

Figure 36. Logistic regression and survival analysis (Left/Right censored + Extreme Value Distribution)

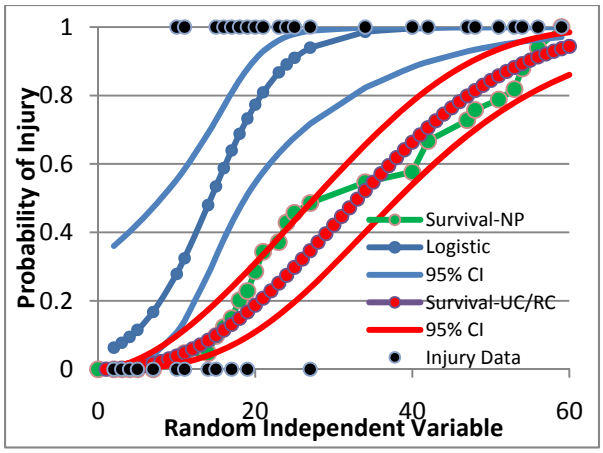

Figure 37. Logistic regression, survival analysis (Uncensored/Right censored + Weibull Distribution) and non-parametric survival analysis.

Figure 38, Table 10 and Table 11 show the fit statistics for logistic regression and survival analysis corresponding to Figures 31-37.

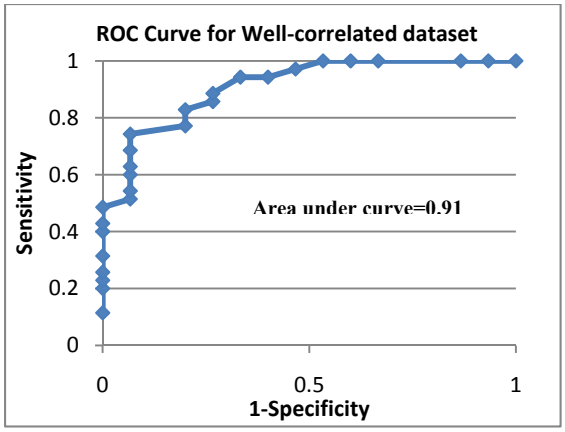

Figure 38. ROC Curve for Dataset 3

Table 10.
Fit Statistics for Dataset 3 (Logistic Regression)

	Hosmer-Lemeshow Goodness-of-Fit	Max Loglikelihood
Logistic Regression (Figures 14-27)	3.35	-16.563

Table 11.
Fit Statistics for Dataset 3 (Survival Analysis)

Survival Analysis	Max Loglikelihood
Figure 31 Normal +LC/RC	-16.61
Figure 32 Log-Normal +LC/RC	-15.84

Figure 33 Logistic +LC/RC	-16.56
Figure 34 Log-logistic +LC/RC	-16.01
Figure 35 Weibull +LC/RC	-16.13
Figure 36 Extreme Value +LC/RC	-17.38
Figure 37 Weibull +UC/RC	-27.69

Based on the study, it was found that survival analysis with left/right data censoring scheme and with Weibull or Log-Normal or Log-Logistic distribution satisfied the conditions of a "good" risk curve and point (0, 0). The corresponding risk curves are plotted and compared with logistic regression risk curve (Figure 39).

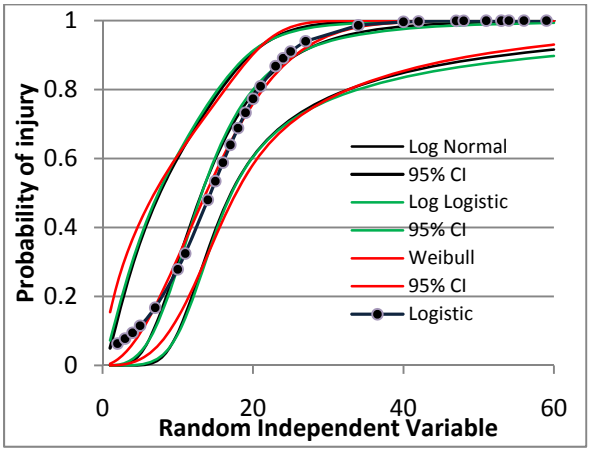

Figure 39. Logistic regression and survival analysis (Left/Right censored + Log-Normal Distribution, Left/Right censored + Log-Logistic Distribution, Left/Right censored + Weibull Distribution)

DISCUSSION

This study was conducted to analyze various statistical methods using non-correlated and well-correlated datasets. It is observed that certain statistical methods generate "good" risk curves even when the underlying data is non-correlated as is evidenced by the Figures 10 through 27.

These methods are: 1) Non-parametric survival analysis with uncensored injury data and censored non-injury data (Figure 14); 2) Parametric survival analysis with uncensored injury data and right censored non-injury data with any assumed underlying distribution (Figures 16, 18, 20, 22, 24 and 26); 3) Survival analysis with normal distribution when injury data is interval censored [*0, failure*] and non-injury data is right censored (Figure 27); and 4) Certainty method and Consistent Threshold method (Figures 10, 11, 12 and 13).

Once data is arranged in ascending order, CTE method computes probability of injury subject to the constraint that the risk of injury at any given stimulus is greater than or equal to the risk at the preceding stimulus. Thus CTE method cannot differentiate between the non-correlated and the well-correlated datasets and always generates an injury risk curve where probability of injury increases over the range of the stimulus (Figures 11 and 13). In addition, the CTE method, just like any other non-parametric method depends on the sample that may not be representative of a population under consideration.

It is observed that logistic regression along with the survival analyses with Normal /Weibull /EVD /Logistic /Log- Logistic /Log-Normal distributions when injury data is left censored and non-injury data is right censored yielded better differentiation of the non-correlated data (Figures 15, 17, 19, 21, 23 and 25). Kent et al [8] suggests that treating the uncensored data as censored data can result in an incorrect risk curve and may in fact suggest no correlation or inverse correlation between injury and a parameter that is actually an accurate predictor of injury. However, it is observed from Figures 16, 18, 20, 22, 24 and 26 that survival analysis with uncensored injury data can generate a "good" risk curve even for the non-correlated dataset whereas left /right censored survival analysis (Figures 15, 17, 19, 21, 23 and 25) is able to capture the poor correlation between the independent and dependent variable appropriately by generating a "bad" risk curve. The Pearson correlation coefficient, Point Biserial correlation coefficient and p-value were computed for two datasets that are used in Kent et al [8] study. These are Banglmaier dataset (Banglmaier et al [18], Banglmaier et al [19]) and Klopp dataset (Klopp et al [20]). Banglmaier dataset (Kent et al [8]) has a Pearson correlation coefficient and Point Biserial correlation coefficient of 0.204 with a p-value of 0.2324 and Klopp dataset (Kent et al [8]) has a Pearson correlation coefficient and Point Biserial correlation coefficient of 0.0044 with a p-value of 0.9758 which indicates poor correlation between the independent and dependent variable. Thus it is observed that in Kent et al [8] study, doubly (left/right) censored survival analysis and logistic regression is able to capture the trend (poor correlation) properly as compared to uncensored survival analysis that generates a "good" risk curve for non-correlated data (Kent et al [8]- Figure 10 and Figure 12). Thus, the ability of uncensored analysis and the inability of censored analysis to generate a "good" risk curve may not necessarily imply that the risk curve generated by uncensored analysis is correct. All it may mean is that the dataset has poor correlation or requires further investigation to find any confounding factors or may require additional tests to add more data points. Kent et al [8] mentions

that it is not necessary to perform non-injury tests when using uncensored analysis for risk curve generation. In our study, from Example 1 and Example 2, it is observed that uncensored analysis has an effect of adding extra points to the analysis (Figure 29), which helps create a good S-shape risk curve with just two injury points and no non-injury points (Figure 30). However, these risk curves may be misleading as the effect of adding extra points changes the underlying population.

From the study of the well-correlated dataset, several observations can be made based on Figures 31 – 37 and Figure 39.

First, uncensored survival analysis gives the best fit for the well-correlated dataset (Figure 37 and Table 11) but we already observed that survival analyses with uncensored injury data generates "good" risk curves even for the non-correlated dataset (Figures 16, 18, 20, 22, 24 and 26). Without this knowledge Figure 37 may be misleading.

Second, logistic regression and survival analysis with normal/logistic distribution when injury data is left censored and non-injury data is right censored, yield similar results (Figures 31 and 33).

Third, survival analysis with Extreme value distribution (EVD) when injury data is left censored and non-injury data is right censored results in a risk curve which differs from logistic regression risk curve in the 0%-30% probability range after which both risk curves are similar (Figure 36). Both the risk curves do not pass through point (0, 0). Finally, survival analysis with Weibull/ Log-Normal/ Log-Logistic distribution when injury data is left censored and non-injury data is right censored resulted in risk curves very similar to that of logistic regression with the exception of the fact that they pass through the point (0,0) (Figures 32, 34 and 35). Because of this the logistic regression and survival risk curves differ in the 0%-18% probability range after which they are very similar. Thus the two analyses i.e. survival analysis (with left censored injury data and right censored non-injury data) and logistic regression yield almost similar results for both the non-correlated and the well-correlated datasets. In addition, survival analysis with Weibull/ Lognormal/ Log-Logistic distribution offers a physically meaningful advantage of passing through point (0, 0). Nakahira et al [15] also suggests "*zero predicted risk for no applied stimulus*" as an assumption for accuracy of risk curve. Since crash performance is evaluated in the lower regions of the risk curve (Banglmaier et al [10]), using left/right censored survival analysis with either Weibull or Log-normal or Log-Logistic distribution for risk curve generation may be more suitable than logistic regression. However, an alternate approach may be to use a combination of logistic regression and survival analysis. As compared to survival analysis, logistic regression provides additional fit statistics which may be useful to determine which covariates or combination of covariates best predict the dependent variable. Thus a combination of logistic regression analysis to determine the best predictive model followed by left/right censored survival analysis using Weibull or Log-normal or Log-Logistic distribution forcing the risk curve through zero may be an alternate approach.

Weibull, Log-normal and Log-logistic distributions offer this meaningful advantage of passing through point (0, 0) because these distributions range from 0 to $+\infty$ (Figure 4 and 5). These distributions show very similar results including 95% CI and "goodness of fit" statistics (Figure 39 and Table 11) and thus the distribution of choice from among them can be based on some sort of fit statistics like Max Loglikelihood, Akaike's Information Criterion (AIC) etc.

It is important to point out that all the datasets (Dataset 1, Dataset 2, and Dataset 3) evaluated in this paper have a sample size greater than or equal to 50. Since many biomechanical studies may have smaller sample size (12-15 data points), the observations made in this paper may or may not extrapolate to smaller datasets.

CONCLUSION

1. This study showed that the following statistical methods do not yield better differentiation between well-correlated and non-correlated datasets:
    a. Survival analysis with the data assumed to be normally distributed when injury data is interval censored, and non-injury data is right censored
    b. Survival Analysis with any distribution when injury data is uncensored and non-injury data is right censored
    c. Non-parametric survival analysis with uncensored injury data and censored non-injury data.
    d. Consistent threshold method and Certainty method
2. Logistic regression and survival analysis with any distribution when injury data is left censored and non-injury data is right censored were able to differentiate better between non-correlated and well-correlated datasets.
3. Survival analysis with Weibull or log-logistic or log-normal distribution when injury data is left censored and non-injury data is right censored offers a physically meaningful advantage (in comparison with logistic regression) of passing

through (0,0) point, i.e. has zero probability of injury at zero stimulus. This may be important when low probabilities of injuries are intended.

4. A combination of logistic regression and left/right censored survival analysis may be used as an alternate approach.

REFERENCES

[1] Kuppa, S., Wang, J., Haffner, M., Eppinger, R., 2001 " Lower Extremity Injuries and Associated Injury Criteria", 17th ESV Conference. Paper No. 457.

[2] Eppinger, E., Sun, E., Bandak, F., Haffner, M., Khaewpong, N., Maltese, M., Nguyen, T., Takhounts, E.G., Tannous, R., Zhang, A., Saul, R., 1999 "Development of Improved Injury Criteria for the Assessment of Advanced Automotive Restraint Systems – II." NHTSA Report.

[3] Mertz, H.J., Irwin, A.L., Prasad, P., 2003. "Biomechanical and Scaling Bases for Frontal and Side Impact Injury Assessment Reference Values." Stapp Car Crash Journal, Vol. 47: 155-188.

[4] Mertz, H.J., Prasad, P., Nusholtz, G., 1996. "Head Injury Risk Assessment for Forehead Impacts" SAE Technical Paper Series, 960099.

[5] Petitjean, A., Trosseille, X., Petit, P., Irwin, A., Hassan, J., Praxl, N., 2009. "Injury Risk Curves for the WorldSID 50th Male Dummy." Stapp Car Crash Journal, Vol. 53, pp. 443-476.

[6] McKay, B.J., Bir, C.A., 2009. "Lower Extremity Injury Criteria for Evaluating Military Vehicle Occupant Injury in Underbelly Blast Events." Stapp Car Crash Journal, Vol. 53, pp. 229-249.

[7] Yoganandan, N., Pintar, F., Boynton, M., Begeman, P., Prasad, P., Kuppa, S.M., Morgan R.M. and Eppinger, R.H. 1996 "Dynamic Axial Tolerance of the Human Foot-Ankle Complex" Society of Automotive Engineers, Paper 962426, Warrendale, PA.

[8] Kent, R.W., Funk, J.R., 2004. "Data Censoring and Parametric Distribution Assignment in the Development of Injury Risk Functions from Biomechanical Data" SAE Technical Paper Series, 2004-01-0317.

[9] Banglmaier R.F., Wang, L., Prasad, P., 2006. "Influence of Interval Censoring and Bias on Injury Risk Curve Development" International Journal of Materials and Product Technology, Vol 25:42-63.

[10] Banglmaier R.F., Wang, L., Prasad, P., 2002. "Various Statistical Methods for the Analysis of Experimental Chest Compression Data" Joint Statistical Meeting.

[11] Nusholtz, G., Mosier, R., 1999. "Consistent Threshold Estimate for Doubly Censored Biomechanical Data" SAE Technical Paper Series, 1999-01-0714.

[12] Domenico, L.D., Nusholtz, G., 2005. "Comparison of Parametric and Non-Parametric Methods for Determining Injury Risk" SAE Technical Paper Series, 2003-01-1362.

[13] Wang, L., Banglmaier, R., Prasad, P., 2003. "Injury Risk Assessment of Several Crash Data Sets" SAE Technical Paper Series, 2003-01-1214.

[14] Domenico, L.D., Nusholtz, G., 2005. "Risk Curve Boundaries" Traffic Injury Prevention, Vol 6: 86-94.

[15] Y. Nakahira, K. Furrkawa, H. Niimi, T. Ishihara, K. Miki, 2000 "A Combined Evaluation Method and A Modified Maximum Likelihood Method for Injury Risk Curves", IRCOBI Conference—Montpellier (France), September 2000.

[16] Hosmer, D. W., Jr. and Lemeshow, S. (2000), Applied Logistic Regression, Second Edition, New York: John Wiley & Sons.

[17]SAS Version 9.1, Cary, NC

[18] Banglmaier, R., Oniang'o, T.E., Haut, R.C., 1999. "Axially Compressive Impacts to the Human Tibiofemoral Joint" ASME Bioengineering Conference, Big Sky, Montana.

[19] Banglmaier, R., Dvoracek-Driksna, D., Oniang'o, T.E., Haut, R.C., 1999. "Axially Compressive Load Response of the 90 Flexed Human Tibiofemoral Joint" Proceedings of the 43rd Stapp Car Crash Conference, SAE Paper 99SC08, pp. 127-139.

[20] Klopp, G.S., Crandall, J.R., Hall, G.W., Pilkey, W.D., 1997. "Mechanisms of Injury and Injuy Criteria for the Human Foot and Ankle in Dynamic Axial Impacts to the Foot" IRCOBI, pp. 73-86.

OPTIMIZATION OF VEHICLE FRONT FOR SAFETY OF PEDESTRIANS

Hariharan Sankarasubramanian

Sudipto Mukherjee

Anoop Chawla

Indian Institute of Technology, Delhi, India.

Paper number: 11-0422

ABSTRACT

During impact with an automobile, a pedestrian suffers multiple impacts with the bumper, hood and the windscreen. Optimisation of the car front using a scalar injury cost function has been demonstrated. The results for impacts simulated in MADYMO show good co-relation with Euro-NCAP ratings for existing vehicles. Optimization of the car front to minimise the injury cost converges to vehicle profiles with features known from earlier studies to be pedestrian friendly. A method to design car fronts for pedestrian safety is evolved.

INTRODUCTION

Vulnerable road users, which include pedestrians and non-motorized two wheeler riders, have been found to be the major constituent in road fatalities in developing countries. Fatalities due to vehicle-pedestrian crash are found to be higher in urban areas in India (Mohan, 2010). In India, the predictions for vehicle sales for the year 2011 show an increased demand for LCVs, utility vehicles and passenger cars (SIAM, 2010). By addressing the design of the front of these automobiles one can contribute a major step in the safety of the vulnerable road users without compromising on the safety of the occupants. In this work, the issue of vehicle-front design for safety of pedestrians is addressed.

MEASURES OF INJURIES

"The abbreviated injury scale (AIS) is the only dictionary specifically designed as a system to define the severity of injuries throughout the body" mentioned by (Gennarelli & Wodzin, 2005). The combined effect of multiple injuries to a particular body part is better represented by Maximum-AIS (MAIS) and Injury Severity Score (ISS). ISS denotes the sum of squares of worst 3 AIS injury scores to a body part and it is number that varies from 0 to 75.

Crash injury databases like German In-Depth Accident Study (GIDAS), Pedestrian Crash Data Study (PCDS), and Advanced Protection Systems (APROSYS) use AIS measure. Studies conducted using these crash databases suggests that the majority of pedestrian-vehicle crash has been frontal impact with pedestrian being hit from the side (Erik& Sander, 2010; Rikard & Erik, 2010)

Multiple measures like Head injury criterion (HIC), Neck injury criterion (N_{ij}), Thoracic Velocity Criterion (VC), Abdomen Peak Force (ABF), Femur Force Criterion (FFC), Tibia Index (TI) and knee bending angles are used to quantify the impact in terms of kinematic and dynamic parameters. The New Car Assessment Program (NCAP) rates vehicles for pedestrian safety through head and leg form impactor tests and the outputs are in terms of points based on forces or torques and other related measurements on impactors. Newer systems of injury measurement, specifically for pedestrian safety during regulatory test, VREPS (Kuehn et al., 2005), using HIC has also been proposed.

Most of injury databases show that injuries in lower extremities and chest are significant. The injury measures for each of these body regions namely head, thorax, abdomen, and lower extremities hence need to be quantified in one score for giving a better picture of the effect of the vehicle front to overall pedestrian safety. To study the effect of a vehicle profile on a pedestrian, it is proposed to consider the effect of injuries on all major segments of the body, in addition to the head.

Work presented here uses a scalar measure "injury cost", calculated as a sum of medical and ancillary

cost given in ISO: 13232: part 5, indicator of crash severity on a pedestrian during a vehicle-pedestrian impact. Pedestrian lateral impact with vehicle front using MADYMO^{TM} (TNO Automotive, Netherlands) 50th percentile pedestrian male dummy in 50% gait stance is simulated. A sample application of this measure is presented on the context of vehicle front shape optimization for safety of pedestrians. The injury risk functions considered are based on limits for occupant safety.

Formulation of "Injury cost"

In motorcycle safety systems research standard (ISO13232, 2002) ISO 13232: part 5, a "cost" measure is defined to estimate the effectiveness of a safety component to motorcycle rider, Probable crash clusters are based on crash data from Los Angeles and Hannover. The "cost" factor is formulated using hospital data linked to the injury severity in AIS. The "injury cost" includes a medical cost and ancillary cost which accounts for partial impairment and even an indicative cost for death (AIS 6).

An injury risk function based on dummy response however entails using lookup tables by (Payne, Patel 2001), to convert the respective kinematic, dynamic and derived measures to corresponding AIS scores.

Vehicle-pedestrian crash simulation

Kinematics of interaction between pedestrian and vehicle during impact are modelled effectively using multibody codes in MADYMO (Mizuno, 2005). The time-history output of such codes can be post-processed to obtain injury scores and force measures. The 50th percentile pedestrian dummy in Madymo has been previously used for reconstruction of a vehicle-pedestrian crash scenario by (Rooij et al., 2003) for speed of 40 kmph in a lateral impact.

It has also been reported (Carter et al., 2005) that the pedestrian kinematics post impact is primarily dependent on the vehicle geometry and stiffness has a secondary role. A frontal crash scenario with pedestrian being hit laterally by the vehicle at a speed of 40 km/hr is modelled. The car profile is simplified to 5 sections shown in Figure 1.

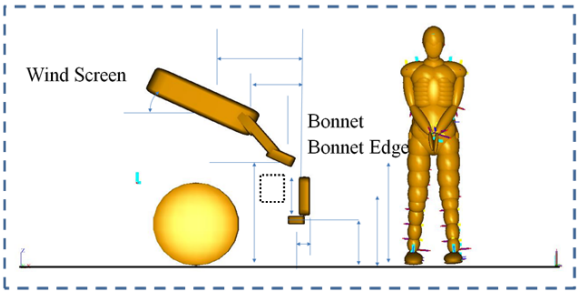

Figure 1 Ellipsoid model of simplified Car profile with pedestrian

The engine is modeled as a rigid mass with high stiffness to have a clearance of minimum of 70 mm from the bonnet of car at the minimum allowed bonnet height. Only the lateral central section of the vehicle is considered (Linder et al., 2005; Carter et al., 2005) A sample population of 12 "in-production" passenger cars across segments from compact to large sedan was considered with details as in Appendix A.

The force deflection characteristics are based on simplification of data from (Rooij et al., 2003) in line with that considered by (Linder et al., 2005). Specifically, negative slopes of the loading curve have been removed and contact damping has not been modelled. The force-deflection relationships are shown in Figure 2, Figure 3, Figure 4, Figure 5 and Figure 6.

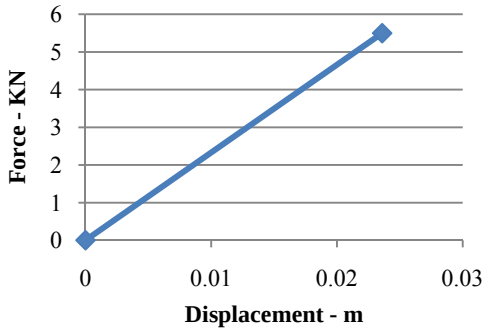

Figure 2 Load-deflection curve of Bonnet Ellipsoid

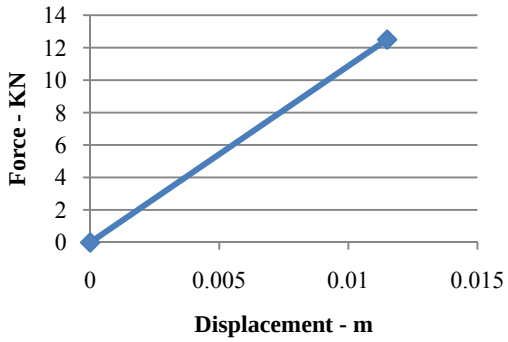

Figure 3 Load-Deflection curve for Leading Edge

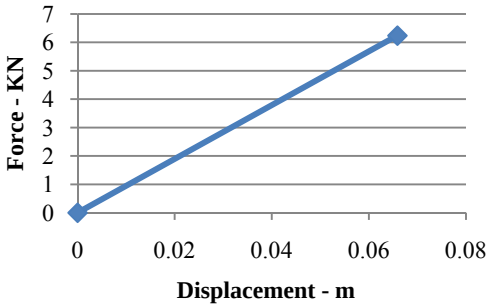

Figure 4 Load-Deflection curve for Windscreen

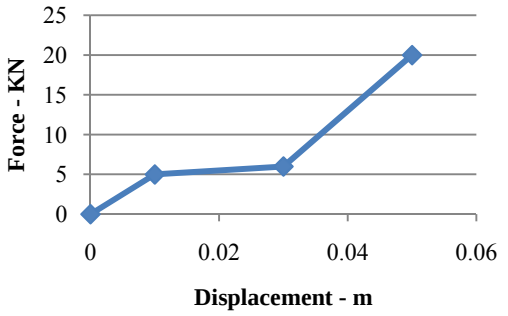

Figure 5 Load-Deflection curve for Cowl Region

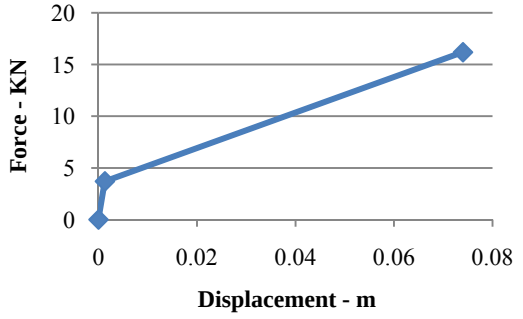

Figure 6 Load -Deflection curve for bumper (lower and stiffener)

Friction between pedestrian and vehicle surface is same as in (Rooij et al., 2003). Braking deceleration of 0.7g is considered all through the impact which is the average braking deceleration on a dry asphalt road. The pedestrian dummy is placed with hands in front and in the 50 % gait stance described in (Kerrigan et al., 2008). An 80 ms period of stabilization is allowed for the dummy to settle under gravity load after which the interaction with vehicle component begins. The crash is simulated for 300 ms of impact

"Injury Cost" Calculation

Table 1 Sample "Injury cost" calculation

Injury Values obtained	Value	AIS	Cost (USD)
HIC	1700	5	583877
Nij	0.52	1	0
VC	0.01	0	0
Pelvis lateral force (kN)	6.22	3	41198
Femur force criterion (kN)	4.72	1	128302
TI	1.511	3	
Force above knee (kN)	8.63	3	
Lower Extremity PPI	0.27	-	-
Total Injury Cost			**753377**

Table 1 shows the cost calculation of one particular geometric profile in a MADYMO crash simulation. For the upper extremity, HIC, neck injury criterion on the neck, viscous criterion on the thorax, lateral peak force for the pelvis, femur force criterion, tibia index and lateral force on knee considered as injury scores for determining the "injury cost".

HIC is formulated as a weighted integration of linear acceleration of head over a time interval specified (15 ms) so it can indicate the direct injury on head. The neck injury criterion is also based on ratio of forces and moments. It is taken as the maximum of combination of four parameters, tension, compression, degree of flexion and extension. The major N_{ij} score observed during crash simulation was for tension-extension. This injury measure was developed as an indicator for occupant neck injury during a frontal collision. For sedan and long bonnet cars, it has been observed that chest contacts do occur with the vehicle and have used the viscous criterion to calculate the injury score.

For accounting the abdomen region, peak pelvis force in lateral direction is considered. The lower extremity

injury cost is based on three separate ratings, the femur force criterion, Tibia Index and force above knee with factor for partial impairment (PPI). These measures were used to calculate injury cost using procedure stated in ISO 13232:part5.

INJURY COST WITH EURONCAP

Euro-NCAP pedestrian scores are based on responses of headform and legform over vehicle profiles at specified wrap around distances (WAD) obtained from crash data analysis (Hobbs & McDonough, 1998). Vehicle designers target to achieve higher NCAP pedestrian scores of their vehicles to prove them to be "safer" cars.

With the sample population of 10 cars (two cars were not tested in Euro-NCAP), a trend of increase in "injury cost" as the pedestrian NCAP points decrease is observed. An increase in "injury cost" implies that the specific geometric profile has a greater cost implication to the pedestrian during an impact as the force-deflection properties are remaining the same not varied.

The "injury cost" was compared with the Euro-NCAP for 10 different passenger car models of 1998 to 2005 The two measures shown in Figure 7 had a linear correlation coefficient of -0.9, indicating a strong inverse relationship between the two factors.

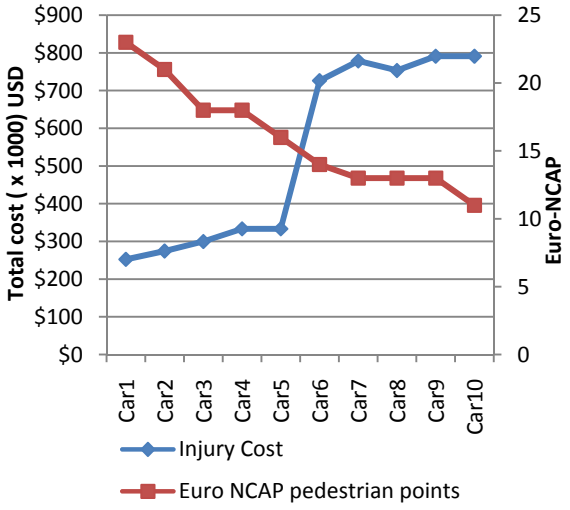

Figure 7 Correlation of "Injury cost" with Euro NCAP pedestrian points

To illustrate the usage of "injury cost" measure, two simple optimization processes for vehicle profile are presented.

VEHICLE PROFILE OPTIMIZATION

There have been earlier attempts to establish the ideal front profile of a passenger car using multibody simulations. Optimization of vehicle font for minimization of head injury using linear programming converging to a solution suggesting a very good reduction in HIC (Linder et al., 2005) was found to be a "local" minimum in their sample space. Simulations with multiple pedestrian dummies representing different gaits and sizes and varied vehicle sizes (Mizuno & Ishikawa 2001) were optimised for multiple objectives using genetic algorithms (Carter et al., 2005). The solution did not converge satisfactorily. Optimization of vehicle front profile based on linear optimization and genetic algorithm formulated to minimise a single objective, the injury cost function has been considered here.

Optimization using MADYMIZER

The MADYMIZER^{TM} is a central linear sequential optimization tool with MADYMO^{TM}. The constraints used are listed below:

- HIC to be below 1000
- FFC less than 10kN
- Tibia index below 1
- Distance between ellipsoids constrained based on a dimensions variation within one segment of cars rather than whole domain from compact to a large luxury car.

When constrained to compact car dimensions, the leading edge and hood length resulted in the profile shown in Figure 8. The optimal geometric profile has enough space to accommodate the engine packaging and requires minimal or no change to the structural elements. The "injury cost" value is compared in Table 2.

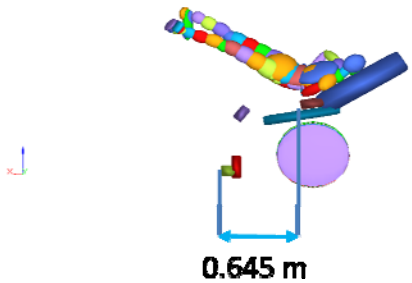

Figure 8 Optimal geometric profile with compact car segment constraints

A comparison of injury cost suggests that by varying the geometry of the vehicle front, a safer vehicle can be obtained. In this case, the distance of the windscreen was the major cause of reduction on the injury cost. The position of the bumper ellipsoids minimised the Tibia Index. The leading edge was allowed to rise up to 0.8m; and resulted in increase of injury to the pelvic region. Bumper ellipsoids were significantly shifted down in (Carter et al., 2005).

Table 2 Comparison of "Injury cost" variation in compact car with optimized shape

S No.	Vehicle	Injury cost (USD)
1	Compact 1	274498
2	Compact 2	753377
3	Compact 3	778609
4	Compact 4	791312
5	**Optimized Shape**	**172948**

Optimization using Genetic Algorithm

A vehicle-front optimization problem was formulated using simple genetic algorithm (Sastry, 2007). Vehicle profiles are shown below with lines joining the centres of the ellipsoids in the vehicle front profile as indicative of the profile. The point on windscreen denotes the top edge of the windscreen and not its centre. A population of 40 is chosen randomly to start with. Dimensional limits based on the car population considered are used to ensure profiles generated resemble a conventional car front.

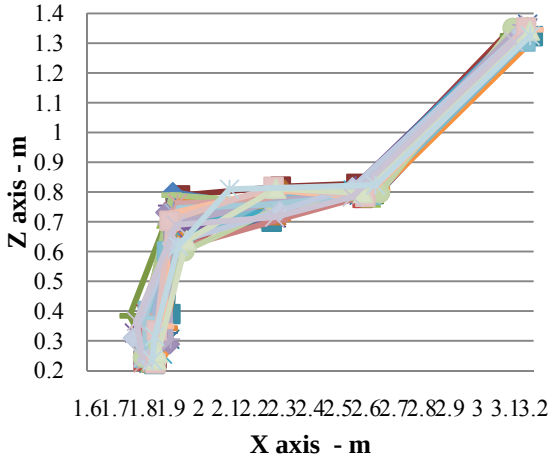

Figure 9 Initial Population for the vehicles - Genetic Algorithm

The initial Population showed a large variation in injury cost, varying from 215081 to 647815 USD. Figure 9 shows the variation of the geometry.

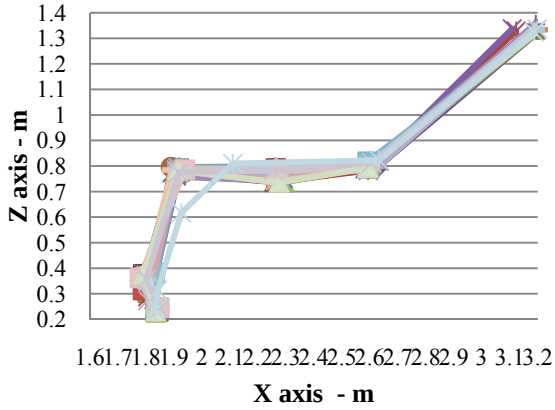

Figure 10 Population at the end of tenth generation - Genetic algorithm

Figure 10, shows the profiles at the end of 10 generations, where the population seems to converge towards one solution and has a variation of injury cost of 113223 to 215081 USD. One isolated solution of 635112 USD was observed.

DISCUSSION

Optimization results

From the linear sequential optimization tool, a local solution for the profile is obtained but it cannot be an indicator for the global minimum as the algorithm works in minimizing every variable separately. The output reflects minimal values for individual variables, with the process repeated a finite number of cycles. As a technique for optimization, this may not lead us to the global minimum. The changed profiles generated had the chest and torso impacting the windscreen first. This makes intuitive sense as the windscreen is a region of lower stiffness. The upper edge of the windscreen is a region of high stiffness but it can removed from the design altogether as shown in Figure 11.

Figure 11 Opel Astra 2006 - new windscreen concept, taken from (Kuehn et al., 2007)

Genetic algorithms based optimization; on the other hand allow starting of search from a random set of population. The optimization problem with the genetic algorithm codes show convergence in tenth generation for the case of 50th percentile male dummy to a single profile. Additionally injury measures for the pedestrian injuries are more comprehensive with consideration for the lower extremity and pelvic region also. The results are not comparable directly with the results of (Carter et al., 2005) because they have also modeled the roof of the vehicle and consequently the stiff member on top of the windscreen.

CONCLUSIONS

Earlier methods used optimization based on single injury measure to obtain a better vehicle profile. In subsequent levels, one additional injury measure was combined using weight factors and optimization extended.

The procedure is built upon and a single objective optimization is proposed. The objective function is derived from multiple injury parameters obtained from statistical analysis of crash and hospital data. It is a better indicator of the "actual" loss to the pedestrian in terms of cost. A direct co-relation of the individual injury severity as well as the gross effect of injuries is possible with this new measure. Analysis of the "injury cost" shown in Table 3 shows the relative distribution of injuries in two regions of body.

Table 3 Injury cost split up for cars

CAR	Total "injury cost" (USD)	Pelvic and below (USD)	Torso region (USD)
Sedan1	252367	237742	14625
Sedan2	299730	237742	61988
Sedan3	333346	169500	163846
Sedan4	333346	169500	163846
Sedan5	726475	142598	583877
Compact1	274498	212510	61988
Compact2	778609	194732	583877
Compact3	753377	169500	583877
Compact4	791312	194732	596580
Compact5	791312	142598	648714
Compact6	252367	237742	14625
Compact7	778609	194732	583877
MADYMIZER optimized	172948	110960	61988
GA optimized	113223	98598	14625

A larger sedan is expected to score better in headform tests indicating less severe head injury of pedestrians as it has a larger bonnet region with comparatively low stiffness. A similar trend is observed with the "injury cost" distribution.

MADYMIZER optimized model showed a 31% reduction from the minimum injury cost observed in production vehicles. The convergence is however to a local minimum within the range specified.

The model optimized using genetic algorithms approach was able to operate on a wider range of dimensions and it showed a reduction of 55% from minimum injury cost observed. It was also observed that the model optimized by genetic algorithm was able to combine the benefits obtained from a longer bonnet car with better bumper and leading edge locations to reduce injuries for pelvic and lower regions. The injury cost for torso shows the minimum observed in the whole population. Similarly, the injury cost for the pelvic and region below is also found to be least.

"Injury cost" is a hence good candidate as a unitary measure of severity of injury to pedestrian in the event of a pedestrian-vehicle crash. It can be used in the vehicle front-profile optimization for reduced pedestrian injury as it acts as a direct indicator of injury severity. Further, this method potentially allows optimisation to be carried across a population of impact cases by weighing the injury cost from each impact case.

REFERENCES:

[1] Linder A, Clark A, Douglas C, Fildes B, Yang J, Sparke L (2005). "Mathematical modelling of pedestrian crashes: Review of pedestrian models and parameter study of the influence of the sedan vehicle contour." Road Safety Conference.

[2] Hobbs A , McDonough P . (1998). "Development of the European New Car

Assessment Programme (EURO NCAP)." ESV, paper number 98-S11-10-06.
[3] Carter E, Ebdon S, Neal-Sturgess C (2005). "Optimization of Passenger Car Design for the Mitigation of Pedestrian Head Injury Using a Genetic Algorithm." GECCO '05 Proceedings of the 2005 conference on Genetic and evolutionary computation . New York, NY, USA.
[4] Gennarelli T, Elaine W (2006). "AIS 2005: A Contemporary Injury Scale". Injury. 1083-1091
[5] Rosén E, Stigson H, Sander U (2010). "Literature review of pedestrian fatality risk as a function of car impact speed". Accident Analysis and Prevention
[6] Rosén E, Ulrich Sander. (2009). "Pedestrian fatality risk as a function of car impact speed". Accident Analysis and Prevention
[7] ISO13232. (2002). "ISO 13232 : Motorcycles − Test and analysis procedures for research evaluation of rider".
[8] Kerrigan J, Subit D, Untaroiu C and Crandall J, Rudd R (2008). "Pedestrian Lower Extremity Response and Injury: A Small Sedan vs. A Large Sport Utility Vehicle". SAE, paper no. 2008-01-1245 .
[9] Rooij L, Bhalla K, Meissner M, Ivarsson J, Crandall J, Longhitano D, Takahashi Y, Dokko Y, Kikuchi Y (2003). "Pedestrian crash reconstruction using multi-body modeling with geometrically detailed, validated vehicle models and advanced pedestrian injury criteria". ESV, paper number 0468-O. Nagoya.
[10] Kuehn M, Froeming R, Schindler V (2005). "Assessment of vehicle related pedestrian safety". ESV paper no. 05-0044. Washington D.C., USA.
[11] Kuehn M, Froeming R, Schindler V (2007). "Fußgängerschutz, Unfallgeschehen, Fahrzeuggestaltung, Testverfahren". Berlin: Springer-Verlag Berlin Heidelberg .
[12] Mizuno Y, Ishikawa H (2001). "Summary of IHRA Pedestrian Safety Working Group activities proposed test methods to evaluate pedestrian protection afforded by passenger cars". 17th ESV (Int. Tech. Conf. on the Enhanced Safety of Vehicles). Amsterdam, The Netherlands.
[13] Mizuno Y. (2005). "Summary of IHRA pedestrian safety WG activities (2005) - proposed test". paper number 05-0138. The 19th International Technical Conference on the Enhanced Safety of Vehicles (ESV). Washington D.C.
[14] Mohan D (2010). "Traffic safety:International status and strategies for the future". 12th WCTR, July 11-15, 2010 – Lisbon, Portugal. Lisbon, Portugal.
[15] Payne A, Patel S (2001). OPERAS. Retrieved September 24, 2010, from http://www.eurailsafe.net/subsites/operas/HTML/appendix/: http://www.eurailsafe.net/subsites/operas/
[16] Fredriksson R, Rosén E (2010). "Priorities of pedestrian protection—A real-life study of severe injuries and car sources". Accident Analysis and Prevention .
[17] Sastry K (2007). http://illigal.org. Retrieved December 11, 2010, from ILLIGAL: http://illigal.org/2007/06/05/single-and-multiobjective-genetic-algorithm-toolbox-for-matlab-in-c/
[18] SIAM. (2010). Society of Indian Automobile Manufacturers. Retrieved February 20, 2011, from http://www.siamindia.com/upload/SIAM-Forecasts-2010-11.pdf

APPENDIX A

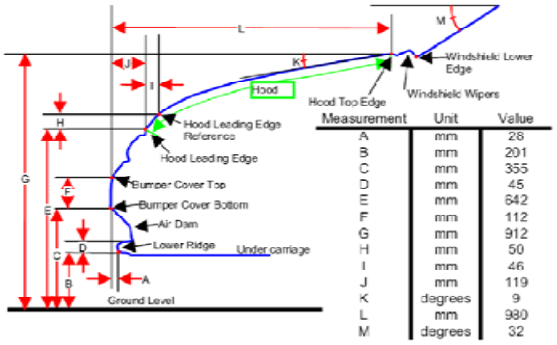

Figure 12 Vehicle dimensions taken from (Kerrigan et al., 2008)

Vehicles were measured using tapes based on the template shown in Figure 12 from (Kerrigan et al., 2008). The vehicles were photographed and processed using PC-RECT to extract the geometry. The dimensions for 12 types of passenger cars are shown in the Table 4.

Table 4 Sample "in-production" vehicle details

Vehicle	A	B	C	D	E	F	G	H	I	J	K	L	M
	mm	mm	mm	mm	mm	mm	mm	mm	mm	mm	deg	mm	deg
Car1	0	263	414	35	601	111	995	222	131	13	20	703	28
Car2	0	237	389	37	535	146	994	136	77	33	16	676	30
Car3	-26	215	451	26	696	86	963	151	171	85	11	761	30
Car4	25	230	391	36	694	142	1010	84	95	83	14	800	25
Car5	19	326	470	43	799	166	1130	116	114	78	16	820	30
Car6	56	314	431	30	686	141	1120	180	83	66	50	375	25
Car7	15	188	368	95	650	128	955	100	50	85	8	890	25
Car8	0	0	259	0	745	320	1040	105	137	116	11	1085	27
Car9	0	280	439	31	727	139	993	114	78	49	3	1064	30
Car10	25	196	440	70	588	98	860	110	0	90	9	1053	26
Car11	98	198	403	57	571	137	937	113	50	90	3	1205	30
Car12	0	259	423	47	623	130	1000	200	128	60	10	983	27

The Clarification of Individual Injury Mechanism Difference in Pedestrian FE Model Utilizing Cadaver Scaling and Posturing Techniques

Shinichi, Takayama
Yoshihiro, Yamamoto
Susumu, Ejima
Koshiro, Ono
Japan Automobile Research Institute, Japan
Koichi Kamiji
Tsuyoshi Yasuki
Japan Automobile Manufacturers Association, Inc., Japan
Paper Number 11-0414

ABSTRACT

In car-pedestrian accidents, the pedestrian's body size exerts strong influence on the degrees of the impacts by the vehicle on the lower limbs and the pelvis. Such individual difference affects the loading mechanism of the pedestrian accident and relates to the injury outcome. The ultimate goal of this research is to clarify the injury mechanisms of accidents of this sort. To fulfill this purpose, a 50th percentile finite element pedestrian model was developed and validated by Japan Automobile Research Institute (JARI) in the human finite element model development project by the Japan Automobile Manufacturers Association (JAMA). This model was employed in this study to reproduce full scale tests in which cadaver (Post Mortem Human Subjects) in standing position were struck by vehicles to investigate the body kinematics and the injuries caused by car-pedestrian impact. In addition, two kinds of individual scaled models were generated based on the 50th percentile standard model. In this process, the radiological data, as well as body external measurements of the cadaver recorded in the experiments, were utilized. The individual scaled models were applied to simulate two full scale tests in which two cadavers of different sizes were struck by a SUV type vehicle and a Small City Car type vehicle, respectively. For the purpose of comparison, the 50^{th} percentile standard model was also applied to the car-pedestrian simulation. The body kinematics and the injury outcome of the models were analyzed and compared with the experimental results. It was found that, while all the models indicated acceptably good kinematics, only the scaled models could reproduce accurate injuries such as the knee ligament rupture found in the experiments.

INTRODUCTION

The number of traffic related fatalities in Japan has shown a constant descending tendency since the early 90's. Moreover, the increasing tendency in the annual number of injuries was inverted and has shown a downward trend since 2005. However, these downward trends seem to have been slowing down since 2007 (Figure 1)[1].

Fig. 1 Traffic related fatalities and injuries in Japan (1990-2010)

Despite the effort made by the automotive industry and the public institutions, the still enormous number of fatalities and injuries demand increased effort to keep on improving vehicle safety. According to the most recent accident data collected and published by the Japanese police, 33% of the traffic related fatalities in 2008 involved pedestrians (Figure 2)[1].

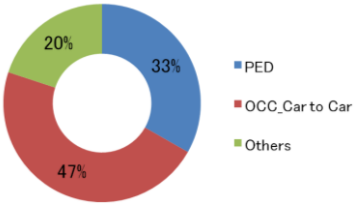

Fig. 2 Traffic fatalities in Japan (2008)

As for pedestrian injuries, the accident data collected by the Institute for Traffic Accident Research and Data Analysis of Japan (ITARDA) indicate that head and lower limbs (including the pelvis) are the most frequently injured body regions (AIS2+ injuries) with over 30% frequency each [2]. This figure indicates that specific countermeasures are needed to reinforce the protection of pedestrians involved in traffic accidents. Among all the methods employed to improve the vehicle safety, human models appear to be the most promising tool. Such models, if used in appropriate combination with experimental bio-mechanics, accident reconstruction, and epidemiology, can contribute to a better understanding of injury mechanisms. The knowledge thus acquired can later be applied to the development of safer vehicles. With the objective of clarifying injury mechanisms in accidents for which adequate countermeasures can be taken to improve vehicle safety, JAMA initiated in 2004 a longitudinal project, and JARI has been developing and validating the human FE models [3] for over 7 years. In the research presented here, the 50th percentile Finite Element (FE) human pedestrian model developed within the frame of this project was utilized (Figure 3).

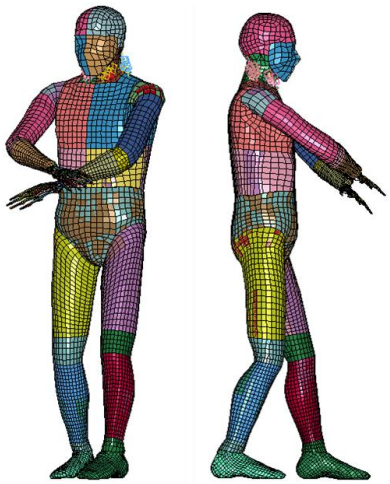

Fig. 3 50th percentile male JAMA Pedestrian model

The use of standard-size Human FE models has already been well established as a research tool to clarify injury mechanisms. The size of the majority of the models represents the standard 50th percentile male population, either in standing position for pedestrian-related research or in driving posture. However, modeling with accuracy the differences between individuals (human factors), as well as different impact environments (extrinsic factors) is essential for the clarification of injuries. The human factors that are necessary for the clarification of injury mechanisms include, among many others, variations in body size, age, gender, biomechanical tolerance, posture at the impact, and muscle activity [4]. Due to the specific nature of car- pedestrian accidents, in particular the body size strongly affects the way the knee and the pelvis are impacted by the vehicle. Such differences between individuals affect the body loading mechanism during the impact, and hence need to be taken into account by the human models to clarify injury mechanisms. As for the extrinsic factors to consider when reproducing car-pedestrian accidents, the posture of the pedestrian surrogates with respect to the vehicle has been experimentally proved to affect, for example, the thrown distance when impacted by vehicles [5]. Moreover, the differences between the types of vehicles involved in this kind of accidents also affect the kinematics of the pedestrians and the injury output. This paper introduces the effect of both intrinsic and extrinsic human factors by employing individual pedestrian model utilizing the cadaver scaling and posturing techniques. In this research, these factors were taken into consideration in simulating full scale car-pedestrian experiments with cadaver in the manner described.

METHODOLOGY

The 50th percentile pedestrian FE model (base model) is now being subjected to continuous validation. For this specific task, validation at the component-level of the lower limbs and the hip was carried out. Then, two full scale car-pedestrian tests were selected. In the first case, a 165cm of height and 60kg of weight cadaver was impacted by a SUV-type car [6]. In the second case, a 161cm of height and 86kg of weight specimen was impacted by a Small City Car-type vehicle [7]. The base model was then scaled by using radiological image data and external measurement data from the cadaver used in the full scale tests. Finally, each of the two experimental cases was simulated with its corresponding scaled model, respectively. In addition, the base model also applied to simulate the Small City Car-pedestrian accident for comparison. Thus, the differences between the base model and the scaled model could be analyzed under the same impact conditions. In

the simulations carried out, an accurate model of the front part of each of the vehicles used in the actual experiments was employed. In addition, the initial posture of the individual models was adjusted by using the position markers from the cadaver just before the impact.

Base Human Model Component Validation

The geometry of the organs of the human model of relevance for injury research has been under continuous improvement. CT scan data from cadaver are being used to remodel the organs. Besides the improved geometry, especial attention is paid on the bio-fidelity of the material models used for the soft tissues and the bones. The modeled tissues behave correctly at different loading strain-rates and can reproduce tissue damage thresholds. After the tissues are validated, the properties are inputted into the respective components and validated based on the component test data. A description of some of the validated components of relevance for this work is as follows.

Flesh of the legs:

The material properties of the leg flesh were validated based on the leg impact experiments employing volunteers, cadavers, and the Hybrid III dummy [8]. In these experiments, the subjects were impacted in the posterior and lateral part of the lower leg using a free flying pendulum. The experimental data used for the validation of the model correspond with the series of tests/experiments in which the impacts were delivered to the lower leg laterally. In the experiments, the foot of the tested leg was plantar flexed and suspended. The cadavers and the Hybrid III dummy were tested in a similar setup. All specimens were impacted at approximately 80% of their own tibial height, measured from the ground. The rigid plate which has a 45mm by 145mm rectangular and 1.84kg total mass was attached to the impactor and the impact of up to 2.5m/s was delivered. The impact force was calculated by multiplying the mass of the pendulum and its acceleration measured with an accelerometer mounted at the end of the pendulum. The displacement of the leg at the site of impact was obtained by tracking the high-speed video data. The experiments were simulated by replicating the boundary conditions, and the experiment and the simulation results were compared. Figure 4 shows a picture of the simulation setup described and a figure comparing the force deflection resulted from the experiment and the numerical simulation.

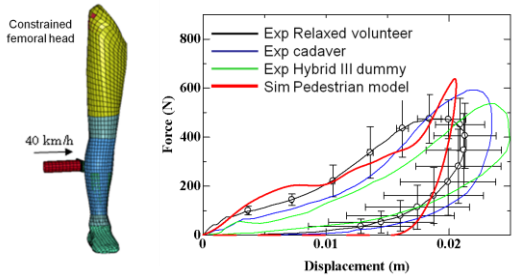

Fig. 4 Flesh validation simulation setup (left) and experiment and simulation results comparison (right).

The simulation results (in red) showed good correlation with the experimental corridor built from the volunteer tests (black), proximity to the cadaver (blue), and the Hybrid III dummy data (green).

Knee complex:

The entire knee complex was remodeled. While the head of the femur, the tibia, and the fibula were redesigned based on CT images, the geometry and the insertions of the ligaments into the bones were modeled by following medical literature [9]. The material properties of the ligaments consisted of a strain-rate based elastic-plastic material model including ultimate strain previously validated in other projects [10]. Figure 5 shows three different views of the new knee complex, including the ligaments.

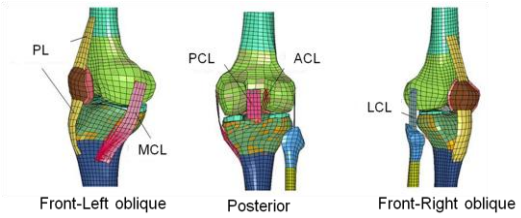

Fig. 5 Remodeled Knee complex

The new knee model was validated against knee bending tests with cadavers [11][12]. In these experiments, the internal part of the right leg of cadaver lying supine on a table was subjected to high speed impacts at the ankle region. To generate bending effort at the knee, the trochanter and the knee were fixed with screws. The impacts were delivered at around 40km/h. Figure 6 shows an image of the simulation setup (left) and the experiment and simulation results

comparison for the bending angle rotated by the knee in the coronal plane (right).

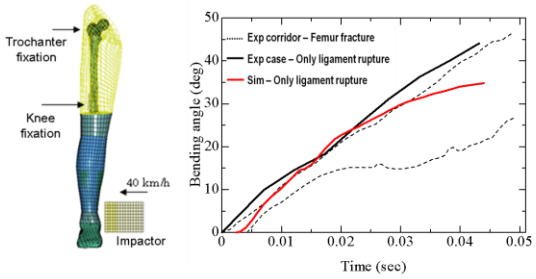

Fig. 6 Knee complex validation simulation setup (left) and experiment and simulation results comparison (right)

The corridor built with the experimental cases that indicate femoral fracture is represented with black dotted lines. The thick black line represents one case in which ligament rupture with no bone fracture occurred. The numerical result, in red, shows ligament rupture with no bone fracture, and it behaves similarly to the experiments

Pelvis Cortical bone thickness and Material properties:

The thickness of the cortical bone of the pelvic bones at eight different segments was modified from the original model based on literature [13]. Such modifications were confirmed by measuring the cortical bone thickness from radiological data of cadavers.

	Cortical thickness (mm)
Face	1
Wing	1.5
Top	2
Notch	2
Acetabulum	1.5
Aceta-Rami	1.25
Rami	1.25
Pubic	1

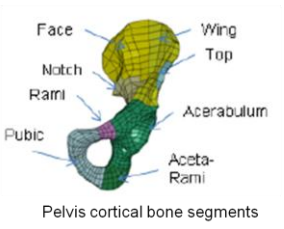

Fig. 7 Pelvic cortical bone thicknesses

The pelvis was validated against dynamic tests on isolated pelvic bony structures [14]. In the experiments, the pelvic structures were immobilized using a low melting temperature alloy, up to the external edge of the ischial tuberosity and leaving the pelvic ring free. The pelvis was oriented so that the line between the two anterior superior iliac spines was vertical. The drop tower was used to guide a falling mass which enabled impact speed at around 4m/s. The mass was equipped with accelerometers, and a displacement sensor was utilized to measure the pelvis deflection. The metallic sphere was fitted into the impacted acetabulum to distribute the load around the joint surface. To avoid direct contact between the metallic impactor and the sphere, 11mm thick silicon padding was fitted at the impacting face of the falling mass. The experiments were simulated by replicating the boundary conditions as described in the original documents, and the experimental and the simulation results were compared. Figure 8 shows an image of the simulation setup (right) and the results comparison for the impact force (left).

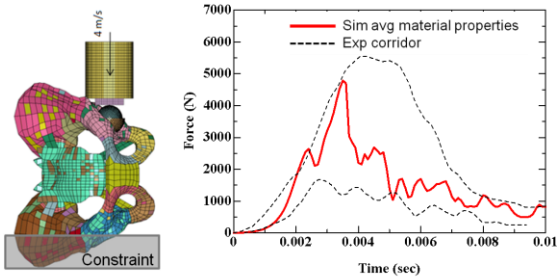

Fig. 8 Pelvis validation simulation setup (left) and experiment and simulation results comparison (right)

The sustained force by the simulated impact presented results within the limits of the experimental corridor.

Scaling Method and posture change

The geometry of the skeleton and the flesh of the validated standard-size model were modified based on individual data taken from the cadaver used in this study. For this modification, a custom-made scaling and posturing software tool was utilized. Such tool modifies the geometry of the base model based on two groups of measurements taken from the cadaver. The first group consists of around 20 measurements from the CT scans. These data include a variety of data such as the length and the dimensions of the cross sections of long bones and key parameters of the pelvis. The second group of measurements consists of around 30 external measurements taken from the cadaver at the specimen's impact position. Figure 9 shows the images with some of the measurements used to scale the models.

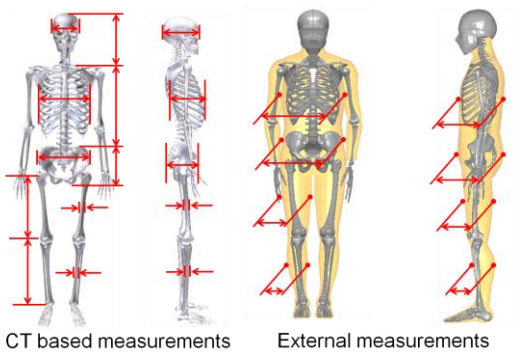

Fig. 9 CT based measurements (left) and external measurement (right) used to scale the base model

As a result of the application of the scaling method, two scaled versions of the JAMA pedestrian model were obtained. The first scaled model corresponds with a subject with a height of 165cm and a body mass of 60kg. The second scaled model is based on a subject 161cm tall and a weight of 86kg (Figure 10).

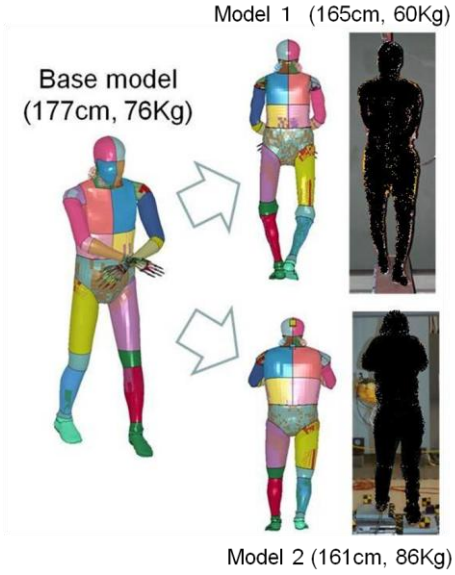

Fig. 10 Base model and scaled models

RESULTS

Body Kinematics

Each of the two experimental cases was simulated with its corresponding scaled model. For the purpose of comparison the base model also applied to this simulation. All the simulations were run until the impact of the head with the vehicle. Figure 11 shows a comparison of the behavior of the cadaver at the experiment and that of the scaled models at the simulated impact. The images on the left correspond with the test in which the frontal part of a SUV-type vehicle was used (impact from the left side of the specimen). The images on the right correspond with the test in which the frontal part of a Small City Car was used (impact from the right side of the specimen). Both simulated cases presented good kinematics in comparison with the experimental results.

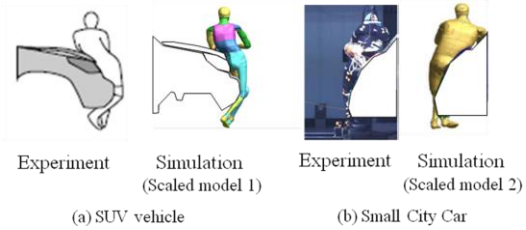

Fig. 11 Comparison of the behavior of the cadaver and the scaled models for the SUV (left) and the Small City Car (right).

Figure 12 shows a comparison of the trajectories in the vertical plane (longitudinal plane of the vehicle) followed by the Head, the 1st and the 6th thoracic vertebra (T1,T6), the fifth lumbar vertebra (L5), the Left Knee, and the Left Foot in the SUV vehicle case. The results correspond with the displacements of the body with respect to the vehicle. The experimental results are represented with black dotted lines, while the simulation results with continuous red lines. The markers represent the position of each marker at 20ms intervals. In a similar way, Figure 13 shows the results of the Small City Car case (from the right side of the body). The trajectories of Head, T1, T8, Right Femur, Tibia, and Heel were used in this case. Both cases show good correlation in the trajectories between the experiments and the simulation.

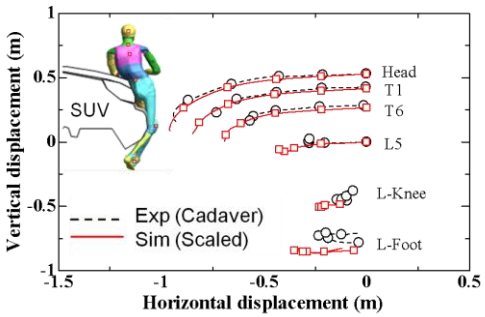

Fig. 12 Comparison of the simulated trajectories with the scaled model (red) and the experimental results (black) in the case of SUV type vehicle

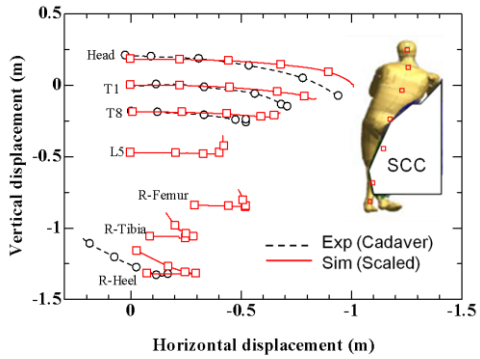

Fig. 13 Comparison of the simulated trajectories with the scaled model (red) and the experimental test results (black) for the case with Small City Car

Leg injuries: Standard model vs Scaled model.

In the experiment with the Small City Car, the cadaver sustained a rupture of the Medial Collateral Ligament (MCL) of the right knee (internal part of the knee at the struck side) by its insertion into the femur. Figure 14 shows a sequence of photos (10ms interval) with the strain distribution sustained by the ligaments of the the internal part of the right knee (struck side) during the simulated impact. The photos above correspond with the impact simulated with the base model, while the photos below correspond with the scaled model. The MCL ruptured in both the simulated cases, at the middle in the base model and at the insertion into the femur in the scaled model.

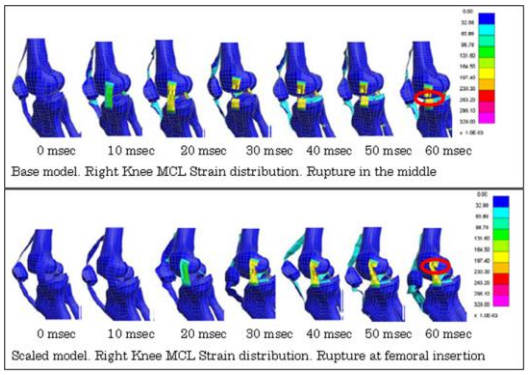

Fig. 14 Strain distribution in the knee ligaments in the Base model (above) and the Scaled model (below) of the test with a Small City Car

DISCUSSION

By using body external measurements and CT scan data measurements, two different scaled versions of the validated base model were developed. The scaled models were employed to simulate two full-scale tests with an SUV and a Small City Car, respectively. Both cases showed good correlation between the trajectories followed by the bodies in the simulations and the experimental results. In the Small City Car case, the scaled model was able to replicate the knee ligament injury sustained by the cadaver in the experiment at the exact injury site. When the same case was simulated with the base model (16cm taller than the scaled model), the same ligament rupture occurred, but at a different location. The difference in body size proved to affect the interaction between the vehicle and the loading mechanism of the lower limbs of the model from the beginning of the impact. The height at which the bumper hit the leg and loaded the knee complex defined the loading mechanism of the MCL until the rupture occurs. In the case of the base model, the bumper starts contacting with the leg at approximately the height of the knee. Both the femoral and the tibial head rotate laterally, causing tension on the MCL until it ruptures in the middle of the ligament. In the case of the scaled model, the impact is delivered at above the femoral head. This allows a bigger amount of energy to be delivered into the upper leg, causing a combined large shear-tension effort in the region closer to the insertion of the ligament into the femur, where the rupture occurs. Since it was reported from the experiments that the cadaver suffered a rupture of the MCL of the right knee at its insertion into the femur, based on the simulation

results, it can be said that only when the scaled version of the pedestrian model was utilized, and the site of the ligament injury could be simulated with accuracy. Although this finding requires further investigation until more reliable conclusions can be extracted, the authors of this study believe that these results indicate the importance of intensifying the ability of human models to simulate individuality with accuracy. Such upgraded human FE models can serve as a very powerful tool to understand injury mechanisms with local accuracy to allow taking efficient countermeasures to enhance the safety of vehicles.

LIMITATIONS

Although big effort was made in order to obtain accurate geometry from the two cadavers, other important human factors were not taken into consideration in this study. For example, the difference in material properties of the tissues between specimens, especially those of bones, ligaments and flesh, was not addressed in the models used in this study. In all cases, the same material properties were used. In addition, the fact that only two experimental cases were used in this research, and each of them was impacted by a different type of vehicle and under slightly different experimental conditions, does not allow isolating factors of interest such as the influence of the type of vehicle on the injury output. Finally, it is important to clarify that, according to ITARDA data, knee ligament ruptures are relatively uncommon in real-life car-pedestrian accidents (less than 3% of the cases). However, both of the experimental cases utilized in this study presented damage at the MCL in the knee of the struck side. This makes the authors of this study suspect that the body position at which the cadaver were impacted may not be representative of the pedestrian's impact position in real-life accidents. Hence, even if the pedestrian models present good correlation with the experiments used in this study, further research to define other real-life accident based on the representative postures of the pedestrian at the impact would be required. New tests with the defined significant postures and the respective improvement of the models should then follow.

CONCLUSIONS

By using body external measurements, radiological data measurements, and a scaling and posturing technique to modify the geometry of FE models, two different scaled versions based on the validated base model were developed. The scaled models were used to simulate 2 full scale car-pedestrian tests and showed good kinematic response in comparison with the experimental data. In the small City Car case, the simulation with the scaled model reproduced with high accuracy the location of the rupture of the Medial Collateral Ligament of the knee of the struck side. However, when the same case was simulated with the base model, a similar injury was observed in the same ligament, but at a different location. These results appear to point out the importance of intensifying the research to generate reliable individual models with the capacity to reproduce injuries with local accuracy.

REFERENCES

[1] http://www.npa.go.jp/toukei/index.htm

[2] Accident Analysis Report (JAPAN) institute for Traffic Accident Research and Data Analysis (ITARDA) 2007.

[3] Sugimoto and Yamazaki: First Results from the JAMA Human Body Model Project, Conference on the Enhanced Safety Vehicle, 2005, paper number 05-0291.

[4] Crandall: Simulating the road forward: the Role of computational modeling in realizing future opportunities in traffic safety, International Research Council on the Biomechanics of Injury, 2009.

[5] Bhalla, Montazemi, Crandall, Yang, Liu, Dokko, Takahashi, Kikuchi, Longhitano: Vehicle impact velocity prediction from pedestrian throw distance, Tradeoffs between throw formulae, crash simulators, and detailed multi-body modeling, International Research Council on the Biomechanics of Impact, 2002.

[6] Schroeder, Fukuyama, Yamazaki, Kamiji, Yasuki: Injury mechanism of pedestrians impact test with a sport-utility vehicle and mini-van, International Research Council on the Biomechanics of Injury, 2008.

[7] Subit, Kerrigan, Crandall, Fukuyama, Yamazaki, Kamiji, Yasuki: Pedestrian-vehicle interaction: kinematics and injury analysis of four full scale tests, International Research Council on the Biomechanics of Injury, 2008.

[8] Dhaliwal, Beillas, Chou, Prasad, Yang, King: Structural Response of Lower Leg Muscles in Compression: a Low Impact Energy Study Employing Volunteers, Cadavers and the Hybrid III, Stapp Car Crash Journal, Vol. 46 (November 2002), pp. 229-243.

[9] Thore, Zantop: Anatomy of the Anterior Cruciate Ligament with Regard to Its Tow Bundles, Clinical Orthopedics and Related Research, January 2007.

[10] Takahashi, Kikuchi, Konosu, Ishikawa: Development and Validation of the Finite Element Model for the Human Lower Limb of Pedestrians, 44th Stapp Car Conference, 2000.

[11] Kajzer, Schroeder, Ishikawa, Matsui, Bosch: Shearing and Bending Effects at the Knee Joint at High Speed Lateral Loading. SAE Paper 973326

[12] Wittek, Ishikawa, Matsui, Konosu: Validation and Parameter Study of a Multi-Body Model for Simulation of Knee Joint Responses in Lateral Impacts Representing Car-Pedestrian Accidents: Influences of Ligament Properties and Boundary Conditions on Model Responses, International Research Council on the Biomechanics of Impact, 2000.

[13] Dalstra et al.: Development and Validation of a Three-Dimensional Finite Element Model of the Pelvic Bone, Journal of Biomechanical Engineering, August 1995. Vol. 117, pp. 272-278.

[14] Guillemot, Besnault, Robin, Got, Yves Le Coz, Lavaste, Lassau: Pelvis Injuries in Side Impact Collisions: A Field Accident Analysis and Dynamic Tests on Isolated Pelvic Bones. SAE Paper 973322